Low Temperature Synthesis of Nanostructured Oxides for Dye Sensitized Solar Cells

CHAO ZHAO

PhD

2016

Low Temperature Synthesis of Nanostructured Oxides for Dye Sensitized Solar Cells

Chao Zhao

A thesis submitted in partial fulfilment
of the requirements of the
University of Northumbria at Newcastle
for the degree of
Doctor of Philosophy

Research undertaken in the
Faculty of Engineering and Environment

May 2016

Declaration

I hereby declare that the thesis is my own work and composed by myself except where are clearly indicated in the acknowledgements, references or text. All the work presented in this thesis has not been submitted in whole or part for any other degree, diploma or professional qualification. Any ethical clearance for the research presented in this thesis has been approved by the University Ethics Committee (Oct/2015) The word count of this thesis is approximate 39820 words.

Name:

Chao Zhao

_____

Date:

20/May/2016

_____

Acknowledgements

I would like to take this opportunity to thank many people for helping and supporting me get through my Ph.D. study.

Firstly and foremost, I express my hearty thanks to my principle supervisor, Dr. Richard Fu, for his supports and guidance during my study. I am appreciated that he provides me so many opportunities of joining in many research projects with different research group and universities. I shall never forget everything he has supported and provided for me.

I would like to express my gratitude to my second supervisor Dr. Guillaume Zoppi for supporting me help and facility training. I would also like to thank Miss. Arezoo Amirkhalili who provide help for magnetron sputtering operation training.

I would like to express my deep thanks to Prof. Neil Robertson (University of Edinburgh, UK) for allowing me to carry out research work in his lab and made me feel welcome. I thoroughly enjoyed all the discussions and experimental process. I would also like to acknowledge my friend Dr. Yue Hu, who provide help and kept me a companion.

Special thanks to Dr. Shun Cai Wang (University of Southampton) for TEM measurements.

I would like to thank Dr. Jia Zhang and Prof. Ping An Hu for offering me the opportunity to collaborate with them and the help of TEM measurements at Harbin Institute of Technology.

I thank all the support and help from Northumbria University, University of Edinburgh, University of the West Scotland and Scottish Universities Physics Alliance (SUPA).

I also thank all of my past and present group members and colleagues as well as technicians Mr. Gerry O'Hare, Mr. Andrew Bunyan, Dr. Liz Porteous and Dr. Pietro Maiello for helping on facilities training and my research work.

Finally, I would like to thank Northumbria University for supporting me the scholarship and all my family for unwavering support and love.

Abstract

Dye-sensitised solar cells (DSSCs) based on metal oxide semiconductor photoanodes (i.e. TiO_2, ZnO) offer a promising route for low-cost and transparent solar cells, especially suitable for indoor/outdoor applications, building and automotive integrated electricity generation. Apart from developing new dyes (or absorbers) for increasing absorption and stable fast-regenerated electrolytes, improving metal oxide photoanodes has also gained great research attention. In a conventional DSSC, the mesoporous TiO_2 photoanodes assembled by TiO_2 nanoparticles can support large surface areas for sufficient dye (absorber) loading, thus result in reasonably good solar cell performance. However, the poor pore-filling of large sized molecules (i.e. solid electrolyte) and inefficient electron transport lead to significant photo-generated charge recombination thus loss of photo-generated energy. Despite the reasonably good electron transport ability of the currently used particulate-based photoanodes, the requirements of high-temperature processes for these photoanodes significantly limit the substrate and material choices. In this thesis, a low-temperature strategy was designed to synthesise crystallised metal oxide (ZnO and TiO_2) nanostructures with controllable morphologies to be used as photoanodes with improved electron transport abilities for DSSCs.

ZnO nanorods (NRs) with tailored nanostructure (i.e. growth direction, aspect ratio and surface distribution density) were synthesised on pre-seeded substrates using zinc salt based aqueous solutions at temperatures generally lower than 95 °C. The influences of reaction temperature, pH, concentration, reaction duration and additives were systematically investigated. The detailed studies of nanostructures, morphology, crystallinity and properties of the ZnO NRs led to an improved understanding of the synthesis process.

Anatase TiO_2 modification layer was achieved using a plasma ion assisted deposition (PIAD) without external heating or subsequent annealing. Effects of the deposition parameters (duration, gas flow rates and plasma energy) on TiO_2 film properties (optical, structural and chemical activities) have been studied. By combining two low-temperature processes (aqueous solution growth of ZnO NRs and PIAD of crystalline TiO_2 nanostructures), nano-sculptured ZnO-TiO_2 nanostructures were achieved. The ZnO NRs were covered with a layer of anatase TiO_2 to form core-shell and foxtail-like nanostructures. These nanostructured photoanodes showed an improved electron transport as well as suppression of recombination capability in the DSSCs assembled by these photoanodes.

A novel in-situ microfluidic control unit (MCU) was designed and applied in the aqueous solutions synthesis process, which provided an easy way to localize liquid-phase reaction and realise selective synthesis and direct growth of nanostructures, all in a low-temperature and ambient pressure environment. The morphology of the nanostructures was controlled by varying the amount of additivities supplied by the MCU. This achieved a facile fabrication of Al-doped ZnO (AZO) nanoflakes vertically grown on flexible polymer substrates with enhanced dye loading and electron transporting capabilities. Flexible DSSCs with a significant enhancement (410% compared to ZnO NRs based devices) in the power conversion efficiency were obtained using the AZO nanoflakes photoanodes of 6 ı m thickness, due to the enhancement in electron transport capability of the photoanodes and reduction in the recombination process.

Contents

List of Figures

List of Tables

List of journal publications and conference presentations

From this thesis

- Chao Zhao, Jia Zhang, Yue Hu, Neil Robertson, Ping An Hu, David Child, Desmond Gibson, Yong Qing Fu: In-situ microfluidic controlled, low temperature hydrothermal growth of nanoflakes for dye-sensitized solar cells. Scientific Reports 12/2015; 5:17750. DOI:10.1038/srep17750
- Chao Zhao, David Child, Yue Hu, Neil Robertson, Des Gibson, Shun Cai Wang, Richard Fu: Low temperature growth of hybrid ZnO/TiO_2 nano-sculptured foxtail-structures for dye-sensitized solar cells. RSC Advances 11/2014; 4(105). DOI:10.1039/c4ra11881b
- Chao Zhao, David Child, Des Gibson, Frank Placido, Yongqing Fu: TiO_2 films prepared using plasma ion assisted deposition. Materials Research Bulletin 12/2014; 60: Pages 890¯894.DOI: 10.1016/j.materresbull.2014.09.022
- Nisar Ali, Arshad Hussain, Rashid Ahmed, Mingkui Wang, Chao Zhao, Bakhtiar Ul Haq, Yongqing Fu: Advances in nanostructured thin film materials for solar cell applications. Renewable and Sustainable Energy Reviews 06/2016; 59:726-737. DOI: 10.1016/j.rser.2015.12.268
- Conference paper on `Dye sensitized Solar cell based on nanostructured ZnO/TiO2 core-shell structures_, Chao Zhao, David Child, Yue Hu, Neil Robertson, Des Gibson, Richard Fu; 7th International Conference on Thin Film Technologies, China, July, 2014.
- Solar Energy Conference 2014, held by Scottish Institute for Solar Energy Research (SISER), Award Poster Highly Commended by SISER
- SUPA Annual Meeting Posters, Glasgow (26/04/2013). `Dye sensitized Solar cell based on ZnO nanostructure_ Poster and presentation
- Research Student Conference/Poster Event, UWS, (May 2013). `Dye sensitized Solar cell based on ZnO NRs_ Poster and presentation

Related journal publications during PhD study

- Jia Zhang, Chao Zhao, Na Liu, Huanxi Zhang, Jingjing Liu, Yongqing Fu, Bin Guo, Zhenlong Wang, Shengbin Lei, PingAn Hu: Tunable electronic properties

of graphene through controlling bonding configurations of doped nitrogen atoms. Scientific Reports, 06/2016; 6:28330. DOI:10.1038/srep28330

¿ Yuaniun Guo, Chao Zhao, Xiaosong Zhou, Yifan Li, Xiaotao Zu, Des Gibson, Yongqing Fu: Ultraviolet sensing based on nanostructured ZnO/Si surface acoustic wave devices. Smart Materials and Structures 12/2015; 24(12):125015. DOI:10.1088/0964-1726/24/12/125015

¿ Haibao Lu, Ming Lei, Chao Zhao, Yongtao Yao, Jihua Gou, David Hui, Yongqing Fu: Controlling Au electrode patterns for simultaneously monitoring electrical actuation and shape recovery in shape memory polymer. Composites Part B Engineering 05/2015; 80. DOI: 10.1016/j.compositesb.2015.05.039

¿ S.Y. Wang, Zhijie Li, Xiaosong Zhou, Chao Zhao, Xiaotao Zu, Yongqing Fu: Advances in Nanostructured Acoustic Wave Technologies for Ultraviolet Sensing. Nanoscience and Nanotechnology Letters 03/2015; 7(3):169-192. DOI:10.1166/nnl.2015.1968

¿ Haibao Lu, Ming Lei, Chao Zhao, Ben Xu, Jinsong Leng, Yongqing Fu: Structural design of flexible Au electrode to enable shape memory polymer for electrical actuation. Smart Materials and Structures 04/2015; 24(4). DOI:10.1088/0964-1726/24/4/045015

¿ Xiaosong Zhou, Chao Zhao, Roger Hou, Jia Zhang, Katherine Kirk, David Hutson, Yuanjun Guo, Pingan Hu, Shuming Peng, Xiaotao Zu, Yongqing Fu: Sputtered ZnO film on aluminum foils for flexible ultrasonic transducers. Ultrasonics 05/2014; 54(7). DOI: 10.1016/j.ultras.2014.05.006

¿ Jia Zhang, Chao Zhao, Pingan Hu, Yongqing Fu, Zhenlong Wang, Wenwu Cao, Bin Yang, Frank Placido: A UV light enhanced TiO_2/graphene device for oxygen sensing at room temperature. RSC Advances 08/2013; 3(44). DOI:10.1039/c3ra43480j

¿ Xiaosong. Zhou, Jia Zhang, Roger. Hou, Chao Zhao, Katherine Kirk, David Hutson, Pingan Hu, S.M. Peng, Xiaotao Zu, Yongqing Fu: Electrode loading effect and high temperature performance of ZnO thin film ultrasonic transducers. Applied Surface Science 10/2014; 315(1):307¯313. DOI: 10.1016/j.apsusc.2014.07.114

¿ Dajian Li, Chao Zhao, Yongqing Fu, Jikui Luo: Engineering silver nanostructures for surface acoustic wave humidity sensors sensitivity

enhancement. Journal of The Electrochemical Society 01/2014; 161: b151. DOI: 10.1149/2.094406jes

- Yongqing Fu, Yifan Li, Chao Zhao, Frank Placido, Anthony J Walton: Surface acoustic wave nebulization on nanocrystalline ZnO film. Applied Physics Letters 11/2012; 101(101):194101. DOI:10.1063/1.4767126
- Des Gibson, David Child, Shigeng Song, Chao Zhao, Yahya Alajlan, Ewan Waddell: Control of ordered mesoporous titanium dioxide nanostructures formed using plasma enhanced glancing angle deposition. Thin Solid Films 04/2015; 592. DOI: 10.1016/j.tsf.2015.04.063
- Yuaniun Guo, Jia Zhang, Chao Zhao, JinYi Ma, Huafeng Pang, Pingan Hu, Frank Placido, Des Gibson, Xiaotao Zu, H Y Zu, Yongqing Fu: Characterization and humidity sensing of ZnO/42 degrees YX LiTaO3 Love wave devices with ZnO nanorods. Materials Research Bulletin 04/2012; 48(12). DOI: 10.1016/j.materresbull.2013.04.072
- Haibing Læ, Shizhen Xu, Haijun Wang, Xiaodong Yuan, Chao Zhao, Yongqing Fu: Evolution of Oxygen Deficiency Center on Fused Silica Surface Irradiated by Ultraviolet Laser and Posttreatment. Advances in Condensed Matter Physics 05/2014; 2014(2):1-4. DOI:10.1155/2014/769059
- Yang Liu, Yifan Li, Ahmed. M. el-Hady, Chao Zhao, Jiangfeng. Du, Yongqing Fu: Flexible and bendable acoustofluidics based on ZnO film coated aluminium foil. Sensors and Actuators B Chemical 07/2015; 221:230-235. DOI: 10.1016/j.snb.2015.06.083
- Ruozhou Hou, Yongqing Fu, David Hutson, Chao Zhao, Esteban Gimenez, Katherine Kirk: Use of sputtered zinc oxide film on aluminium foil substrate to produce a flexible and low profile ultrasonic transducer. Ultrasonics 02/2016; 68. DOI: 10.1016/j.ultras.2016.02.008
- Liu Yong, Jingting Luo, Chao Zhao, Jian Zhou, Sameer Ahmad Hasan, Yifan. Li, Michael Cooke, Qiang Wu, Waipang Ng, Jiangfeng Du, Qi Yu, Yang Liu, and Yongqing Fu, Annealing Effect on Structural, Functional, and Device Properties of Flexible ZnO Acoustic Wave Sensors Based on Commercially Available Al Foil. IEEE Transactions on Electron Devices, 2016. 63(11): p. 4535-4541.

Chapter 1 Introduction

1.1 Research motivation

The world˘s rapid economic and industrial development results in an increase in energy demands. However, the paradox is that the growing energy demand cannot be met by the limited fossil energy reserves. Additionally, although the fossil fuel energy boosted the industrial revolution in 18~19th century, the use of fossil energy has already caused lots of negative effects on the environment (i.e. acid rain, ozone depletion and global warming).[1, 2] The general consensus on how to solve this problem is to develop renewable energy technologies, which mainly include solar energy, wind energy, biomass, biofuel, tidal wave energy and hydropower. Among these, solar energy shows a promise as one of the best renewable energy sources and tranhas the most abundant reserves of energy storage to be collected.[3] If a small fraction of this huge amount of energy can be changed to usable energy forms, the increasing demand of energy can be easily tackled. Solar energy (sunlight) can be collected either by converting sunlight into electricity or using sunlight to heat or drive chemical reactions. The device used for achieving the conversion of sunlight to electricity is called photovoltaic (PV) solar cells.[4] In the past decades, PV has attracted continuous research interest due to its unique functions.

Dye sensitised solar cell (DSSC) has received enormous research attention since the well-known titanium dioxide (TiO_2) mesoporous photoanode based DSSC was proposed by Gr±tzel et al in 1991.[5, 6] DSSCs have advantages of low cost and easy fabrication process (only need 1/10~1/15 of the cost used for conventional Si-based solar cell), adjustable light absorption range, a variety of appearance colour and possibility of fabrication on flexible substrates.[7-10] Their unique advantages also make

the DSSCs as one of the most promising candidates for both indoor and building integrated PV applications.[7] After two decades of studies, the overall performance has improved slowly and achieved a power conversion efficiency (PCE) of 13.1%, reported by Y ella et al.[9] Recently, one of the major reasons for preventing further improvements in performance is the inefficient electron transport, typically the TiO_2 mesoporous photoanode, which causes recombination between photo-generated electrons and the oxidised redox species in the electrolyte (and/or oxidised dye). Improving photoanode properties are considered as a possible breakthrough to overcome this limitation.

Zinc oxide (ZnO) is an alternative wide bandgap semiconductor, compared to the TiO_2 which has been widely used so far in DSSCs, due to its similar energy-band structure to those of TiO_2 but with a much higher electron mobility.[11] In addition, ZnO is a low-cost oxide semiconductor material which can be produced in a large variety of nano-morphologies using inexpensive synthesis processes. Although a lot of efforts have been made on developing ZnO nanostructured DSSCs with a high PCE, so far, the PCE of ZnO based DSSCs is still relatively low (generally lower than 7 %) when compared with those of the TiO_2 based DSSCs. The main drawbacks of the ZnO based DSSC are the unstable chemical properties of ZnO in acidic solution environment (i.e. acidic dye solution cause dissolution/correction of ZnO surface, as a result, Zn^{2+}/dye agglomerates will form) and inefficient electron-injection from dyes to ZnO. The Zn^{2+}/dye agglomerates will cause photocurrent reduction because they hamper the normal electron injection from dye to metal oxide. In addition, these agglomerates will block the spaces which are needed for the dye, thus reducing the dye loading capability of the nanostructure.

In order to overcome these problems, core-shell and hybrid structures have been proposed for improving the photoanode stability.[12, 13] This has also been considered as an efficient way to improve the interfacial electron injection and suppress recombination at the semiconductor/dye/electrolyte interfaces for achieving the best performance of the DSSCs. By modifying the ZnO with another buffer material layer on its surface, a large surface area can be maintained and also the requirements for electron injection and suppressed electron back transfer and recombination can be achieved. Therefore, combination of ZnO with other materials would improve the development of ZnO based DSSCs. Different materials (i.e. TiO_2, SiO_2, Al_2O_3 and MgO) have been studied as the modification shell/layer, because their band gaps match those of the dye and electrolyte,[14, 15] which make them suitable as alternative materials for improving electron mobility as well as preventing electron back transport. Although the use of these semiconductor shells can improve ZnO nanostructure based DSSCs, the shell and hybrid material effects on the DSSC performance are still not very clearly. Further investigation is needed for a better understanding of the shell effects as well as how to achieve an optimal enhancement of overall performance of the DSSCs. Despite improved electrical properties (i.e. electron transport and recombination suppression ability) and porosity of the photoanode, the required high-temperature process to achieve typical DSSC photoanodes limit the choices of substrate and material. Therefore, the objective of this thesis is to achieve different low-temperature synthesis strategies for producing crystallised ZnO based (with crystallised TiO_2 as the shell) nanostructures with controllable morphology as the photoanode for the DSSCs.

1.2 Outline of the thesis

For the structure of the thesis, a literature review of the DSSCs, ZnO based nanostructure synthesis and its applications for DSSCs is presented in Chapter 2. In Chapter 3, details of the experimental work including DSSC fabrication and characterisation processes carried out in this study are provided. In Chapter 4, low-temperature synthesis of crystallised ZnO NRs using a aqueous solution process is introduced in detail. Effects of reactants, chemical reaction factor and additive effects on the ZnO NRs growth are discussed. The major objective of Chapter 5 is to develop a low-temperature process for preparing the anatase TiO_2 layer which can be used to assemble ZnO/TiO_2 core-shell structure. Particularly, the effects of process gas, plasma and plasma energy on structure and properties of as-prepared low temperature crystallised TiO_2 film are investigated. In Chapter 6, a low-temperature synthesis strategy of ZnO/TiO_2 nanostructure is discussed, which using two sequential cost-effective processes combining aqueous solution growth of ZnO NRs (developed in Chapter 4) and anatase crystalline TiO_2 (developed in Chapter 5). Therefore, the photoanodes with controllable morphologies as well as function properties of photoanodes are discussed. In Chapter 7, a unique low-temperature, template-free approach to produce vertically aligned Al doped ZnO nanoflakes and ZnO NRs/Al doped ZnO nanoflakes hybrid structures is demonstrated for the DSSC photoanode application. The material synthesis, characterisation and its effect on device performance are summarised and discussed. Lastly, conclusions of this work and suggested future work are listed in Chapter 8.

Reference

1. Houghton, J.T., Global warming: the complete briefing. 4th ed. ed. 2009, Cambridge: Cambridge University Press.
2. IEA., CO_2 Emissions from Fuel Combustion 2012. OECD Publishing.
3. Morton, O., Solar energy: A new day dawning?: Silicon Valley sunrise. Nature, 2006. 443(7107): p. 19-22.
4. Kalyanasundaram, K., Dye-sensitized Solar Cells. 2010: CRC Press.
5. EarlyHistory. Workspace.imperial.ac.uk. Retrieved on 30 May 2013.
6. O'Regan, B. and M. Gratzel, A low-cost, high-efficiency solar cell based on dye-sensitized colloidal TiO_2 films. Nature, 1991. 353(6346): p. 737-740.
7. Fakharuddin, A., R. Jose, T.M. Brown, F. Fabregat-Santiago, and J. Bisquert, A perspective on the production of dye-sensitized solar modules. Energy & Environmental Science, 2014. 7(12): p. 3952-3981.
8. Green, M.A., K. Emery, Y. Hishikawa, W. Warta, and E.D. Dunlop, Solar cell efficiency tables (Version 45). Progress in Photovoltaics: Research and Applications, 2015. 23(1): p. 1-9.
9. Yella, A., H. W. Lee, H.N. Tsao, C. Yi, A.K. Chandiran, M.K. Nazeeruddin, E.W. G. Diau, C. Y. Yeh, S.M. Zakeeruddin, and M. Gr±tzel, Porphyrin-Sensitized Solar Cells with Cobalt (II/III)¯Based Redox Electrolyte Exceed 12 Percent Efficiency. Science, 2011. 334(6056): p. 629-634.
10. Marchioro, A., J. Teuscher, D. Friedrich, M. Kunst, R. van de Krol, T. Moehl, M. Gratzel, and J. E. Moser, Unravelling the mechanism of photoinduced charge transfer processes in lead iodide perovskite solar cells. Nat Photon, 2014. 8(3): p. 250-255.
11. Zhao, C., D. Child, Y. Hu, N. Robertson, D. Gibson, S.C. Wang, and Y.Q. Fu, Low temperature growth of hybrid ZnO/TiO_2 nano-sculptured foxtail-structures for dye-sensitized solar cells. RSC Advances, 2014. 4(105): p. 61153-61159.
12. Anta, J.A., E. Guill¶n, and R. Tena-Zaera, ZnO-Based Dye-Sensitized Solar Cells. The Journal of Physical Chemistry C, 2012. 116(21): p. 11413-11425.
13. Gong, J., J. Liang, and K. Sumathy, Review on dye-sensitized solar cells (DSSCs): Fundamental concepts and novel materials. Renewable and Sustainable Energy Reviews, 2012. 16(8): p. 5848-5860.
14. Zhang, Z., S. Ito, B. O'Regan, D. Kuang, S.M. Zakeeruddin, P. Liska, R. Charvet, P. Comte, M. K. Nazeeruddin, P. P¶chy, R. Humphry-Baker, T. Koyanagi, T. Mizuno, and M. Gr±tzel, The Electronic Role of the TiO_2 Light-Scattering Layer in Dye-Sensitized Solar Cells. Z. Phys. Chem, 2007. 221: p. 319-328.
15. Xu, Y. and M.A.A. Schoonen, The absolute energy positions of conduction and valence bands of selected semiconducting minerals. American Mineralogist, 2000. 85(3-4): p. 543-556.

Chapter 2 Literature review

2.1 Introduction

Photovoltaic (PV) effect was discovered by Edmond Becquerel in the 19th century. Subsequently, it has been identified as one of the promising alternative renewable energy resources. Solar energy appears not only as a clean energy resource, but also as a better off-grid choice in the integrated applications for small scale and portable electronics. Research on the solar cells has been established for around 60 years since the first practical solar cell was fabricated.[1] In recent decades, incremental improvements of materials have been made and benefited the solar cells development. With the constant development of new materials and solar cell structures, the record of highest solar power conversion efficiency (PCE) is constantly refreshed. Until now (Aug/2016), the highest PCE (46%) of solar cell is achieved by Fraunhofer Institut für Solare Energiesysteme (Figure 2-1).[2]

Solar cells nowadays can be divided into three main types:[1, 3] (a) silicon based solar cells; (b) thin film solar cells (i.e. CdTe, $CuInGaSe_2$) which are normally made of thin layers of semiconductor materials with much thinner thickness (~ several microns) than the conventional silicon ones (~300-400 μm); (c) molecular absorber mesoscopic solar cells in which nanostructured materials have been used as electrodes for holding organic/inorganic molecule absorbers. These molecular absorbers involved in the solar cells are normally known as `the third generation solar cell'.[1] Typical examples of the molecular absorber mesoscopic solar cells are organic solar cells, DSSCs, quantum dot solar cells as well as recently emerged perovskite solar cells.

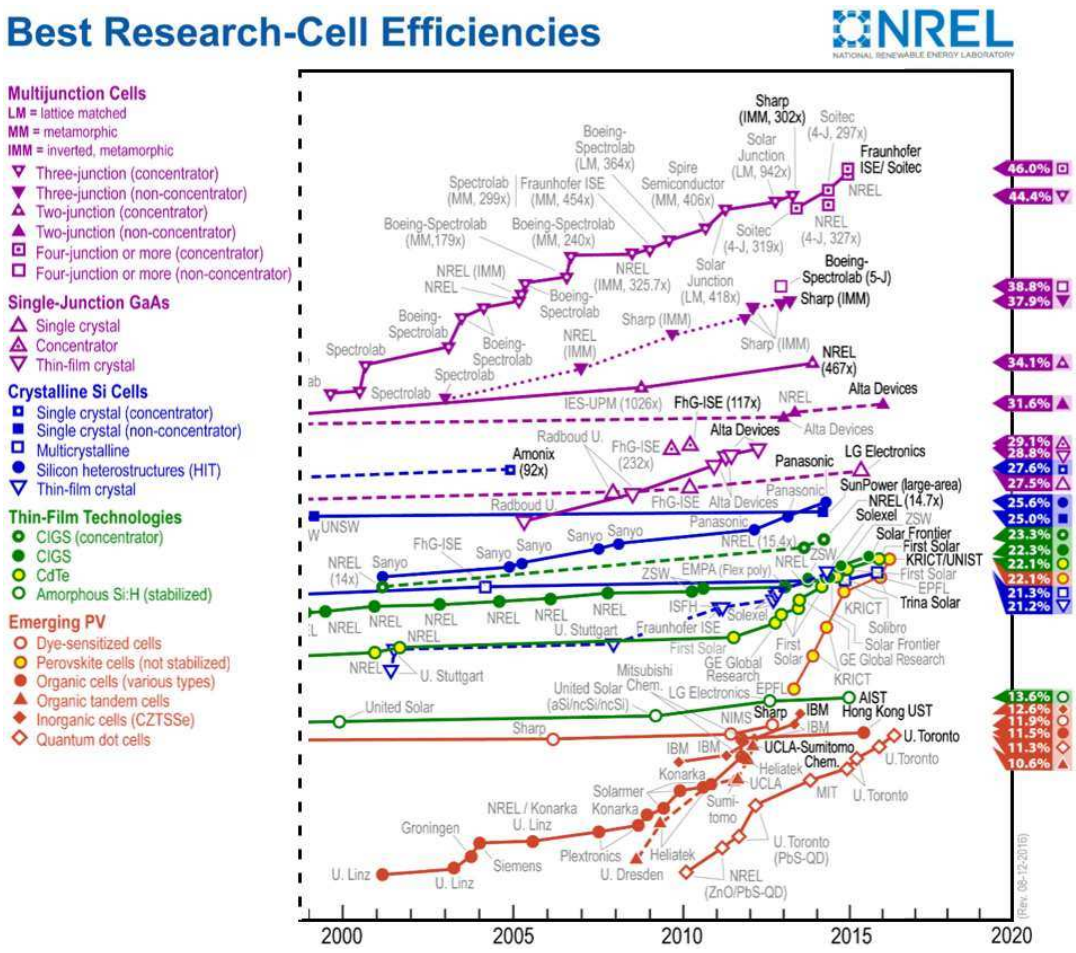

Figure 2-1 NREL ˇs latest chart of classification and development of solar cells (cited in Aug/2016, From http://www.nrel.gov/pv/assets/images/efficiency_chart.jpg).[2]

The DSSC has dramatically attracted researchers ˇ attention from its early research stage. After nearly two decades of studies, the DSSCs have achieved a PCE over 12% with advantages of low-cost fabrication, a variety of appearance colour and possibility of fabrication on flexible substrates.[4-6] The DSSCs have widely been regarded as one of the most promising candidate PV devices for both indoor and building integrated PV applications (Figure 2-2).[1, 7-9] Extensive research has been done to realise the DSSCs for indoor and building integrated PV applications in many industries and research institutes, for example Dyesol (Australia), Solaris (USA), Mitsubishi (Japan), G24i (UK).[1, 6, 10-12]

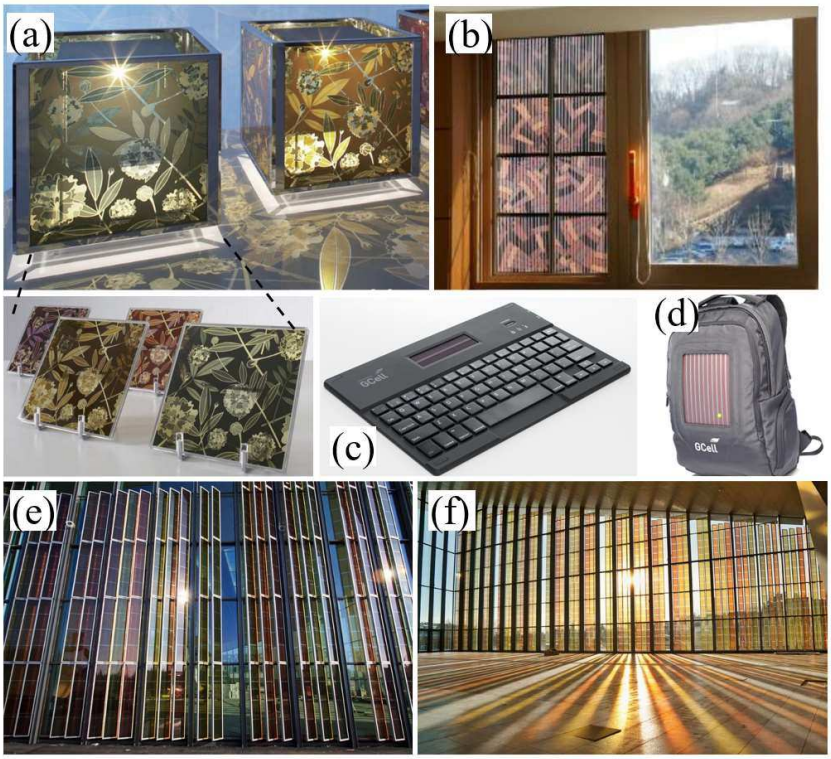

Figure 2-2 Examples of DSSC based indoor and building integrated PV applications (a) Hana-Akari lantern with changeable pattern and colour; (b) an example of commercial DSSC window demonstration; (c) and (d) images of some commercial DSSC products (products of G24i); (e) and (f) large scale building integrated DSSC application in § cole polytechnique f¶d¶rale de Lausanne (EFPL) campus.[1, 7-9]

2.2 Dye sensitized solar cell

The well-known nano-crystalline TiO_2 mesoporous DSSC with a high PCE was proposed by Brian O˘Regan and Michael Gr±tzel in 1991.[13-15] Afterwards, the DSSCs have attracted great attention and been considered as promising devices for solar energy conversion because of their unique advantages. [13-15] The conventional DSSCs have a sandwich structure with the following components from bottom to top as shown in Figure 2-3 (a):[15]

(1) A transparent photoanode made up of a fluorine doped tin oxide (FTO) or indium tin oxide (ITO) coated glass substrate with a mesoporous metal oxide (MO) layer (typically TiO_2) for supporting a monolayer of chemisorbed dye molecules on its surface as well as acting as a medium for electron transportation. Generally, FTO and ITO are called transparent conducting oxides (TCOs).

(2) A liquid electrolyte containing redox couples (typically, iodide (I^-)/triiodide (I_3^-)) for sufficient dye regeneration;

(3) A transparent counter electrode (CE) is made of an ITO or FTO glass substrate with catalyst (typically platinum (Pt)) to reduce oxidised redox mediator (typically, I_3^- to I^-).

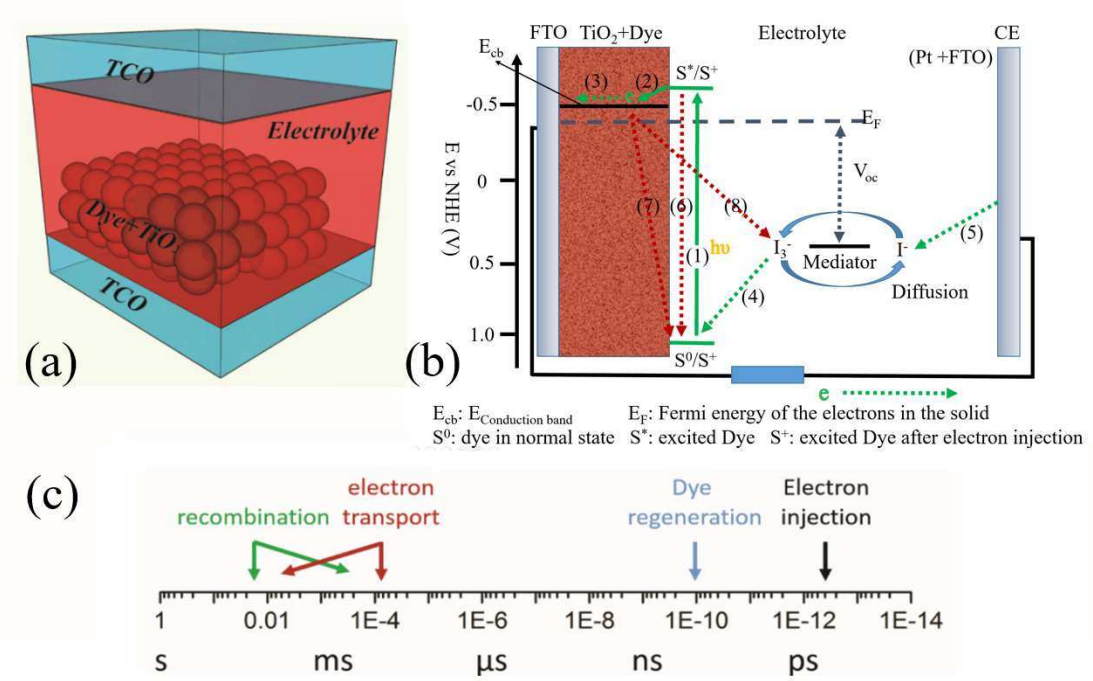

Figure 2-3 Schematic illustration of (a) standard DSSCs structure (b) the operation principle of a DSSC: the processes line mark in green stands for light to electric power conversion process; in red the processes degrading the DSSCs˘ performance. (c) Typical operation of the DSSCs with time requirement for each step.[15, 16]

The DSSCs work like an artificial leaf. Mesoporous MO photoanode can be considered as thylakoid which is mainly used for supporting sufficient absorber as well as transporting photo-generated electrons. Dye molecules are working as chlorophyll for absorbing light and producing electrons. The electrolytes with the redox couple work as a base material in the leaf to reduce the oxidised absorber. When the DSSC is exposed to the sunlight, light is absorbed/harvested by the absorber (dye molecules) chemisorbed on the surface of TiO_2 nanoparticle. Light excited absorbers inject electrons into the conduction band (CB) of the MO (typically, TiO_2 nanoparticles) on photoanode. These electrons are then transported through the TiO_2 nanoparticle mesoporous films and external circuits. The rest of oxidised dyes (after dye molecules injected electron to MO) are regenerated to the normal state by redox couple (i.e. I_3^- and I^-) in the electrolytes. The I_3^- and I^- redox couple works in the following steps. After I^- is used for regenerated dye molecule back to the normal state, it will change to I_3^- which will then be reduced back to I^- by the electrons from the Pt coated CE.[11] The detailed working principle can be described as follow (Figure 2-3 (b)):[15-18]

(1) Photo-excitation of dye molecules. When the dye molecule is excited by a photon, an electron will be promoted from highest occupied molecular orbital (HOMO, a low-energy state) to lowest unoccupied molecular orbital (LUMO, a high-energy state).

Excitation 侦鼾厦伝尭嚇喘金絲km³侦是厦伝尭* (Eq. 2-1)

(2) The photo-generated electron will be injected into the CB of the MO semiconductor with a typical rate of 10^{10}~10^{12} s^{-1}.

Injection 侦是厦伝尭*km³侦鼾厦伝尭嚇喘佳嚇 (Eq. 2-2)

(3) Then the injected electron travels through the MO semiconductor by diffusion with random pathways until it reaches the TCO substrate which is contacted to the external circuit. The rate of this process is normally 10^0~10^3 s^{-1} which is strongly dependent on the MO properties (i.e. electron mobility).

Charge transport in MO (Eq. 2-3)

(4) After the electron injection step (step (2)), the excited dye becomes to its oxidised state. Then the oxidised dye is reduced by redox pair rapidly and returns back to the original state. The typical rate of this process is ~10^8 s^{-1} as shown in Figure 2-3 (c).

Regeneration (Eq. 2-4)

(5) Electrons travel through external circuit (Step (3)) and back to Pt CE. The) ions diffuse through the electrolyte to the Pt CE, where it will be reduced back to I^- by the electrons from the Pt CE.

Deoxidizing reaction (Eq. 2-5)

The electrons, which are collected by the MO semiconductor material on the TCO substrate, will go through the outer circuit, and then reach the Pt CE, forming an integrated circuit. Compared with the conventional p-n junction based solar cells, the semiconductor component in a typical DSSC does not perform the double functions of light absorption and free carrier transportation.[15, 19] The dual functions in the DSSC are decoupled by the separating components (dye for light absorption, MO semiconductor and electrolyte for carrier transport).[15, 19] This means that for the DSSCs, the requirements of high purity semiconductor materials for achieving a

controllable doping as well as preventing recombination in p-n junction solar cell is unnecessary.[13-15]

Numerous research attempts have been made to further improve the overall performance of the DSSCs for practical applications. Unfortunately, the overall performance is still limited to around 12% despite different attempts (thousands of papers had been published) being made in the past 10 years.[11] One of the major reasons for this performance limitation is that several reverse reactions simultaneously exist along with the operation reaction. These reverse reactions limit the performance of the cell as illustrated in Figure 2-3 (b) by red arrows and Figure 2-3 (c) with relative reaction time.[17, 20] The electrons which have been injected into MO will not only travel through MO but also have a very high chance to recombine with the oxidised dye molecules (Figure 2-3 (b), (7), Eq. 2-6) and/or acceptors in the electrolyte (Figure 2-3 (b), (8), Eq. 2-7).

Recombination (Eq. 2-6)

Electron recaptures (Eq. 2-7)

These reversed reaction time are similar to those required for electron transportation (as shown in Figure 2-3 (c)), which indicates that the electrons cannot be transported to the outer circuit because of recombination. This has been considered as one of the major drawbacks of the DSSCs that limit the further improvement of device performance. In contrast to the theoretical performance and the achieved best overall performance in different types of DSSCs, the practical performance of the DSSCs is still very low. Therefore, it is believed that there is a large chance for the improvement of the DSSCs performance by solving the problem mentioned above. The fundamental understanding

of the underlying mechanism in the DSSCs and applicable innovations of materials and structures are critical for further improving the overall performance. Apart from developing more efficient and stable absorbers, redox species (and/or hole transport material (HTM)), modification of the photoanode has also been suggested to solve this problem.[10, 17, 20] In this thesis, we will focus on photoanode modification for improving the DSSC performance.

2.2.1 Basic concepts in characterisation of solar cells

2.2.1.1 Air mass

The solar radiation reaching the surface of earth is dependent on a number of factors. Before the sunlight arrives at the surface of the earth, it has to travel through the atmosphere. While the sunlight goes through the atmosphere, ultraviolet light has been absorbed by ozone (O_3) and oxygen (O_2), and the infrared region and part of visible range light has been absorbed by water vapour (H_2O) with nitrous oxide (N_2O), carbon dioxide (CO_2) and methane (CH_4) interaction and scattered by dust and/or particles. [21, 22] As a result, the sunlight reaching the earth surface at different angles and/or different part of atmosphere will have different spectra as shown in Figure 2-4.

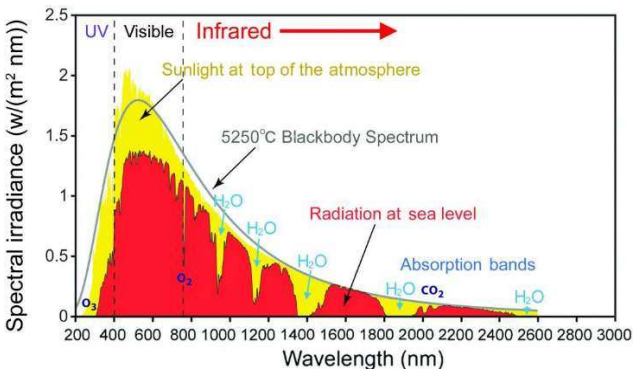

Figure 2-4 Solar irradiance spectrum changing from top of the atmosphere to sea level earth surface;[21, 22]

Air mass (AM) coefficient has been employed to identify this issue, which describes the direct optical path length through the earth˘s atmosphere. It can be simplified to the relationship between light path length (L), the thickness of atmosphere (L_A) and solar radiation incident angle :; expressed as:

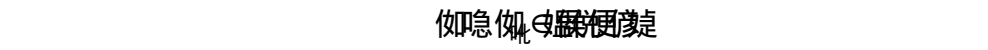

(Eq. 2-8)

where ::is the angle between sea leave and zenith, the ratio L/L_A is called air mass coefficient.

Thus, the solar radiation spectrum outside the atmosphere is defined as `AM0_ which means zero atmosphere. The solar radiation spectrum travelling through atmosphere to sea level vertically (:=90°C) is defined as `AM 1_. The well-known AM 1.5 standard testing condition generally used by solar cell researchers and industry organization has been chosen because it is useful to represent the overall annually average value for mid-latitude and suitable for most of countries in the temperate latitudes.[22]

2.2.1.2 Current¯voltage curve

Current density-voltage (J-V) curve is one of the important characteristic outputs for any photovoltaic cells, in which the current density (J) refers to the ratio of the current output from the testing solar cell to cell area. From J-V curve (Figure 2-5), the voltage and current density of a solar cell changes with load resistance varying from infinity (open circuit) to zero (short circuit). Additionally, the power output of the cell per unit area can also be obtained using a simple equation,

$$P = JV \qquad \text{(Eq. 2-9)}$$

Thus, from J-V (and P-V) curve (Figure 2-5), the basic solar cell parameters of open circuit voltage (Voc) and circuit current density (Jsc) can be readily obtained. Fill factor (FF) and the overall power conversion efficiency (PCE) can then be calculated. FF is defined as following equation:

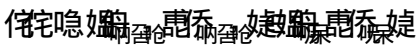

(Eq. 2-10)

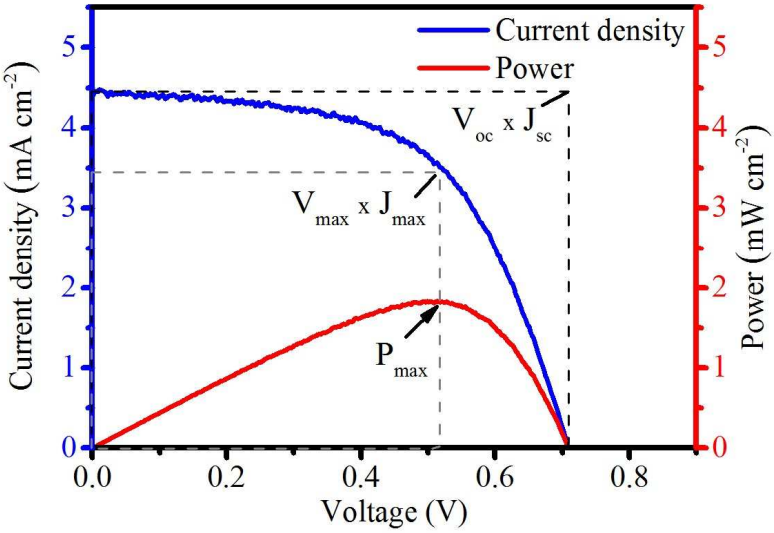

Figure 2-5 Example performance J-V and P-V curve for DSSCs with solar cell parameters.

The solar cell PCE is the ratio between the solar cell˘s maximum output power density (P_{max}) and the power of incident light (P_{in}) which can be expressed as:

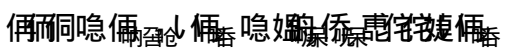

(Eq.2-11)

Though the basic operating principle of the DSSC is different from the well-known Si-based p-n junction solar cells, J-V characteristics can still be explained using the classical equivalent circuit designed to describe non-ideal diode behaviour of the p-n junction based cells, with modified identification of each components as proposed in previous researchers˘ study.[23, 24]

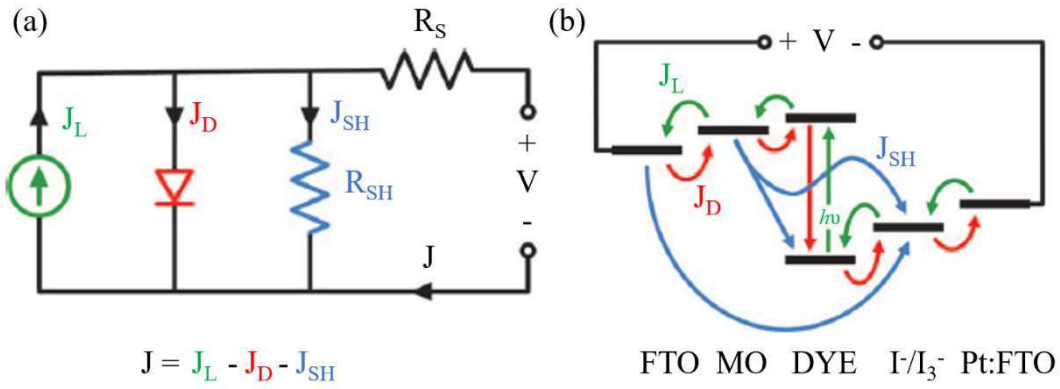

Figure 2-6 (a) Simplified equivalent circuit for modelling DSSC current-voltage characteristics with (b) its unique working principle and energy level diagram of the various charge transfer processes in a cell. Resistance and diode after these components in DSSC was not shown in this figure.[23, 24]

As shown in Figure 2-6 (a), a simplified DSSC can be considered as a current density source (J_L) in parallel with linear (J_{SH}), and non-linear (J_D) reverse current density in parallel and a series resistance (Rs) to account for electrode resistance. Considering the complex working principle of the DSSCs, each component can be attributed to multiple charge transfer processes that occur in the cell (shown in Figure 2-6 (b) marked with different colour corresponding to the components). J_L refers to the `positive_ process in the DSSC which contains light absorption and excitation of dye molecular, electron injection and transport through the MO to the outside of the cell (i.e. circuit), marked as green in Figure 2-6 (b). J_{SH} and J_D refer to current densities in different recombination processes (marked as blue and red in Figure 2-6 (b)) in the cell working process. Thus, according to this simplified model, the output current of the DSSC can be expressed as a function of applied bias voltage:

佾隐佾营佾□□□

where J_0 is the reverse saturation current, T is the absolute temperature, A is the DSSC active area, q is the electronic charge, 伾is the ideality factor and k is the Boltzmann constant. The R_{SH} and Rs mainly affect the FF of the cell, as shown in Figure 2-7. Rs is the sum of net resistance in the DSSC model. It is mainly affected by resistance of the redox couple in electrolyte, MO and electrodes. [23, 24] R_{SH} is mainly attributed to the recombination of carriers (i.e., injected electrons oxidised dye molecules and acceptors in the electrolyte) in the cell.[23, 24]

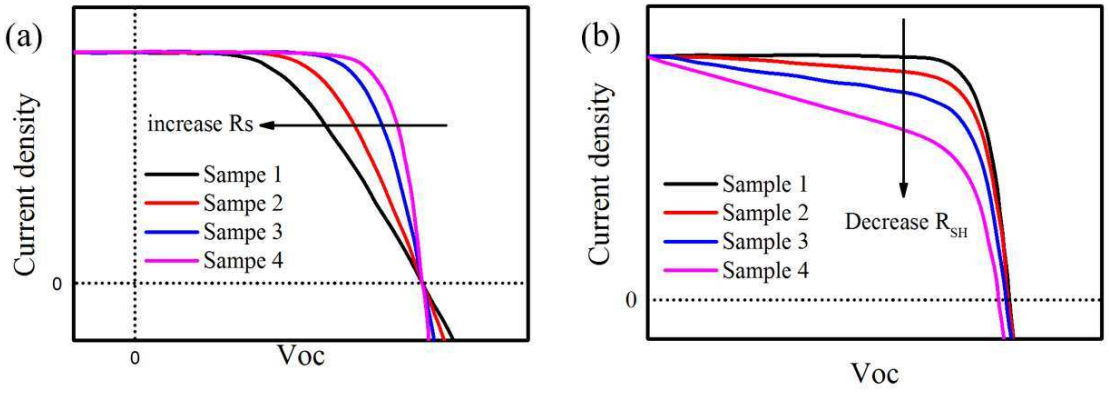

Figure 2-7 Impact of (a) series resistances and (b) shunt resistances on the J-V characterisation of DSSCs.[23]

However, it is hard to identify this directly from this simple model to understand the recombination issue in the DSSCs. To obtain a deeper understanding of working behaviour of the DSSCs and overcome the limitation of simple current-voltage analysis, measurements of solar cells after optical or electrical perturbations have been developed to meet this requirement. These techniques test the responses of cells to periodic perturbations (i.e. intensity modulated photocurrent (or photovoltage) spectroscopy (IMPS or IMVS) and electrochemical impedance spectroscopy (EIS)). Testing the response of the cell to a single perturbation (i.e. transient photo voltage/current measurement) which will be the primary focus of this thesis. This is because the single

perturbation transient measurements do have some unique advantages. The testing can be done at an adjustable condition more rapidly without limitation of periodic perturbation requirement; the results and information obtained from the measurements are simple and easier to understand;[25] and electron transport time and lifetimes can be easily obtained without any equivalent circuits.[25] In this thesis, it is aimed to use transient photo-voltage/current to investigate the electron transport and recombination kinetics of the DSSCs.

The DSSC is one complex photocurrent conversion system. The whole process is accomplished by the different components with various functional properties. In the following sections, each component will be discussed in details.

2.3 Components of DSSC

2.3.1 The nanostructured metal oxide photoanode

TiO_2 is the photoanode material in the first DSSC announced by Gr±tzel in 1991.[14] This TiO_2 mesoporous layer is normally 5-20 ı m thick which is made of ~10-20 nm nanoparticle. The mesoporous layer can support a large internal surface area accessible to dye molecules, resulting in sufficient dye loading on its surface and thus high light harvesting efficiency, resulting in a high output of PCE. In the DSSC, this part plays an important role in both dye supporting and electron transport process. It is generally agreed that a desired photoanode should not only support sufficient reachable surfaces for the dye loading, but also act as a perfect photo-electron acceptor and transporter with the ability for supporting light harvesting. To date, lots of effort has been made on research of photoanodes for improving overall performance of the DSSCs. These

include: (1) to enhance light trapping ability in the mesoporous photoanode by introducing a light scattering layer. The layer is normally made by large sized nanoparticles (>800 nm) and placed on the top of the typical mesoporous film which is assembled by small sized particles. It can extend the optical transport length in the MO layer, thus enhancing the light absorption efficacy;[26] (2) to improve the dye loading ability and suppress recombination by surface modifications. Nazeeruddin et al proposed to use a $TiCl_4$ chemical bath deposition to modify the mesoporous film in order to achieve an ultrathin TiO_2 shell on the initial nanostructure.[27] The use of $TiCl_4$ treatment can increase roughness, and thus intensify the dye adsorption and simultaneously suppress recombination.[28-30] However, to date, lots of efforts have been made on the TiO_2 photoanode but the recombination issues still have not been solved because electrons in the particle based mesoporous MO film diffuse to the surface of TCO through a random and/or zig-zag pathway. The disadvantages of using TiO_2 nanoparticle based mesoporous photoanodes limit further improvement of DSSCs, and the reasons include:[27, 30] (1) a low electron mobility which causes a high rate of combination and limits efficiency improvement; (2) an expensive way to produce nanostructures for further improvement of dye absorption per unit volume; (3) a normal route for synthesis of the anatase TiO_2 usually needs high temperature post-treatments such as annealing which is typically used for removing additives for increasing porosity of the photoanode and/or crystallisation of the MO.

2.3.2 The absorber (Dye)

Generally, the dye molecules are chemically absorbed on the MO (i.e. TiO_2) surface by electronically favourable binding (i.e., forming coordinative bond) as shown in Figure

2-8. They do not only anchor the dye molecules to the MO surface, but also enhance electronic coupling of the dye LUMO with the CB of the MO. [23, 31] After absorbing the photons from incident light, the electron density shift from HOMO (Ru-NCS moiety) to LOMO (ligands connect surface of MO) from where electron injected into MO rapidly as shown in (Figure 2-8, Step 1 to Step 3).[23, 31] Photon-induced electron generation and injection for light harvest all perform by dye molecules in DSSC.[32] This means the amount of dye molecules available in the DSSCs for light harvest depends upon dye loading on the MO photoanode.[23, 31]

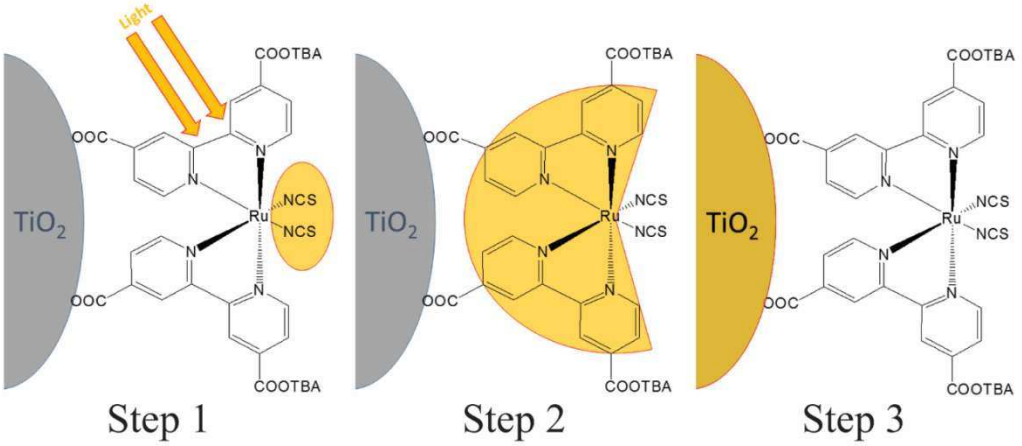

Figure 2-8 Dye absorption on the surface of the metal oxide and illustration of electrons density distribution (yellow area) after light absorption. Step 1: before the excitation; Step 2: after the excitation (immediately) and Step 3: after electron injection.[23, 31]

Organic/inorganic compound dyes have been developed and investigated as photosensitizers, such as ruthenium (Ru)-based complexes, Zinc-based complexes and metal-free organic compounds.[1, 33] The first Ru-based complexes for sensitization of TiO_2 single crystals was used by Anderson and co-workers in 1979, and they noticed that the sensitised TiO_2 crystals have photovoltaic behaviour and produce an overall PCE of 0.44 %.[34] In 1991, O˜Regan and Gr±tzel applied Ru-based complex based dye

to a mesoporous TiO_2 film and achieved a high DSSC PCE of 7.1-7.9 %.[14] Afterwards a series of Ru-based dyes (cis-(X)2bis(2,2˘-bipyridyl-4,4˘-dicarboxylate) ruthenium(II)) have been developed and studied, in which, X can be replaced by I, Br, CN, Cl, and thiocyanate (NCS).[35] One of these dyes (X replaced by NCS) can be strongly bonded onto the TiO_2 and exhibits a broad visible light absorption (up to 800nm) with a longer excited state lifetime of 20 ns than previous dyes. They named this dye as N3, which can be used in the DSSC to achieve a PCE up to 10%.[35] Based on N3 achievement and understanding, a modified dye (well known as N719) was produced with an absorption peak optimised to suit solar visible light (N3 has an absorption maxima at 518 nm and 380 nm, whereas those of the N719 are 535 nm and 395 nm, respectively) with a strong bonding ability on MO surfaces (due to its four carboxyl groups) and long excited state lifetime.[36] For application to further broad light range, one dye called N749 (also known as `black dye_) was developed and the resulted absorption range was extended to 920 nm.[37] On the other hand, aiming to prevent dye molecule self-aggregation, Gr±tzel˘s group developed a dipolar ruthenium complex, by modifying the (µ)conjugation of the dye, and an optimised chemical structure was obtained and named Z910, which provided an output PCE higher than 10%.[38, 39] Generally, the current dye structures are working in a similar principle as demonstrated in Figure 2-8.[23, 31]

Some dyes like those based on porphyrin and phthalocyanines were considered as a potential dye group to achieve a `full spectrum_ absorber,[40] because of their unique absorption behaviour which has two strong absorption ranges at 400-450 nm and 500-700 nm, respectively. However, the performance of the DSSCs based on these TiO_2

nanostructures were not over 8% for a very long period,[41, 42] until a new donor-`(u) bridge_-acceptor (well known as `D-(u)A _, Figure 2-9) structure was employed for the dye design. Good performance DSSCs with 11% PCE was achieved by the new Y D2 Porphyrin dye.[43] `D-(u)A _ structure is the key feature of the organic dye, as shown in Figure 2-9, in a pure organic dye molecule. Comparing with the Ru based dye, the pure organic dye has the advantages of structural diversity, ease of design, and high molar absorption coefficient which make it as another hot area of research. So far, hundreds of organic dyes have been developed, such as, coumarin dyes,[44, 45] indoles-based dyes,[46, 47] triarylamine-based dyes,[48, 49] alkyl-functionalized organic dyes[50, 51] and aromaticacids based dyes[51, 52].

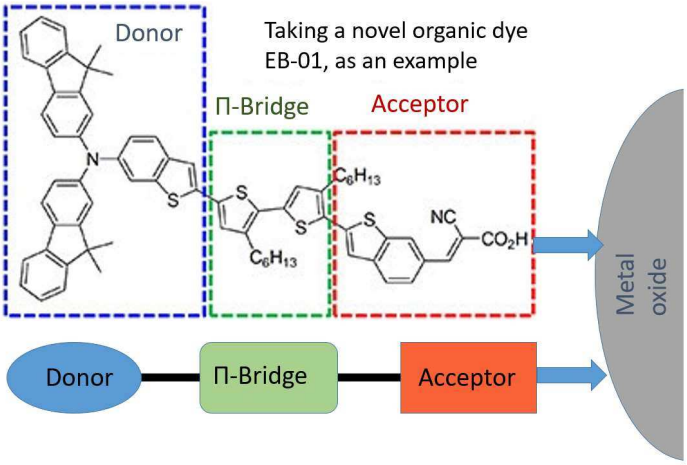

Figure 2-9 Typical D-(u)A structure of dye molecular.[11, 53]

Most of these dyes still face the challenges of long term stability which makes the DSSC have a short lifetime. Currently the N3 and N719 dyes remain the most commonly used ones. The injection kinetics of the N719 and N3 are well studied by previous researchers. Both of them have very fast injection rates (timescale between 0.1-100 ps) which can satisfy the quantum yield of charge injection efficiency close to 100%.[5, 54, 55] Therefore,

N719 will be used as a standard dye in this thesis for understanding the nanostructured MO effects on the DSSCs, recombination kinetics as well as electron transport behaviour.

2.3.3 Electrolyte in DSSCs

Electrolyte is an essential part in DSSC. It is not only responsible for the regeneration of oxidised dye but also in charge of transporting the electrons. Typically, the classical liquid electrolyte contains a redox couple (i.e.)歷/)鷹, suitable organic solvents (to make sure solutes dissolve properly and distributed uniformly) and additives (i.e. improve stability or viscosity). The redox couple is the functional part for dye molecules regeneration and a suitable redox potential with respect to dye as well as electrical property of MO.[56] Thermodynamically, the Voc of the DSSC is adjustable by varying redox potential which is controlled by the electron quasi-Fermi level ($E_{ŧ}$) in the MO (under light illumination condition) and the Nernst potential ($E_{ox/red}$) of the redox couple in the electrolyte (Figure 2-10).[11] Different redox couple has been studied for faster dye regeneration as well as improving electron transportation function. Recently, adjusting the redox couple used in the electrolyte, the cell output Voc can be turned up to 1 V.[11]

Though the most common used ()歷/)鷹 redox couple in an acetonitrile and valeronitrile mixture-solvent can benefit the regeneration of oxidised dye, the limitation of the DSSC output Voc (below 0.8 V) and its corrosive nature still need more research efforts to improve it.[56] Thus, efforts to find redox couples have been made. Various redox couples other than)歷/)鷹 have been studied, such as pseudohalogen based redox (SCN_2/SCN^-), and cobalt (III/II)-based redox complex.[5, 57, 58] Even though the other

redox couples have been studied and used in the DSSCs as electrolytes with better Voc performance, the ()歷/)鬮 redox couple is still the most commonly used and well-studied one due to having cost-efficient and its easy preparation.[59, 60] Hence it is normally used as a standard electrolyte for photoanode and dye performance studies in the DSSCs.

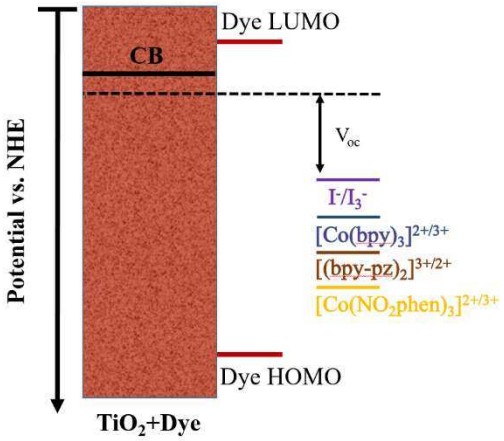

Figure 2-10 Energy diagram of)歷/)鬮 and some selected Co-polypyridyl redox.[11]

In addition, to the redox couples, much effort has also been made to achieve solid types of electrolytes for solving the leakage and self-evaporation problems. Y anagida group developed an additive (low-molecular-weight gelatos) to achieve a kind of temperature-dependent (solution-to-gel) electrolyte for DSSC applications.[61] Due to temperature-related molecular forces and interactions between amide bonds and long aliphatic chains, this electrolyte can be changed into a liquid phase at a high temperature, and turned back to a gel after the temperature is decreased to room temperature, thus reducing the leakage and evaporation opportunity. This type of solid DSSC showed a comparable PCE to the conventional liquid cells with a reasonable stability.

Inspired by this successful work, more additives have been employed to develop quasi-solid state electrolytes, including ionic polymer gels containing vinylidenefluoride-co-

hexafluoropropylene (PVDF) or polyethylene oxide (PEO).[38, 61, 62] These additives cannot improve the performance of the devices, however, these gel-liked electrolytes indeed relieve leakage problem. So far, much effort has been made to develop the solid state electrolyte, focusing on p-type inorganic semiconductors and organic hole transport materials (HTMs). In 1995, O¯Regan et al discovered the copper(I) thiocyanate (CuSCN) can be used as the HTM and studied its performance as a solid electrolyte in TiO_2/dye/CuSCN and ZnO/dye/CuSCN DSSCs, and obtained a highest PCE of 1.5%.[63] Three years later, Tennakone group developed a sandwich structured solid DSSC and found preparation processes affected the DSSCs performance. Additionally, the introduced 1-ethyl-3-methylimidazolium selenocyanate (EMISeCN) into the HTM reduced the degradation of current under a constant light irradiation and yielded a good contact with different layer.[64] However, this type of the DSSC still has a big challenge on improving PCE (<3%). Recently, Chung et al used $CsSnI_3$ as the HTM and N719 as the dye to achieve a solid state DSSC with a PCE of 8.5%. However, because the $CsSnI_3$ is not stable in atmosphere and difficult to synthesise, its use is limited in the DSSCs. Compared with the inorganic p-type semiconductor material, inorganic based HTMs have attracted more attention due to their compatibility for solution process, better pore-filling ability and properties by additives in solution process. Most of the conventional conducting organics, such as polythiophene (PEDOT), polypyrrole (PPy) and polyaniline series, have p-type properties, and the potentials to be used as the solid HTMs for the DSSCs.[65-67]

2.3.4 Counter electrodes

The CE is the last part on the sandwich DSSC structure which completes the cell and the electrical circuit of DSSC. The surface of CE which contacts the electrolyte, also has an important function for reducing the oxidised redox mediator (i.e.)鬳) back to the non-oxidised form (i.e.)歷) by receiving electrons.[15, 68, 69] Therefore, most studies on the CE have been focused on: (1) making the CE to be chemically stable with good electrocatalytic properties; (2) improving contact resistant and exhibit a good charge transfer resistance.[70] In terms of contact resistant and charge transfer resistance, the Pt coated CE immersed in I^-/I^{-3} electrolyte commonly has been studied using dummy cell with EIS measurement.[25, 71, 72] As shown in Figure 2-11(a), the dummy cell consists of two identical CEs and a thin layer of electrolyte solution between them.[71, 72] In such configuration, the photoanode contribution can be eliminated. Only the CE can be measured and investigated under a simulated DSSC operating conditions.[71, 72] The dummy cell used for CE investigation can be explained by a well-studied equivalent circuit (Figure 2-11(b)). The equivalent circuit is also used for fitting EIS data and determination of CE parameters. The charge-transfer resistance between electrolyte and CE interface ($R_{ct\,(CE)}$) is one of the important parameters.[71, 72] The lower value of $R_{ct\,(CE)}$ means the reduction rate of redox couple is faster. Values of the R_s and $R_{ct\,(CE)}$ also affect the FF of the cell, i.e. the lower the value, the higher the FF will be obtained. Georgiou et al[69, 73] reported that Pt clusters with the particle sizes up to 20 nm were formed using thermal decomposition on TCO at 380 °C and it exhibited an $R_{ct\,(CE)}$ value of 0.07 'n/cm^2 with Pt loading of 5 ı g/cm^2. In this case, the CE still remained transparent after very low Pt loading.[74] In addition, 450 nm thick sputtered Pt layers

on the TCO substrate shows 0.05 'n /cm^2, as compared with 25 'n /cm^2 for the TCO substrate.[71] For reducing the cost as well as for the following the requirements of new electrolyte system, various new CEs have been developed, such as metal based, carbon based, inorganic compound and organic conductive polymer based counter electrode.[25, 75]

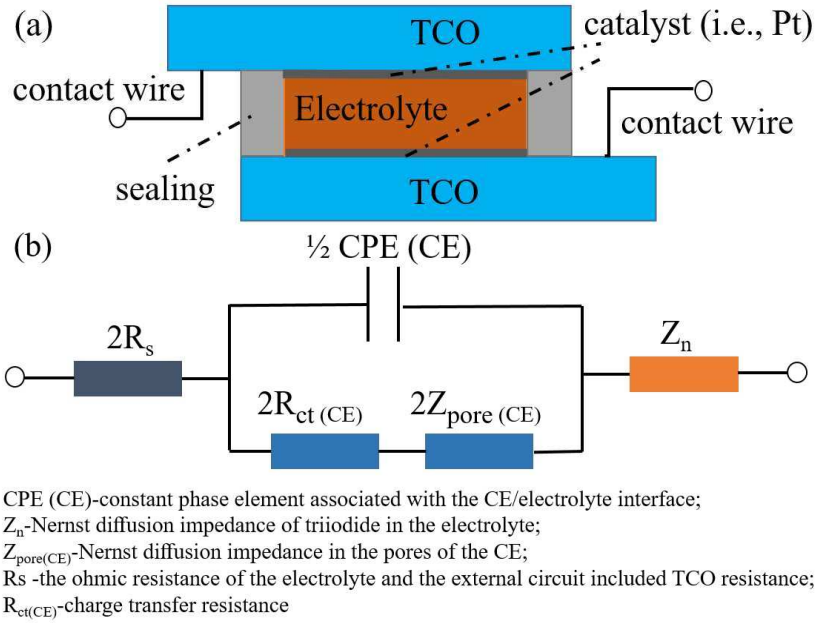

CPE (CE)-constant phase element associated with the CE/electrolyte interface;
Z_n-Nernst diffusion impedance of triiodide in the electrolyte;
$Z_{pore(CE)}$-Nernst diffusion impedance in the pores of the CE;
Rs -the ohmic resistance of the electrolyte and the external circuit included TCO resistance;
$R_{ct(CE)}$-charge transfer resistance

Figure 2-11 (a) Schematic of dummy cell used for CE measurements, (b) relative equivalent circuit.[71, 72]

2.4 ZnO nanostructures and its application for DSSC

As discussed in Section 2.1, the basic working principle of the DSSC indicated that there are several reverse reactions which prevent the photo-generated electrons to be transported to the outer circuit. These reverse reactions cause recombination of photo-generated carriers (i.e. photo-generated electrons recombined with the oxidised dye molecules and/or redox-couple) thus causing energy loss which limit further improvement of DSSCs performance.[1, 11, 76]

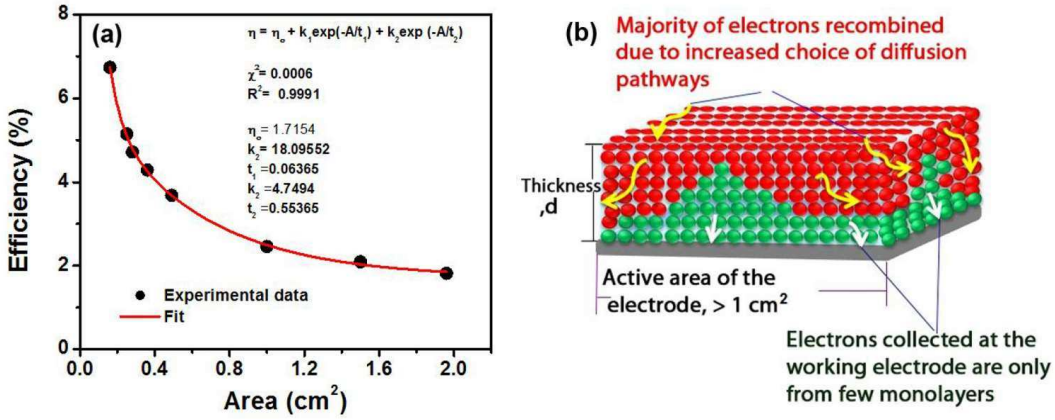

Figure 2-12 (a) the efficiency of a DSSC decreases exponentially with the increasing active area in a range between 0.15 - 2 cm^2; (b) illustration of electron collection case in a large area photoanode in DSSC.[1, 77]

Such carrier recombination is predominant due to slow electron transportation in the conventional TiO_2 nanoparticle based photoanode, due to trapping of the electrons in the grain boundaries and the relatively long and zig-zag random paths of the electrons to the TCO substrates.[78, 79] Taking a 10 ı m thick nanoparticle based mesoporous film as an example, an electron needs to go through ~ 10^6 nanoparticles on average before reaching the TCO surface.[80] This recombination loss will become severe when the photoanode thickness is larger than a critical value (~15 ı m in a single cell, area Ħ0.2 cm^2). Furthermore, the mesoporous film area in the DSSC will also affect the recombination loss. Though the dye loading (per unit area) and film thickness are constant in different sized samples, the PCE dropped dramatically after the cell area was increased from 0.15 to 2.00 cm^2 (Figure 2-12 (a)).[1, 77] According to the further study of the charge transport of these devices, the recombination resistance was decreased and electron transport time was increased with the increased photoanode area.[1, 77] Diffusive charge transport is complicated, where the generated electrons are rapidly intercepted by the ions in the electrolyte, and thus, limits the diffusion length

(L_n). Recent studies indicated that not only the film thickness, but also cell area will cause the increases of paths or lengths of electron diffusion during scaling up the cell, thus limiting the performance of the devices.[1, 77, 81]

Therefore, suppressing the reverse reactions process (recombination) in the cell has been considered as an effective way to improve the DSSCs.[82-84]. Changing the material and material properties are considered as a possible breakthrough to overcome this limitation.

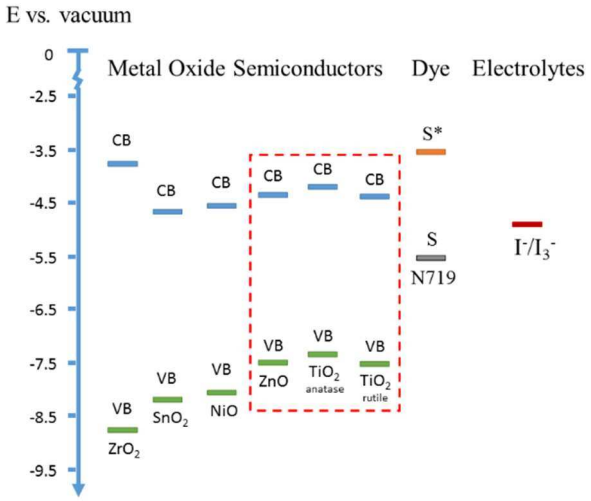

Figure 2-13 Conduction band (CB) and valence band (VB) energy levels for some metal oxide semiconductors, HOMO and LUMO levels of ruthenium-based dye (N719) and potential levels of electrolytes.[85, 86]

Various MO semiconductors, such as SnO_2, ZnO, MgO, NiO and Al_2O_3, etc., have been explored for their potentials as the photoanodes to overcome the limitation of TiO_2 for achieving improved DSSCs.[68, 87-89] Among these oxides, ZnO is one of the most promising wide bandgap semiconductors for the DSSCs, due to its similar properties (i.e. energy-band structure as shown in Figure 2-13) to those of the TiO_2 but with a bulk electron mobility three orders of magnitude higher than that of the TiO_2 (shown in

Table 2-1).[90] The high electron mobility of the ZnO can effectively separate the injected electrons from the adjoining oxidised species of the electrolyte, which can improve the carrier collection efficiency of the DSSCs.[68, 90] Therefore, ZnO has a large potential to achieve a photoanode which has high electron mobility as well as suppressing recombination for further improving overall performance of the DSSCs. However, compared to TiO_2, the chemical stability of ZnO is not comparable due to its amphoteric oxide nature (dissolves in both acidic and alkaline environments). Typically, dye loading process is performed by soaking MO photoanode into dye solution for achieving dye molecular bonding. Generally used dye molecules contain acidic carboxylic anchoring groups, which makes the dye loading solution as acid.[91] Thus the dye loading solution concentration and dye loading time in the solution need to be precisely controlled. In the acid dye solution, ZnO surface dissolved into the solution which prevent dye bonding on the MO. In addition, Zn^{2+} in the solution (and/or at ZnO/dye interface) also react with the dye molecule and form insoluble complexes.[92] These complexes cannot work as light absorbers. Simultaneously, they cover on the ZnO surface and prevent the normal dye bonding which affects electron injection and acts as a recombination centre.[93] The problem caused by the ZnO amphoteric oxide nature can be overcome using the following ways. Dye molecules which are specially designed to match ZnO photoanode could promote the electron injection efficiency and prevent complex formation, thus improving the ZnO based DSSCs performance. On the other hand, MO modified layers could be used on top of ZnO for enhancing stability and good dye combination.[20, 94, 95]

Table 2-1 Comparison of ZnO and TiO_2 physical properties.[96-102]

	ZnO	TiO_2	Ref
Band gap (eV)	3.2-3.3	3.0-3.2	[96-98]
Refractive index	2.0	2.5	[99]
Electron mobility ($cm^2 V s^{-1}$)	1000 (Single nanowire) 200-300 (bulk ZnO)	0.1-4	[96, 97, 100]
Electron diffusion coefficient($cm^2 s^{-1}$)	$1.7x10^{-4}$ (nano-particulate film) 5.2 (bulk ZnO)	$1B10^{-8}$~$1B10^{-4}$ (nano-particulate film) 0.5 (bulk TiO_2)	[101, 102]

The ease of crystallisation and anisotropic growth of ZnO is also important for achieving a desirable photoanode which has a high charge transfer efficiency and sufficient dye loading ability. Many efforts have been made on synthesising a wide variety of ZnO nanostructures with various potentials in electron transport, light propagation or energy harvesting applications.[95, 103-109] In the following, the basic properties of nanostructured ZnO, particularly its application in DSSCs will be reviewed.

2.4.1 Basic properties of ZnO

ZnO normally is present as a white or yellowish powder, and has a molecular weight of 81.37 g/mol. It is nontoxic, odourless and insoluble in water but soluble in acid and alkali, and belongs to the dass of amphoteric oxides. ZnO exists in a steady state as the wurtzite crystallizes structure at ambient pressure and temperature (Figure 2-14).[110, 111] In ZnO wurtzite crystal structure, each O^{2-} is surrounded by four Zn^{2+} at the corners of a tetrahedron (as shown in Figure 2-14 (a)), and vice versa.[96] These tetrahedrons (consist of O^{2-} and Zn^{2+}) are stacked and arranged alternately along the c-axis oriented

direction of the hexagonal lattice (Figure 2-14 (a)).[96, 112, 113] This tetrahedral arrangement leads to polar symmetry along the hexagonal axis.[104, 113-116] In the typical wurtzite ZnO crystal, there are a polar zinc plane (0001), a basal polar oxygen plane ($000\bar{1}$) and low index faces ($\{01\bar{1}0\}$, parallel to c-axis) consisting of a family of non-polar planes.[96, 112, 113] The wurtzite structure and the polar faces are related to various of ZnO chemical and physical properties.[19] Such as piezoelectricity, spontaneous polarization, as well as crystal growth/etching preferred orientation and defect generation.[104, 114-116]

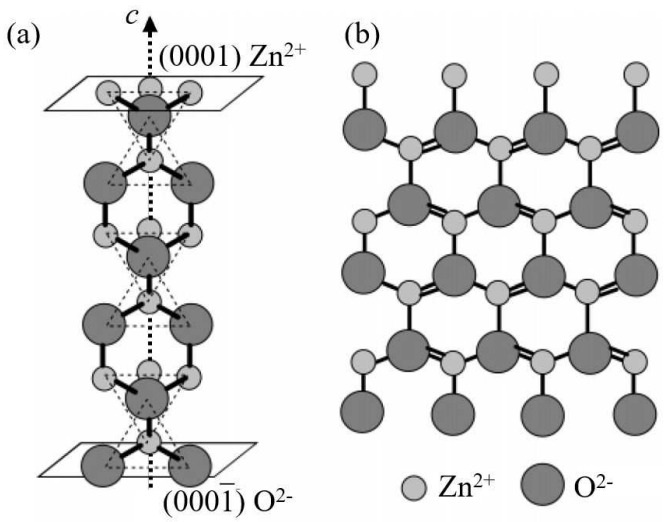

Figure 2-14. The ball-stick model of the wurtzite ZnO crystal structure: (a) along the <0001> direction; (b) the $\{01\bar{1}0\}$ face. [96, 112]

As one of the II-IV semiconductors, ZnO has many promising properties for optical and electrical applications.[96] Nanostructured ZnO further improves these properties not only because the nanostructure providing large specific surface areas, but also because of benefits in the view of quantum-confinement effect, and/or photo-localization. During the past decades, various forms of ZnO nanostructures have been achieved including: nanoparticles,[117, 118] nanowires (NWs), nanorods (NRs),[119-121]

nanotubes,[120] nanobelts,[120, 122] nanosheets[119] and nanotips.[103, 123, 124] These nanostructures can be obtained through either vapour/gas phased processes (i.e. magnetron sputtering, chemical vapor deposition, thermal evaporation deposition and pulse laser deposition) or solution based processes (i.e. hydrothermal and low temperature aqueous nanostructure growth, sol-gel synthesis and electrochemical deposition method).[118-120, 122, 125-127] These will be discussed in the flowing section.

2.4.2 ZnO nanostructures Synthesis

For the nanostructured ZnO materials to meet the application requirements, it is required that their morphology, crystalline structure, orientation and surface property are controllable and reproducible to achieve the best performance. Various synthesis techniques have been explored to grow ZnO nanostructures. Broadly, these synthesis techniques can be separated into two main categories: vapour-phase technologies and solution-phase technologies.

2.4.2.1 Vapour phase techniques

Vapour phase techniques are well studied because of their unequal advantages on producing high-quality ZnO crystalline nanostructures. However, due to that the process is heavily relied on the carrier gas and source material vapours, these techniques normally require either expensive vacuum facilities or relative high synthesis temperatures (typically ranging from 400-1400 ^{o}C). The high temperature processes restrict the usage of many common substrates.[128-130] Furthermore, these methods have challenges for achieving good sample uniformity and efficient production yields. Typical vapour phase techniques can be separately discussed as below:

(1) Vapor transport technique

Vapor transport technique is a very popular technique for ZnO nanostructure synthesis.[131] A variety of ZnO nanostructures have been synthesised by this method. It is based on transport of growth source vapor to a target area (i.e., substrate) where they react to form ZnO.[131] This technique generally requires a horizontal tube furnace with gas control system to carry out nanostructure synthesis (Figure 2-15).[131] As demonstrated in Figure 2-15, the source material is placed at the centre of the high temperature area in the tube furnace for material vapor generation. The carrier gas (and/or reaction gas) is introduced from the right end of the tube and pumped out at the left end. The source material vapor can be transported by the carrier gas to the substrate for nanostructure growth. The growth vapor can be obtained from directly decompose ZnO powder, but it requires quite high process temperature (ZnO melting temperature is around 1975^{o}C).[131] To reduce ZnO decomposition temperature, carbothermal method (source material is ZnO mixed with graphite) has been developed. ZnO reacts with graphite at 800 to 1100 ^{o}C and produce CO, CO_2 and Zn vapor for ZnO nanostructure growth.[131] An alternative to significantly reduce the requirement of process temperature is using Zn metal (melting point is around 420 ^{o}C) as source material.[131] Therefore oxygen is required for ZnO formation which needs to be particularly controlled to avoid ZnO formation away from substrate.[131] In addition, the vapor pressure ratio of Zn/O is critical for ZnO nanostructure formation and structure morphology control.[131]

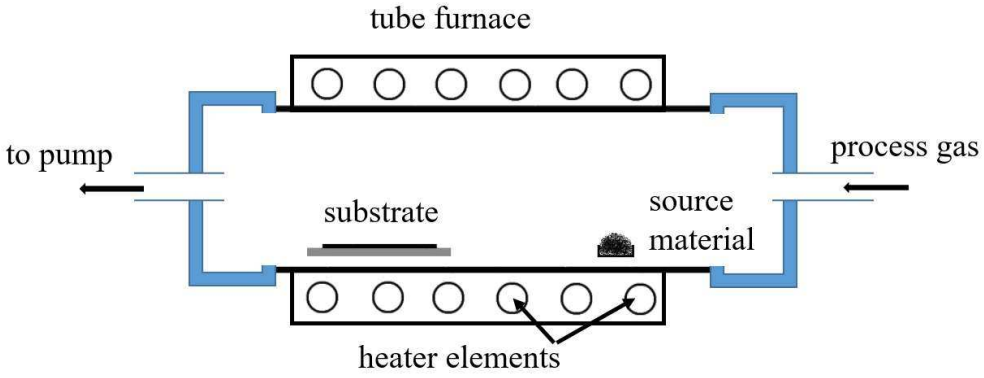

Figure 2-15 Schematic illustration of the horizontal tube furnace for vapour phase transport process.[131]

The growth of ZnO nanostructures by vapor transport process usually follows the well-known metal catalyst-assisted (i.e., Au, Fe) vapor-liquid-solid (VLS) approach (vapor-solid approach if without the catalyst).[131] Various ZnO nanostructures (i.e., nanobelts, nanorods, nanowires, nanosprial) can be produced by catalyst free vapor-solid approach.[131] ZnO nanobelts with the typical thickness and widths with the range of 10-30 nm and 50-300 nm can be obtained by catalyst-free vapor-solid approach with ZnO power as source material.[128, 131] ZnO nanopropeller arrays were obtained on catalyst-free Al_2O_3 substrate by a two-step process temperature approach.[131, 132] Though catalyst is not essential for formation of ZnO nanostructure using vapor transport process. The vapor-liquid-solid (VLS) process can provide more control of nanostructure growth (i.e., morphology, location and density). Besides, ZnO nanostructure can also be patterned by applying catalysts assistant growth.[131, 133] By patterning the catalyst (Au) thin film on the sapphire substrates, selective ZnO nanowires growth was achieved through VLS process.[121] The ZnO nanowires grown only on the Au coating (patterned catalyst) areas where the typical diameters are in the range of 20-150 nm.[121, 131] Using self-organized polystyrene nanosphere as a mask on

GaN substrates during catalyst (Au) deposition, well-ordered ZnO nanorods ([0001] oriented) were obtained at 750 ºC by Zhou et al.[134].

(2) Oblique angle deposition

Oblique angle deposition (OAD) is a geometrical vapour deposition technique. This technique is a deposition configuration in which the source material vapor arrives at the surface of a substrate at an adjustable oblique angle (Figure 2-16 (a)).[135, 136] The nanostructures formed by OAD is based on the ::shadowing effect_.[136] As demonstrated in Figure 2-16 (b), the initial arrived material particles assemble together and form some larger material particle clusters.[136] These initial formed clusters will cause a shadow area behind themselves which blocks the deposition of any further material vapor.[136] The continuous arriving source material particles lead to the formation of separated and tilted nano-columns ((Figure 2-16 (c) to (d)).[135, 136] This growth behaviour can be controlled by adjusting incident deposition angle to create some controllable properties such as porosity.[136] The source material vapor can be supplied by various techniques. Such as sputtering deposition, electron beam (E-beam) evaporation technique and plasma enhanced chemical vapor deposition (PECVD).[135, 136] By using OAD technical with an incident angle of 70º, Chu et al.[137] obtained well crystallised ZnO nanorods arrays with a substrate temperature at 350 ºC by sputtering (substrate temperature). The synthesised ZnO nanorods have an average length of 쭔25 nm and the rod diameter of 150¯300 nm.[137] Toledano et al.[138] found that the porosity of ZnO nanostructures can be adjusted by controlling the deposition angles in a range between 0é and 85é.[138] The refractive index of the nanostructured ZnO films can also be tuned from 1.5 to 1.9 with the deposition angle changed from 85é to 0é.[138] Though nanorods and even more complex nanostructures (i.e., zig-zag nanorods arrays, nano-

spiral arrays) can be obtained by OAD with substrate position manipulation. This technique is still facing challenges such as the formation of other non-column based nanostructures, simplification of fabrication process, low product yield and relative high cost.[136]

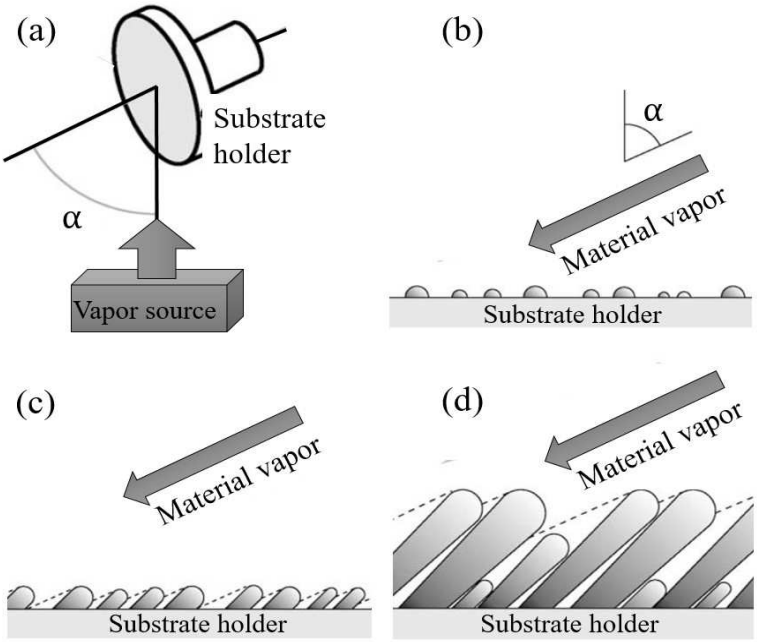

Figure 2-16 (a) Schematic view of oblique angle deposition; (b) to (d) illustration of the shadowing effect for nanostructure growth during the OAD.[135]

2.4.2.2 Solution phase techniques

The advantage of solution phase techniques to grow the ZnO nanostructures is that the nanostructures can be obtained at a relative low temperature (normally below 200 °C). Furthermore, most of solution phase techniques are simple, low cost and environmentally friendly compared with most high temperature (and/or vacuum) gas phase techniques. Solution phase techniques are strongly dependent on chemical reaction conditions which can be readily adjusted. As a low-temperature processes, they hold a great promise in integrating with variety of substrates for future foldable and

portable electronics.[116] They also are possibly emerging gas-phase techniques to achieve complex/accurate nanostructure control. Major challenges of these techniques are in the difficulties in precise control of the synthesis process, accurate doping control and ability for reproducible uniformity on a large-scale substrate/sample. These solution-based techniques typically include:

(1) Electrochemical deposition

Electrochemical deposition (ECD) is based on cathode and anode in the growth solution with an external power supply. The source material cation in the growth solution is reduced at the cathode to form nanostructure. It is widely used in making thin films on large surface due to its strong external driving force which can be easily controlled by not only changing growth solution parameters but also changing external power supplied to the electrodes. The ECD has been successfully used for synthesis of uniform ZnO nanostructures (i.e. NRs and nanotubes) on a large sized conductive substrate, even if the substrate is curved.[116, 139] Zinc (Zn) or platinum (Pt) metal anode is commonly used in ZnO ECD process. Pt anode does not involved in the ZnO formation, but completes the electrical circuit.[140, 141] Zn anode not only completes the electrical circuit but also supplies zinc ions (Zn^{2+}) for growth (Eq. 2-13). [140, 141]

: ā kḿ: ā 厭斷喵□惿歷 (Eq. 2-13)

The ZnO growth solution normally contains an oxygen precursor (i.e., molecular oxygen, nitrate ions or hydrogen peroxide) and Zn^{2+}.[19, 141] Zinc salt (i.e. zinc chloride or zinc nitrate) is commonly used in the growth solution to provide Zn^{2+}.[19, 141] The reduction of the oxygen precursor at the surface of substrate generates hydroxide ions

(OH^-) in the growth solution during the ECD process (reduction of oxygen precursors as shown in Eq. 2-14 to Eq. 2-17).

Molecular oxygen (Eq. 2-14)

(Eq. 2-15)

Nitrate ions (Eq. 2-16)

Hydrogen peroxide (Eq. 2-17)

The generated OH^- then react with the Zn^{2+} to form ZnO on the surface of the cathode (Eq. 2-18).

(Eq. 2-18)

With an external electric filed presented during the growth, the obtained ZnO NRs showed a good alignment of NRs and strong adhesion to the target surface.[142] Elias et al.[141] prepared ZnO nanorods arrays with tailored dimensions on FTO substrates using molecular oxygen as oxygen precursor in the zinc chloride/potassium chloride/water mixed growth solution. The obtained ZnO NRs have a height between 1 to 3.4 ı m and a diameter between 65 and 110 nm.[141] In addition, due to the external driving force present during growth, it can also be used as an effective way of doping ZnO nanostructures by adjusting power supply and adding doping element into relative reactants in the growth solution.[116, 143-145] For example, Cui et al.[145] obtained vertically aligned Ni doped ZnO nanowires on the silicon substrates using a nickel nitrate, $Zn(NO_3)_2$ and hexamethylenetetramine $C_6H_{12}N_4$ mixed electrolyte at 90 °C.[145]

(2) Templated assistant growth

Template assistant nanostructure synthesis is commonly used in ZnO nanostructure growth. A template can be utilized to force the material to form a desired morphology. Various templets with nano-channels and/or mesoporous structures have been explored for morphology control of the nanostructures. Generally-used and commercially available templates are anodic aluminium oxide (AAO) templates, nano-structured glass and polycarbonate based membrane templates. Among them, in the literatures, the most commonly used for 1-D nanostructure synthesis is AAO which meets the requirements of cost efficiency and capability of large area synthesis.[116, 146] The AAO template commonly coupled with ECD process for achieve good crystallization. The template is firstly attached to surface of the substrate.[116] Then the whole set is placed as the cathode in the ECD growth solution. Under the electric field, cation growth units (i.e. zinc ions) diffuse towards the templated attached substrate (cathode) which goes into the gaps and/or pores of the template.[116] Simultaneously, hydroxide ions (OH^-) are generated at the cathode and thus the ZnO is formed into the nano-sized channels and/or pores of the template.[116] The ZnO nanostructures can be obtained by selectively removing the template.[116] Zheng et al. reported that the large-scale uniform ZnO NRs arrays can be obtained by one-step template assistant ECD.[146] However, due to ZnO and Al_2O_3 are both amphoteric oxides, there is still challenge on selectively removing AAO template without causing damages of ZnO nanostructures.[116] As an alternative, polycarbonate template have been studied and used for ZnO NRs synthesis. Zhou et al reported [147] that by reliably varying the nano-channel size of the polycarbonate template, the resulted ZnO NRs diameters can be adjusted from 60 to 260 nm.[147] In addition, this method also can easily produce other MO (i.e., CuO) in the same morphology.[116, 147] Besides porous membranes with nano-sized channels, biological

template could also be used for ZnO nanowires synthesis. Atanasova et al.[148] showed that ZnO NWs can be fabricated by solution growth process using ≅-DNA as a template. Continuous ZnO NWs of about 10 ı m in length were obtained, and the authors found that the electrically resistance of the obtained ZnO NWs is the order of several ohm.[148]

(3) Hydrothermal growth in aqueous solutions

Lots of researchers have reported the controllable growth of oriented ZnO NRs/NWs using the hydrothermal aqueous solution processes. Normally a solution containing zinc ions (Zn^{2+}) and a source of hydroxide ions (OH^-) is used. The OH^- will react with the Zn^{2+} to form ZnO. Several zinc salts can be used in the process (i.e. zinc acetate dehydrate[149], zinc chloride[150]) to provide Zn^{2+}, and the OH^- source could be generated using ammonia and ammonium chloride. The advantages of using aqueous solution methods include: low temperature (below 100 ^oC), cheap chemical agent and easier operation, in addition to the low cost and great potential for scale-up.[116, 151] As this method will be used in our project, it will be reviewed and discussed in detail in the following section.

2.4.2.3 Aqueous solution growth process

The aqueous solution hydrothermal growth method is one of the commonly used solution phase synthesis technologies. In this growth process, an alkaline solution reaction condition is commonly required for the ZnO nanostructure formation, as the divalent metal ions do not hydrolyse in acidic solution environments.[152-154] For the classical aqueous solution growth of ZnO nanostructures, a ZnO seed layer is commonly applied on the desired substrate surface which is crucial to obtain a uniform growth of the nanostructures and good adhesion with substrates.[116] Pre-seeded

substrates are then placed into aqueous reaction solutions which normally contains OH^- to achieve a proper supersaturation for nanostructure growth (as shown in Figure 2-17).[116, 151] When the aqueous reaction solution is set to the right temperature (40 to 100°C depending on the reactions), nanostructured (and/or micro-structured) ZnO starts to epitaxially grow from the seed layer by a heterogeneous nucleation process.[116]

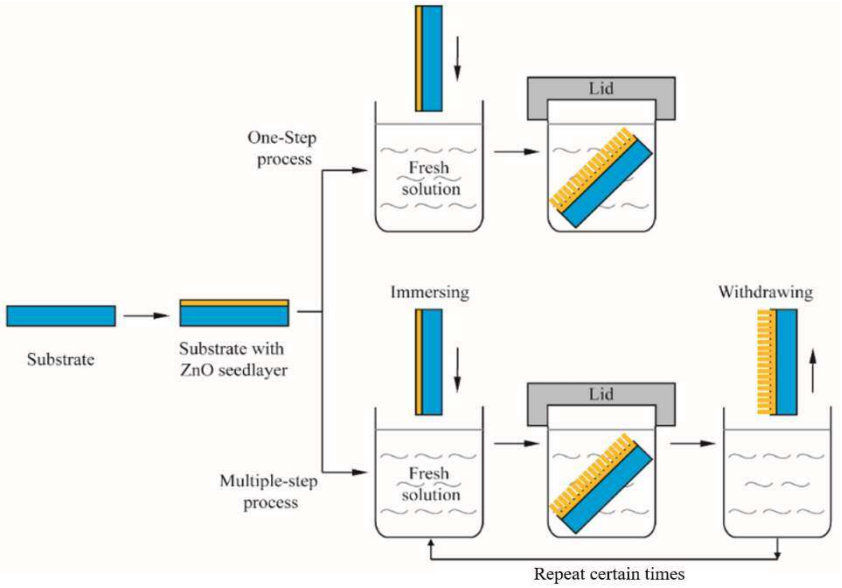

Figure 2-17 Schematic process of the aqueous solution growth for the fabrication of ZnO nanorods.[151]

Many growth parameters (briefly summarised in Table 2-2) have been previously explored to manipulate the morphology of aqueous solution synthesised ZnO nanostructures, including pH effect to the growth of morphology, reaction temperature, concentration of reactants and different additives effects in the solutions. The most commonly used chemical reagents can be briefly summarised as below:

(1) Soluble Zn source reagents/materials, for example, zinc nitrate ($Zn(NO_3)_2$), zinc acetate ($Zn(O_2CCH_3)_2$), zinc sulphate ($ZnSO_4$), zinc chloride ($ZnCl_2$) and zinc formate ($Zn(CHO_2)_2$);

(2) Basic reagents, for examples, ammonia hydroxide (NH_4OH), sodium hydroxide (NaOH), hexamethylenetetramine (HMTA, $C_6H_{12}N_4$), ethylenediamine ($C_2H_4(NH_2)_2$, EDA) and triethanolamine (TEA, $C_6H_{15}NO_3$);

(3) Additives, for examples, ammonia chloride (NH_4Cl), citrate, polyethylenimine (PEI), poly ethylene glycol (PEG), polyvinylpyrrolidone (PVP), sodium dodecyl sulphate (SDS) and polyvinyl alcohol (PVA);

Table 2-2 Brief summary of different methods and results of solution processed ZnO nanostructures.[155-177]

Reactant	pH	morphology	Key growth factors for structure and crystal control
$Zn(NO_3)_2$, NH_4OH	7.5 to12	NRs and nanoparticle	Reaction duration time, reaction solution pH and temperature [156-158]
$Zn(NO_3)_2$, HMTA($C_6H_{12}N_4$)	7 to13	NRs, nanotubes, NWs and nanoplates	Reaction time, as well as influence of seed layer and substrates [159-162]
$Zn(NO_3)_2$, Citrates and $C_6H_{12}N_4$	ħ7	NRs with good order	Influence of additive(citrate) effect on the morphology [163]
$Zn(O_2CCH_3)_2$, $Zn(NO_3)_2$, Sodium hydroxide	6.8 to 13.2	NRs with good order	Influence of additive, reaction time, reaction solution pH and concentration [163, 164]
$ZnCl_2$ and NH_4OH	10 to 13	Flower-like and rotor like nanostructure	Effects of reaction solution pH and usage of different substrate [165, 166]
$ZnCl_2$, thiourea ($SC(NH_2)_2$), NH_3XH_2O and NH_4Cl	>7	NWs, tube-like, flower-like and tower-like nanostructure	Reaction duration and temperature, substrates pre-treatment effects [167, 168]
$Zn(NO_3)_2$ and NaOH	>7	NRs, nanoflower and nanodisk	Influence of reaction pH adjusted by NaOH [169-171]
Comparison of various growth reaction solution	6 to 13	NRs and star-like nanostructure	Different reaction condition had been studied, influence of different reactants, pH, duration substrates and ionic strength [155]
Zn metal foil, $ZnSO_4$	>7	Nanobelts arrays and NRs	Concentration of different reactants in the reaction solution and reaction temperature influence [172-174]
$Zn(C_5H_7O_2)_2$ xH_2O and organic surfactants	7 to 13	NRs, flower-like	Influences of surfactants: PEG, CTAB and PVA [175-177]

So far, varied dimensional (0D to 3D) ZnO nanostructure materials can be achieved using the aqueous solution process by adjusting the synthesis parameters. As one of the most important effects on nanostructure growth, supersaturation is well known for its effects on crystal growth rate as well as nanostructure morphology. Figure 2-18 shows the superstation levels and their effects on ZnO nanostructure growth rate as well as growth behaviour. Under different supersaturation conditions, different growth behaviours can dominate growth.

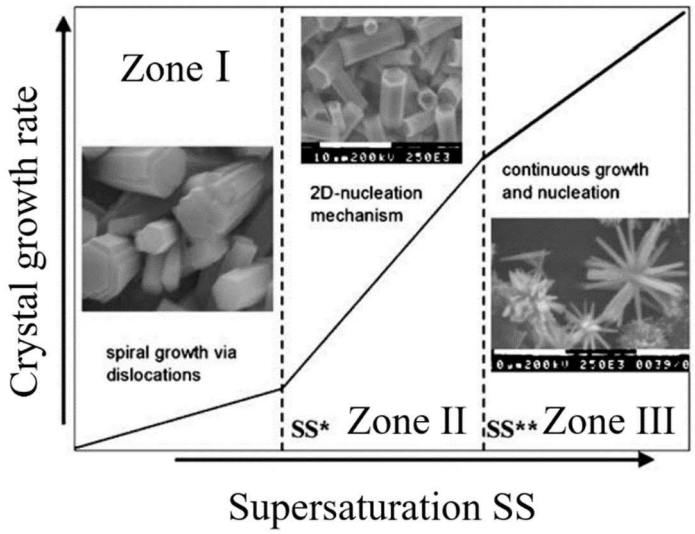

Figure 2-18 A brief summary of relationship between supersaturation in the growth solution, crystallite growth rate and crystal morphology.[155]

In relatively low degrees of supersaturation condition (Zone I in Figure 2-18), heterogeneous nucleation dominates. ZnO crystal faces growth is mainly dominated by the outward displacement of a growth spiral generated by screw dislocations.[155] On the other hand, in the very high degree of supersaturation condition (Zone III in Figure 2-18) homogeneous nucleation is dominant.[116, 155] The crystal faces grow rough and continuous linear growth occurs. ZnO morphology is dominated by dendritic to

spherulitic which has been affected by diffusion in the bulk solution (due to increased viscosity).[116, 155] Between low and high degree supersaturation, the intermediate range (Zone II in Figure 2-18), growth occurs through a mixture of nucleation processes. 2D growth mechanism is dominated in this condition.[116, 155]

The reaction conditions strongly influence the supersaturation of the solution and result in changes in morphology of ZnO nanostructures. The crystallographic characteristic is another key factor that determines the growth process as well as final morphology of the nanostructure. An insight understanding of the nucleation process as well as nanostructure formation is critical to optimise the growth conditions so that the growth and morphological evolutions (including microstructure, density, crystallisation, grain size and its distribution) of nanostructures could be tailored. As it is well known that the nanostructure crystallisation properties and morphology are critically linked to the function of devices, hence it is required for controllable properties tuning for the optimal device performance. Therefore, a deep understanding of synthesis mechanisms and a possible reaction model are needed to enable structure tuning, and this would be helpful for the device application. Better understanding of growth factors and mechanism will be the first step for achieving this objective.

2.4.2.4 Growth mechanisms in the solution phased process

Generally speaking, in the aqueous solution growth, the formation of ZnO (solid phase) is a result of growth source accumulation and condensation. During the whole growth, nucleation processes and chemical reaction processes are involved for achieving the nanostructures.[116, 178] In the growth solution, once the driving force causes the system to depart from its equilibrium condition, generally a nucleus of an initial crystal is

formed and the growth begins.[19] This growth process can take place in various ambient phases (i.e. solid and liquid phase). The essential differences in these processes are summarised in Table 2-3.[179]

Table 2-3 Characteristics of crystal growth in liquid phase.[179]

	Melt phase	Solution phase		
		High-temperature Solution	Hydrothermal solution	Ordinary temperature solution
State	Condensed	Ⅶ" " " "

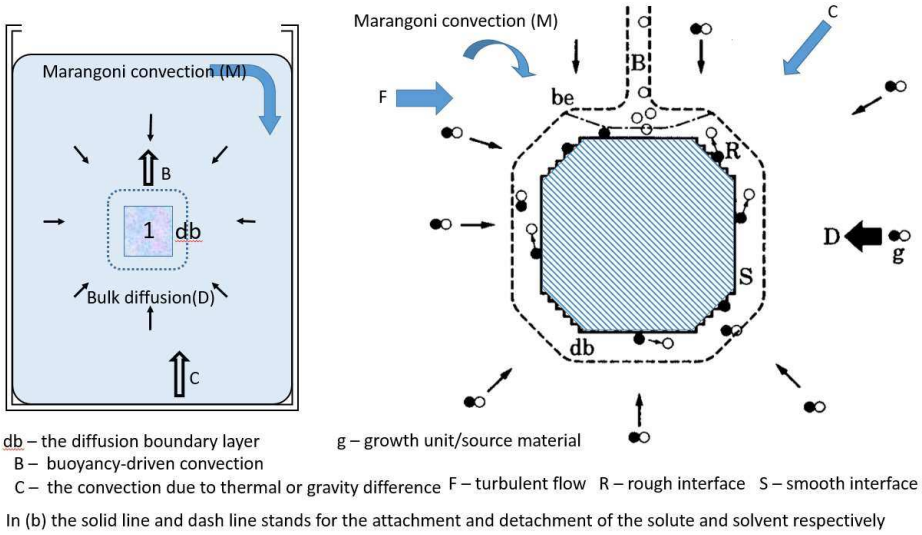

Figure 2-19 A brief image summary of crystal growth in solution phase with possible associated diffusion and convection (a) growth in a container filled with growth solution (b) enlarged image in area 1 marked in (a) which stands for a small crystal with corresponding surrounding environment.[179]

As shown in Figure 2-20, for normal sphere sharped nuclei with radius r, the energy ∀G required for nucleation is increased as r increases, reaches a maximum energy ∀G* at r_c and then decreases after this point (where í ' ι ì 俸隐 □). r_c which gives the highest energy ∀G* is called the critical nucleus. Free energy is added into the molecules to this initial cluster, until the radius reaches critical radius r_c.[115, 183, 184] Once the cluster is larger than the relative critical radius, there is no such limitation for nucleation, thus new molecules can be easily added to clusters by diffusion (i.e. the supply of molecules) for continuing growth. The following step of continuous growth can be simplified as a thermally activated process associated with the specified reaction.[179-182]

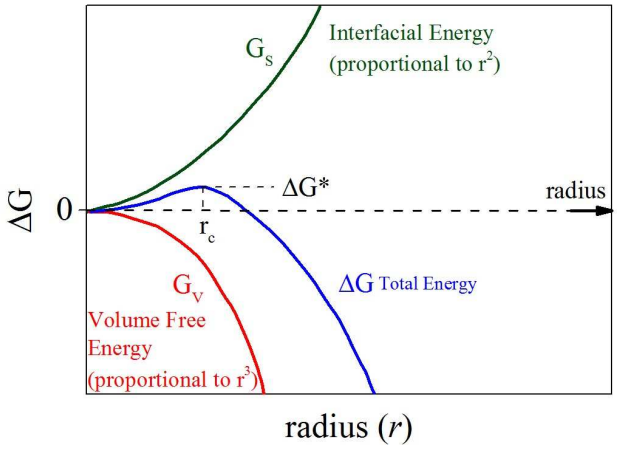

Figure 2-20 Nucleation energy change ∀G as a function of a nucleus radius (r).[115]

In solution, the nucleation can take place either in the bulk solution (homogeneous nucleation) or on the desired surfaces such as seed layer on substrates (heterogeneous), depending on the synthesis condition. Normally, they are happening in the same time in the solution.[185, 186]

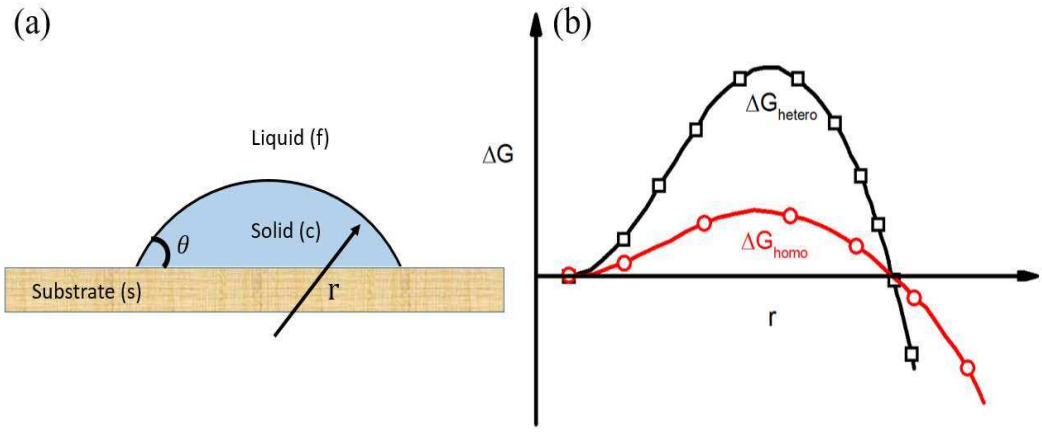

Figure 2-21 (a) Schematic illustration of the nucleation on a foreign flat surface, : :is the virtual contact angle between substrate and nucleating phase. (b) Simplified free energy changes as a function of radius for homogeneous and heterogeneous nucleation respectively. Activation barrier for homogenous nucleation process is higher than heterogeneous nucleation process by the interfacial correlation factor (shape of the heterogeneous system).[185, 186]

In the bulk solution, a homogeneous nucleation process begins at tiny nuclei in a supersaturated medium. The nucleation and growth from solution onto a substrate (or called foreign body) is also affected by the wetting property of the surface and the geography feature of the surface (as shown in Figure 2-21(a)). Thus, the energy change with an interfacial correlation factor can be expressed as:

$$\Delta G_{het} = \Delta G_{hom} \cdot f(m) \quad \text{(Eq. 2-20)}$$

where ΔG_{het} is the changing of heterogeneous nucleation energy and ΔG_{hom} is the changing of homogeneous nucleation. For a normal flat foreign body, the interfacial correlation factor $f(m)$ can be described as:[185, 186]

$$f(m) = \frac{2 - 3m + m^3}{4} \quad \text{(Eq. 2-21)}$$

where m is given by the following equation

$$m = \frac{\gamma_{1,3} - \gamma_{2,3}}{\gamma_{1,2}} = \cos\theta \quad \text{(Eq. 2-22)}$$

where $\gamma_{1,2}$ is the surface free energy between two phases.

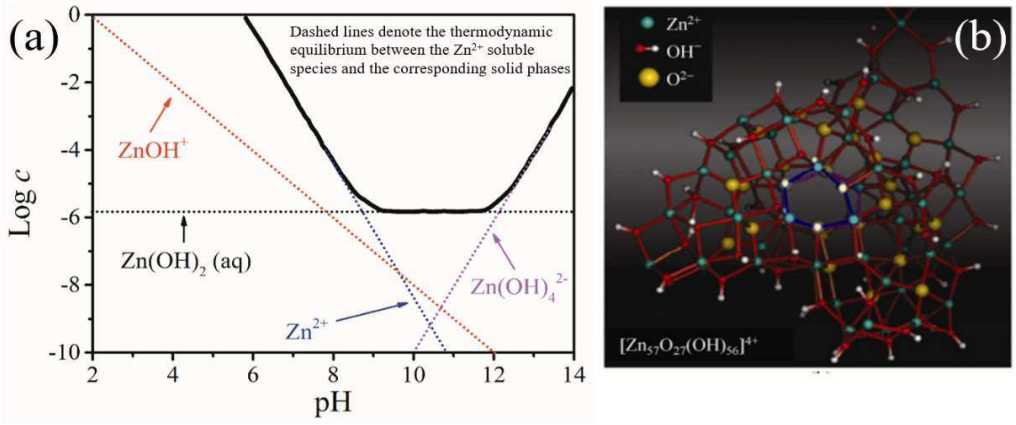

Figure 2-22 (a) Phase changing as a function of reactant concentration (c) and solution pH for the ZnO relevant complexes system at 25 éC (b) the simulated structure of aggregation and nucleation of domains in the wurtzite ZnO.[178, 187]

Considering the chemical reactions in the aqueous solution of ZnO NRs growth, the synthesis processes are typically based on the following basic reactions:

: ā厲斷喵⊡7 (慼 m/s² : ā媼(媧覆 (Eq. 2-23)

: ā厲斷喵/ (慼m/s: ā媼(媫斷 (Eq. 2-24)

: ā媼(媧覆喵⊡7 (慼m/s² 媮ā媼(媧敞爲慼 (Eq. 2-25)

媮ā媼(媧敞爲慼 m/s : ā/ 厦慼喵⊡(厦/ (Eq. 2-26)

: ā/ 厦慼喵(厦/ m/s : ā/ 喵⊡7 (慼 (Eq. 2-27)

In this reaction series, the Zn complexes $Zn(OH)_n^{(2-n)}$ (n=1, 2, 3, 4) could be in different forms depending on the reaction conditions (i.e., reaction solution pH, reactants concentration), which is generally accepted that it is associated with the hydroxyl ions to drive the solid ZnO formation (as shown in Figure 2-22 (a)).[19, 188] Thus the whole ZnO crystal growth can be briefly described as follows:[116, 178] the growth process starts from zinc ion (Zn^{2+}) and hydroxide ion (OH^-) which coordinate with each other and leads to octahedral geometry agglomeration of the complex. With the reactions continuing, the agglomerates become much larger and then reach to the condition (i.e. critical size) which the nucleation of the wurtzite ZnO dominates in the centre (Figure 2-22 (b)).[116, 178] The aggregate contains stable core (initial ZnO part) area and active surface area. Unlike the stable core area, the active surface is mainly covered by Zn^{2+} and OH^- which will maintain the aggregates and keep growing. Once reaching the critical size (r_c) by continuing growth and reaction, the aggregate will exhibit as a nanometre sized wurtzite structure ZnO cluster and become thermodynamically

stable.[116, 178] These clusters thus will form precipitates either on seed layers or in the bulk solution as a basis for continuing crystal growth.[116, 178]

2.4.2.5 ZnO nanostructures for DSSCs application

A large reachable internal surface area is desirable for high performance DSSC photoanodes, which can lead to sufficiently dye loading for the capture of photons. The various morphologies of ZnO nanostructures achievable by aqueous solution growth processes support more opportunities to obtain morphologies with high surface area, which can contribute to dye loading and extend light path length in the photoanode.

ZnO nanoparticles for the DSSC applications have been extensively studied by the inspiration of TiO_2 nanoparticle based DSSC photoanodes (these types of the DSSCs are also known as Gratzel-type cells or conversional DSSCs). The strategy for using the ZnO nanoparticle as the photoanode is almost the same as that using nanocrystallite TiO_2 particles in conversional DSSCs. In this kind of the DSSC, the nanocrystallite TiO_2 particles are displaced by ZnO nanoparticles while other parts remain unchanged. However, in the early research stage, most of the ZnO nanoparticle based DSSCs showed low performance, with the PCEs from 0.4 to 2.2% [189-191] which is much lower than those of the TiO_2 nanoparticle based DSSCs. The low performance is similar to that of the early staged TiO_2 particle based DSSCs, which means the performance of DSSC is very sensitive to photoanode factors (i.e. particle size and morphology, porosity of the MO photoanode, post-treatment).[11, 192] Wong et al studied the effects of ZnO nanoparticle properties (i.e. morphology porosity) on the performance of the DSSCs.[94] As shown in Figure 2-23, there is a complex relationship between the DSSC performance and nanoparticle morphology, defects as well as dye absorption. To

achieve a good DSSC, it is necessary to find an optimised photoanode which can support good electron transport, good match with dye molecules (fast electron injection), suppressed recombination (extended electron life time) and large amount of dye loading.[94]

Among various types of nanoparticle films, some researchers demonstrated advantages of using nanoporous films formed by embedding particles with nanowalls vertically grown on the surface.[193] This type of nanostructure would be favourable for electron transport and could provide reasonable space for electrolyte diffusion through the gaps between each sheet/wall.[193] As reported by Hosono et al.[194, 195], nanoporous ZnO was applied to the DSSCs and an overall PCE of 3.9% was achieved by using a ~10ı m thick ZnO film which was sensitised by the N719 dye.[194] The nanoporous film was achieved using a two-step process: firstly, layered zinc acetate was applied onto the substrates by hydrolysis of zinc acetate dihydrate in methanol at 60 ºC; secondly, a post-heat treatment (above 150ºC) was carried out to transform the layered zinc acetate into crystallised ZnO. During this process, the porous structured film was obtained by heterogeneous nucleation. PCE of 4.3% was also reported by using nanoporous ZnO photoanode by Hosono et al. In their research group, the N719 dye was replaced with D149 dye (an organic metal-free dye).[196] The enhancement in the overall PCE was attributed to the organic dye and shorter immersion time for preventing the formation of a Zn^{2+}/dye complex which is normally considered as a passivation of dye. This is because the points of zero charge (PZC) of the TiO_2 (linked with a pH value of 5.5¯6.5 [197]) is much lower than that of the ZnO (linked with a pH value of 8¯9,[198] whereas the pH value for the dye solution was ~5.[90] Therefore, ZnO photoanodes using the

same dye solution for dye loading process have to compromise the immersion time and sufficient dye loading.[90]

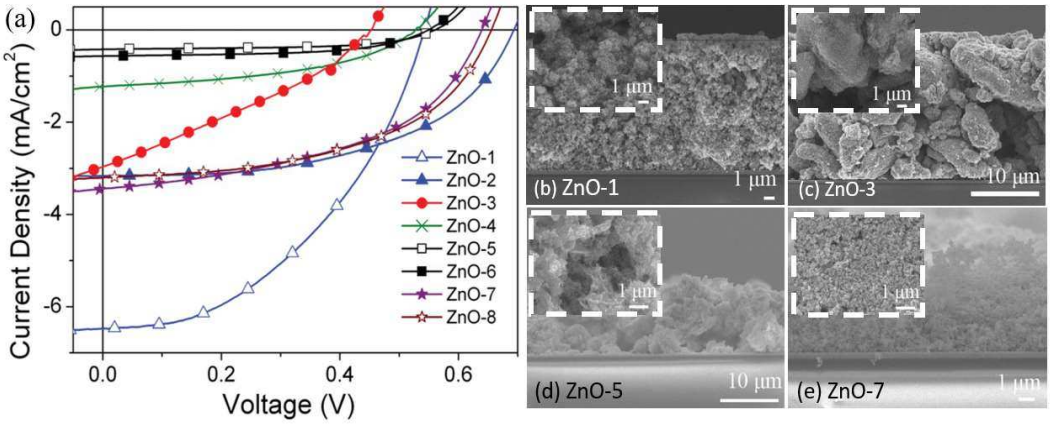

Figure 2-23 ZnO nanoparticle based DSSCs. (a) J-V curves of DSSCs assembled by different ZnO nanoparticle photoanode. (b) to (e) representative cross-section SEM images of the corresponding sample ZnO-1, ZnO-3, ZnO-5 and ZnO-7. The inset in each image ((b) to (e)) is the corresponding top view SEM image of the sample.[94]

Other morphologies of ZnO structures, such as large nanoparticle with nanosheet cluster, nanotetrapods and nanobelts have also been studied for DSSCs. Not only because these structures may bring sufficient reachable surface area for dye loading, but also it is believed that the specific morphology/structure could provide electron transport and/or light trapping properties. Peng et al showed that the nanoflakes (NFs) with small sizes can cause a random light scattering.[199] They also found that the larger sized NFs (> 2 ı m) could significantly improve the light trapping effects of the NFs film.[199, 200] ZnO nanoparticle with nanoplates dispersed in-between have been used as the photoanode for DSSCs applications, which results in a relatively low PCE of 1.6%, possibly due to the loss of reachable internal surface area.[201] Photoanodes based on micro-spheres (size around 4 ≈m), consisting of nanosheets interconnected to each other, were obtained by using acid capping agents during the hydrothermal process.[201] It was

found that the right ordered nanosheet morphology causes a great improvement in reachable surface area, and achieved DSSC PCE up to 2.6%.[193]. Similar strategy using a 3D ZnO tetrapod structures with four adjustable arms (1-20 ı m) extending from one shared core was used as the building block for a photoanode film of the DSSCs (as shown in Figure 2-24).[202] The porous photoanode film was obtained by heaping up these blocks layer by layer deposition, which achieved a porous film with highly reachable surface areas. Additionally, the tetrapods contacted with each other by arms which was believed to be good for electron transport. The DSSCs showed an overall PCE of 1.2% to 3.3%.[202]

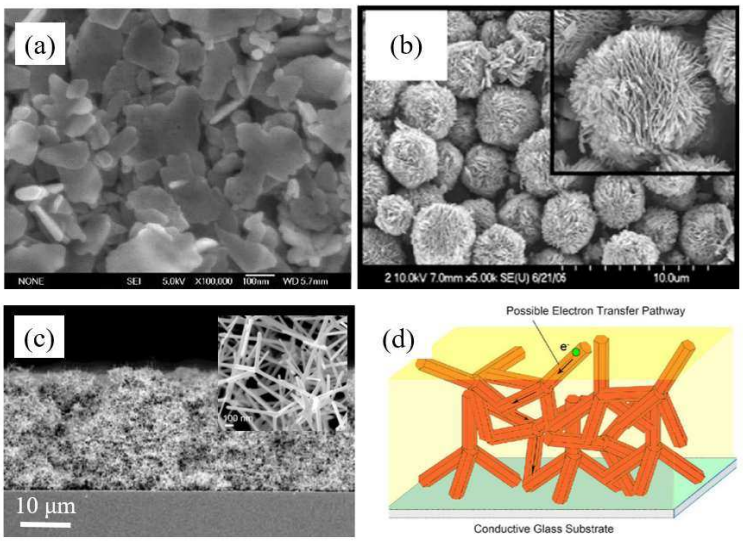

Figure 2-24 SEM images of nanostructured ZnO build blocks (a) nanoporous material assembled by dispersed nanosheets in nanoparticles; (b) nanoporous film assembled by nanosheet-assembled spheres; (c) nanoporous photoanode made by interconnected ZnO tetrapods. The inset is high resolution images; (d) Schematic diagram of nanoporous film assembled by interconnected ZnO tetrapods.[193, 201, 202]

Along with the research work, percolation theory has been used to study the influences of the network morphology/nanostructure on the electron transport behaviour/dynamics in the DSSCs based on MO nano-particulate photoanode. Using typical mesoporous

nanoparticle based photoanode as an example, electron transport through the mesoporous nanoparticles assembled network was correlated with the film thickness (or the coordination numbers of the particles) and porosity of the film.[203] Therefore, during electron transportation through MO nanoparticles based semiconductors mesoporous layer, there could have negative effects: (1) between the trap states on contiguous particles, a series of hoping events may happen;[203] (2) transport have been slowed down by trapping and de-trapping issue;[78] (3) random zig-zag pathway during the transport occurs.[203]

Currently, ZnO one-dimensional (1D) nanostructured materials have been considered as one of the promising ways to overcome the problem mentioned above. Using an array of oriented single-crystalline ZnO 1D nanostructures instead of mesoporous TiO_2 nanoparticle Elm can incur the fast collection of photo-generated carriers throughout the DSSCs as the nanostructures can provide a direct path to the conducting substrate, thus suppressing the recombination losses.[204] Take single-crystalline ZnO NRs as an example, their excellent crystallinity and morphology feature provide good electron transport ability of the ZnO NRs. The electron transport in single ZnO NRs can achieve several orders of magnitude greater than general TiO_2 nanoparticle based photoanode.[205, 206] The carrier collection can be enhanced by a radial electric field within each ZnO NRs which repels the injected-electrons from the surrounding electrolyte.[207] It could reduce the recombination of the majority-carrier electrons at the surface of each ZnO NR.[207] Recombination may remain diffusion controlled. [207] However, the rate of electron transport at the MO surface is mainly affected by the surface field rather than the ZnO diffusion constant for electrons in the NR core. [207] It

is therefore possible that diffusion lengths are significantly larger than those of nanoparticle based films.[207]

ZnO NWs arrays were employed firstly as photoanodes in DSSC applications, by repeatedly replacing samples into fresh growth solution (with additive of PEI) under 92°C. The length of ZnO NWs can be modified and controlled. The longest NW arrays could reach around 20-25 ı m with the NW diameter around 130 to 200 nm (as shown in Figure 2-25), though the reachable internal surface area was only around 1/15 compared to a conventional nanoparticle based mesoporous film.[95] The overall PCE was 1.2 to 1.5 % which is around 1/8 compare to a conventional nanoparticle based mesoporous film. The electron concentration of a single ZnO NW is 1-5B10^{18} cm^{-3} with a mobility of 1-5 cm^2 V^{-1} s^{-1}. [95] The electron diffusivity of a single ZnO NW is 0.05-0.5 cm^{2}s^{-1}, which is much higher than those of the TiO_2 nanoparticle based DSSCs under a light illustration working condition.[17, 95, 103, 104]

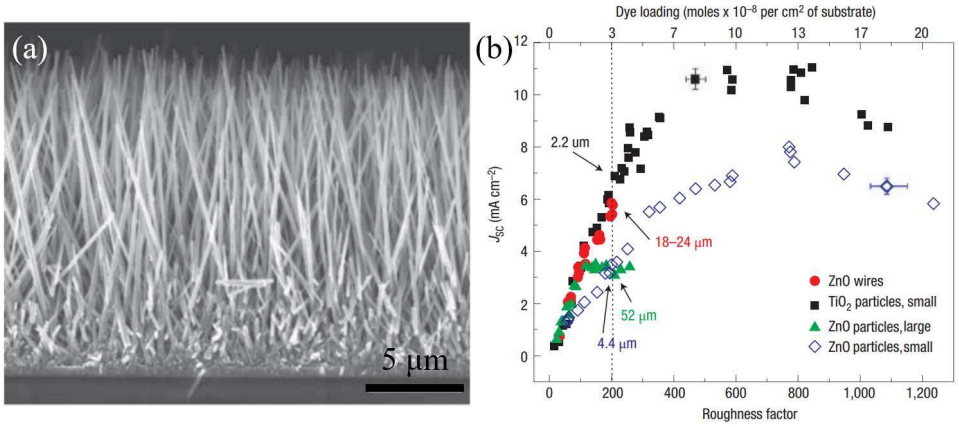

Figure 2-25 (a) the representative SEM image of the ZnO NRs on FTO used as photoanode in DSSC. (b) Summary and comparative performance of NRs and nanoparticle based DSSCs.[95]

To confirm that the ZnO NWs can bring the benefits for electron transport, Jsc as a function of nanostructure roughness factor (reachable surface area /projected surface

area) was studied.[95] As shown in Figure 2-25 (b), the DSSCs were made using the ZnO NWs, ZnO NPs or TiO_2 NPs based DSSCs were chosen as the experimental group.[95] Either TiO_2 NPs or ZnO NPs shows a prompt saturation and a subsequent decrease in the Jsc with continuing increased roughness. This indicated that the performance of the cell decreases above a certain MO photoanode thickness due to increased recombination losses. On the other hand, the ZnO NRs/NWs based photoanode shows a linear increase in the Jsc even though the photoanode are around 25 ı m thick. This indicated that the ZnO NRs/NWs based photoanode could reduce the recombination losses because of its high electron transport efficiency.[95] The ZnO NRs/NWs DSSCs produced a higher Jsc than those of the NPs based DSSCs over the accessible range of roughness. [95] This confirms that the NRs/NWs support higher electron transport abilities in DSSCs when compared with NPs. Similar results have been reported for the DSSCs with higher PCEs.[95, 208-210]

Since changing the NRs/NWs morphologies have been demonstrated as a potential way for improving electron transport in the pioneer˘s work, many attempts have been made to explore this approach. One approach is using ZnO nanotube arrays as the morphology can not only support the electron conductive pathway but may also support more porosity by its typical cavity structures. It can be produced by a growth-etching aqueous solution method which contains typical NR growth and selective etching process for the tube like morphology.[116, 211] However, the performance of the ZnO nanotube based DSSCs only achieved PCE value of 1.6% due to etching/reaction with dye molecules in weak acid dye loading environment, which results in low injection efficiency and insufficient dye loading. Some researchers tried to increase the dye capability by

modifying the NRs/NWs structure, which can be achieved by dendritic structures or NRs/NWs structure filling with particles.[212] Dendritic structures formed by a NRs/NWs core-bone with branches were formed by more complicated processes than NWs/NRs required.[68, 116] Baxter et al. developed a multiple-generation growth for obtaining NW structures with branches for improving dye loading capabilities, however, only 1.1% PCE was achieved by this kind of DSSCs.[68] On the other hand, the NRs/NWs array-nanoparticles composite films have been demonstrated to significantly increase the overall PCE of the DSSCs from 0.84% (pure NRs) to 2.2% (NRs array-nanoparticles composites). This have been achieved by filling 5-30 nm NPs inside the NRs by Ku et al.[212]

2.4.3 Hybrid ZnO nanostructures for DSSC applications

In order to overcome the disadvantage of ZnO used in DSSCs, core-shell and hybrid structures have been proposed. Much effort has been made in this area for preventing the formation of Zn^{2+}/dye agglomerates and improving the ZnO stability. This has also been considered as an efficient way to improve the interfacial electron injection and suppress recombination at the semiconductor/dye/electrolyte interfaces for achieving the best performance of the DSSCs. Modifying the ZnO, by applying another buffer layer on its surface, a high reachable surface area can be maintained and also the requirements for electron injection and suppressed electron back transfer and recombination can be achieved. Thus, successively using ZnO associated with other materials would improve the development of ZnO based DSSC. Different materials (i.e. TiO_2, SiO_2, ZrO_2, Al_2O_3 and MgO) have been studied as the modification shell/layer for photoanode usage. Diversified materials support more choices of photoanode

material design with varying degrees of success in improving electron mobility as well as preventing electron back transport.[85, 86] Table 2-4 summarises some recently reported hybrid and/or core-shell structures for the DSSCs using different MO materials.

Table 2-4 A brief summary of core-shell nanostructure based DSSCs.[31, 87, 213-220]

Material/band gap (eV)		Shell concentration or thickness/ dye	Parameters of DSSCs with (without) shell				Summary
Core	Shell		Voc (V)	Jsc (mA/cm^2)	FF (%)	PCE (%)	
TiO_2 (3.3)	Al_2O_3 (9.9)	N719 [213]	0.76 (0.55)	12.1 (9.1)	61.1 (55.1)	5.6 (3.7)	Thicker shell limits electron injection
		4 times coated /N719[213]	0.86 (0.55)	2.45 (9.1)	65.6 (55.1)	1.4 (3.7)	
TiO_2 (3.3)	SiO_2 (8.9)	N719 [208]	0.71 (0.74)	10.6 (9.1)	58.1 (55.1)	4.4 (3.7)	Increase in Voc, larger Jsc obtained with N719
		0.53/Eosin [214]	0.60 (0.58)	0.55 (0.37)	54.0 (54.0)	0.18 (0.12)	
TiO_2 (3.3)	ZrO_2 (4.7)	1:0.38/N3 [215]	-	-	-	2.27 (0.42)	Improve cell performanc.
		N3[220]	-	-	-	2.3 (1.4)	
TiO_2 (3.3)	MgO (7.2)	N3[216]	0.72 (0.64)	11.7 (6.4)	53.5 (47.3)	4.5 (3.1)	Large increase in Jsc
ZnO (3.3)	TiO_2 (3.3)	10-25 nm shell /N3 [217]	0.8	2.0	60 (36)	2.0 (0.9)	Improve Voc Jsc and FF
		0-34 nm shell /N719 [207]	0.78 (0.56)	4.7 (2.2)	62 (30)	2.25 (0.37)	
ZnO (3.3)	SiO_2 (8.9)	1:5/N719 [218]	0.68 (0.67)	7.7 (1.0)	69.0 (73.0)	3.6 (0.5)	Greatly improved Jsc
SnO_2 (3.5)	TiO_2 (3.2)	35%/N719 [219]	0.66 (0.48)	10.9 (6.4)	54.0 (40.0)	3.9 (1.2)	Improve Jsc, Voc as well as FF
SnO_2 (3.5)	Al_2O_3 (9.9)	6%/N719 [219]	0.74 (0.48)	10.0 (6.4)	70.0 (40.0)	5.2 (1.2)	Improve Jsc

SiO_2 has been used for the shell because it changes the surface charge due to the change in the isoelectric point of SiO_2, and protects the ZnO surface from the acid solution environment. The formation of Zn^{2+}/dye agglomerates can also be prevent.[31] As a result, an increase in Jsc (1.00 to 7.66 mA/cm^2) has been observed, which results in an increased PCE from 0.52 to 3.2 %.[31, 218] Similar improvement has also been reported by Shin et al., who demonstrated that using SiO_2 decorated ZnO NP based photoanode, the DSSCs achieved an overall PEC of 4.4%.[221]

TiO_2 is considered as a suitable material for the buffer layer for forming a shell on the core nanomaterial, because its chemical stability and good matches with most types of dye molecules. A typical solution process for applying a modification TiO_2 layer on the ZnO nanostructure can be realised by simply immersing/dipping ZnO sample into a reaction solution containing titanium alkoxide ($Ti(OBu)_4$), followed by annealing process at 400 °C for crystallisation.[95] The TiO_2 layer on the nanostructure was also achieved by electrochemical deposition.[222, 223] However, these techniques have limited capability for accurate thickness control. Atomic layer deposition (ALD) is commonly used technique for the synthesis of a high-quality nanoscale thin layer (1 nm to 50 nm), and has been employed for coating TiO_2 modification layer on ZnO. Law et al. had successfully achieved thickness control of TiO_2 layers on the order of 1 nm.[207] As shown in Figure 2-26, the core-shell structures of ZnO-Al_2O_3 and ZnO-TiO_2 NRs were easily obtained using this method. In their experiment, the crystals of TiO_2 were strongly dependent on film shell thickness (amorphous with thickness less than 5 nm; but changed to anatase TiO_2 by a thicker shell (> 5 nm)).[207] On the other hand, only an amorphous Al_2O_3 shell was achieved in their study, which served as an insulator layer

and caused the decrease of Jsc. Similar to SiO_2 layer, TiO_2 buffer layer can also be served as a protection layer to improve ZnO stability (i.e. prevent the formation of Zn^{2+}/dye complex).[207] The core-shell structure of ZnO-TiO_2 was also believed to form an energy barrier that suppressed the injected-electrons back transfer to the surface which will recombine with oxide dye and/or redox couples in the electrolyte. Thus, the overall PCE of the cell was improved. The values of Voc and Jsc were also increased after the TiO_2 shell was coated on ZnO, and the overall PCE performance of the DSSCs has been improved substantially to 2.25%.[207] Balaya et al also reported that after applying a 10-25 nm thickness TiO_2 shell on the ZnO NRs, the FF of the cell was significantly increased.[217]

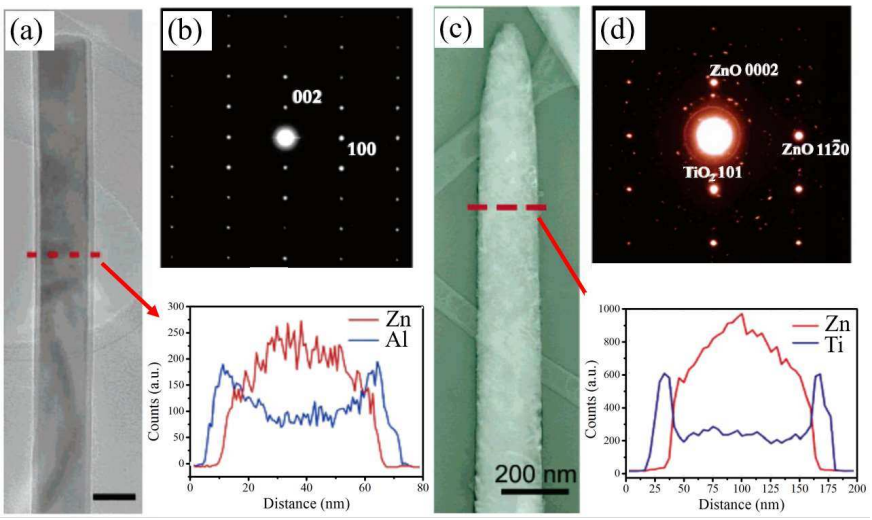

Figure 2-26 Characterisation of the (a) to (b) ZnO-Al_2O_3 and (c) to (d) ZnO-TiO_2 core-shell NRs. (a) & (c) the TEM images and (b) & (d) the relative electron diffraction pattern of the ZnO-Al_2O_3 and ZnO-TiO_2 NR. The insect in (a) and (c) is the corresponding EDS element examination.[207]

As explained above, amorphous Al_2O_3 has been studied as a shell on the ZnO NRs and designed for preventing electron back transport.[207] Compared with normally used energy barrier materials (i.e. TiO_2 or SiO_2), the Al_2O_3 shell as an insulating barrier was

found to lead to a slight increase in Voc of the DSSCs but a decrease in Jsc and PCE with increasing shell thickness.[207] The slight increase of Voc could be attributed to the Al_2O_3 shell which acts as a tunnel barrier when it is very thin. This improves Voc by reducing recombination.[207] However, the thick Al_2O_3 shell suppress electron injection more than recombination which decreases the DSSC performance.[207]

Although the use of a modification MO semiconductor (i.e. Al_2O_3, TiO_2 or SiO_2) shells can improve ZnO nanostructure based DSSCs, the resultant effects on the DSSC performance with varying degree of success had been reported by pioneer research works. Further investigation is still needed for a detailed understanding of the shell effects as well as how to select suitable materials for the optimal enhancement of overall performance of the DSSCs. In general, the shell modification effects are related to two main effects:[18, 20] (1) the enhancement effect is affected by the surface morphology changing and the methods used for applying and/or synthesis MO shell materials on the target core; (2) different MO materials used for shell which have different chemical bonding between the cations (i.e. Si^{4+}, Al^{3+}, Ti^{4+}) and O^{2+}, and affect different interfacial states, thus leading to different results in electron-injection processes.

2.5 Summary and motivation

In brief, for further improving the performance of the DSSCs, there are several ways which can be applied:[11, 95, 224, 225]

(1) Increasing the porosity (or reachable surface area) of MO photoanode, thus increasing the amounts of dye molecules absorbed on the surface of the photoanode material (MO semiconductor) for improving light harvest;

(2) Improving the electrical properties of the MO semiconductor to achieve a better electron collection efficiency (i.e. faster electron transport);

(3) Suppressing the reverse reactions in DSSC and decreasing the recombination loss thus leading to an increase in the efficiency;

(4) Synthesis high performance absorbers (i.e. dye) to harvest more light to increase the DSSC performance;

(5) Modifying and improving the redox couples as well as additives in electrolytes to decrease recombination and improve stability and overall performance of DSSC;

(6) Improving CE catalytic activity and meet the requirement of new designed electrolyte for achieving fast regeneration and charge transport.

Herein, the objective of this thesis is to achieve the low-temperature synthesis strategies for producing crystallised ZnO based (crystallised TiO_2 as shell) nanostructure with controllable morphology and composite which will be used as photoanode for typical DSSCs. Low-temperature synthesis crystallised ZnO NRs using aqueous solution process will be investigated in detail (i.e. influences of reactants, chemical reaction factor and additives effects on the ZnO NRs growth). A low-temperature modification method is developed for preparing the crystallised TiO_2 layer which can be used to assemble ZnO/TiO_2 core-shell structure. The ZnO nanostructure with TiO_2 modification layer will then be used as the photoanode and assembled to DSSCs. The influence of these ZnO nanostructure based photoanode properties on the DSSCs performance will be studied.

Reference

1. Fakharuddin, A., R. Jose, T.M. Brown, F. Fabregat-Santiago, and J. Bisquert, A perspective on the production of dye-sensitized solar modules. Energy & Environmental Science, 2014. 7(12): p. 3952-3981.
2. NREL, Photovoltaic Research, Efficiency chart. [cited 2016 20, August]; Available from: http://www.nrel.gov/ncpv/images/efficiency_chart.jpg.
3. Ali, N., A. Hussain, R. Ahmed, M.K. Wang, C. Zhao, B.U. Haq, and Y.Q. Fu, Advances in nanostructured thin film materials for solar cell applications. Renewable and Sustainable Energy Reviews, 2016. 59: p. 726-737.
4. Green, M.A., K. Emery, Y. Hishikawa, W. Warta, and E.D. Dunlop, Solar cell efficiency tables (Version 45). Progress in Photovoltaics: Research and Applications, 2015. 23(1): p. 1-9.
5. Yella, A., H. W. Lee, H.N. Tsao, C. Yi, A.K. Chandiran, M.K. Nazeeruddin, E.W. G. Diau, C. Y. Yeh, S.M. Zakeeruddin, and M. Gr±tzel, Porphyrin-Sensitized Solar Cells with Cobalt (II/III)¯Based Redox Electrolyte Exceed 12 Percent Efficiency. Science, 2011. 334(6056): p. 629-634.
6. Marchioro, A., J. Teuscher, D. Friedrich, M. Kunst, R. van de Krol, T. Moehl, M. Gratzel, and J. E. Moser, Unravelling the mechanism of photoinduced charge transfer processes in lead iodide perovskite solar cells. Nat Photon, 2014. 8(3): p. 250-255.
7. Form. Nł 254, Farbstoffsolarzellen. From DIY to Solar Chic. [Web page] [cited 2015 11, November]; Available from: http://www.form.de/en/magazine/form254/files.
8. DYESOL Ltd, Global Leaders in Dye Solar Cell Technology. 2012 [cited 2015 11, November];Available from: https://www.dyesol.com/media/wysiwyg/Documents/investorpresentations/DYESOL_LIMITED_Investor_Update_Presentation_June_2012.pdf.
9. Corporation, S. Research and Development on the Dye-Sensitized Solar Cell Taking Full Advantage of the Characteristics of the Materials and Aiming to Open New Markets. [cited 2014 5, May]; Available from: http://www.sony.net/Products/SC-HP/cx_news_archives/img/pdf/vol_56/sideview56.pdf#page=1.
10. Gong, J., J. Liang, and K. Sumathy, Review on dye-sensitized solar cells (DSSCs): Fundamental concepts and novel materials. Renewable and Sustainable Energy Reviews, 2012. 16(8): p. 5848-5860.
11. Zhang, S., X. Yang, Y. Numata, and L. Han, Highly efficient dye-sensitized solar cells: progress and future challenges. Energy & Environmental Science, 2013. 6(5): p. 1443-1464.
12. Dai, S., K. Wang, J. Weng, Y. Sui, Y. Huang, S. Xiao, S. Chen, L. Hu, F. Kong, X. Pan, C. Shi, and L. Guo, Design of DSC panel with efficiency more than 6%. Solar Energy Materials and Solar Cells, 2005. 85(3): p. 447-455.
13. EarlyHistory. Workspace.imperial.ac.uk. Retrieved on 30 May 2013.
14. O'Regan, B. and M. Gratzel, A low-cost, high-efficiency solar cell based on dye-sensitized colloidal TiO_2 films. Nature, 1991. 353(6346): p. 737-740.
15. Gratzel, M., Photoelectrochemical cells. Nature, 2001. 414(6861): p. 338-344.
16. Yang, B., Y. Yuan, P. Sharma, S. Poddar, R. Korlacki, S. Ducharme, A. Gruverman, R. Saraf, and J. Huang, Tuning the Energy Level Offset between Donor and Acceptor with Ferroelectric Dipole Layers for Increased Efficiency in Bilayer Organic Photovoltaic Cells. Advanced Materials, 2012. 24(11): p. 1455-1460.
17. Concina, I. and A. Vomiero, Metal Oxide Semiconductors for Dye- and Quantum-Dot-Sensitized Solar Cells. Small, 2015. 11(15): p. 1744-1774.
18. Xu, J., Z. Chen, J.A. Zapien, C. S. Lee, and W. Zhang, Surface Engineering of ZnO Nanostructures for Semiconductor-Sensitized Solar Cells. Advanced Materials, 2014. 26(31): p. 5337-5367.

19. Xu, S. and Z.L. Wang, One-dimensional ZnO nanostructures: Solution growth and functional properties. Nano Research, 2011. 4(11): p. 1013-1098.
20. Anta, J.A., E. Guill¶n, and R. Tena-Zaera, ZnO-Based Dye-Sensitized Solar Cells. The Journal of Physical Chemistry C, 2012. 116(21): p. 11413-11425.
21. Tanaka, Y., K. Matsuo, and S. Yuzuriha, Long-Lasting Muscle Thinning Induced by Infrared Irradiation Specialized With Wavelengths and Contact Cooling: A Preliminary Report. Eplasty, 2010. 10: p. e40.
22. Gueymard, C.A., D. Myers, and K. Emery, Proposed reference irradiance spectra for solar energy systems testing. Solar Energy, 2002. 73(6): p. 443-467.
23. Piotrowiak, P., Solar Energy Conversion : Dynamics of Interfacial Electron and Excitation Transfer 09 Oct 2013 ed. 2013.
24. Konezny, S.J. and V.S. Batista, CHAPTER 1 Computational Modeling of Photocatalytic Cells, in Solar Energy Conversion: Dynamics of Interfacial Electron and Excitation Transfer. 2013, The Royal Society of Chemistry. p. 1-36.
25. Barnes, P.R.F., K. Miettunen, X. Li, A.Y. Anderson, T. Bessho, M. Gratzel, and B.C. O'Regan, Interpretation of Optoelectronic Transient and Charge Extraction Measurements in Dye-Sensitized Solar Cells. Advanced Materials, 2013. 25(13): p. 1881-1922.
26. Huang, F., D. Chen, X.L. Zhang, R.A. Caruso, and Y. B. Cheng, Dual-Function Scattering Layer of Submicrometer-Sized Mesoporous TiO_2 Beads for High-Efficiency Dye-Sensitized Solar Cells. Advanced Functional Materials, 2010. 20(8): p. 1301-1305.
27. Nazeeruddin, M.K., A. Kay, I. Rodicio, R. Humphrybaker, E. Muller, P. Liska, N. Vlachopoulos, and M. Gratzel, Conversion of light to electricity by cis-X2bis(2,2'-bipyridyl-4,4'-dicarboxylate)ruthenium(II) charge-transfer sensitizers (X = Cl-, Br-, I-, CN-, and SCN-) on nanocrystalline titanium dioxide electrodes. Journal of the American Chemical Society, 1993. 115(14): p. 6382-6390.
28. Barbe, C.J., F. Arendse, P. Comte, M. Jirousek, F. Lenzmann, V. Shklover, and M. Gratzel, Nanocrystalline titanium oxide electrodes for photovoltaic applications. Journal of the American Ceramic Society, 1997. 80(12): p. 3157-3171.
29. Ito, S., P. Liska, P. Comte, R.L. Charvet, P. Pechy, U. Bach, L. Schmidt-Mende, S.M. Zakeeruddin, A. Kay, M.K. Nazeeruddin, and M. Gratzel, Control of dark current in photoelectrochemical (TiO_2/I^--I_3^-) and dye-sensitized solar cells. Chemical Communications, 2005(34): p. 4351-4353.
30. Sommeling, P.M., B.C. O'Regan, R.R. Haswell, H.J.P. Smit, N.J. Bakker, J.J.T. Smits, J.M. Kroon, and J.A.M. van Roosmalen, Influence of a $TiCl_4$ post-treatment on nanocrystalline TiO_2 films in dye-sensitized solar cells. Journal of Physical Chemistry B, 2006. 110(39): p. 19191-19197.
31. Thavasi, V., V. Renugopalakrishnan, R. Jose, and S. Ramakrishna, Controlled electron injection and transport at materials interfaces in dye sensitized solar cells. Materials Science and Engineering: R: Reports, 2009. 63(3): p. 81-99.
32. Gr±tzel, M., Nanocrystalline Injection Solar Cells, in Thin Film Solar Cells. 2006, John Wiley & Sons, Ltd. p. 363-385.
33. Tian, J., Z. Zhao, A. Kumar, R.I. Boughton, and H. Liu, Recent progress in design, synthesis, and applications of one-dimensional TiO_2 nanostructured surface heterostructures: a review. Chemical Society Reviews, 2014. 43(20): p. 6920-6937.
34. Anderson, S., E.C. Constable, M.P. Dare-Edwards, J.B. Goodenough, A. Hamnett, K.R. Seddon, and R.D. Wright, Chemical modification of a titanium(IV) oxide electrode to give stable dye sensitisation without a supersensitiser. Nature, 1979. 280(5723): p. 571-573.
35. Nazeeruddin, M.K., A. Kay, I. Rodicio, R. Humphry-Baker, E. Mueller, P. Liska, N. Vlachopoulos, and M. Graetzel, Conversion of light to electricity by cis-X2bis(2,2'-

bipyridyl-4,4'-dicarboxylate)ruthenium(II) charge-transfer sensitizers (X = Cl-, Br-, I-, CN-, and SCN-) on nanocrystalline titanium dioxide electrodes. Journal of the American Chemical Society, 1993. 115(14): p. 6382-6390.
36. Nazeeruddin, M.K., S.M. Zakeeruddin, R. Humphry-Baker, M. Jirousek, P. Liska, N. Vlachopoulos, V. Shklover, C. H. Fischer, and M. Grätzel, Acid–Base Equilibria of (2,2'-Bipyridyl-4,4'-dicarboxylic acid)ruthenium(II) Complexes and the Effect of Protonation on Charge-Transfer Sensitization of Nanocrystalline Titania. Inorganic Chemistry, 1999. 38(26): p. 6298-6305.
37. Nazeeruddin, M.K., P. Péchy, T. Renouard, S.M. Zakeeruddin, R. Humphry-Baker, P. Comte, P. Liska, L. Cevey, E. Costa, V. Shklover, L. Spiccia, G.B. Deacon, C.A. Bignozzi, and M. Grätzel, Engineering of Efficient Panchromatic Sensitizers for Nanocrystalline TiO_2-Based Solar Cells. Journal of the American Chemical Society, 2001. 123(8): p. 1613-1624.
38. Wang, P., S.M. Zakeeruddin, I. Exnar, and M. Gratzel, High efficiency dye-sensitized nanocrystalline solar cells based on ionic liquid polymer gel electrolyte. Chemical Communications, 2002(24): p. 2972-2973.
39. Wang, P., S.M. Zakeeruddin, J.E. Moser, M.K. Nazeeruddin, T. Sekiguchi, and M. Gratzel, A stable quasi-solid-state dye-sensitized solar cell with an amphiphilic ruthenium sensitizer and polymer gel electrolyte. Nat Mater, 2003. 2(6): p. 402-407.
40. Lammi, R.K., R.W. Wagner, A. Ambroise, J.R. Diers, D.F. Bocian, D. Holten, and J.S. Lindsey, Mechanisms of Excited-State Energy-Transfer Gating in Linear versus Branched Multiporphyrin Arrays. The Journal of Physical Chemistry B, 2001. 105(22): p. 5341-5352.
41. Borgström, M., E. Blart, G. Boschloo, E. Mukhtar, A. Hagfeldt, L. Hammarström, and F. Odobel, Sensitized Hole Injection of Phosphorus Porphyrin into NiO: Toward New Photovoltaic Devices. The Journal of Physical Chemistry B, 2005. 109(48): p. 22928-22934.
42. Hasobe, T., P.V. Kamat, V. Troiani, N. Solladié, T.K. Ahn, S.K. Kim, D. Kim, A. Kongkanand, S. Kuwabata, and S. Fukuzumi, Enhancement of Light-Energy Conversion Efficiency by Multi-Porphyrin Arrays of Porphyrin–Peptide Oligomers with Fullerene Clusters. The Journal of Physical Chemistry B, 2005. 109(1): p. 19-23.
43. Bessho, T., S.M. Zakeeruddin, C. Y. Yeh, E.W. G. Diau, and M. Grätzel, Highly Efficient Mesoscopic Dye-Sensitized Solar Cells Based on Donor–Acceptor-Substituted Porphyrins. Angewandte Chemie International Edition, 2010. 49(37): p. 6646-6649.
44. Wang, Z.S., Y. Cui, K. Hara, Y. Dan-oh, C. Kasada, and A. Shinpo, A High-Light-Harvesting-Efficiency Coumarin Dye for Stable Dye-Sensitized Solar Cells. Advanced Materials, 2007. 19(8): p. 1138-1141.
45. Wang, Z. S., Y. Cui, Y. Dan-oh, C. Kasada, A. Shinpo, and K. Hara, Thiophene-Functionalized Coumarin Dye for Efficient Dye-Sensitized Solar Cells: Electron Lifetime Improved by Coadsorption of Deoxycholic Acid. The Journal of Physical Chemistry C, 2007. 111(19): p. 7224-7230.
46. Howie, W.H., F. Claeyssens, H. Miura, and L.M. Peter, Characterization of Solid-State Dye-Sensitized Solar Cells Utilizing High Absorption Coefficient Metal-Free Organic Dyes. Journal of the American Chemical Society, 2008. 130(4): p. 1367-1375.
47. Horiuchi, T., H. Miura, K. Sumioka, and S. Uchida, High Efficiency of Dye-Sensitized Solar Cells Based on Metal-Free Indoline Dyes. Journal of the American Chemical Society, 2004. 126(39): p. 12218-12219.
48. Baheti, A., P. Tyagi, K.R.J. Thomas, Y. C. Hsu, and J.T.s. Lin, Simple Triarylamine-Based Dyes Containing Fluorene and Biphenyl Linkers for Efficient Dye-Sensitized Solar Cells. The Journal of Physical Chemistry C, 2009. 113(20): p. 8541-8547.

49. Hagberg, D.P., J. H. Yum, H. Lee, F. De Angelis, T. Marinado, K.M. Karlsson, R. Humphry-Baker, L. Sun, A. Hagfeldt, M. Gr±tzel, and M.K. Nazeeruddin, Molecular Engineering of Organic Sensitizers for Dye-Sensitized Solar Cell Applications. Journal of the American Chemical Society, 2008. 130(19): p. 6259-6266.
50. Wang, Z. S., N. Koumura, Y. Cui, M. Takahashi, H. Sekiguchi, A. Mori, T. Kubo, A. Furube, and K. Hara, Hexylthiophene-Functionalized Carbazole Dyes for Efficient Molecular Photovoltaics: Tuning of Solar-Cell Performance by Structural Modification. Chemistry of Materials, 2008. 20(12): p. 3993-4003.
51. Koumura, N., Z. S. Wang, S. Mori, M. Miyashita, E. Suzuki, and K. Hara, Alkyl-Functionalized Organic Dyes for Efficient Molecular Photovoltaics. Journal of the American Chemical Society, 2006. 128(44): p. 14256-14257.
52. Burke, A., S. Ito, H. Snaith, U. Bach, J. Kwiatkowski, and M. Gr±tzel, The Function of a TiO_2 Compact Layer in Dye-Sensitized Solar Cells Incorporating `Planar_ Organic Dyes. Nano Letters, 2008. 8(4): p. 977-981.
53. Kim, B. G., C. G. Zhen, E.J. Jeong, J. Kieffer, and J. Kim, Organic Dye Design Tools for Efficient Photocurrent Generation in Dye-Sensitized Solar Cells: Exciton Binding Energy and Electron Acceptors. Advanced Functional Materials, 2012. 22(8): p. 1606-1612.
54. Ameri, T., P. Khoram, J. Min, and C.J. Brabec, Organic Ternary Solar Cells: A Review. Advanced Materials, 2013. 25(31): p. 4245-4266.
55. Klahr, B.M. and T.W. Hamann, Performance Enhancement and Limitations of Cobalt Bipyridyl Redox Shuttles in Dye-Sensitized Solar Cells. The Journal of Physical Chemistry C, 2009. 113(31): p. 14040-14045.
56. Boschloo, G. and A. Hagfeldt, Characteristics of the Iodide/Triiodide Redox Mediator in Dye-Sensitized Solar Cells. Accounts of Chemical Research, 2009. 42(11): p. 1819-1826.
57. Wang, M., N. Chamberland, L. Breau, J.-E. Moser, R. Humphry-Baker, B. Marsan, S.M. Zakeeruddin, and M. Gr±tzel, An organic redox electrolyte to rival triiodide/iodide in dye-sensitized solar cells. Nat Chem, 2010. 2(5): p. 385-389.
58. Oskam, G., B.V. Bergeron, G.J. Meyer, and P.C. Searson, Pseudohalogens for Dye-Sensitized TiO_2 Photoelectrochemical Cells. The Journal of Physical Chemistry B, 2001. 105(29): p. 6867-6873.
59. Nusbaumer, H., J.E. Moser, S.M. Zakeeruddin, M.K. Nazeeruddin, and M. Gratzel, Co-II(dbbiP)(2)(2+) complex rivals tri-iodide/iodide redox mediator in dye-sensitized photovoltaic cells. Journal of Physical Chemistry B, 2001. 105(43): p. 10461-10464.
60. Hara, K., T. Horiguchi, T. Kinoshita, K. Sayama, and H. Arakawa, Influence of electrolytes on the photovoltaic performance of organic dye-sensitized nanocrystalline TiO_2 solar cells. Solar Energy Materials and Solar Cells, 2001. 70(2): p. 151-161.
61. Kubo, W., K. Murakoshi, T. Kitamura, S. Yoshida, M. Haruki, K. Hanabusa, H. Shirai, Y. Wada, and S. Yanagida, Quasi-Solid-State Dye-Sensitized TiO_2 Solar Cells:厑 Effective Charge Transport in Mesoporous Space Filled with Gel Electrolytes Containing Iodide and Iodine. The Journal of Physical Chemistry B, 2001. 105(51): p. 12809-12815.
62. Cao, F., G. Oskam, and P.C. Searson, A Solid State, Dye Sensitized Photoelectrochemical Cell. The Journal of Physical Chemistry, 1995. 99(47): p. 17071-17073.
63. O'Regan, B. and D.T. Schwartz, Efficient Photo-Hole Injection from Adsorbed Cyanine Dyes into Electrodeposited Copper(I) Thiocyanate Thin Films. Chemistry of Materials, 1995. 7(7): p. 1349-1354.

64. Tennakone, K., G.R.R.A. Kumara, I.R.M. Kottegoda, K.G.U. Wijayantha, and V.P.S. Perera, A solid-state photovoltaic cell sensitized with a ruthenium bipyridyl complex. Journal of Physics D: Applied Physics, 1998. 31(12): p. 1492-1496.
65. O'Regan, B., D.T. Schwartz, S.M. Zakeeruddin, and M. Gratzel, Electrodeposited nanocomposite n-p heterojunctions for solid-state dye-sensitized photovoltaics. Advanced Materials, 2000. 12(17): p. 1263-1267.
66. Chung, I., B. Lee, J. He, R.P.H. Chang, and M.G. Kanatzidis, All-solid-state dye-sensitized solar cells with high efficiency. Nature, 2012. 485(7399): p. 486-489.
67. Kumara, G.R.A., A. Konno, K. Shiratsuchi, J. Tsukahara, and K. Tennakone, Dye-Sensitized Solid-State Solar Cells: Use of Crystal Growth Inhibitors for Deposition of the Hole Collector. Chemistry of Materials, 2002. 14(3): p. 954-955.
68. Baxter, J.B. and E.S. Aydil, Dye-sensitized solar cells based on semiconductor morphologies with ZnO nanowires. Solar Energy Materials and Solar Cells, 2006. 90(5): p. 607-622.
69. Papageorgiou, N., Counter-electrode function in nanocrystalline photoelectrochemical cell configurations. Coordination Chemistry Reviews, 2004. 248(13-14): p. 1421-1446.
70. Boennemann, H., G. Khelashvili, S. Behrens, A. Hinsch, K. Skupien, and E. Dinjus, Role of the platinum nanoclusters in the iodide/triiodide redox system of dye solar cells. Journal of Cluster Science, 2007. 18(1): p. 141-155.
71. Hauch, A. and A. Georg, Diffusion in the electrolyte and charge-transfer reaction at the platinum electrode in dye-sensitized solar cells. Electrochimica Acta, 2001. 46(22): p. 3457-3466.
72. Casaluci, S., M. Gemmi, V. Pellegrini, A. Di Carlo, and F. Bonaccorso, Graphene-based large area dye-sensitized solar cell modules. Nanoscale, 2016. 8(9): p. 5368-5378.
73. Papageorgiou, N., W.F. Maier, and M. Gr±tzel, An Iodine/Triiodide Reduction Electrocatalyst for Aqueous and Organic Media. Journal of the Electrochemical Society, 1997. 144(3): p. 876-884.
74. Xu, S., Y. Wei, M. Kirkham, J. Liu, W. Mai, D. Davidovic, R.L. Snyder, and Z.L. Wang, Patterned Growth of Vertically Aligned ZnO Nanowire Arrays on Inorganic Substrates at Low Temperature without Catalyst. Journal of the American Chemical Society, 2008. 130(45): p. 14958-+.
75. Yun, S., A. Hagfeldt, and T. Ma, Pt-Free Counter Electrode for Dye-Sensitized Solar Cells with High Efficiency. Advanced Materials, 2014. 26(36): p. 6210-6237.
76. Bai, Y., H. Yu, Z. Li, R. Amal, G.Q. Lu, and L. Wang, In Situ Growth of a ZnO Nanowire Network within a TiO_2 Nanoparticle Film for Enhanced Dye-Sensitized Solar Cell Performance. Advanced Materials, 2012. 24(43): p. 5850-5856.
77. Fakharuddin, A., P.S. Archana, Z. Kalidin, M.M. Yusoff, and R. Jose, Standardization of photoelectrode area of dye-sensitized solar cells. RSC Advances, 2013. 3(8): p. 2683-2689.
78. Bisquert, J., D. Cahen, G. Hodes, S. Rühle, and A. Zaban, Physical Chemical Principles of Photovoltaic Conversion with Nanoparticulate, Mesoporous Dye-Sensitized Solar Cells. The Journal of Physical Chemistry B, 2004. 108(24): p. 8106-8118.
79. Nissfolk, J., K. Fredin, A. Hagfeldt, and G. Boschloo, Recombination and Transport Processes in Dye-Sensitized Solar Cells Investigated under Working Conditions. The Journal of Physical Chemistry B, 2006. 110(36): p. 17715-17718.
80. Kopidakis, N., K.D. Benkstein, J. van de Lagemaat, and A.J. Frank, Transport-Limited Recombination of Photocarriers in Dye-Sensitized Nanocrystalline TiO_2 Solar Cells. The Journal of Physical Chemistry B, 2003. 107(41): p. 11307-11315.

81. Halme, J., P. Vahermaa, K. Miettunen, and P. Lund, Device Physics of Dye Solar Cells. Advanced Materials, 2010. 22(35): p. E210-E234.
82. Adachi, M., Y. Murata, J. Takao, J. Jiu, M. Sakamoto, and F. Wang, Highly Efficient Dye-Sensitized Solar Cells with a Titania Thin-Film Electrode Composed of a Network Structure of Single-Crystal-like TiO_2 Nanowires Made by the `Oriented Attachment_ Mechanism. Journal of the American Chemical Society, 2004. 126(45): p. 14943-14949.
83. Law, M., J. Goldberger, and P. Yang, SEMICONDUCTOR NANOWIRES AND NANOTUBES. Annual Review of Materials Research, 2004. 34(1): p. 83-122.
84. Yu, K. and J. Chen, Enhancing Solar Cell Efficiencies through 1-D Nanostructures. Nanoscale Research Letters, 2008. 4(1): p. 1-10.
85. Zhang, Z., S. Ito, B. O'Regan, D. Kuang, S.M. Zakeeruddin, P. Liska, R. Charvet, P. Comte, M.-K. Nazeeruddin, P. P¶chy, R. Humphry-Baker, T. Koyanagi, T. Mizuno, and M. Gr±tzel, The Electronic Role of the TiO_2 Light-Scattering Layer in Dye-Sensitized Solar Cells. Z. Phys. Chem, 2007. 221: p. 319-328.
86. Xu, Y. and M.A.A. Schoonen, The absolute energy positions of conduction and valence bands of selected semiconducting minerals. American Mineralogist, 2000. 85(3-4): p. 543-556.
87. Snaith, H.J. and C. Ducati, SnO_2-Based Dye-Sensitized Hybrid Solar Cells Exhibiting Near Unity Absorbed Photon-to-Electron Conversion Efficiency. Nano Letters, 2010. 10(4): p. 1259-1265.
88. Brennan, T.P., J.R. Bakke, I.K. Ding, B.E. Hardin, W.H. Nguyen, R. Mondal, C.D. Bailie, G.Y. Margulis, E.T. Hoke, A. Sellinger, M.D. McGehee, and S.F. Bent, The importance of dye chemistry and $TiCl_4$ surface treatment in the behavior of Al_2O_3 recombination barrier layers deposited by atomic layer deposition in solid-state dye-sensitized solar cells. Physical Chemistry Chemical Physics, 2012. 14(35): p. 12130-12140.
89. Qian, J., P. Liu, Y. Xiao, Y. Jiang, Y. Cao, X. Ai, and H. Yang, TiO_2-Coated Multilayered SnO_2 Hollow Microspheres for Dye-Sensitized Solar Cells. Advanced Materials, 2009. 21(36): p. 3663-3667.
90. Zhao, C., D. Child, Y. Hu, N. Robertson, D. Gibson, S.C. Wang, and Y.Q. Fu, Low temperature growth of hybrid ZnO/TiO_2 nano-sculptured foxtail-structures for dye-sensitized solar cells. RSC Advances, 2014. 4(105): p. 61153-61159.
91. Nazeeruddin, M.K., S.M. Zakeeruddin, R. Humphry-Baker, M. Jirousek, P. Liska, N. Vlachopoulos, V. Shklover, C.H. Fischer, and M. Gratzel, Acid-base equilibria of (2,2 '-bipyridyl-4,4 '-dicarboxylic acid)ruthenium(II) complexes and the effect of protonation on charge-transfer sensitization of nanocrystalline titania. Inorganic Chemistry, 1999. 38(26): p. 6298-6305.
92. Chou, T.P., Q. Zhang, and G. Cao, Effects of Dye Loading Conditions on the Energy Conversion Efficiency of ZnO and TiO_2 Dye-Sensitized Solar Cells. The Journal of Physical Chemistry C, 2007. 111(50): p. 18804-18811.
93. Nguyen, H. M., R.S. Mane, T. Ganesh, S. H. Han, and N. Kim, Aggregation-Free ZnO Nanocrystals Coupled HMP-2 Dye of Higher Extinction Coefficient for Enhancing Energy Conversion Efficiency. The Journal of Physical Chemistry C, 2009. 113(21): p. 9206-9209.
94. Wong, K.K., A. Ng, X.Y. Chen, Y.H. Ng, Y.H. Leung, K.H. Ho, A.B. DjuriçiP, A.M.C. Ng, W.K. Chan, L. Yu, and D.L. Phillips, Effect of ZnO Nanoparticle Properties on Dye-Sensitized Solar Cell Performance. ACS Applied Materials & Interfaces, 2012. 4(3): p. 1254-1261.
95. Zhang, Q., C.S. Dandeneau, X. Zhou, and G. Cao, ZnO Nanostructures for Dye-Sensitized Solar Cells. Advanced Materials, 2009. 21(41): p. 4087-4108.

96. ª zgæ r, - ., Y.I. Alivov, C. Liu, A. Teke, M.A. Reshchikov, S. Do Ÿ an, V. Avrutin, S.-J. Cho, and H. Morko´, A comprehensive review of ZnO materials and devices. Journal of Applied Physics, 2005. 98(4): p. 041301.
97. Tang, H., K. Prasad, R. Sanjin· s, P.E. Schmid, and F. L ¶ vy, Electrical and optical properties of TiO_2 anatase thin films. Journal of Applied Physics, 1994. 75(4): p. 2042-2047.
98. Oskam, G., Z. Hu, R.L. Penn, N. Pesika, and P.C. Searson, Coarsening of metal oxide nanoparticles. Physical Review E, 2002. 66(1): p. 011403.
99. Keis, K. and A. Roos, Optical characterization of nanostructured ZnO and TiO_2 films. Optical Materials, 2002. 20(1): p. 35-42.
100. Bae, H.S., M.H. Yoon, J.H. Kim, and S. Im, Photodetecting properties of ZnO-based thin-film transistors. Applied Physics Letters, 2003. 83(25): p. 5313-5315.
101. Noack, V., H. Weller, and A. Eychmæ ller, Electron Transport in Particulate ZnO Electrodes: Æ A Simple Approach. The Journal of Physical Chemistry B, 2002. 106(34): p. 8514-8523.
102. Wu, J. J., G. R. Chen, C. C. Lu, W. T. Wu, and J. S. Chen, Performance and electron transport properties of TiO_2 nanocomposite dye-sensitized solar cells. Nanotechnology, 2008. 19(10): p. 105702.
103. Zhong Lin, W., Zinc oxide nanostructures: growth, properties and applications. Journal of Physics: Condensed Matter, 2004. 16(25): p. R829.
104. Schmidt-Mende, L. and J.L. MacManus-Driscoll, ZnO ¯ nanostructures, defects, and devices. Materials Today, 2007. 10(5): p. 40-48.
105. Tornow, J. and K. Schwarzburg, Transient Electrical Response of Dye-Sensitized ZnO Nanorod Solar Cells. The Journal of Physical Chemistry C, 2007. 111(24): p. 8692-8698.
106. DjuriPiP, A.B. and Y.H. Leung, Optical Properties of ZnO Nanostructures. Small, 2006. 2(8-9): p. 944-961.
107. Bandara, J., K. Tennakone, and P.P.B. Jayatilaka, Composite Tin and Zinc oxide nanocrystalline particles for enhanced charge separation in sensitized degradation of dyes. Chemosphere, 2002. 49(4): p. 439-445.
108. Xu, F. and L. Sun, Solution-derived ZnO nanostructures for photoanodes of dye-sensitized solar cells. Energy & Environmental Science, 2011. 4(3): p. 818-841.
109. Saito, M. and S. Fujihara, Large photocurrent generation in dye-sensitized ZnO solar cells. Energy & Environmental Science, 2008. 1(2): p. 280-283.
110. Kisi, E.H. and M.M. Elcombe, u parameters for the wurtzite structure of ZnS and ZnO using powder neutron diffraction. Acta Crystallographica Section C, 1989. 45(12): p. 1867-1870.
111. Jaffe, J.E. and A.C. Hess, Hartree-Fock study of phase changes in ZnO at high pressure. Physical Review B, 1993. 48(11): p. 7903-7909.
112. Xu, L., Y. Guo, Q. Liao, J. Zhang, and D. Xu, Morphological Control of ZnO Nanostructures by Electrodeposition. The Journal of Physical Chemistry B, 2005. 109(28): p. 13519-13522.
113. Morko´, H. and - . ª zgæ r, General Properties of ZnO, in Zinc Oxide. 2009, Wiley-VCH Verlag GmbH & Co. KGaA. p. 1-76.
114. Klingshirn, C., ZnO: Material, Physics and Applications. ChemPhysChem, 2007. 8(6): p. 782-803.
115. Sunagawa, I., Crystals: Growth, Morphology, & Perfection. 2005: Cambridge University Press.
116. Xu, S. and Z. Wang, One-dimensional ZnO nanostructures: Solution growth and functional properties. Nano Research, 2011. 4(11): p. 1013-1098.

117. Meulenkamp, E.A., Synthesis and Growth of ZnO Nanoparticles. The Journal of Physical Chemistry B, 1998. 102(29): p. 5566-5572.
118. Vafaee, M. and M.S. Ghamsari, Preparation and characterization of ZnO nanoparticles by a novel sol¯gel route. Materials Letters, 2007. 61(14¯15): p. 3265-3268.
119. Kar, S., A. Dev, and S. Chaudhuri, Simple Solvothermal Route To Synthesize ZnO Nanosheets, Nanonails, and Well-Aligned Nanorod Arrays. The Journal of Physical Chemistry B, 2006. 110(36): p. 17848-17853.
120. Li, Q., V. Kumar, Y. Li, H. Zhang, T.J. Marks, and R.P.H. Chang, Fabrication of ZnO Nanorods and Nanotubes in Aqueous Solutions. Chemistry of Materials, 2005. 17(5): p. 1001-1006.
121. Huang, M.H., S. Mao, H. Feick, H. Yan, Y. Wu, H. Kind, E. Weber, R. Russo, and P. Yang, Room-Temperature Ultraviolet Nanowire Nanolasers. Science, 2001. 292(5523): p. 1897-1899.
122. Wang, X., Y. Ding, C.J. Summers, and Z.L. Wang, Large-Scale Synthesis of Six-Nanometer-Wide ZnO Nanobelts. The Journal of Physical Chemistry B, 2004. 108(26): p. 8773-8777.
123. Pal, U., J.G. Serrano, P. Santiago, G. Xiong, K.B. Ucer, and R.T. Williams, Synthesis and optical properties of ZnO nanostructures with different morphologies. Optical Materials, 2006. 29(1): p. 65-69.
124. Lobacheva, O., M.W. Murphy, J.Y.P. Ko, and T.-K. Sham, Morphology-dependent luminescence from ZnO nanostructures ´ An X-ray excited optical luminescence study at the Zn K-edge. Canadian Journal of Chemistry, 2009. 87(9): p. 1255-1260.
125. Xi, Y.Y., Y.F. Hsu, A.B. DjurišiP, and W.K. Chan, Electrochemical Synthesis of ZnO Nanoporous Films at Low Temperature and Their Application in Dye-Sensitized Solar Cells. Journal of the Electrochemical Society, 2008. 155(9): p. D595-D598.
126. Nonomura, K., T. Yoshida, D. Schlettwein, and H. Minoura, One-step electrochemical synthesis of ZnO/Ru(dcbpy)2(NCS)2 hybrid thin films and their photoelectrochemical properties. Electrochimica Acta, 2003. 48(20¯22): p. 3071-3078.
127. Wang, M., C. H. Ye, Y. Zhang, G. M. Hua, H. X. Wang, M. G. Kong, and L. D. Zhang, Synthesis of well-aligned ZnO nanorod arrays with high optical property via a low-temperature solution method. Journal of Crystal Growth, 2006. 291(2): p. 334-339.
128. Pan, Z.W., Z.R. Dai, and Z.L. Wang, Nanobelts of semiconducting oxides. Science, 2001. 291(5510): p. 1947-1949.
129. Huang, M.H., Y.Y. Wu, H. Feick, N. Tran, E. Weber, and P.D. Yang, Catalytic growth of zinc oxide nanowires by vapor transport. Advanced Materials, 2001. 13(2): p. 113-116.
130. Yao, B.D., Y.F. Chan, and N. Wang, Formation of ZnO nanostructures by a simple way of thermal evaporation. Applied Physics Letters, 2002. 81(4): p. 757-759.
131. Morko´, H. and - . ª zgær, ZnO Nanostructures, in Zinc Oxide. 2009, Wiley-VCH Verlag GmbH & Co. KGaA. p. 365-386.
132. Gao, P.X. and Z.L. Wang, Nanopropeller arrays of zinc oxide. Applied Physics Letters, 2004. 84(15): p. 2883-2885.
133. Morko´, H. and - . ª zgær, ZnO Growth, in Zinc Oxide. 2009, Wiley-VCH Verlag GmbH & Co. KGaA. p. 77-129.
134. Zhou, H., M. Wissinger, J. Fallert, R. Hauschild, F. Stelzl, C. Klingshirn, and H. Kalt, Ordered, uniform-sized ZnO nanolaser arrays. Applied Physics Letters, 2007. 91(18): p. 181112.
135. Taschuk, M.T., M.M. Hawkeye, and M.J. Brett, Chapter 13 - Glancing Angle Deposition A2 - Martin, Peter M, in Handbook of Deposition Technologies for Films and Coatings (Third Edition). 2010, William Andrew Publishing: Boston. p. 621-678.

136. Barranco, A., A. Borras, A.R. Gonzalez-Elipe, and A. Palmero, Perspectives on oblique angle deposition of thin films: From fundamentals to devices. Progress in Materials Science, 2016. 76: p. 59-153.
137. Chu, J., X. Peng, M. Sajjad, B. Yang, and P.X. Feng, Nanostructures and sensing properties of ZnO prepared using normal and oblique angle deposition techniques. Thin Solid Films, 2012. 520(9): p. 3493-3498.
138. Toledano, D., R.E. Galindo, M. Yuste, J.M. Albella, and O. S®nchez, Compositional and structural properties of nanostructured ZnO thin films grown by oblique angle reactive sputtering deposition: effect on the refractive index. Journal of Physics D: Applied Physics, 2013. 46(4): p. 045306.
139. Izaki, M., M. Watanabe, H. Aritomo, I. Yamaguchi, S. Asahina, T. Shinagawa, M. Chigane, M. Inaba, and A. Tasaka, Zinc Oxide Nano-Cauliflower Array with Room Temperature Ultraviolet Light Emission. Crystal Growth & Design, 2008. 8(4): p. 1418-1421.
140. Ray, A., Electrodeposition of Thin Films for Low-cost Solar Cells. Electroplating of Nanostructures. 2015.
141. Elias, J., R. Tena-Zaera, and C. L¶vy-Cl¶ment, Effect of the Chemical Nature of the Anions on the Electrodeposition of ZnO Nanowire Arrays. The Journal of Physical Chemistry C, 2008. 112(15): p. 5736-5741.
142. Yu, L., G. Zhang, S. Li, Z. Xi, and D. Guo, Fabrication of arrays of zinc oxide nanorods and nanotubes in aqueous solution under an external voltage. Journal of Crystal Growth, 2007. 299(1): p. 184-188.
143. KØnenkamp, R., K. Boedecker, M.C. Lux-Steiner, M. Poschenrieder, F. Zenia, C. Levy-Clement, and S. Wagner, Thin film semiconductor deposition on free-standing ZnO columns. Applied Physics Letters, 2000. 77(16): p. 2575-2577.
144. Cui, J.B. and U.J. Gibson, Electrodeposition and room temperature ferromagnetic anisotropy of Co and Ni-doped ZnO nanowire arrays. Applied Physics Letters, 2005. 87(13): p. 133108.
145. Cui, J.B., Y.C. Soo, T.P. Chen, and U.J. Gibson, Low-Temperature Growth and Characterization of Cl-Doped ZnO Nanowire Arrays. The Journal of Physical Chemistry C, 2008. 112(12): p. 4475-4479.
146. Zheng, M.J., L.D. Zhang, G.H. Li, and W.Z. Shen, Fabrication and optical properties of large-scale uniform zinc oxide nanowire arrays by one-step electrochemical deposition technique. Chemical Physics Letters, 2002. 363(1¯2): p. 123-128.
147. Zhou, H. and S.S. Wong, A Facile and Mild Synthesis of 1-D ZnO, CuO, and -Fe_2O_3 Nanostructures and Nanostructured Arrays. Acs Nano, 2008. 2(5): p. 944-958.
148. Petia, A., R.T. Weitz, G. Peter, S. Vesna, K. Peter, A.v.A. Peter, B. Marko, and B. Joachim, DNA-templated synthesis of ZnO thin layers and nanowires. Nanotechnology, 2009. 20(36): p. 365302.
149. Greene, L.E., M. Law, J. Goldberger, F. Kim, J.C. Johnson, Y.F. Zhang, R.J. Saykally, and P.D. Yang, Low-temperature wafer-scale production of ZnO nanowire arrays. Angewandte Chemie-International Edition, 2003. 42(26): p. 3031-3034.
150. Wei, A., X.W. Sun, J.X. Wang, Y. Lei, X.P. Cai, C.M. Li, Z.L. Dong, and W. Huang, Enzymatic glucose biosensor based on ZnO nanorod array grown by hydrothermal decomposition. Applied Physics Letters, 2006. 89(12).
151. Ting, C. C., chapter2 Structure, Morphology, and Optical Properties of the Compact, Vertically-Aligned ZnO Nanorod Thin Films by the Solution-Growth Technique. Nanorods, 2012(InTech, Chapters published).
152. Laudise, R.A. and A.A. Ballman, HYDROTHERMAL SYNTHESIS OF ZINC OXIDE AND ZINC SULFIDE1. The Journal of Physical Chemistry, 1960. 64(5): p. 688-691.

153. Li, W.J., E.W. Shi, W.Z. Zhong, and Z.W. Yin, Growth mechanism and growth habit of oxide crystals. Journal of Crystal Growth, 1999. 203(1-2): p. 186-196.
154. Demianets, L.N., D.V. Kostomarov, I.P. Kuz'mina, and S.V. Pushko, Mechanism of growth of ZnO single crystals from hydrothermal alkali solutions. Crystallography Reports (Translation of Kristallografiya), 2002. 47(1): p. S86-S98.
155. Govender, K., D.S. Boyle, P.B. Kenway, and P. O'Brien, Understanding the factors that govern the deposition and morphology of thin films of ZnO from aqueous solution. Journal of Materials Chemistry, 2004. 14(16): p. 2575-2591.
156. Baruwati, B., D.K. Kumar, and S.V. Manorama, Hydrothermal synthesis of highly crystalline ZnO nanoparticles: A competitive sensor for LPG and EtOH. Sensors and Actuators B: Chemical, 2006. 119(2): p. 676-682.
157. Lu, C.H. and C.H. Yeh, Influence of hydrothermal conditions on the morphology and particle size of zinc oxide powder. Ceramics International, 2000. 26(4): p. 351-357.
158. Tak, Y. and K. Yong, Controlled Growth of Well-Aligned ZnO Nanorod Array Using a Novel Solution Method. The Journal of Physical Chemistry B, 2005. 109(41): p. 19263-19269.
159. Vayssieres, L., Growth of Arrayed Nanorods and Nanowires of ZnO from Aqueous Solutions. Advanced Materials, 2003. 15(5): p. 464-466.
160. Greene, L.E., M. Law, D.H. Tan, M. Montano, J. Goldberger, G. Somorjai, and P. Yang, General Route to Vertical ZnO Nanowire Arrays Using Textured ZnO Seeds. Nano Letters, 2005. 5(7): p. 1231-1236.
161. Vayssieres, L., K. Keis, S. E. Lindquist, and A. Hagfeldt, Purpose-Built Anisotropic Metal Oxide Material: 3D Highly Oriented Microrod Array of ZnO. The Journal of Physical Chemistry B, 2001. 105(17): p. 3350-3352.
162. Sun, Y., D.J. Riley, and M.N.R. Ashfold, Mechanism of ZnO Nanotube Growth by Hydrothermal Methods on ZnO Film-Coated Si Substrates. The Journal of Physical Chemistry B, 2006. 110(31): p. 15186-15192.
163. Tian, Z.R., J.A. Voigt, J. Liu, B. McKenzie, M.J. McDermott, M.A. Rodriguez, H. Konishi, and H. Xu, Complex and oriented ZnO nanostructures. Nat Mater, 2003. 2(12): p. 821-826.
164. Lee, Y.J., T.L. Sounart, J. Liu, E.D. Spoerke, B.B. McKenzie, J.W.P. Hsu, and J.A. Voigt, Tunable Arrays of ZnO Nanorods and Nanoneedles via Seed Layer and Solution Chemistry. Crystal Growth & Design, 2008. 8(6): p. 2036-2040.
165. Shao, S., P. Jia, S. Liu, and W. Bai, Stable field emission from rose-like zinc oxide nanostructures synthesized through a hydrothermal route. Materials Letters, 2008. 62(8-9): p. 1200-1203.
166. Gao, X.P., Z.F. Zheng, H.Y. Zhu, G.L. Pan, J.L. Bao, F. Wu, and D.Y. Song, Rotor-like ZnO by epitaxial growth under hydrothermal conditions. Chemical Communications, 2004(12): p. 1428-1429.
167. Wang, Z., X. f. Qian, J. Yin, and Z. k. Zhu, Large-Scale Fabrication of Tower-like, Flower-like, and Tube-like ZnO Arrays by a Simple Chemical Solution Route. Langmuir, 2004. 20(8): p. 3441-3448.
168. Li, H., M. Xia, G. Dai, H. Yu, Q. Zhang, A. Pan, T. Wang, Y. Wang, and B. Zou, Growth of Oriented Zinc Oxide Nanowire Array into Novel Hierarchical Structures in Aqueous Solutions. The Journal of Physical Chemistry C, 2008. 112(45): p. 17546-17553.
169. Zhang, H., D. Yang, D. Li, X. Ma, S. Li, and D. Que, Controllable Growth of ZnO Microcrystals by a Capping-Molecule-Assisted Hydrothermal Process. Crystal Growth & Design, 2005. 5(2): p. 547-550.

170. Zhang, H., D. Yang, S. Li, X. Ma, Y. Ji, J. Xu, and D. Que, Controllable growth of ZnO nanostructures by citric acid assisted hydrothermal process. Materials Letters, 2005. 59(13): p. 1696-1700.
171. Zhang, D. F., L. D. Sun, J. Zhang, Z. G. Yan, and C. H. Yan, Hierarchical Construction of ZnO Architectures Promoted by Heterogeneous Nucleation. Crystal Growth & Design, 2008. 8(10): p. 3609-3615.
172. Xu, F., Z.Y. Yuan, G.H. Du, T.Z. Ren, C. Volcke, P. Thiry, and B.L. Su, A low-temperature aqueous solution route to large-scale growth of ZnO nanowire arrays. Journal of Non-Crystalline Solids, 2006. 352(23–25): p. 2569-2574.
173. Lu, C., L. Qi, J. Yang, L. Tang, D. Zhang, and J. Ma, Hydrothermal growth of large-scale micropatterned arrays of ultralong ZnO nanowires and nanobelts on zinc substrate. Chemical Communications, 2006(33): p. 3551-3553.
174. Li, X., F. Zhao, J. Fu, X. Yang, J. Wang, C. Liang, and M. Wu, Double-Sided Comb-Like ZnO Nanostructures and Their Derivative Nanofern Arrays Grown by a Facile Metal Hydrothermal Oxidation Route. Crystal Growth & Design, 2009. 9(1): p. 409-413.
175. Tang, L., X. B. Bao, H. Zhou, and A. H. Yuan, Synthesis and characterization of ZnO nanorods by a simple single-source hydrothermal method. Physica E: Low-dimensional Systems and Nanostructures, 2008. 40(4): p. 924-928.
176. Li, F., L. Hu, Z. Li, and X. Huang, Influence of temperature on the morphology and luminescence of ZnO micro and nanostructures prepared by CTAB-assisted hydrothermal method. Journal of Alloys and Compounds, 2008. 465(1–2): p. L14-L19.
177. Zhou, X., D. Zhang, Y. Zhu, Y. Shen, X. Guo, W. Ding, and Y. Chen, Mechanistic Investigations of PEG-Directed Assembly of One-Dimensional ZnO Nanostructures. The Journal of Physical Chemistry B, 2006. 110(51): p. 25734-25739.
178. Kawska, A., P. Duchstein, O. Hochrein, and D. Zahn, Atomistic Mechanisms of ZnO Aggregation from Ethanolic Solution: Ion Association, Proton Transfer, and Self-Organization. Nano Letters, 2008. 8(8): p. 2336-2340.
179. Sunagawa, I., Growth, Morphology, & Perfection. 2005: Cambridge University Press; 1 edition (August 13, 2007).
180. Burton, W.K., N. Cabrera, and F.C. Frank, The Growth of Crystals and the Equilibrium Structure of their Surfaces. Philosophical Transactions of the Royal Society of London A: Mathematical, Physical and Engineering Sciences, 1951. 243(866): p. 299-358.
181. Richard, P.S., Nucleation: theory and applications to protein solutions and colloidal suspensions. Journal of Physics: Condensed Matter, 2007. 19(3): p. 033101.
182. Cooper, S., Crystallisation Kinetics. (Durham University). 17 Aug 2015, Durham University: http://community.dur.ac.uk/sharon.cooper/lectures/cryskinetics/handoutsalla.html
183. Liu, X.Y., K. Maiwa, and K. Tsukamoto, Heterogeneous two-dimensional nucleation and growth kinetics. The Journal of Chemical Physics, 1997. 106(5): p. 1870-1879.
184. Liu, X.Y., Interfacial Effect of Molecules on Nucleation Kineticsè. The Journal of Physical Chemistry B, 2001. 105(47): p. 11550-11558.
185. Gao, Y. and K. Koumoto, Bioinspired Ceramic Thin Film Processing: Present Status and Future Perspectives. Crystal Growth & Design, 2005. 5(5): p. 1983-2017.
186. Crystallization Processes. 1997: John Wiley and Sons Ltd.
187. Yamabi, S. and H. Imai, Growth conditions for wurtzite zinc oxide films in aqueous solutions. Journal of Materials Chemistry, 2002. 12(12): p. 3773-3778.
188. Niesen, T.P. and M.R. De Guire, Review: deposition of ceramic thin films at low temperatures from aqueous solutions. Solid State Ionics, 2002. 151(1–4): p. 61-68.

189. Rani, S., P. Suri, P.K. Shishodia, and R.M. Mehra, Synthesis of nanocrystalline ZnO powder via sol¯gel route for dye-sensitized solar cells. Solar Energy Materials and Solar Cells, 2008. 92(12): p. 1639-1645.
190. Redmond, G., D. Fitzmaurice, and M. Graetzel, Visible Light Sensitization by cis-Bis(thiocyanato)bis(2,2'-bipyridyl-4,4'-dicarboxylato)ruthenium(II) of a Transparent Nanocrystalline ZnO Film Prepared by Sol-Gel Techniques. Chemistry of Materials, 1994. 6(5): p. 686-691.
191. Zeng, L., S. Dai, W. Xu, and K. Wang, Dye-Sensitized Solar Cells Based on ZnO Films. Plasma Science and Technology, 2006. 8(2): p. 172.
192. Li, C., L. Yang, J. Xiao, Y. C. Wu, M. Sondergaard, Y. Luo, D. Li, Q. Meng, and B.B. Iversen, ZnO nanoparticle based highly efficient CdS/CdSe quantum dot-sensitized solar cells. Physical Chemistry Chemical Physics, 2013. 15(22): p. 8710-8715.
193. Akhtar, M.S., M.A. Khan, M.S. Jeon, and O.B. Yang, Controlled synthesis of various ZnO nanostructured materials by capping agents-assisted hydrothermal method for dye-sensitized solar cells. Electrochimica Acta, 2008. 53(27): p. 7869-7874.
194. Hosono, E., S. Fujihara, I. Honma, and H. Zhou, The Fabrication of an Upright-Standing Zinc Oxide Nanosheet for Use in Dye-Sensitized Solar Cells. Advanced Materials, 2005. 17(17): p. 2091-2094.
195. Hosono, E., S. Fujihara, T. Kimura, and H. Imai, Growth of layered basic zinc acetate in methanolic solutions and its pyrolytic transformation into porous zinc oxide films. Journal of Colloid and Interface Science, 2004. 272(2): p. 391-398.
196. Hosono, E., Y. Mitsui, and H. Zhou, Metal-free organic dye sensitized solar cell based on perpendicular zinc oxide nanosheet thick films with high conversion efficiency. Dalton Transactions, 2008(40): p. 5439-5441.
197. Kosmulski, M., The significance of the difference in the point of zero charge between rutile and anatase. Advances in Colloid and Interface Science, 2002. 99(3): p. 255-264.
198. Blok, L. and P.L.D. Bruyn, The ionic double layer at the ZnOsolution interface: I. The experimental point of zero charge. Journal of Colloid and Interface Science, 1970. 32(3): p. 518-526.
199. Yin, P. F., T. Ling, Y. R. Lu, Z. W. Xu, S. Z. Qiao, and X. W. Du, CdS Nanoflake Arrays for Highly Efficient Light Trapping. Advanced Materials, 2015. 27(4): p. 740-745.
200. Zhao, C., J. Zhang, Y. Hu, N. Robertson, P.A. Hu, D. Child, D. Gibson, and Y.Q. Fu, In-situ microfluidic controlled, low temperature hydrothermal growth of nanoflakes for dye-sensitized solar cells. scientific reports, 2015. 5: p. 17750.
201. Elkhidir Suliman, A., Y. Tang, and L. Xu, Preparation of ZnO nanoparticles and nanosheets and their application to dye-sensitized solar cells. Solar Energy Materials and Solar Cells, 2007. 91(18): p. 1658-1662.
202. Chen, W., H. Zhang, I.M. Hsing, and S. Yang, A new photoanode architecture of dye sensitized solar cell based on ZnO nanotetrapods with no need for calcination. Electrochemistry Communications, 2009. 11(5): p. 1057-1060.
203. Benkstein, K.D., N. Kopidakis, J. van de Lagemaat, and A.J. Frank, Influence of the Percolation Network Geometry on Electron Transport in Dye-Sensitized Titanium Dioxide Solar Cells. The Journal of Physical Chemistry B, 2003. 107(31): p. 7759-7767.
204. Morko´, H. and - . ª zgær, Processing, Devices, and Heterostructures, in Zinc Oxide. 2009, Wiley-VCH Verlag GmbH & Co. KGaA. p. 387-467.
205. Beermann, N., L. Vayssieres, S.E. Lindquist, and A. Hagfeldt, Photoelectrochemical Studies of Oriented Nanorod Thin Films of Hematite. Journal of the Electrochemical Society, 2000. 147(7): p. 2456-2461.

206. Baxter, J.B. and C.A. Schmuttenmaer, Conductivity of ZnO Nanowires, Nanoparticles, and Thin Films Using Time-Resolved Terahertz Spectroscopyè. The Journal of Physical Chemistry B, 2006. 110(50): p. 25229-25239.
207. Law, M., L.E. Greene, A. Radenovic, T. Kuykendall, J. Liphardt, and P. Yang, ZnOБAl$_2$O$_3$ and ZnOБTiO$_2$ CoreБShell Nanowire Dye-Sensitized Solar Cells. The Journal of Physical Chemistry B, 2006. 110(45): p. 22652-22663.
208. Guo, M., P. Diao, and S. Cai, Hydrothermal growth of perpendicularly oriented ZnO nanorod array film and its photoelectrochemical properties. Applied Surface Science, 2005. 249(1¯4): p. 71-75.
209. Baxter, J.B., A.M. Walker, K.v. Ommering, and E.S. Aydil, Synthesis and characterization of ZnO nanowires and their integration into dye-sensitized solar cells. Nanotechnology, 2006. 17(11): p. S304.
210. Cheng, A. J., Y. Tzeng, Y. Zhou, M. Park, T. h. Wu, C. Shannon, D. Wang, and W. Lee, Thermal chemical vapor deposition growth of zinc oxide nanostructures for dye-sensitized solar cell fabrication. Applied Physics Letters, 2008. 92(9): p. 092113.
211. Vayssieres, L., K. Keis, A. Hagfeldt, and S. E. Lindquist, Three-Dimensional Array of Highly Oriented Crystalline ZnO Microtubes. Chemistry of Materials, 2001. 13(12): p. 4395-4398.
212. Ku, C. H. and J. J. Wu, Electron transport properties in ZnO nanowire array/nanoparticle composite dye-sensitized solar cells. Applied Physics Letters, 2007. 91(9): p. 093117.
213. Palomares, E., J.N. Clifford, S.A. Haque, T. Lutz, and J.R. Durrant, Control of Charge Recombination Dynamics in Dye Sensitized Solar Cells by the Use of Conformally Deposited Metal Oxide Blocking Layers. Journal of the American Chemical Society, 2003. 125(2): p. 475-482.
214. Nguyen, T.V., H.C. Lee, M. Alam Khan, and O.B. Yang, Electrodeposition of TiO$_2$/SiO$_2$ nanocomposite for dye-sensitized solar cell. Solar Energy, 2007. 81(4): p. 529-534.
215. Menzies, D., R. Cervini, Y.-B. Cheng, G. Simon, and L. Spiccia, Nanostructured ZrO$_2$-Coated TiO$_2$ Electrodes for Dye-Sensitised Solar Cells. Journal of Sol-Gel Science and Technology, 2004. 32(1-3): p. 363-366.
216. Jung, H.S., J. K. Lee, M. Nastasi, S. W. Lee, J. Y. Kim, J. S. Park, K.S. Hong, and H. Shin, Preparation of Nanoporous MgO-Coated TiO$_2$ Nanoparticles and Their Application to the Electrode of Dye-Sensitized Solar Cells. Langmuir, 2005. 21(23): p. 10332-10335.
217. Balaya, P., J. Jamnik, J. Fleig, and J. Maier, Mesoscopic Hole Conduction in Nanocrystalline SrTiO$_3$: A Detailed Analysis by Impedance Spectroscopy. Journal of the Electrochemical Society, 2007. 154(6): p. P69-P76.
218. Tributsch, H., Dye sensitization solar cells: A critical assessment of the learning curve. Coordination Chemistry Reviews, 2004. 248(13-14): p. 1511-1530.
219. Kroeze, J.E., N. Hirata, S. Koops, M.K. Nazeeruddin, L. Schmidt-Mende, M. Gr±tzel, and J.R. Durrant, Alkyl Chain Barriers for Kinetic Optimization in Dye-Sensitized Solar Cells. Journal of the American Chemical Society, 2006. 128(50): p. 16376-16383.
220. Menzies, D., Q. Dai, Y.B. Cheng, G.P. Simon, and L. Spiccia, Improvement of the Zirconia shell in nanostructured titania core¯shell working electrodes for dye-sensitized solar cells. Materials Letters, 2005. 59(14¯15): p. 1893-1896.
221. Shin, Y. J., J. H. Lee, J. H. Park, and N. G. Park, Enhanced Photovoltaic Properties of SiO$_2$-treated ZnO Nanocrystalline Electrode for Dye-sensitized Solar Cell. Chemistry Letters, 2007. 36(12): p. 1506-1507.

222. Kang, S.H., J. Y. Kim, Y. Kim, H.S. Kim, and Y. E. Sung, Surface Modification of Stretched TiO_2 Nanotubes for Solid-State Dye-Sensitized Solar Cells. The Journal of Physical Chemistry C, 2007. 111(26): p. 9614-9623.
223. Shin, Y.J., K.S. Kim, N.G. Park, K.S. Ryu, and S.H. Chang, Enhancement of photovoltaic properties of Ti-modified nanocrystalline ZnO electrode for dye-sensitized solar cell. Bulletin of the Korean Chemical Society, 2005. 26(12): p. 1929-1930.
224. Law, M., L.E. Greene, J.C. Johnson, R. Saykally, and P.D. Yang, Nanowire dye-sensitized solar cells. Nature Materials, 2005. 4(6): p. 455-459.
225. Hagfeldt, A., Brief Overview of Dye-Sensitized Solar Cells. Ambio, 2012. 41: p. 151-155.

Chapter 3 Methodology

In this chapter, details about all the experimental work and characterisation processes developed/carried out in this thesis are provided. Briefly, it can be divided into the following parts (Figure 3-1):

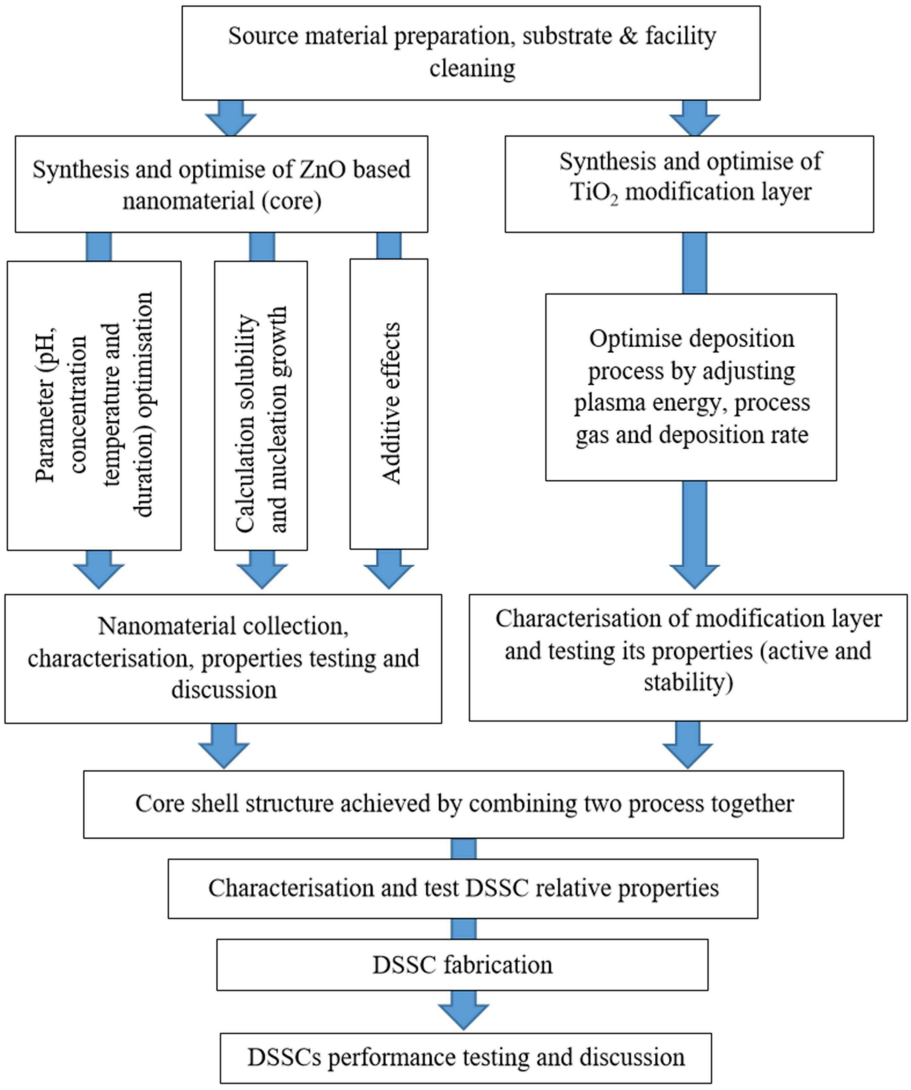

Figure 3-1 Diagram of the experimental flow

(1) Details of materials and reagents

(2) Synthesis procedures

(3) Characterisation of materials and nanostructures

(4) Dye sensitised solar cell fabrication and its characterisation

Some of the specific procedures for the measurement will be described in the corresponding Chapters.

3.1 Materials and Reagents

In this thesis, unless otherwise stated, all chemicals and solvents used were at least reagent grade purchased from Sigma-Aldrich and used without further purification. Details of the source materials, chemicals and solvents are listed in Table 3-1.

Table 3-1 Reagents, solvents and materials used in the work.

Reagents and solvents	Standard	Supplier
zinc nitrate hexahydrate	99.0%	Sigma
ammonium hydroxide	28 wt% in water,	Sigma
hexamethylenetetramine	99.0%	Sigma
ammonium chloride	99.5%	Sigma
aluminum nitrate nonahydrate	98.5%	Sigma
NaOH	98%	Sigma
LiI	99.9%	Sigma
iodine	99.99%	Sigma
4-tert-butylpyridine	96%	Sigma
tetrabutylammonium iodide	99.0%	Sigma
acetonitrile	99.9%	Sigma
acetone	99.8%	Sigma
ethanol	99.5%	Sigma
I_2	99.8%	Sigma
N719 dye	95.0%	Sigma
polyethylenimine (PEI)	Average M_n ~600	Sigma
Material	**Standard**	**Supplier**
Zn target	99.9 at%	
Pt Target	99.0 at%	
Ti_3O_5	99.9 at%	Materion Inc.
hot melt surlyn film	25~50 ı m	Solaronix

3.2 Synthesis procedures

In this section, different synthesis instruments and processes will be introduced. Nanostructures are synthesised by the low temperature aqueous solution growth approach and modification layers achieved by plasma enhanced electron beam (e-beam) evaporation will be described in the Sections 3.2.1 and 3.2.2, respectively.

3.2.1 Growth of ZnO nanostructures

3.2.1.1 Pre-treatment of substrates

(1) Substrate cleaning

For the preparation of the nanostructured materials grown on the substrate, the requirements of the surface quality are critical. This is mainly because that any surface defects (i.e. metal tarnished, organic tarnished, tarnished dust, etc.) on the substrate will cause negative effects on the whole growth process. Therefore, it will affect the quality of the materials and the performance of the devices. Accordingly, the cleaning of the substrate becomes one of the critical steps of nanomaterial fabrication. Substrates are all cleaned using a typical solvent clean (acetone bath and ultrasonic clean for 10 minutes, then ethanol 5-10 minutes ultrasonic clean) followed by a deionized water rinse and N_2 blow dry process.

(2) Seed layer preparation

In the aqueous solution ZnO nanostructure synthesis, the ZnO seed layer is important to control the growth of ZnO nanostructure. It defines heterogeneous nucleation as well as nanostructure growth on pre-seed surface. Therefore, most common substrates can be used for ZnO growth such as, Si (100) wafer, flexible polymer, silica, TCO coated substrates, as long as the seed layer can be applied on the material properly (i.e., good

adhesion with substrates) and the material is compatible with the reaction temperature and chemical solution.

ZnO seed layer was applied on the surface of the substrate using a typical DC magnetron sputtering process. A metal Zn target was used as the source material and a working mixture gas of Ar and O_2 was used with a flow rate ratio of 50 sccm / 50 sccm. The deposition was started once the base chamber vacuum reached to 5.0B10^{Б6} mbar. ZnO seed layers with a thickness of 50 nm were deposited using power of 400 W. For the substrates used as the photoanode for assembling DSSCs, an ITO layer of 250 nm thick (18 W/□) were deposited onto the cleaned glass substrates surface using a magnetron sputter system (MicroDyn-®) before the deposition of ZnO seed layer.[1] In this process, a high purity In-Sn alloy (>99.99%, 90:10) target was used as the source material with sputtering power set at 1.64 kW. The mixture of Ar and O_2 with a flow rate ratio of 80 sccm / 36 sccm had been used as working gas. The substrates holder was rotated for improve uniformity at a rotation rate of 1 cycle/second. The deposition was started once the base chamber vacuum reached to 1.0B10^{Б5} mbar. The film thickness was set at 250 nm which had been monitored by a quartz crystal thickness sensor and controlled by the computer.[1]

3.2.1.2 Low temperature aqueous solution method for nanostructured materials

For a typical growth process (as shown in Figure 2-17), the transparent aqueous reaction solution was prepared by dissolving various concentrations of zinc nitrate hexahydrate ($Zn(NO_3)_2$ ð6H_2O) with different reactants for achieving various morphologies as well as properties. Reactants such as ammonium water (NH_4OH), ammonium chloride (NH_4Cl), Hexamethylenetetramine ($(CH_2)_6N_4$), hydrochloric acid (HCl) and sodium

hydroxide (NaOH) were used for starting the reaction with different function. NH_4OH and NH_4Cl were used for providing enough NH_4^+ to react with Zn^{2+} and achieving a complex to serve as a Zn buffer in the reaction. $(CH_2)_6N_4$ and NaOH were employed for supporting OH^- and adjusting pH value (HCl and/or NaOH) of the reaction solution (measured by Orion Star A211 pH meter, Thermo Scientific) to a desired value. Additives such as PEI and metal cation (in this thesis Al^{3+} was chosen) were used for nanostructure morphology and property control, and the details will be further discussed in the corresponding chapter 4 and chapter 7.

Various chemicals were used in order to optimise growth parameters, simultaneously understanding the relationship between growth parameters and supersaturation, and the driving mechanisms of nucleation growth. Although solution processed ZnO nanostructures have been studied for years, the growth mechanism of ZnO nanostructures is still not fully understood. It is still required further investigation to develop a low-cost, controllable and easy processing solution synthesis method. Therefore, in this work, a series of experiments were carried out (as shown in Table 3-2 and Table 3-3) to find the optimised parameters for the DSSC applications.

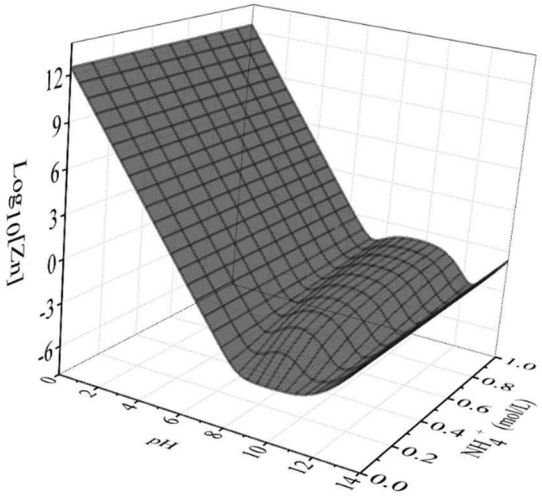

Reaction	Log K
$Zn^{2+} + 2OH^- \leftrightarrow ZnO\,(s) + H_2O$	15.5
$NH_4^+ + OH^- \leftrightarrow NH_3 + H_2O$	4.4
$Zn^{2+} + OH^- \leftrightarrow [Zn(OH)]^+$	5.0
$Zn^{2+} + 2OH^- \leftrightarrow Zn(OH)_2(aq)$	11.1
$Zn^{2+} + 3OH^- \leftrightarrow [Zn(OH)_3]^-$	13.6
$Zn^{2+} + 4OH^- \leftrightarrow [Zn(OH)_4]^{2-}$	14.8
$Zn^{2+} + NH_3 \leftrightarrow [Zn(NH_3)]^{2+}$	2.2
$Zn^{2+} + 2NH_3 \leftrightarrow [Zn(NH_3)]_2^{2+}$	4.5
$Zn^{2+} + 3NH_3 \leftrightarrow [Zn(NH_3)]_3^{2+}$	6.86
$Zn^{2+} + 4NH_3 \leftrightarrow [Zn(NH_3)]_4^{2+}$	8.86

Figure 3-2 Solubility plot as a function of pH/[NH_4^+]with possible reactions in the inset table.[2]

Table 3-2 Experiment factors for the solution synthesis of ZnO NRs investigation.

Growth in hexamethylenetetramine aqueous solution (section 4.2.1)						
Factors	$Zn(NO_3)_2$ and $(CH_2)_6N_4$ concentration (molar ratio 1:1)			Duration hours (hrs)		Temperature
Temperature effects (section 4.2.1.1)	0.05 M			3 hrs and 12 hrs for 35 °C 3 hrs for the rest (45 °C-95 °C)		35 °C to 95 °C
Influence of reactants and durations (section 4.2.1.2)	0.030 to 0.110 M			3 hrs		90 · C
	0.025 M 0.050 M			0-10 hrs		90 °C
Growth in an alkaline solution (section 4.2.2)						
Factors	$Zn(NO_3)_2$ concentration	T	Duration hours (hrs)	PEI	$[NH_4^+]$	pH
Influence of pH and reactant concentration (section 4.2.2.1)	0.020 M	80 °C	3 hrs	0	0.025 M	10 to 12
	0.005 to 0.2 M	80 °C	3 hrs	0	0.025 M	10.55
Influence of ammonia (section 4.2.2.2)	0.020 M	80 °C	3 hrs	0	0 to 0.55 M	10.51
Influence of additive PEI (section 4.2.2.3)	0.025 M	80 °C	0- 20 hrs	5-50 mM 0 -5 mM	0.025 M	10.51

In order to predict the solubility of ZnO, all the reactions under certain factor (i.e. reactant concentration) was assumed as equilibrium between ZnO and aqueous reaction solution. A simplified solubility plot calculation was used for analysing experimental results in the alkaline growth solution (calculation Matlab code show in appendix).[2] The possible chemical reactions in the growth process with relative equilibrium constant are listed in Figure 3-2.[2] The z-axis ($[NH_4^+]$) shown in Figure 3-2 represent the applied reactant concentration in the growth solution after pH adjustment. The y-axis indicated the maximum concentration of Zn^{2+} (all the zinc containing species) without formation of ZnO. The 3D-image in Figure 3-3 indicates there is a boundary

condition in the reaction solution, if the reaction elements (Zn^{2+}, NH_4^+ and OH^-) condition (i.e. concentration) is below the boundary plane, there will be no ZnO precipitation occurring. On the other hand, if the conditions reach above the boundary plane, there will be a supersaturation condition, where the ZnO solid may start participation.[2-5]

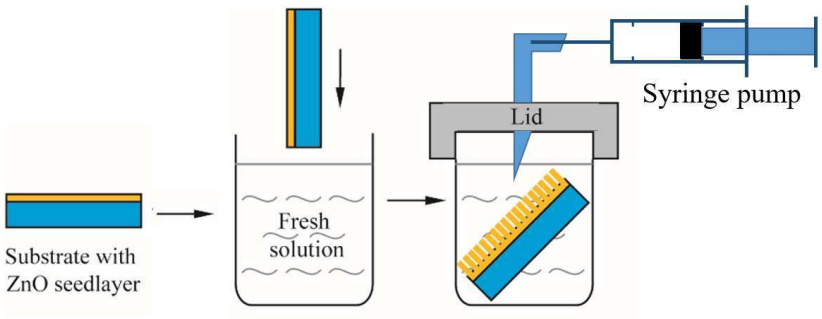

Figure 3-3 Schematic process of the hydrothermal growth with syringe pump.

Al doped ZnO (AZO) nanoflake synthesis (Chapter 7) was prepared using the following experimental setting (Table 3-3). The basic solution was 100 ml transparent aqueous solution containing 25 mM zinc nitrate hexahydrate and 400 mM ammonium chloride with a pH value of 10.8 (adjusted by NaOH).[6] The ITO coated PET substrate was placed upside down in the solution in a sealed reaction vessel, connected with a syringe pump (as shown in Figure 3-3). All the synthesis was performed at 80 °C by placing the reaction vessel into a pre-heated water bath. During the film growth, aluminium nitrate nonahydrate ($Al(NO_3)_3$ ð$9H_2O$) with final total concentrations of 1 mM to 4 mM was injected into the solution through the syringe pump, and control of the nanostructures was achieved by varying the injection speed and concentration (Figure 7-1).[6] The concentrations of the solutions used for injection at a speed of 2 mL/hour were set at 1, 2, 3 and 4 mM, which were denoted as samples AZ1, AZ2, AZ3 and AZ4, respectively. The injection speeds were varied between 2 mL/hr to 4 mL/hr with a total injected final

content of 2 mM, which were denoted as samples AZ1S-2 mL/hour, AZ2S-3 mL/hour and AZ3S- 4 mL/hour.[6] The duration of the reaction was fixed at four hours. One control group was set to investigate the in-situ MCU effects; one sample (AZ1-C) was prepared using the hydrothermal solution method with the same chemical solution and reaction conditions as AZ1 but without in-situ microfluidic unit.[6] Additional, to clarify the substrate effect on the nanostructures, sample AZ1 had also been synthesised on one piece of ITO coated glass substrate (AZ1-G). For thickness effect test, the duration of the growth was varied from 1 to 12 hrs (1, 2, 4, 8, 12) with 4 mM of the Al source solution used for injection at a speed of 2 mL/hr, which were named as AZ4-1hr, AZ4-2hr, AZ4, AZ4-8hr, AZ4-12hr. After synthesis, all the samples were rinsed with DI water and dried with N_2 gas before testing and/or other process.[6] For DSSC photoanode testing, a layer of anatase TiO_2 (~ 50 nm) was deposited on the as-prepared samples using a low temperature deposition process optimised in Chapter 6.

Table 3-3 Experimental setting for the solution synthesis of AZO nanostructures.

Fixed parameters for all the following experiments	$Zn(NO_3)_2$	Temperature	pH	$[NH_4^+]$
	0.025 M	80 °C	10.8	0.4 M
Factors	Sample	$Al(NO_3)_3$	Duration	Injection rate
Influence of injection concentration	AZ1	1 mM	4 hrs	2 ml/hour
	AZ2	2 mM	4 hrs	2 ml/hour
	AZ3	3 mM	4 hrs	2 ml/hour
	AZ4	4 mM	4 hrs	2 ml/hour
Influence of injection rate	AZ1S	2 mM	4 hrs	2 ml/hour
	AZ2S	2 mM	4 hrs	3 ml/hour
	AZ3S	2 mM	4 hrs	4 ml/hour
Influence of growth duration	AZ4-1hr	4 mM	1 hrs	2 ml/hour
	AZ4-2hr	4 mM	2 hrs	2 ml/hour
	AZ4-8hr	4 mM	8 hrs	2 ml/hour
	AZ4-12hr	4 mM	12 hrs	2 ml/hour
Control group				
	Sample	$Al(NO_3)_3$	Duration	injection rate
without MCU	AZ1-C	1 mM	4 hrs	N/A
ITO coated glass slice used for substrate	AZ1-G	1 mM	4 hrs	2 ml/hour

3.2.2 Low temperature synthesis and crystallisation of TiO_2 modification layer

In this thesis, a typical electron beam (E-beam) thermal evaporation with a home-made plasma source was employed for achieving a crystallised TiO_2 modification layer on ZnO nanostructures. The main apparatus was an E-beam evaporation system (SATIS MS LAB 380 series), which had two E-beam sources and a sweep generator as demonstrated in Figure 3-4 (a) to (c). The electron beam was produced from a heated filament under a high vacuum and focused onto the evaporant (target material) by magnetic fields (see Figure 3-4 (d)). The source material was placed at the bottom of the system and the substances were placed on top of the chamber. Once the base pressure reached at $5B10^{\beta 5}$ mbar, the source material was heated and melted, and then the working gas was introduced from the bottom part of the chamber. The carrier gas was coming from the bottom because it is good for carrying source material and getting more chance to react with the working gas. Because of the relatively low temperature of the substrate, the evaporated materials were condensed then grown on the target surface. In a typical deposition process, oxygen and nitrogen gases were used for achieving oxide or nitride films under an operating pressure at around 10^{-4} mbar. By using the software with the SATIS MS LAB 380 evaporation system, the electron beam energy as well as the magnetic field can be adjusted. This could achieve a stable and controllable evaporation rate of the source material. After several calibration runs and updating the parameters into the software, film deposition rate can be easily controlled. The film thickness was monitored using a quartz crystal micro-balance (QCM) sensor beside the substrate holder.[7]

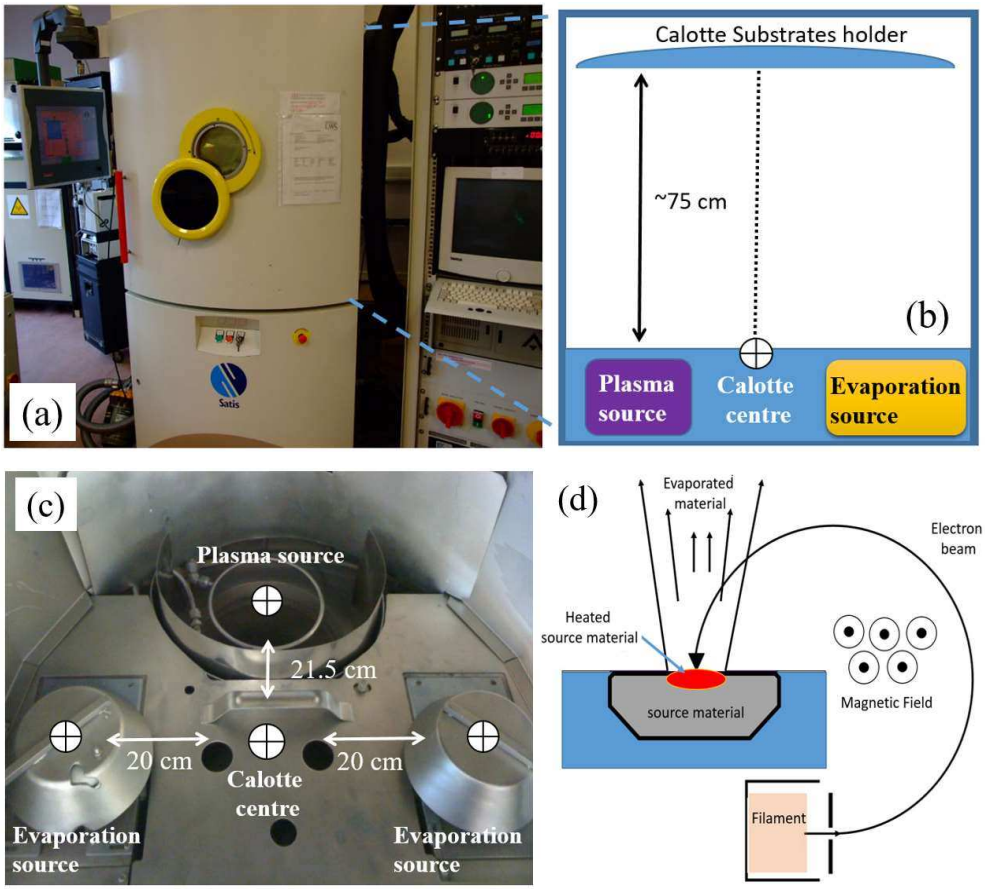

Figure 3-4 (a) SATIS MS LAB 380 E-beam evaporation system. (b) Schematic drawing from side view of the deposition chamber. (c) Plan view of the deposition chamber floor. (d) E-beam evaporation working principle.

Various deposition parameters were investigated in order to achieve an optimised deposition process for TiO_2 shell coating. In order to avoid the influences of other impurities, high purity Ti_3O_5 granules were chosen as the evaporation source. Ti_3O_5 has a lower evaporation temperature which could effectively avoid outgassing and particle ejection, compared with the pure TiO_2 evaporant. Most importantly, the evaporated vapour of the Ti_3O_5 powder produced only one titanium species (Ti-O), leading to a uniform film composition.[7, 8] Effects of the working gas (O_2) and plasma enhancement on the morphology, crystallinity as well as their functional properties of resultant TiO_2 films were investigated. The working gas was a mixture of Ar and O_2. For understanding O_2 effects to the film, the Ar flow rate was set to be 10 sccm, but the O_2

flow rate was set at 10, 15, 20, 25 and 30 sccm. The base pressure was 5B10^{57} Pa and deposition was done at room temperature (RT) without heating. Plasma analysis was carried out using a Faraday Cup (CCC Technology, USA) to obtain the plasma current density and ion/adatom arriving rate which can be adjusted by adjusting plasma power source (i.e. working voltage and current).[7] Deposition parameters and plasma analysis results are listed in Table 3-4.[7] During deposition, plasma enhancement was provided by a thermionic plasma source, which enabled ionizing the working argon atoms and the processing oxygen gas molecules. The plasma source position and relative distances between other components (inside E-Beam deposition chamber) are summarized in Figure 3-4 (b) & (c). The ion energy and arrival ratios of the ion to adatom were varied during film deposition and they were chosen in this study as the optimum rates for densification, but without causing severe re-sputtering effects based on the parameters reported from reference.[7] The deposition rate was ~0.20 nm/s and the substrate holder was rotated at 20 rpm.[7]

Table 3-4 Deposition and plasma analysis parameters for PIAD TiO_2 films.[7]

Samples	O_2 flow rate (sccm)	Ar flow rate (sccm)	Voltage/current (V/A)	Plasma current density (mA/cm^2)	Ion/adatom arrival rate
T10	10	10	N/A	N/A	N/A
T15	15	10	N/A	N/A	N/A
T20	20	10	N/A	N/A	N/A
T25	25	10	N/A	N/A	N/A
T30	30	10	N/A	N/A	N/A
T10P13(P13)	10	10	212/13	0.63	6.2
T10P17(P17)	10	10	212/17	0.78	7.6
T10P21(P21)	10	10	212/21	0.93	9.1

3.3 Material and nanostructure characterisation

Crystalline structures of the deposited films were analysed using a Siemens D5000 x-ray diffraction (XRD) spectrometer, with a Bragg¯Brentano configuration and a Cu K line as an excitation source (40 kV/30 mA). The scan speed was set as 2 degree/min with 0.05 degree/step. Qualitative analysis was performed by comparing the XRD spectra with the reference JCPDS PDF card.[7]

Scanning electron microscope (SEM), model S-4100 Hitachi SEM, with an Oxford Instruments INCA Energy Dispersive X-ray Spectrometer (EDS) was used for morphology study as well as element confirmation. Transmission electron microscope (TEM, JEOL, 3010 and JEM-2100) were used for core-shell structures and single crystal features of the nanostructure confirmation. The thickness of the nanostructured films had been measured by stylus profilometry (Dektak XT, BRUKER) and cross-section SEM images.

Atomic force microscope (AFM, NanoScope III, Digital Instruments) was utilised to study the surface of the resultant films. For the AFM, typical scans were taken over an area of 5 ı m B 5 ı m at a constant scan speed of 1 Hz. The film roughness was obtained based on analysis of the AFM images. Hardness (H) and Young˘s modulus (E) of the material as a function of the displacement of the nano-indenter were obtained from the loading¯unloading of the indenter using a TriboScope nanomechanical test instrument (Hysitron Inc., USA) in conjunction with the Atomic Force Microscope. A Berkovich diamond indenter with a tip radius of 135 nm was used.[7]

Optical properties were investigated using a spectrophotometer. Optical transmittance (T) and reflectance (R) measurements were carried out using a NKD-8000 Aquila

spectrophotometer with a scan speed at 5 nm/step and scan range from 350 nm to 1050 nm. Photoluminescence (PL) spectra was measured using a LS 55 Fluorescence Spectrometer (PerkinElmer) at room temperature with 325 nm excitation wavelength. The scan range was set from 350 nm to 600 nm, and scan speed was 120 nm/min.

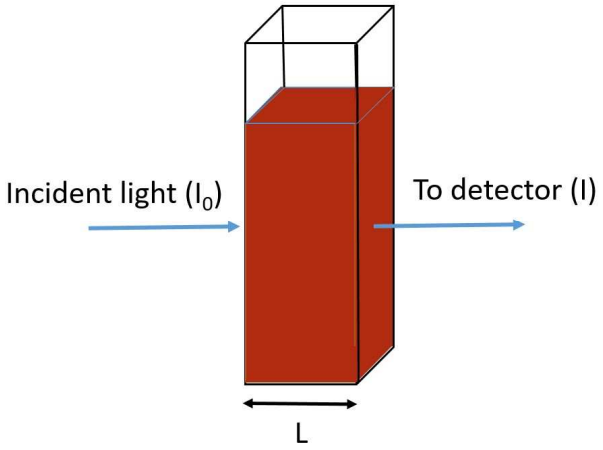

Beer-Lambert law

$$A = log_{10}(I_0/I) = \varepsilon Lc$$

ε is molar absorption coefficient
c is the concentration of the solution sample
L is the light path length of the solution
I_0 is the intensity of incident light
I is the intensity of the light after passing through the sample

Figure 3-5 Set-up of absorption spectroscopy experiment and Beer-Lambert law.

Measurements of optical absorption and scattering properties were performed using a double beam ultraviolet¯visible (UV-Vis) spectrophotometer (Lambda 40, PerkinElmer). An integrating sphere appendix was used for studying scattering effects. For solution samples, all the measurements were carried out by filling testing samples in quartz cells (Figure 3-5) at room temperature. The scan range was set from 220 nm to 700 nm, and scan speed was 60 nm/min. The corresponding concentration of the testing solution was obtained by Beer-Lambert law. In this thesis, molar absorption coefficient for dyes solution had been obtained by the Beer-Lambert plot (Figure 3-6), which is a graph of absorbance against concentration. The corresponding molar absorption coefficient was calculated by the gradient of straight line. If the Beer-Lambert plot turns out as non-linear, then it means that the absorption is independent of concentration which is not observed in this thesis.

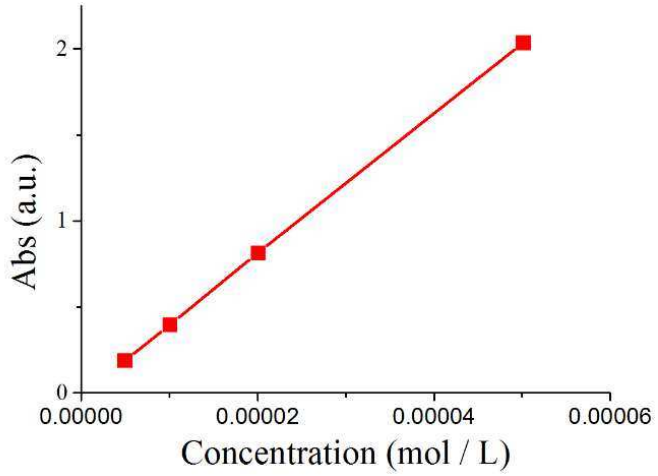

Figure 3-6 An example of a Beer-Lambert plot with linear fitting line for determining molar absorption coefficient.

3.4 Dye sensitised solar cell fabrication

3.4.1 Sensitised photoanode

To fabricate the DSSC devices, the nanostructured photoanodes were immersed into a solution of N719 dye (0.3 mM) dissolved in a solvent of MeCN/t-Butanol (1:1) in a dark environment for overnight for complete dye uptake.[9-11] The sensitised samples were rinsed with the same solvent to remove the excess physical absorbed dyes.[11]

3.4.2 Preparation of Pt counter electrodes

To prepare the CE, a hole (~1-mm diameter) was drilled through ITO coated substrates (glass slices and PET) using a diamond drilling bit. After cleaning process, the Pt catalyst was deposited onto the ITO surface using a DC sputter. The thickness of the Pt layer was set to 5 nm.

3.4.3 Electrolyte

The electrolyte used in this thesis was a solution containing 0.1 M LiI, 0.1 M I_2, 0.5 M 4-tert-butylpyridine, and 0.6 M tetrabutylammonium iodide in acetonitrile.

3.4.4 DSSC assembly

The sensitised photoanode and Pt decorated CE were assembled as a sandwich structured cell (Figure 3-7) and sealed using a hot melt Surlyn gasket (25 - 50 ≈m). It should be noted that the photoanode in this sandwich structure has an active area of ~0.28 cm^2. The as-prepared electrolyte was then injected through the hole of the back surface of the CE to the DSSC by placing it in a small vacuum chamber to achieve a vacuum back-filling. At the end, the hole though the CE was sealed by the hot melt Surlyn film covered with one piece of thin cover glass/PET.

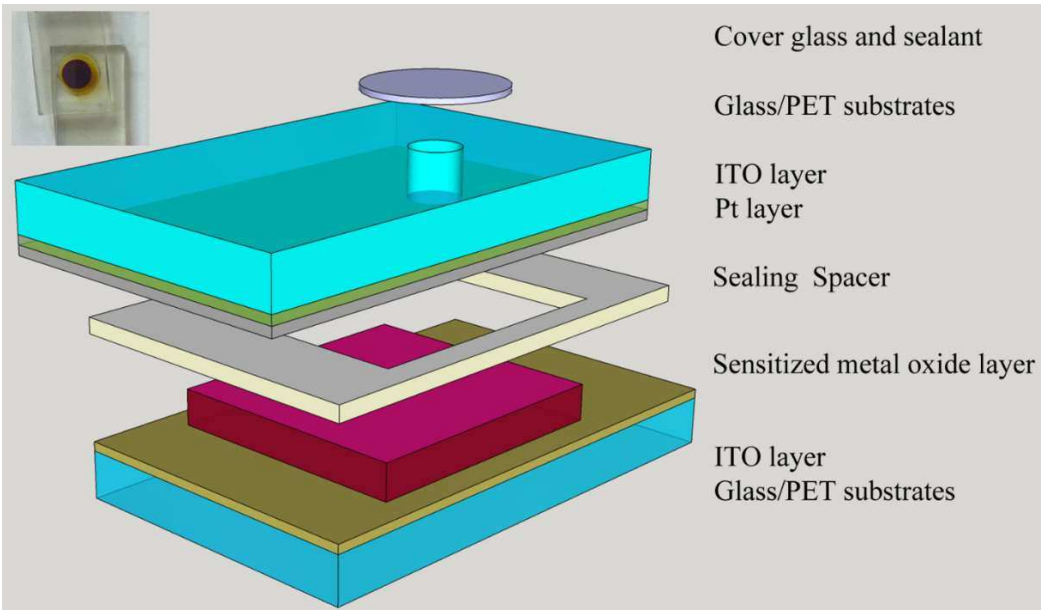

Figure 3-7 Configuration of sandwich structured dye sensitised solar cells with represented digital image of DSSC sample list in the inset.

3.5 DSSC characterisation

3.5.1 Photovoltaic characterisation

For the DSSCs, the photo current-voltage (I-V) results were measured under both light and dark conditions (Figure 3-8 (a)) using an electrochemical instrument (PGSTAT302N, Auto lab) or 2400 Source Meter (KEITHLEY) while the cell was covered by a mask (same area as active area of photo anode) to prevent extra light.[11] With the specific area during testing, the current density (J) can be obtained and used instated of current in practice, thus the I-V curve can be changed to a J-V curve. AM 1.5 solar illumination (100 mW/cm^{-2}) was provided by a solar simulator (SCIENCETECH Inc. SF150 or Abet Tech. Sun 2000) with an AM 1.5 filter. The output light intensity of the simulator was calibrated (100 mW/cm^{-2}) using a reference Si photodiode, which had been calibrated at 100 mW/cm^{-2} by GBSOL. With the obtained J-V results from samples, important parameters such as Voc, Jsc, and FF as well as PCE can be obtained (Figure 2-5). The meanings of these parameters were discussed in Chapter 2.

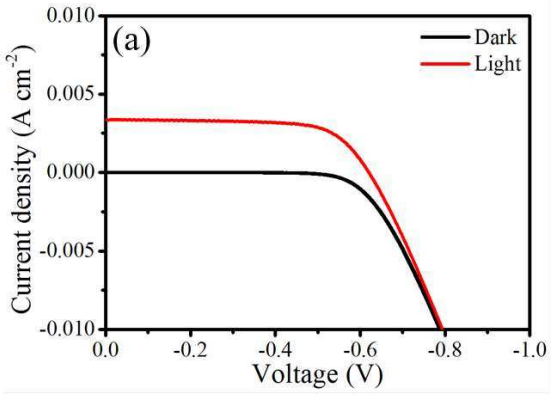

Figure 3-8 Typical J-V curves under light and dark condition.

3.5.2 Electrochemical impedance spectroscopy

Electrochemical impedance spectroscopy (EIS) is a well-known perturbative characterisation method which can be used to study the dynamics of an electrochemical process. It measures the responses of a testing sample after applied frequency-changed electrical perturbation. For the DSSC, EIS has been employed for recording the impedance response of the cell and studying the various interface behaviour in the cell (i.e. the photoanode/dye interface, photoanode/electrolyte interface and CE/electrolyte interfaces). The recorded data usually require a model (it is also known as equivalent circuit) to analyse. Applying a suitable equivalent circuit, results can be extracted from EIS measurements. Due to the complex working principle in the DSSCs and its complicated structure, an equivalent circuit suitable to describe the DSSCs is difficult to obtain. However, the normally used and well know equivalent circuits are still reasonably good to qualitatively analyse the interface behaviour (i.e. recombination and contact resistance). The typical MO (i.e. TiO_2) photoanode could be explained using a transmission line model shown in Figure 3-9 (a) which considered different interfaces as well as component of DSSCs.[12, 13] This model can be simplified to Figure 3-9 (b) if the MO photoanode become more conducting (i.e. the photoanode under high voltages or the MO material has better electron mobility).[12-14] Generally, a Nyquist plot as shown Figure 3-10 (a), with a Bode impedance plot as shown Figure 3-10 (b) is commonly used for analysis of DSSCs.

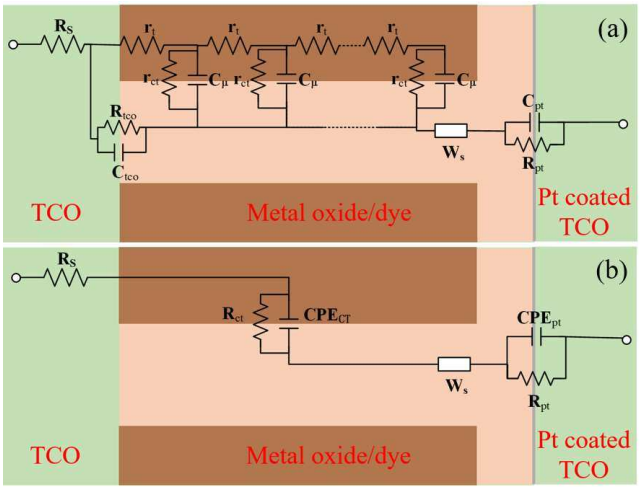

Figure 3-9 (a) Typical equivalent circuit of the DSSCs. (b) A simplified equivalent circuit of the DSSC.[14]

A typical Nyquist plot of the DSSC generally has three sections (Figure 3-10 (a)):[15] (1) the first semicircle (from the right) is the low frequency range (<1 Hz), which is assigned to the electrolyte diffusion; (2) the second semicircle is the middle frequency range (from 1 Hz to 10 kHz), which is linked with the charge transfer across interfaces amongst the semiconductor/dye/electrolyte; (3) the last semicircle is the high frequency ranges (in the kHz range and above), which is related to the electrochemical reaction at the Pt CE. As the only parameter varied in the DSSC of this study is the photoanode, the second ¯semi-circle is the part of the interest.[11] By applying a suitable equivalent circuit to fit the Nyquist plot, the electron transfer and recombination behaviour information on the photoanode/dye/electrolyte can be extracted. The Bode plot, is explicitly linked with frequency information, thus it is better to consider both plots for gathering more information about the properties of the tested DSSCs.[11, 14-16]

In this thesis, the EIS measurements were recorded using the AUTOLAB PGSTAT302N potentiostat with a frequency response analyser (FRA) software. The cells were measured in a frequency range from 0.1 Hz to 1 MHz. The applied bias

voltage and its amplitude were set as open-circuit and 10 mV.[11, 16] The obtained impedance spectra results were analysed using a Z-view software (Scribner Associate Inc.) with a simplified equivalent circuit (Figure 3-9).

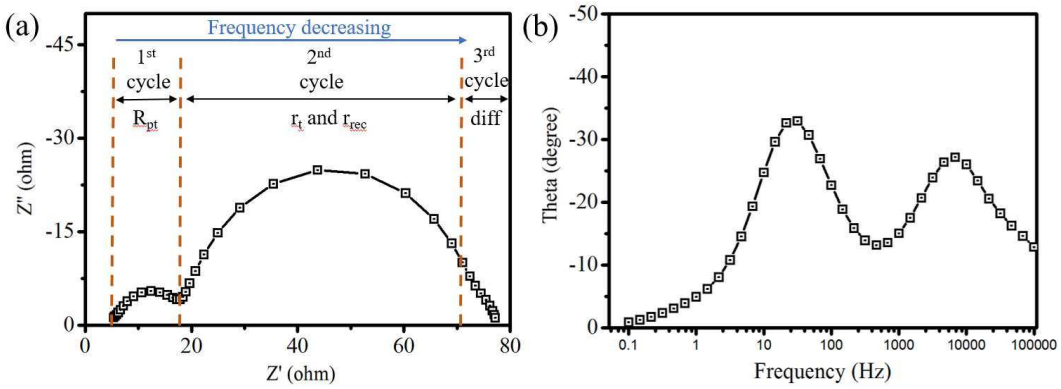

Figure 3-10 Typical (a) Nyquist plot with equivalent (b) Bode plot of a DSSC when performing EIS measurement under Voc.

3.5.3 Transient measurement

In this thesis, transient photo voltage/current was measured to understand electron transport and recombination kinetics. The theory in this work is based on the following assumptions:[14]

(1) Electrolyte is homogeneous and any variation in its concentration can be neglected;

(2) Total electron concentration (n) in the MO photoanode is considered as the dominant transport of charge within the DSSC. The concentration refers to the ratio between the number of electrons and the volume of the effective medium.[14]

(3) Contribution of electric caused by electron transport is negligible;

(4) Quasistatic assumption. The charges are all considered to be in equilibrium on the timescale of all the interrelated measurements in the thesis (i.e. which is not involve

either in the transport nor recombination process; 侈¯concentration of conducting charge).[11, 14] Therefore, the total electron concentration can be expressed:[14, 17]

侈嗯侈喵侈 (Eq. 3-1)

Under a typical working condition of the DSSCs, the 侈can be assumed much larger than 侈which result in n ū 侈(this assumption will be applied to the whole thesis)

(5) The optical light perturbation is strongly absorbed after illuminated into the cells shown in Figure 3-11.

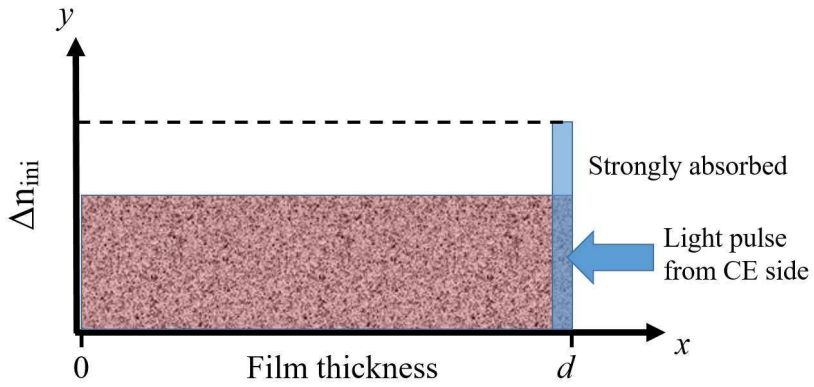

Δn_{ini} - excess electrons initially generated excess electrons

CE - counter electrode

Figure 3-11 Idealised schematic plot of the profile of ∀h$_{ini}$ while the excitation pulse illumination strongly absorbed from CE side.[14]

(6) To simplify the approaches of analysing photocurrent/voltage transient, for photocurrents, it is assumed that time is long enough to complete thermalisation of electrons with trap states and variation of the effective diffusion coefficient (D_n) is not significant with changing of position.

(7) For photo-voltage transient, the capacitance of the MO is assumed as an approximate constant during the measurement. Additionally, small changes of voltage are proportional to changes in electron concentrations at the surface of substrate:[14]

た侨乏た㑩戳嗯□婕 (Eq. 3-2)

Under the consumptions (1) to (7), the well-known multi-trapped framework proposed by Bisquert and Vikhrenko [18] is suitable to explain transient behaviour. In the proposed model, the variation of n can be expressed as the sum of generated, transport and recombined electrons:[14, 19]

$$\frac{\partial n}{\partial t} = \nabla \cdot \left(D_n \nabla n - \mu_n n \frac{\partial \phi}{\partial x} \right) + G - \frac{n}{\tau_n} \qquad \text{(Eq. 3-3)}$$

where G is the rate of electron generation as a function of position, D_n is the effective diffusion coefficient which can be expressed as:[14]

$$D_n = D_0 \left(\frac{\partial n}{\partial n + n_c} \right) \approx D_0 \left(1 - \frac{n}{n + n_c} \right) \qquad \text{(Eq. 3-4)}$$

where D_0 is the diffusion coefficient of free electrons in E_{CB} of the MO and it has a relationship [20] with the tracer (or jump) diffusion coefficient (D) as: [14]

$$D = \frac{n_c}{n} D_0 \qquad \text{(Eq. 3-5)}$$

and electron lifetime (τ_n) is defined as: [14]

$$\tau_n = \tau_0 \frac{n}{n_c} \qquad \text{(Eq. 3-6)}$$

τ_0 is the lifetime of free electrons (n_c).[14]

Therefore, a small perturbation can be introduced to a DSSC operated at a steady state condition and its return to the initial working condition can be recorded. [14] While a light perturbation introduced to the DSSC results in an increase of electrons (with the variable δn) into the semiconductor of the device, the variation of n can be expressed as:[14]

$$\frac{\partial (n + \delta n)}{\partial t} = \nabla \cdot \left(D_n \nabla n - \mu_n n \frac{\partial \phi}{\partial x} \right) + G - \frac{n + \delta n}{\tau_n} \qquad \text{(Eq. 3-7)}$$

The perturbation electron lifetime, -$_n$, is define as below: [14]

$$\text{偉} = \text{噫}\frac{\text{査}}{\text{査}} \text{偉} \qquad \text{(Eq. 3-8)}$$

Considering the background conditions of the tested device are at steady states, , (Eq. 3-8) can be simplified to: [14]

$$\frac{\text{呣}}{\text{呣}} \text{噫} \text{侖} = \frac{\text{呣}}{\text{呣}} \text{営} \frac{}{} \qquad \text{(Eq. 3-9)}$$

Once a pulse (strongly absorbed) was introduced into the devices from the CE side of the DSSC (i.e. 1/ << d), the corresponding photocurrent changes are directly linked to the electrons diffused across the semiconductor photoanode. (Figure 3-12). The initial (t=0) distribution of charge is estimated using a delta function:[14]

$$\text{た} = \text{噫} \text{噫} = \text{た} \qquad \text{(Eq. 3-10)}$$

where $\forall Q_{ini}$ is the total initially generated charge.[14]

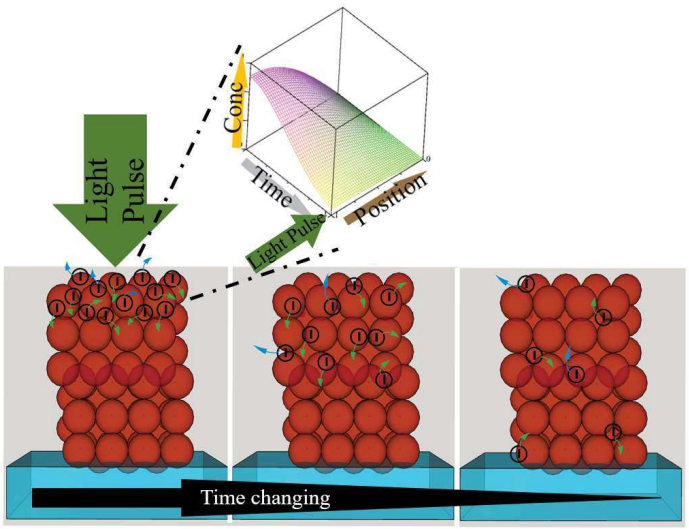

Figure 3-12 Idealised schematic images of the excess electrons changing with variation of time (t) and position (x) after one light pulse. The insert shows an idealised example calculation plot of distribution profiles (Eq. 3-11). of excess electrons generated after light pulse.[14]

Considering boundary conditions:[14]

(1) ∀n (x=0, t>0) =0 (current collection at the substrate);

(2) $\frac{\partial n}{\partial x}$ = 0 (no electron crossing the CE boundary);

Evolution of the charge concentrations as a function of time after the light pulse can be expressed as:

$$n(x,t) = \frac{\alpha I_0}{2D_n(\alpha^2 - \beta^2)}\left[(\alpha + \frac{S_n}{D_n})e^{-\alpha x} - (\beta + \frac{S_n}{D_n})e^{\beta x}\right]e^{-t/\tau} + \frac{\alpha I_0}{2D_n(\alpha^2 - \beta^2)}\left[(\beta + \frac{S_n}{D_n})e^{\beta(x-L)} - (\alpha + \frac{S_n}{D_n})e^{-\alpha(x-L)}\right]e^{-t/\tau}$$

$$+ \frac{\alpha I_0 \tau}{\alpha^2 L^2 - 1}e^{-\alpha x}(1 - e^{-t/\tau}) \quad \text{(Eq. 3-11)}$$

Considering Fick's law of diffusion at x=0,[14]

$$J_n(t) = -qD_n\frac{\partial n(x,t)}{\partial x}\Big|_{x=0} \quad \text{(Eq. 3-12)}$$

The corresponding current can be written as:[14, 21, 22]

$$J(t) = \frac{qA(1-R)\alpha I_0 \tau}{\alpha L + 1} + \frac{\alpha I_0}{2(\alpha^2 - \beta^2)}\left[(\alpha + \frac{S_n}{D_n})e^{-\alpha x} - (\beta + \frac{S_n}{D_n})e^{\beta x}\right]e^{-t/\tau} + \frac{\alpha I_0}{2(\alpha^2 - \beta^2)}\left[(\beta + \frac{S_n}{D_n})e^{\beta(x-L)} - (\alpha + \frac{S_n}{D_n})e^{-\alpha(x-L)}\right]e^{-t/\tau} \quad \text{(Eq. 3-13)}$$

Under the assumption of strong absorption that time is sufficiently long, thus $e^{-t/\tau}$ in Eq. 3-13 can be negligible. The excess electrons reach to the outer electrode and the corresponding current decrease can be expressed as:[14]

$$J(t) = \frac{qA(1-R)\alpha I_0 \tau}{\alpha L + 1} + \frac{\alpha I_0}{2(\alpha^2 - \beta^2)}\left[(\alpha + \frac{S_n}{D_n})e^{-\alpha x} - (\beta + \frac{S_n}{D_n})e^{\beta x}\right]e^{-t/\tau} \quad \text{(Eq. 3-14)}$$

Therefore, the photocurrent relaxation time ($-_j$) in the system for ∀j includes the recombination during transport is:[14]

$$\tau_{eff} = \frac{\alpha I_0 \tau}{\alpha^2 L^2 - 1}e^{-\alpha x} \quad \text{(Eq. 3-15)}$$

For photovoltage transient measurement, the process is similar to the photocurrent measurement, but the DSSCs are measured under an open circuit working conditions so that there is no complete circuit for current exit the cell.[14] Thus after a pulse light introduces the perturbation, the voltage decay is related to the variation of corresponding electron concentrations at x=0 (substrate position) and is independent of the initial pulse generation in the DSSC.[14] Eq. 3-9 can be reduced to the following express:[14]

$$\frac{\partial \delta n}{\partial t} = \frac{\partial \delta n}{\partial x} \qquad \text{(Eq. 3-16)}$$

The photovoltage decay after the perturbation introduced by the excitation pulse can be obtained as below:[14]

$$\delta V = \frac{k_B T}{q} \frac{\partial \delta n / \partial x}{n_0 / L} = \frac{k_B T}{q} \frac{\partial \delta n}{n_0} \qquad \text{(Eq. 3-17)}$$

Using the same initial boundary conditions as we have used in the transient current, the above equation can be described as the changes in photovoltage at position x=0:

$$\delta V = \frac{k_B T}{q} \frac{\delta n_0}{n_0} \exp\left(-\frac{t}{\tau_n}\right) \qquad \text{(Eq. 3-18)}$$

According to the research results reported by Barnes et al. the first two series (m= 0, 1) of this equation are sufficient to express δn_0 unless L>>d.[14] Thus, the process can be simplified to extract $-\tau_n$ using simplified process as shown below,[14]

$$\delta V = \frac{k_B T}{q} \frac{\delta n_0}{n_0} \exp\left(-\frac{t}{\tau_n}\right) \qquad \text{(Eq. 3-19)}$$

In this thesis, photocurrent and photovoltage transient measurements were carried out using a self-build measurement set-up according to Ref [14]. The set-

up contains background normal white light emitting diodes (LEDs) and green LEDs ($\cong_{peak}$ =530 nm) controlled by a programing ARDUINO board. The wave form generator (33220A, KEYSIGHT) was employed to operate the pulse LEDs. The illumination was from CE of the DSSC. The electron kinetics in the resultant DSSCs was investigated by measuring the transient electrical signals (voltage/current) after the optical pulse (perturbation).[6] The time corresponding to voltage/current decay measurements was recorded using an oscilloscope (MSO-X, 3054A, Agilent).[6] The current was determined by Ohm˜s Law from measuring the voltage drop across a measurement resistor (36 |) which was operated in series with the DSSCs. Multi-runs were performed for noise reduction.[6]

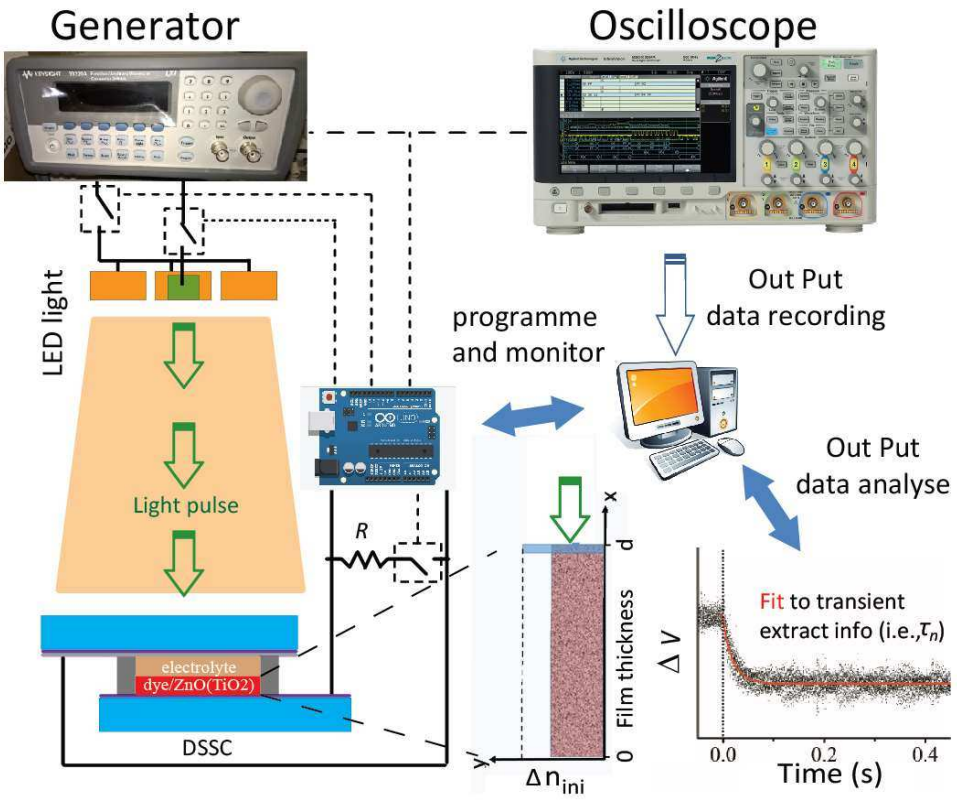

Figure 3-13 Experimental set up and apparatus used for transient measurement of the DSSC. The light perturbation is supplied by a waveform signal generator and the respond of the DSSC is collected by an oscilloscope. ARDUINO digital card is used for synchronization control all the relative facilities as well as delivery data to oscilloscope.

Reference

1. Meng, L.J. and F. Placido, Annealing effect on ITO thin films prepared by microwave-enhanced dc reactive magnetron sputtering for telecommunication applications. Surface and Coatings Technology, 2003. 166(1): p. 44-50.
2. Joo, J., B.Y. Chow, M. Prakash, E.S. Boyden, and J.M. Jacobson, Face-selective electrostatic control of hydrothermal zinc oxide nanowire synthesis. Nat Mater, 2011. 10(8): p. 596-601.
3. Konezny, S.J. and V.S. Batista, CHAPTER 1 Computational Modeling of Photocatalytic Cells, in Solar Energy Conversion: Dynamics of Interfacial Electron and Excitation Transfer. 2013, The Royal Society of Chemistry. p. 1-36.
4. Shock, E.L., D.C. Sassani, M. Willis, and D.A. Sverjensky, Inorganic species in geologic fluids: Correlations among standard molal thermodynamic properties of aqueous ions and hydroxide complexes. Geochimica et Cosmochimica Acta, 1997. 61(5): p. 907-950.
5. Richardson, J.J. and F.F. Lange, Rapid synthesis of epitaxial ZnO films from aqueous solution using microwave heating. Journal of Materials Chemistry, 2011. 21(6): p. 1859-1865.
6. Zhao, C., J. Zhang, Y. Hu, N. Robertson, P.A. Hu, D. Child, D. Gibson, and Y.Q. Fu, In-situ microfluidic controlled, low temperature hydrothermal growth of nanoflakes for dye-sensitized solar cells. scientific reports, 2015. 5: p. 17750.
7. Zhao, C., D. Child, D. Gibson, E. Placido, and R.Y.Q. Fu, TiO_2 films prepared using plasma ion assisted deposition for photocatalytic application. Materials Research Bulletin, 2014. 60: p. 890-894.
8. Linsbod, R., E. Ritter, and K. Leitner, Evaluation of the oxidation of TiO_2 films during reactive evaporation of Ti_3O_5 and during exposure of the films to the atmosphere. Applied Optics, 2003. 42(22): p. 4580-3.
9. Xu, C., P. Shin, L. Cao, and D. Gao, Preferential Growth of Long ZnO Nanowire Array and Its Application in Dye-Sensitized Solar Cells. The Journal of Physical Chemistry C, 2010. 114(1): p. 125-129.
10. Zhang, Q., C.S. Dandeneau, X. Zhou, and G. Cao, ZnO Nanostructures for Dye-Sensitized Solar Cells. Advanced Materials, 2009. 21(41): p. 4087-4108.
11. Zhao, C., D. Child, Y. Hu, N. Robertson, D. Gibson, S.C. Wang, and Y.Q. Fu, Low temperature growth of hybrid ZnO/TiO_2 nano-sculptured foxtail-structures for dye-sensitized solar cells. RSC Advances, 2014. 4(105): p. 61153-61159.
12. Fabregat-Santiago, F., J. Bisquert, G. Garcia-Belmonte, G. Boschloo, and A. Hagfeldt, Influence of electrolyte in transport and recombination in dye-sensitized solar cells studied by impedance spectroscopy. Solar Energy Materials and Solar Cells, 2005. 87(1¯4): p. 117-131.
13. Fabregat-Santiago, F., G. Garcia-Belmonte, J. Bisquert, A. Zaban, and P. Salvador, Decoupling of Transport, Charge Storage, and Interfacial Charge Transfer in the Nanocrystalline TiO_2/Electrolyte System by Impedance Methods. The Journal of Physical Chemistry B, 2002. 106(2): p. 334-339.
14. Barnes, P.R.F., K. Miettunen, X. Li, A.Y. Anderson, T. Bessho, M. Gratzel, and B.C. O'Regan, Interpretation of Optoelectronic Transient and Charge Extraction Measurements in Dye-Sensitized Solar Cells. Advanced Materials, 2013. 25(13): p. 1881-1922.
15. Adachi, M., M. Sakamoto, J. Jiu, Y. Ogata, and S. Isoda, Determination of Parameters of Electron Transport in Dye-Sensitized Solar Cells Using Electrochemical Impedance Spectroscopy. The Journal of Physical Chemistry B, 2006. 110(28): p. 13872-13880.
16. Bai, Y., H. Yu, Z. Li, R. Amal, G.Q. Lu, and L. Wang, In Situ Growth of a ZnO Nanowire Network within a TiO_2 Nanoparticle Film for Enhanced Dye-Sensitized Solar Cell Performance. Advanced Materials, 2012. 24(43): p. 5850-5856.

17. Barnes, P.R.F., A.Y. Anderson, J.R. Durrant, and B.C. O'Regan, Simulation and measurement of complete dye sensitised solar cells: including the influence of trapping, electrolyte, oxidised dyes and light intensity on steady state and transient device behaviour. Physical Chemistry Chemical Physics, 2011. 13(13): p. 5798-5816.
18. Bisquert, J. and V.S. Vikhrenko, Interpretation of the Time Constants Measured by Kinetic Techniques in Nanostructured Semiconductor Electrodes and Dye-Sensitized Solar Cells. The Journal of Physical Chemistry B, 2004. 108(7): p. 2313-2322.
19. Bisquert, J., A. Zaban, M. Greenshtein, and I. Mora-SerÆ, Determination of Rate Constants for Charge Transfer and the Distribution of Semiconductor and Electrolyte Electronic Energy Levels in Dye-Sensitized Solar Cells by Open-Circuit Photovoltage Decay Method. Journal of the American Chemical Society, 2004. 126(41): p. 13550-13559.
20. Bisquert, J., Chemical Diffusion Coefficient of Electrons in Nanostructured Semiconductor Electrodes and Dye-Sensitized Solar Cells. The Journal of Physical Chemistry B, 2004. 108(7): p. 2323-2332.
21. Duffy, N.W., L.M. Peter, and K.G.U. Wijayantha, Characterisation of electron transport and back reaction in dye-sensitised nanocrystalline solar cells by small amplitude laser pulse excitation. Electrochemistry Communications, 2000. 2(4): p. 262-266.
22. Nakade, S., Y. Saito, W. Kubo, T. Kanzaki, T. Kitamura, Y. Wada, and S. Yanagida, Enhancement of electron transport in nano-porous TiO_2 electrodes by dye adsorption. Electrochemistry Communications, 2003. 5(9): p. 804-808.

Chapter 4 Fabrication of ZnO nanorods array

4.1 Introduction

ZnO nanostructures have attracted great research interests due to their unique electronic, piezoelectric and optical properties, which are strongly contingent on their morphology, crystallinity and composition. Particularly, ZnO 1D nanostructures (i.e. NRs) provide large surface areas and direct pathways for electron transport, which makes them as one of the most promising candidates for the photoanode used in the DSSCs.[1] Much effort has been devoted to optimise synthesis methods, improve understanding of chemical synthesis process and investigate their fundamental function properties.[2-4]

One of the most promising processes for production of the ZnO NRs is the aqueous solution based method which typically requires zinc salt and hydroxide sources in a basic aqueous solution. As a low temperature and cost effective process, it has a great potential in scale up ZnO synthesis. Much effort has been made to optimise the growth factors (i.e. temperature, reactant concentration, additives and pH) as well as understand their growth behaviour. However, much effort is still needed to find out the best governing factors (such as supersaturation condition in the reaction solution) and the detailed understanding of growth behaviour.[5-7]

In this chapter, we examined effects of reactants, chemical reaction factor and additive effects on the ZnO NRs growth. By analysing experiment results, the effects of the reaction parameters on NRs growth and the relationship between ZnO NRs growth and supersaturation conditions of the solution were obtained.

4.2 Results and discussion

As discussed in the Chapter 2, ZnO is a kind of amphoteric oxide which can be

dissolved in either alkalis or acid solution with an isoelectric point value at around 9.5.[8] Typically, an alkaline growth environment is required for the ZnO 1-D nanostructure growth in aqueous solutions.[4] Similar to most aqueous solution methods, ZnO NR growth is largely dependent on the chemical composition of the reaction solution. The influences of the chemical composition of the growth solution such as reactants, pH of reaction solution, reactants concentration, reaction temperature, reaction duration and additives on the ZnO nanostructure will be studied. Table 4-1 is a list of the experimental conditions to be discussed in this chapter (detailed experimental conditions have been listed in Section 3.2.1 and Table 3-2).

Table 4-1 Summary of experimental parameters for the solution processed ZnO NRs growth.

Parameter	pH	Duration (minute)	Temperature (°C)	Concentration (mM)	Additive	OH source
Condition	7-12	0-600 0-900	45-95	30-110 0-600	PEI, (NH_4^+), $(CH_2)_6N_4$	$(CH_2)_6N_4$ NaOH and NH4.OH
Influence	Density Saturation	Growth & reaction	Reaction rate morphology	Morphology and NRs size	Bulk nucleation suppress	Supersat-uration and pH

4.2.1 Growth of ZnO NRs using hexamethylenetetramine aqueous solution

4.2.1.1 Temperature effects

The growth solution containing $Zn(NO_3)_2$ - $(CH_2)_6N_4$ group is one of the most commonly used reactant combinations for the aqueous solution processed ZnO NRs growth.[7, 9] However, the effects and exact functions of the $(CH_2)_6N_4$ during the ZnO NR growth are still unclear. Functions of $(CH_2)_6N_4$ have been suggested as: (1) a pH buffer which can continually supply OH^- to the reaction;[4, 10] (2) morphology control

agent which can be adhered to the non-polar faces of the crystal (i.e., NRs) during its inherent growth along the polar direction of the wurtzite ZnO. It is necessary to carry out a series of experiments for gathering the basic knowledge of synthesis of ZnO NRs in $Zn(NO_3)_2$ - $(CH_2)_6N_4$ aqueous solution and achieving the optimised growth parameters with a good reproducibility.

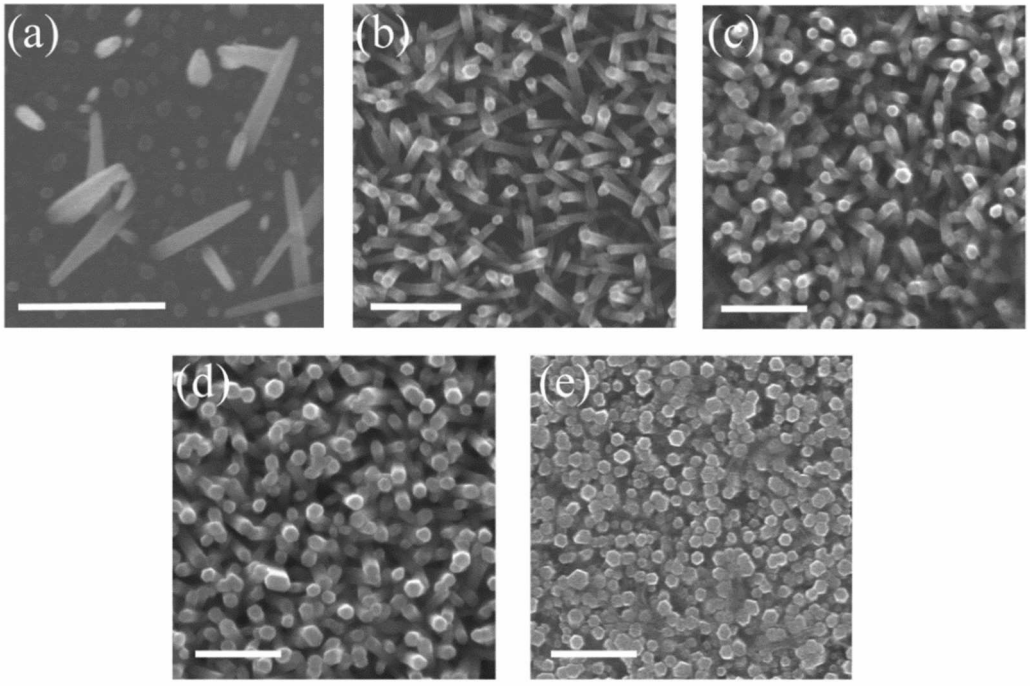

Figure 4-1 Top view SEM images of ZnO NRs arrays synthesised at different reaction temperatures (a) 45 °C, (b) 65 °C, (c) 75 °C , (d) 90 °C and 95 °C. All other parameters ($Zn(NO_3)_2$-50 mM, $(CH_2)_6N_4$-50 mM, growth duration of 3 hrs) were fixed except variable temperature. All scale bars are 500 nm

Temperature is one of the key parameters in the solution processed ZnO nanostructure growth.[4, 11] In general, the temperature is not only related to the choice of substrates, but also the reaction rate. The temperature effects were investigated by varying the solution temperature from 35 °C to 95 °C. As shown in Table 3-2, all other parameters ($Zn(NO_3)_2$-50 mM, $(CH_2)_6N_4$-50 mM, growth duration of 3 hrs) were fixed except variable temperature. The corresponding morphologies of the obtained ZnO NRs are shown in Figure 4-1.When the reaction temperature was set at 35 °C, no ZnO NRs and

precipitates were observed in this study. Though further extending the reaction time up to 12 hours under the reaction temperature at 35 °C, the reaction solution was still transparent without visible precipitation and visible ZnO nanostructures on the pre-seed substrates. During this low temperature (35 °C) process, $(CH_2)_6N_4$ had an extremely low decomposition rate which slowed down the ZnO growth reaction.[12-14] This will suppress the reaction solution to reach a supersaturation state for forming solid ZnO.[7]

After increasing the reaction temperature to 45 °C, ZnO NRs was observed on the pre-seeded substrate (Figure 4-1 (a)). Discrete hexagonal shaped rods of initial-growing ZnO NRs were observed but with a large space among each other. In Figure 4-1 (b), a ZnO NR array was achieved at the reaction temperature of 65 °C. With further increase of the reaction temperature from 65 °C to 95 °C (Figure 4-1 (c) to (e)), the density and diameters of the ZnO NRs were increased with the temperature raise. Typically, all the ZnO NRs showed a hexagonal shape.

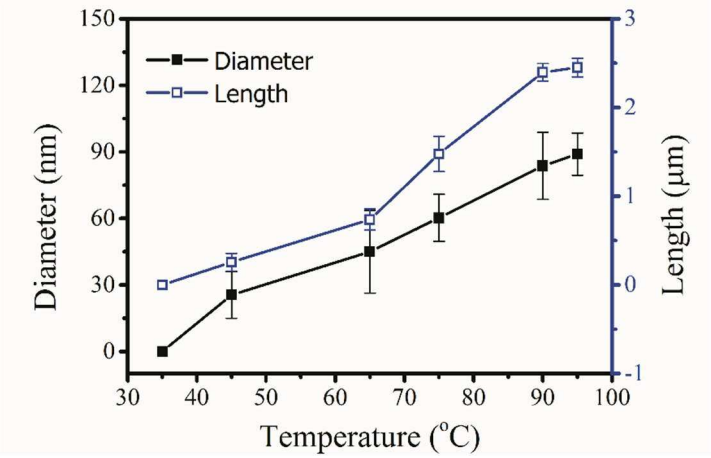

Figure 4-2 Temperature effects on the diameter and length of ZnO NRs. All other parameters ($Zn(NO_3)_2$-50 mM, $(CH_2)_6N_4$-50 mM, growth duration of 3 hrs) were fixed except variable temperature. Error bars represent standard deviation.

In Figure 4-2, the temperature effects on the morphology factors (length and diameter) of the resultant ZnO NRs are summarised. The length and diameter of ZnO NRs

increase with the reaction temperature up to 95 °C. The growth occurs along the c-axis as well as lateral of the ZnO NRs. Higher temperature activates the chemical reaction in this aqueous solution which results in a faster growth rate for the ZnO crystal growth at the initial stage (i.e. beginning growth at the seed layer). Therefore, more ZnO seed crystals on the seed layer could gain more opportunities to reach the crystal critical size for further growth, which can be considered as one reason for the denser morphology we observed.[4]

Therefore, it can be concluded that the lowest growth temperature is 45 °C for the ZnO NRs growth on the pre-seeded substrates. The process temperature strongly affect the growth rate and morphology (density and diameter). Therefore, there is a proper range of the growth temperatures for the well-arranged ZnO NRs array, i.e. 75 to 90 °C commonly used in this research work.

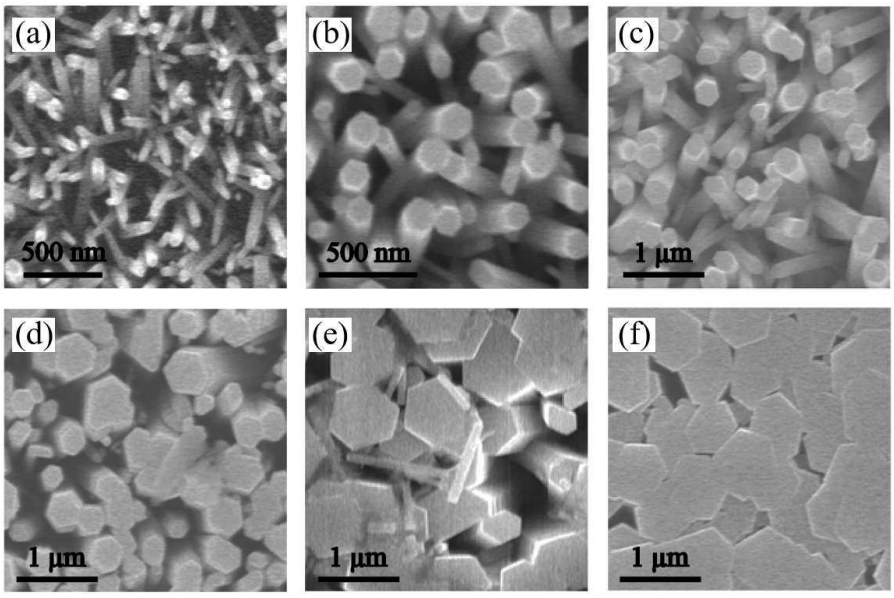

Figure 4-3 A series of SEM images of ZnO NRs grown with the reactants concentration of (a) 30 mM, (b) 40 mM, (c) 50 mM, (d) 70 mM, (e) 90 mM and (f) 110 mM. All other parameters (growth at 90 °C for 3 hrs) were fixed except variable reactants ($Zn(NO_3)_2$ and $(CH_2)_6N_4$ with molar ratio 1:1) concentration.

4.2.1.2 Influence of reactants and durations

Typically, the concentration of the reactants will influence the chemical reaction thus affect the growth of ZnO NRs. To evaluate this, the concentration of reactants ($(CH_2)_6N_4$ and $Zn(NO_3)_2$ with a molecular ratio of 1:1) was varied from 30 to 110 mM, with other factors fixed (growth temperature set at 90 · C and duration for the growth is 3 hours) as shown in Table 3-2. Figure 4-3 displays the morphological transformation of the ZnO NRs caused by changing the chemical concentrations of the reaction solution. Figure 4-3 shows the hexagonal ZnO NR arrays obtained with different reactant concentrations from 30 to 110 mM. The SEM images clearly reveal the morphology evolution of the ZnO NR as a function of reactant concentrations. The morphology is changed gradually from discrete 1D ZnO NR arrays to dense nanostructure (i.e. dense thin film assembled by larger sized NRs). For the samples grown with the lowest concentration of the reaction solutions used in this experiment (i.e. 30 mM), the NRs showed a low density and a less faceted shape than the others. At a relative low concentration (30-50 mM) condition (Figure 4-3 (a) to (c)), the density (as well as diameter) of the ZnO NRs were increased with the reactant concentration. For higher concentrations (70 to 110 mM) as shown in Figure 4-3 (d) to (f), the ZnO NRs started to grow together, forming larger sized NRs and the spaces between each NRs were decreased. In the case of the highest concentration (110 mM) used in our study, a dense thin film was obtained. Similar to the most other chemical reaction cases, the reaction solution with a higher concentration yields a faster reaction speed. During the ZnO nanostructure growth, the changes of the concentration of the reactants ($(CH_2)_6N_4$ and Zn^{2+}) will vary the supply of `nutrition_ (i.e. OH^-, Zn^{2+}) for ZnO crystal growth. The higher concentrations of the reactant solution used in the growth process, the more ZnO precursor can be formed. The dense nanostructures obtained at a high

concentration can be explained by the Ostwald-ripening mechanism in the aggregation-crystallisation growth process.[15] Under a high concentration of `nutrition_ growth source, $\{01\bar{1}0\}$ planes of the crystal particles are more energy favourable which will lead to an enhanced absorption-aggregation phase during the growth. This will result in that the growth rate along radial direction has a similar speed as the preferable c-axis growth, which typically is the fast growth direction under a normal growth condition.[7] This will accelerate the growth of the ZnO crystal, which results in an increased size of the ZnO NRs and dense nanostructures. This can be confirmed by the cross-section morphology in the investigation of effects of the reaction durations (shown in Figure 4-4).

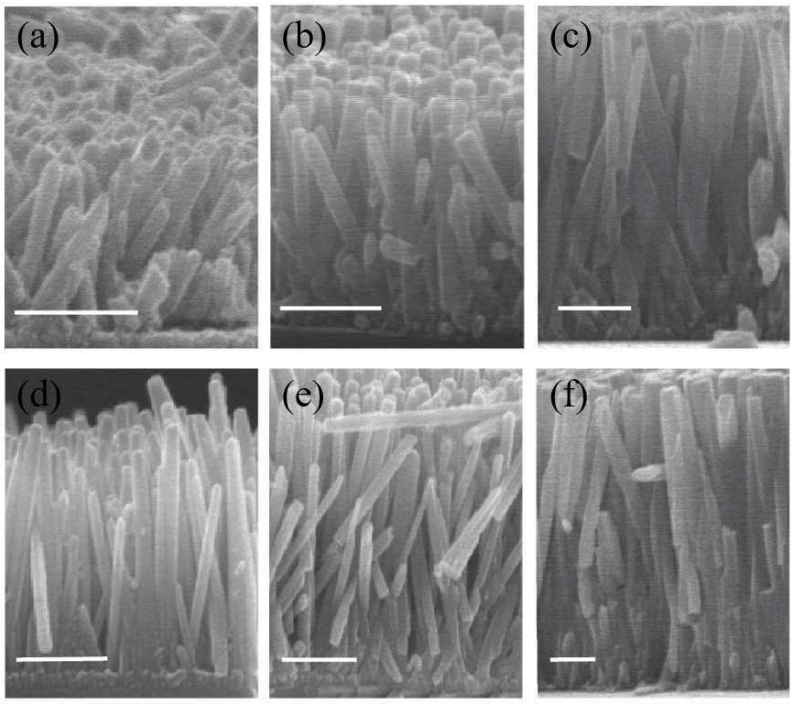

Figure 4-4 Cross-section SEM images showing the morphological evolution of ZnO NRs obtained with set concentration and varied reaction duration time. All other parameters ($Zn(NO_3)_2$-25 mM, $(CH_2)_6N_4$-25 mM, 90 °C; $Zn(NO_3)_2$-50 mM, $(CH_2)_6N_4$-50 mM, 90 °C) were fixed except variable reaction duration time. (a) 25 mM-90 minutes; (b) 25 mM -150 minutes; (c) 25 mM -210 minutes; (d) 50 mM-90 minutes; (e) 50 mM -150 minutes and (f) 50 mM -210 minutes. All scale bars are 500 nm.

To reveal the effects of growth duration, the tests were carried out by varying reaction durations using a fixed concentration of reactants under a fixed growth temperature at 90 °C (Table 3-2). The reactant concentrations were set at 25 and 50 mM, respectively. As shown in Figure 4-4, the diameters and lengths of the ZnO NRs were all increased when the reaction duration was increased under both reaction concentration conditions. The detailed relationship between the ZnO NRs length and growth duration are shown in Figure 4-5, which was obtained by varying reaction durations under two different reactant concentrations (i.e. 25 mM and 50 mM). The growth of the ZnO NRs under a higher concentration showed a faster average growth rate. Additionally, the ZnO NRs synthesised under both reaction concentration conditions (25 mM and 50 mM) demonstrated a similar trend, which shows that the growth rate gradually decreased.

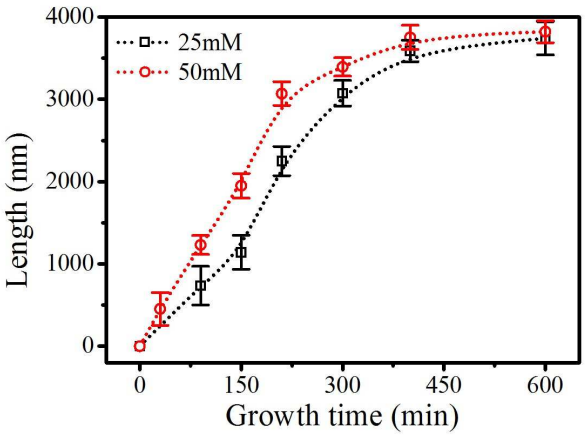

Figure 4-5 Dependence of the ZnO NRs length on varying growth time under reaction concentration of 25 mM and 50 mM, respectively. All other parameters ($Zn(NO_3)_2$-25 mM, $(CH_2)_6N_4$-25 mM, 90 °C; $Zn(NO_3)_2$-50 mM, $(CH_2)_6N_4$-50 mM, 90 °C) were fixed except variable growth time.

The whole growth process can be explained based on the chemical reaction occurring in the aqueous solution of $Zn(NO_3)_2$ and $(CH_2)_6N_4$. The ZnO formation starts from thermal decomposition of $(CH_2)_6N_4$, which will release OH^-, NH_4^+ and formaldehyde. The produced OH^- thus drives the formation of ZnO as a typical reaction product in an

alkali solution process.[4] By maintaining the reaction solution at the given temperature (i.e. 90 °C in this case), the $(CH_2)_6N_4$ provides a convenient source of OH^- which leads to the continuing reaction. Eventually, the reactants tend to be exhausted, causing a decreased reaction rate.[4] As a result, the reaction normally stops after 2-3 hours in this study due to the depletion of the chemical reactants in the solution. The growth resumes by replacing the samples into a fresh growth solution (the detailed experiment process listed in section 3.2.1). However, after 450 minutes, or further extending growth duration to 600 minutes with all fresh growth solution, the length of ZnO NRs does not change apparently under two reaction concentration conditions (Figure 4-5). This may be caused by two main reasons:[4] (1) the longer reaction duration will cause sealing of the ZnO NRs with each other because the NRs not only grow from the c-axis direction (along length) but also grow in the radial direction. The growth rate along the radial direction is much slower than the growth rate along the preferable direction; (2) in the growth process, as the ZnO NRs form not only on the pre-seeded substrates but also in the bulk solution. This homogeneous nucleation growth in the bulk reaction solution will consume the growth precursor nutrition. This results in that only a limited amount of the growth nutrition has been used for the formation of ZnO NRs on the pre-seed surface, which slows down the growth rate. The ZnO crystal with larger sizes requires more precursors to continue growth. As a result the growth rate decreases after a long term growth.

The investigation into the morphology evolution of the ZnO NRs using $Zn(NO_3)_2$ and $(CH_2)_6N_4$ with various reaction conditions (concentration, temperature and duration) indicates that the density, length as well as size of the ZnO NRs increased with the temperature. Similar trend has been observed for reaction concentrations. By studying

the concentration effect, the higher concentration resulted in a faster growth rate, but the growth rate decreases with extended growth durations.

4.2.2 ZnO NRs growth in an alkaline solution

If only $(CH_2)_6N_4$ is used in the NRs growth, only shorter (< 4 ı m) ZnO NRs can be obtained with good morphology control and reproducibility. A major drawback of this growth method is that ZnO growth happens not only on the pre-seeded target surface but also in the whole aqueous solution simultaneously. This causes a competition to consume the source material in the solution, which results in a decreased growth rate of the ZnO NRs on the target surface. In addition, further increase of the growth duration may cause fusion of the NRs and loss of the internal surfaces. Therefore, we proposed a feasible process, i.e. using additives in an alkaline solution to suppress ZnO formation in the bulk solution but also maintain the features of the NRs without growing together.

4.2.2.1 Influence of pH and reactant concentration on the growth of ZnO nanorods

The growth solution supersaturation condition is the key driving force for the ZnO formation, which is affected by pH (OH^- for ZnO growth) and reactant concentration. The solubility can be used as an indicator for the solution supersaturation. To study the relationship between supersaturation degree (calculated solubility as indicator) and NRs growth behaviour, various NR length have been chosen to evaluate the influence of the reactant concentration and solution pH on the ZnO NRs in an alkaline growth condition.[16]

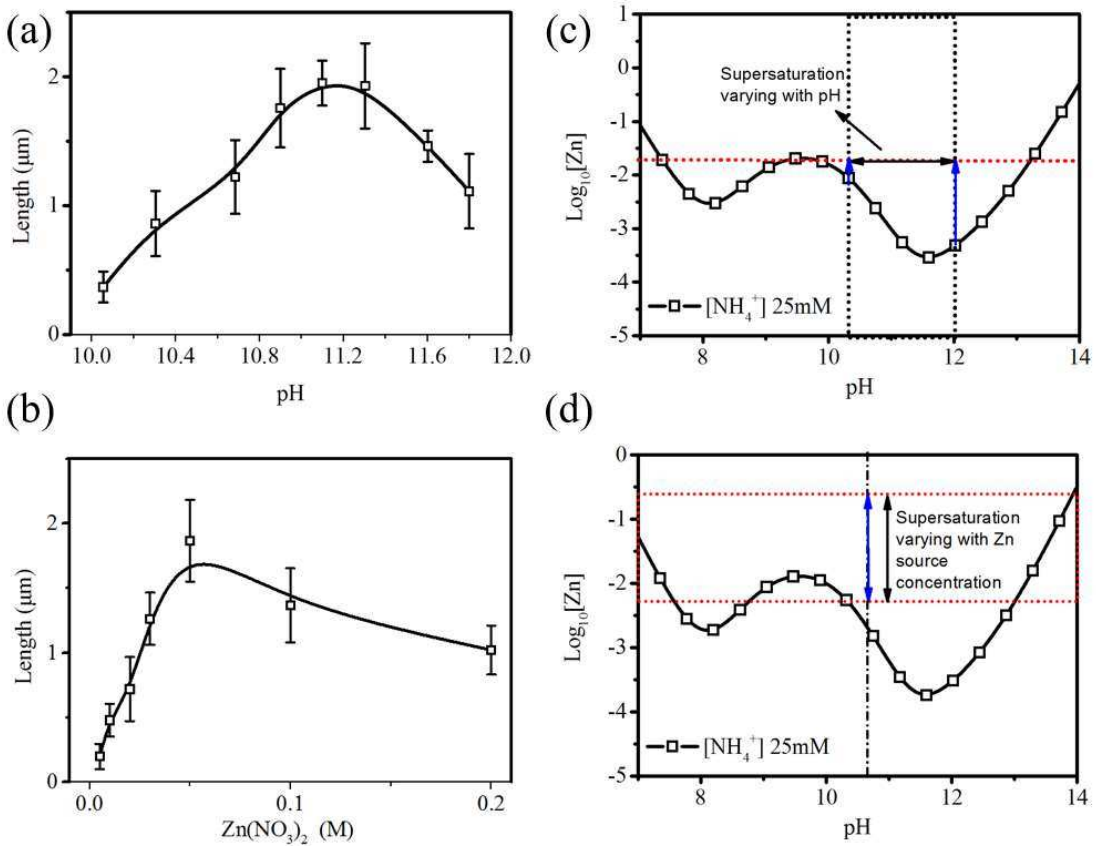

Figure 4-6 (a) pH effects on ZnO NRs growth. All other parameters ($Zn(NO_3)_2$-20 mM, $[NH_4^+]$-25 mM, 80 °C, 3 hrs) were fixed except variable pH of the solution. (b) zinc source concentration effects on ZnO NRs growth. All other parameters ($[NH_4^+]$-25 mM, 80 °C, 3 hrs, pH 10.5) were fixed except variable zinc source concentration; solubility plot as a function of pH under experiment using solution condition with superstation changing with varying (c) pH and (d) zinc source concentration.

Figure 4-6 (a) & (b) shows the effects of the pH and zinc source concentration on the ZnO NRs growth, respectively. All the other reaction conditions were fixed during this testing as shown in Table 3-2, i.e. the growth solution of 25 mM; temperature of 80 °C and duration 3 hours. The pH of the growth solution was tailored using proper amounts of HCl and/or NaOH. After introducing pre-seeded substrates into the reaction vessel with 100 ml solution, the vessel was heated to 80 °C for 3 hours. The corresponding data of the solubility as a function of pH with the superstation rate varying by modifying pH (Figure 4-6 (c)) and zinc source concentrations (Figure 4-6 (d)) are also shown in

Figure 4-6 for a comparison. Comparing the length results of the ZnO NRs with the calculated solubility plots, it can be noted that the growth rate is linked with the superstation condition of the growth solution. When a low pH value was used in this study (lower than 10), there was no NRs obtained and the seed layer was etched. From Figure 4-6 (c), it demonstrates that the solution is not in a supersaturation condition in this range. In the pH range between 10 and 11, the growth of ZnO NRs increased with pH increase because the degree of the supersaturation (this can be considered as the growth driving force) in the solution increased. However, this driving force not only boosts the growth of pre-existing seed layer for ZnO NRs on substrates, but also increases the homogeneous nucleation in the bulk reaction solution. Additionally, in the growth solution, a higher degree of the supersaturation is favourable for homogeneous nucleation in the bulk reaction solution which could consume the nutrition quickly and suppress the ZnO NRs growth on the sample surface.[16] This explains that higher pH values ranged from 11 to 12 used in the experiments did not result in an improvement in the NRs growth. Similar growth behaviour can also be observed by varying zinc source concentrations with the other parameters fixed as constants. Comparing Figure 4-6 (b) and 4-6 (d), a proper increase in the supersaturation rate will result in an increase of NRs growth. The higher reactant concentration will result in a higher degree of supersaturation as well as increase in the ZnO particle formation in the bulk solution, which competes with the ZnO NRs growth on the pre-seeded substrates. In the growth solution with a higher degree of supersaturation, the growth rate will be faster than the heterogeneous nucleation process of ZnO NRs growth, thereby suppressing the ZnO NRs growth on pre-seeded substrates. Thus, the reduced growth of ZnO NRs in the growth solution with a higher degree of supersaturation was observed.[16]

4.2.2.2 Influence of ammonia on the growth of ZnO nanorods

Ammonium hydroxide is frequently used as both hydroxide source and Zn source buffer reaction medium (ammonia react with zinc ions and form complex ($Zn(NH_3)_n^{2+}$, n=1, 2, 3 or 4). The experimental observation of the effect of the ammonia on the NRs growth is summarised in Figure 4-7 (a), with the other growth parameters fixed during the experiments (Table 3-2). With the increase of [NH_4^+] (in the low concentration range between 0 and 0.3 M) in the growth solution, growth rate of ZnO NRs was increased. With further increase of the [NH_4^+] up to 0.55 M, a decreased ZnO NRs growth rate was observed. However, in the calculated solubility curve shown in Figure 4-7 (b), with given values of pH and [Zn^{2+}], the supersaturation rate was decreased as the increase of [NH_4^+]. This improved ZnO NRs growth within a certain [NH_4^+] concentration range though the degree of supersaturation was decreased. This improvement is caused by the $Zn(NH_3)_n^{2+}$ buffer effect as well as suppression of ZnO particle formation in the bulk reaction solution.[17, 18] The [NH_4^+] introduced in the growth solution can react with zinc ions and form $Zn(NH_3)_n^{2+}$ complexes which can continuously supply zinc ions for supporting the NRs growth even under lower degree of supersaturation of the growth solution. Even though the degree of supersaturation was decreased, the NR growth was not suppressed but improved by increasing [NH_4^+] in a proper range (0 to 0.3 M). However, a high concentration of (NH_4^+) in the reaction solution under a set pH condition will reach to an excessively low degree of supersaturation, resulting in very slow growth of ZnO NRs. [17, 18]

In summary, we studied the relationship between the supersaturation condition and growth behaviour of the solution processed ZnO NRs. The experimental results provide a guide on the driving force of the ZnO NRs growth. Suppressed ZnO NRs growth on

the pre-seed substrates was observed when a critical degree of supersaturation is reached, which is caused by the competition growth of the ZnO between those on the pre-seeded surface and homogeneous nucleation growth in the bulk reaction solution. With a lower degree of the supersaturation and a proper value of [NH_4^+] applied, the homogeneous nucleation can be suppressed and ZnO growth on the pre-seed substrates can be improved.

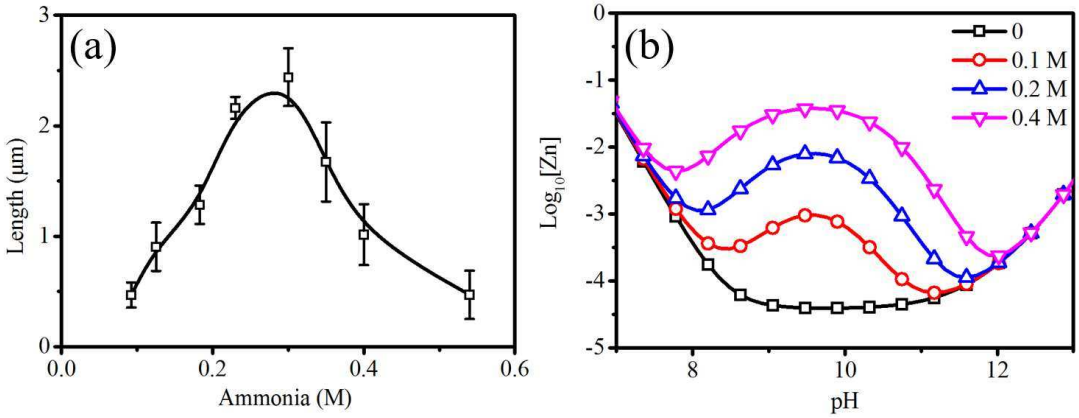

Figure 4-7 (a) [NH_4^+] influence on the ZnO NRs growth. All other parameters ($Zn(NO_3)_2$-20 mM, pH 10.5, 80 °C, 3 hrs) were fixed except variable [NH_4^+]; (b) a calculated solubility plot as a function of solution pH value with variable concentration of [NH_4^+].

4.2.2.3 Influence of additives on the growth of ZnO nanorods

The homogeneous nucleation process in the solution condition can be further suppressed by using a higher concentration of ammonium hydroxide, which can effectively decrease the degree of the supersaturation (i.e. by applying NH_4^+ for complex as demonstrated in above section). However, this will also suppress the ZnO NRs growth on the pre-seeded substrates. To solve this, PEI was introduced into the reaction solution in order to suppress the ZnO homogeneous nucleation in the bulk reaction solution. Additionally, the PEI is one additive which is normally used for reducing the growth along the radial direction, through its absorbing on the NRs wall side.

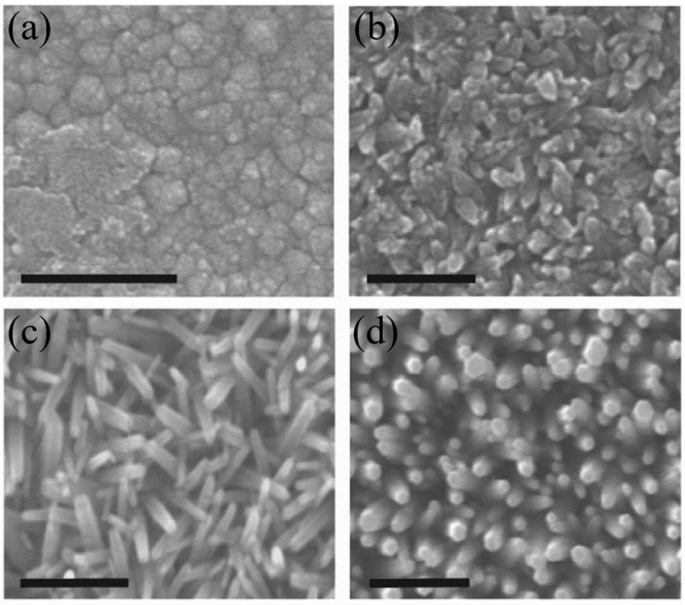

Figure 4-8 SEM images of ZnO NRs obtained with variable PEI added into the solution. (a) 50 mM, (b) 30 mM, (c) 15 mM and (d) 5 mM. All other parameters ($Zn(NO_3)_2$-25 mM, [NH_4^+]-25 mM, pH 10.5, 80 ^oC, 1.5 hrs) were fixed except variable PEI concentration The scale bars in the images are 500 nm.

The influence of the PEI was tested by varying the amount of additives added into the reaction solution (Table 3-2). The PEI concentration in the reaction solution was varied from 5 mM to 50 mM, and in this range, ZnO NRs growth was suppressed with the increase of the PEI addition (Figure 4-8 (a) to (d)). It can be noticed that, the alignment of the ZnO NRs deteriorated and the NRs stopped growing in the growth solution which contains the highest amount of PEI (50 mM). The large amount of the PEI in the solution will not only inhibit the crystal growth in the bulk solution, but also have chance to be absorbed on the surface of the ZnO seed layer on the target surface. Thus it may disturb its initial nucleation on the target surface, and stop growth of ZnO NRs. This influence on the ZnO NRs growth was reduced with the less PEI used in the solution as shown in Figure 4-8 (a) to (d).

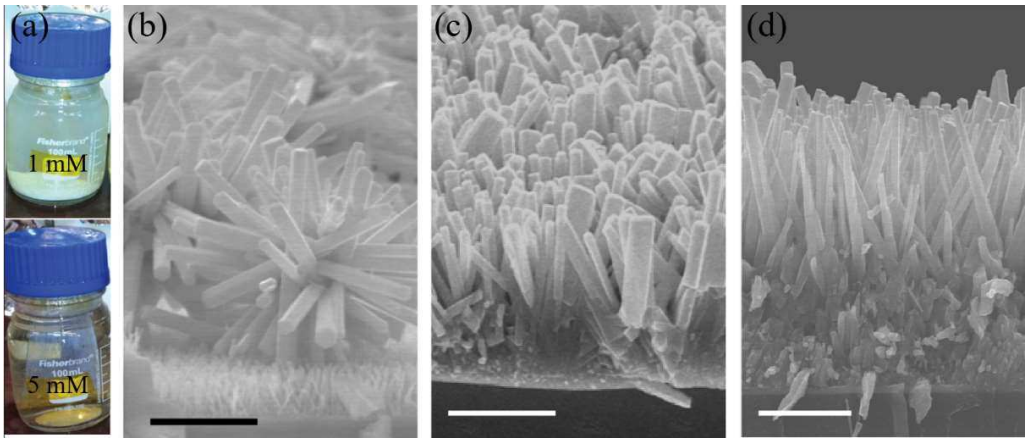

Figures 4-9 (a) Images of the reaction bottles after 6 hours reaction with different PEI amount added. Cross-section SEM images of ZnO NRs obtained with variable PEI added into the solution. (b) 1 mM, (c) 3 mM and (d) 5 mM. All other parameters ($Zn(NO_3)_2$-25 mM, [NH_4^+]-25 mM, pH 10.5, 80 °C, 6 hrs) were fixed except variable PEI concentration Scale bars in the SEM images are all 2.5 ı m.

To further investigate this effect, the low concentrations (1 mM to 5 mM) of the PEI was used (Table 3-2). The influence of the PEI on suppression of the ZnO particle formation in the bulk solution has been observed (shown in Figures 4-9 (a)). When the 5 mM PEI was added, a transparent solution without large amounts of white particles was obtained after reaction and up to 8 ı m ZnO NRs was obtained without adding new solutions during growth (in a single reaction bath). Figures 4-9 (b) to (d) show cross-section SEM images of the ZnO NRs obtained after 6 hours growth in a single reaction with different amount of PEI added in the solution. As demonstrated in Figures 4-9 (a) & (b), 1 mM PEI added in reaction solution is not sufficient to suppress the nucleation in the bulk reaction solution , thus resulting in formation of particles (as can be seen from the cloudy solution as well as large amount white particles on the bottom in Figures 4-9 (a)). As shown in Figures 4-9 (b), larger particles contaminate the ZnO NRs by adsorbing on the top of the NRs. Compared with samples prepared by increased amount of PEI (3 and 5 mM) used in the solution, the ZnO NRs obtained by using 1 mM PEI additive is the shortest (~ 1.5 ı m). With further increase of the PEI additive

concentration up to 5 mM, both the ZnO NRs length and aspect ratio are increased with more additives added inside the solution (as shown in Figures 4-9 (c) & (d)). In addition, when the 5 mM PEI was added into the solution, formation of large amount of ZnO particles in the bulk solution has been suppressed (as demonstrated in Figures 4-9 (a)). After the growth process, the solution is still transparent without a large amount of white particles at the bottom of the bottle.

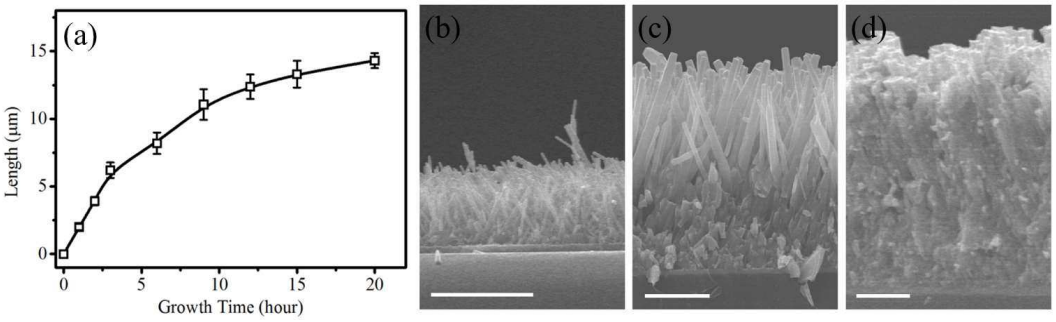

Figure 4-10 (a) ZnO NRs length plot as a function of growth duration at opmitized growth condition with 5 mM PEI added. All other parameters ($Zn(NO_3)_2$-25 mM, $[NH_4^+]$-25 mM, pH 10.5, 80 °C) were fixed except variable growth duration. Representive SEM images of ZnO NRs in varied length (b) 2.5 μm; (c) 8 μm and (d) 11 μm. Scale bars in the SEM images are 2.5 μm.

A proper amount of the PEI added in the reaction solution played a key role of the NRs growth. Generally, small amount of the PEI is used as an additive in ZnO NRs growth due to its selective absorption on the NR surface.[17, 18] During the growth, the PEI may preferentially cover on a given surface (i.e. $(0\bar{1}0)$ of the ZnO NRs, therefore increase their aspect ratio while the NRs keep growing along <001> direction.[17, 18] In addition, the PEI may play a disruption role for the initial ZnO nucleation in the bulk solution. The homogeneous distributed PEI molecular in the bulk solution could clad/wrap the initial formed ZnO crystals/particles, thus preventing their further growth.[17, 18]

Figure 4-11 shows normalized XRD patterns of the ZnO NRs fabricated using varied growth parameters (i.e. temperatures, growth durations, concentration and additives).

Obviously, all the images exhibit one high intensity diffraction (002) peak of wurtzite ZnO (ZnO PDF-card JCPDS No. 36-1451). All the as-prepared ZnO NRs possess a highly-preferred orientation with c-axis. This is mainly due to the c-plane is the thermodynamically favourable plane of ZnO wurtzite.[4, 19] No other impurity peaks were observed except low intensity ZnO (100) peaks, indicating that all the obtained ZnO NRs have a crystalline structure.

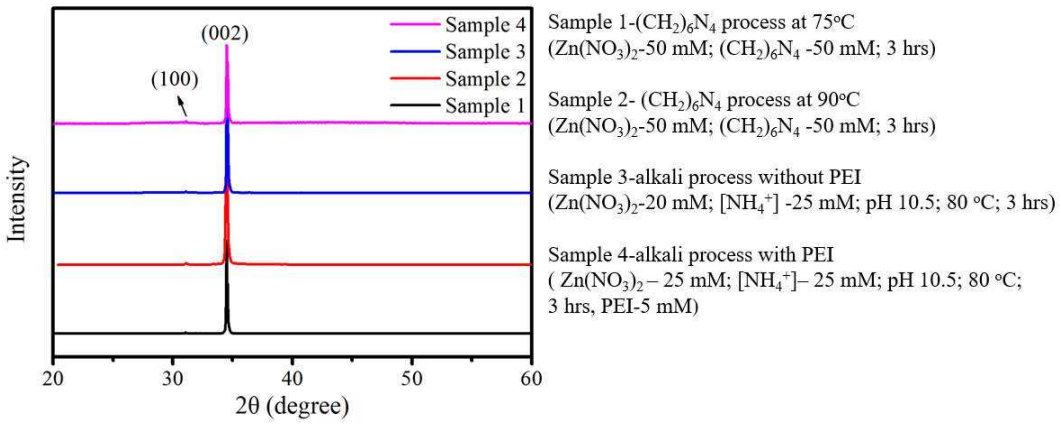

Figure 4-11 XRD patterns of ZnO NRs obtained by different aqueous solution reaction factors.

Figure 4-12 shows the PL results of ZnO NRs which had been measured at RT. All the ZnO NR samples showed one strong near band edge emission peak at ~385 nm and several weak peaks with visible range light emission at around 423 nm, 450 nm and 485 nm. The PL spectrum of the pure ZnO nanostructures is composed of two parts: the yellow-green light emission zone (i.e. the visible region light emitting) and ultraviolet light emission (i.e. the near band edge emission).[20, 21] Yellow-green light emitting peak is generally much wider, whereas the near band edge peak is relatively sharp. Specific luminescence mechanism for these two regions are not clear, but most of researchers agreed that the ultraviolet light emitting is mainly due to exciton recombination and inter band transitions, and yellow-green light emitting is mainly caused by various intrinsic defects of ZnO samples (i.e. the oxygen vacancies (V_o), the

substitution impurity (O_{Zn}/Zn_O), the interstitial oxygen (O_i), the zinc vacancy (V_{Zn}) and the interstitial zinc (Zn_i).[20-22] The strong near band edge emission peaks at caused by the band edge emission show a little differences in their intensity, but no clear peak shift was observed. This indicates that there is no clear optical band gap changes of these samples (Sample 1 to Sample 4). The intensity changes may be caused by the morphology variations. The varied surface and/or morphology may lead to different proportions of emissions from the related surfaces (which are associated to band edge emission).[20, 21]

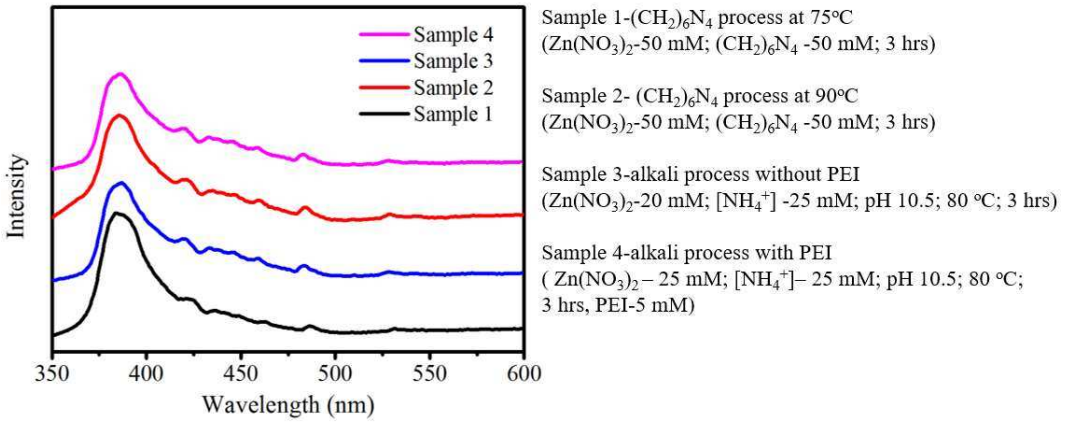

Figure 4-12 Room temperature PL spectrum of different ZnO NRs samples obtained by different aqueous solution reaction factors

4.3 Summary

In this chapter, influences of various growth parameters (i.e. type of reactants, concentration of reactants, pH, temperature, growth duration and additive) on the morphology and growth of ZnO NRs in the solution method were investigated and discussed. We found the temperature, concentration and duration of the reaction influence on the growth and morphology control in the reaction solution only containing $Zn(NO_3)_2$ and $(CH_2)_6N_4$, which demonstrated a good controllable growth of short ZnO NRs (0-4 ı m). Ammonia involved in the alkali aqueous solution with the

PEI used as additives could be used for achieving longer ZnO NRs (0-15 ı m). Using both ammonia and PEI can suppress the ZnO formation in the bulk solution which helps the ZnO NRs growth on the pre-seeded substrates. The observation of the experimental results also indicated that the calculated solubility can be used as an indicator for supersaturation which has a strong relationship with ZnO NRs growth. Crystalline and optical properties of the as-prepared ZnO NRs samples by variable reaction factors indicated all the ZnO NRs samples are single crystalline with highly oriented wurtzite structure.

Reference

1. Baxter, J.B. and E.S. Aydil, Nanowire-based dye-sensitized solar cells. Applied Physics Letters, 2005. 86(5): p. 053114.
2. Baxter, J.B., A.M. Walker, K.v. Ommering, and E.S. Aydil, Synthesis and characterization of ZnO nanowires and their integration into dye-sensitized solar cells. Nanotechnology, 2006. 17(11): p. S304.
3. Anta, J.A., E. Guill¶n, and R. Tena-Zaera, ZnO-Based Dye-Sensitized Solar Cells. The Journal of Physical Chemistry C, 2012. 116(21): p. 11413-11425.
4. Xu, S. and Z. Wang, One-dimensional ZnO nanostructures: Solution growth and functional properties. Nano Research, 2011. 4(11): p. 1013-1098.
5. Wang, J.X., X.W. Sun, Y. Yang, H. Huang, Y.C. Lee, O.K. Tan, and L. Vayssieres, Hydrothermally grown oriented ZnO nanorod arrays for gas sensing applications. Nanotechnology, 2006. 17(19): p. 4995.
6. Kreye, M., B. Postels, H.H. Wehmann, D. Fuhrmann, A. Hangleiter, and A. Waag, Aqueous chemical growth and patterning of ZnO nanopillars on different substrate materials. physica status solidi (c), 2006. 3(4): p. 992-996.
7. Vayssieres, L., Growth of Arrayed Nanorods and Nanowires of ZnO from Aqueous Solutions. Advanced Materials, 2003. 15(5): p. 464-466.
8. Zang, J., C.M. Li, X. Cui, J. Wang, X. Sun, H. Dong, and C.Q. Sun, Tailoring Zinc Oxide Nanowires for High Performance Amperometric Glucose Sensor. Electroanalysis, 2007. 19(9): p. 1008-1014.
9. Xu, S. and Z.L. Wang, One-dimensional ZnO nanostructures: Solution growth and functional properties. Nano Research, 2011. 4(11): p. 1013-1098.
10. McPeak, K.M., T.P. Le, N.G. Britton, Z.S. Nickolov, Y.A. Elabd, and J.B. Baxter, Chemical Bath Deposition of ZnO Nanowires at Near-Neutral pH Conditions without Hexamethylenetetramine (HMTA): Understanding the Role of HMTA in ZnO Nanowire Growth. Langmuir, 2011. 27(7): p. 3672-3677.
11. Demianets, L.N., D.V. Kostomarov, I.P. Kuz˘mina, and S.V. Pushko, Mechanism of growth of ZnO single crystals from hydrothermal alkali solutions. Crystallography Reports (Translation of Kristallografiya), 2002. 47(1): p. S86-S98.
12. Strom, J.G., Jr. and H.W. Jun, Kinetics of hydrolysis of methenamine. Journal of Pharmaceutical Sciences, 1980. 69(11): p. 1261-1263.
13. Yang, P., H. Yan, S. Mao, R. Russo, J. Johnson, R. Saykally, N. Morris, J. Pham, R. He, and H.J. Choi, Controlled Growth of ZnO Nanowires and Their Optical Properties. Advanced Functional Materials, 2002. 12(5): p. 323-331.
14. Tada, H., Decomposition Reaction of Hexamine by Acid. Journal of the American Chemical Society, 1960. 82(2): p. 255-263.
15. Tong, Y., Y. Liu, L. Dong, D. Zhao, J. Zhang, Y. Lu, D. Shen, and X. Fan, Growth of ZnO Nanostructures with Different Morphologies by Using Hydrothermal Technique. The Journal of Physical Chemistry B, 2006. 110(41): p. 20263-20267.
16. Joo, J., B.Y. Chow, M. Prakash, E.S. Boyden, and J.M. Jacobson, Face-selective electrostatic control of hydrothermal zinc oxide nanowire synthesis. Nat Mater, 2011. 10(8): p. 596-601.
17. Xu, C., P. Shin, L. Cao, and D. Gao, Preferential Growth of Long ZnO Nanowire Array and Its Application in Dye-Sensitized Solar Cells. The Journal of Physical Chemistry C, 2009. 114(1): p. 125-129.
18. Wu, W., G. Hu, S. Cui, Y. Zhou, and H. Wu, Epitaxy of Vertical ZnO Nanorod Arrays on Highly (001)-Oriented ZnO Seed Monolayer by a Hydrothermal Route. Crystal Growth & Design, 2008. 8(11): p. 4014-4020.
19. Li, Q., V. Kumar, Y. Li, H. Zhang, T.J. Marks, and R.P.H. Chang, Fabrication of ZnO Nanorods and Nanotubes in Aqueous Solutions. Chemistry of Materials, 2005. 17(5): p. 1001-1006.

20. Djurišić, A.B. and Y.H. Leung, Optical Properties of ZnO Nanostructures. Small, 2006. 2(8-9): p. 944-961.
21. Shalish, I., H. Temkin, and V. Narayanamurti, Size-dependent surface luminescence in ZnO nanowires. Physical Review B, 2004. 69(24): p. 245401.
22. Zhang X. T., X. Z. Y., Zhang W. L., Gao H., Wang Y. X., Liu Y. C., Zhang J. Y., Xu W., A study on photoluminescence characterization of high-quality nanocrystalline ZnO thin films. Acta Physica Sinica, 2003. 52(3): p. 740-744.

Chapter 5 Low temperature synthesis of crystallised TiO_2 thin films

5.1 Introduction

As discussed in Chapter 2, TiO_2 for the DSSC application has been extensively studied since 1991 and it has been used as the first high efficiency DSSC photoanode material.[1] TiO_2 presents its advantages including good chemical bonding with dyes, good stability in acid dye socking process and good photo-electron acceptor after dye bonding and good long term stability in DSSC working cycles. Its band structure matches well with most available dyes.[2, 3] In addition, crystallised anatase TiO_2 generally allows a better dye bonding and photo-electron transportation efficiency is much higher than those of the amorphous TiO_2 as well as other TiO_2 crystal phase.[4-6] It is ideal to be used as a modification layer on the top of ZnO nanomaterial to improve the stability of the ZnO.

However, to achieve anatase TiO_2, a strong acid reaction environment and high temperature (400 to 500 ^oC) process are normally required.[6-8] For the standard preparation processes of the mesoporous TiO_2 photoanode preparation processes, an annealing process is commonly used for removing organic additives and/or crystallisation of amorphous TiO_2.[9] High temperature or strong acid required processes limit the choices of substrates (restricting the usage of temperature and/or pH sensitive substrates), reactants as well as combination of other materials (i.e. strong acid reaction environment will etch ZnO). Various techniques or methods have been studied for achieving either low temperature or mild reaction environment processes to synthesise a crystallised TiO_2 modification layer. However, limited success was achieved so far.[7, 8, 10] There are still challenges on how to achieve a good crystallised TiO_2 modification

layer with a simple set-up and a cost-effective way without using complicated techniques, a strong acid reaction environment or a high temperature process.

Anatase TiO_2 layer can be obtained without the need of high temperature processing, i.e. using a plasma ion assisted deposition (PIAD).[11, 12] This is possible because the energy of the deposited adatoms with ion assistance increases the probability of lattice relaxation and transitions from a metastable state to a stable state.[12-14] However, the PIAD process is rarely applied to prepare DSSC photoanodes as it is considered that the resultant increased density and reduction in surface roughness could reduce the surface porosity and internal areas, thus reducing the dye loading abilities.[12]

The major objective of this chapter therefore is to develop a low-temperature process for preparing the anatase TiO_2 layer which can be used to assemble the ZnO/TiO_2 core-shell structure. Particularly, optimisation of the low temperature process for fabrication of anatase TiO_2 will be discussed. Effects of process gas, deposition rate, plasma and plasma energy on structure and properties of as-prepared TiO_2 film will be investigated.

5.2 Results and discussions

The effects of O_2 gas flow rate and plasma-enhancing effects on structure and functional properties of the TiO_2 films will be firstly studied. Table 3-4 (in section 3.2.2) summarises all the experimental conditions.

5.2.1 Structure and morphology

Figure 5-1 shows the XRD patterns of the films prepared with and without plasma enhancement, respectively. As shown in Figure 5-1 (a), the TiO_2 Elms obtained under different gas flow conditions without plasma treatment are all amorphous, whereas Figure 5-1 (b) shows that the Elms obtained with plasma enhancement show several

peaks. Comparing with JC PDF #21-1272 marked as small bar in Figure 5-1 (b)), the observed peaks correspond to anatase phases of (101), (004), (200), (105) and (211). No other TiO_2 phase peaks (i.e. rutile or brookite) were observed. It can also be noticed that peak intensity of TiO_2 anatase increases slightly with the increase of the current density (from sample T10P13 to T10P17). With further increase of current density (from samples T10P17 to T10P21), there is no observation of increased intensity. Detailed data have been listed in Table 5-1 which shows the variation of the diffraction angles and Full Width at Half Maximum (FWHM) of the anatase TiO_2 (101) diffraction peaks. It is observed that the (101) peak shifts towards to lower angle as the plasma current densities increases. Additionally, the FWHM value of the (101) peak shows a similar decreased trend. These indicate that an increase in the plasma current density leads to an increase in the crystal sizes.[11] The changes of temperature during the synthesis were recorded by a temperature sensor beside sample holder. The temperature was changed from 19 ºC to 60ě5 ºC during deposition. This confirmed that the enhancement in crystallinity in this synthesis is not caused by thermal heating effects but mainly caused by enhanced adatoms movements by plasma treatment.[11, 12]

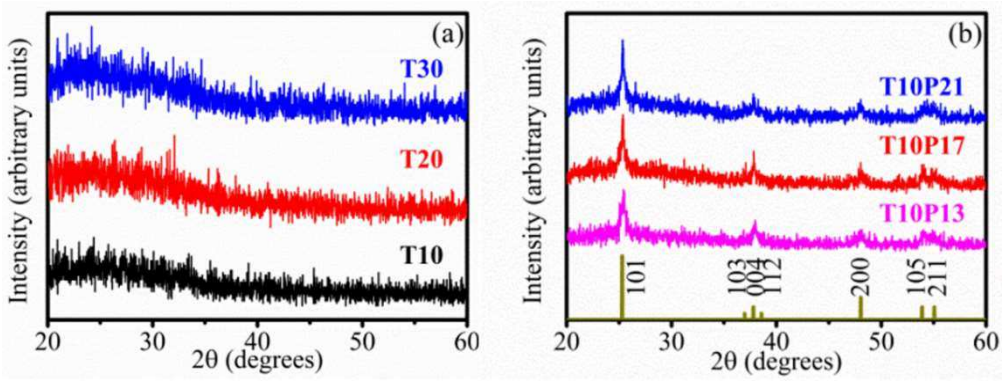

Figure 5-1 XRD patterns of the as-prepared TiO_2 samples. (a) TiO_2 deposited with different oxygen flow rates without plasma enhancement (T10-10 sccm; T20-20 sccm; T30-30 sccm); (b) deposited under 10 sccm O_2 flow rate with different plasma current densities.(T10P13-0.63 mA/cm^{-2}; T10P17-0.78 mA/cm^{-2}; T10P21-0.93 mA/cm^{-2}).[12]

Table 5-1 XRD analysis results of the TiO_2 films prepared with different plasma current densities.[12]

Sample	Current density (mA/cm^2)	2θ (deg)	FWHM (deg)	Grain Size (nm)
T10P13	0.63	25.48	1.10	7.4
T10P17	0.78	25.34	0.63	13.1
T10P21	0.93	25.31	0.61	13.4

Figure 5-2 shows representative AFM images of the TiO_2 films as functions of different deposited conditions (variations of oxygen flow rates, with and without plasma) with their corresponding height scale bars. Based on the AFM analysis, it can be observed that the resultant TiO_2 film has an increased root mean squared (RMS) roughness when the O_2 flow rate was increased from 10 sccm (T10) to 30 sccm (T30). As plotted in Figure 5-3 (a), the values of average RMS roughness are increased from ~1.5 nm to ~2.1 nm. Those films obtained with plasma enhancement during deposition at a fixed O_2 flow rate of 10 sccm show a sharply decrease in the average RMS roughness. Films obtained under O_2 flow rate of 10 sccm has an average RMS roughness of ~1.5 nm, whereas those films obtained with plasma enhancement have relatively low RMS roughness values (~0.725 nm). Plasma current density (in the range of our experiment setting) has little effect on the surface roughness compared to those from the gas flow rate. As shown in Figure 5-3 (a), with the increase of the plasma current density (0.63 to 0.93 mA/cm^2), the roughness changes slightly from 0.72 to 0.73 nm, indicating that significant re-sputtering effect did not take place.[15] These conclusions can also be confirmed from the AFM and SEM images as shown in Figure 5-2 and Figure 5-3 (b) to (d). For the samples deposited without plasma enhancement, the increased O_2 flow rate results in a rougher surface (Figure 5-2 (T10 to T30) and Figure 5-3 (e) to (g). It can be noticed that cracks were observed occasionally on the samples deposited at

higher O_2 flow rates which are probably due to large film stress and porous structures in the films. In the case of the films obtained with plasma enhancement, there is no significant difference in surface morphology as shown in Figure 5-2 (P13 to P21) and Figure 5-3 (b) to (d).[12] Only slightly increased surface roughness was observed with the increase of the plasma current density.[12]

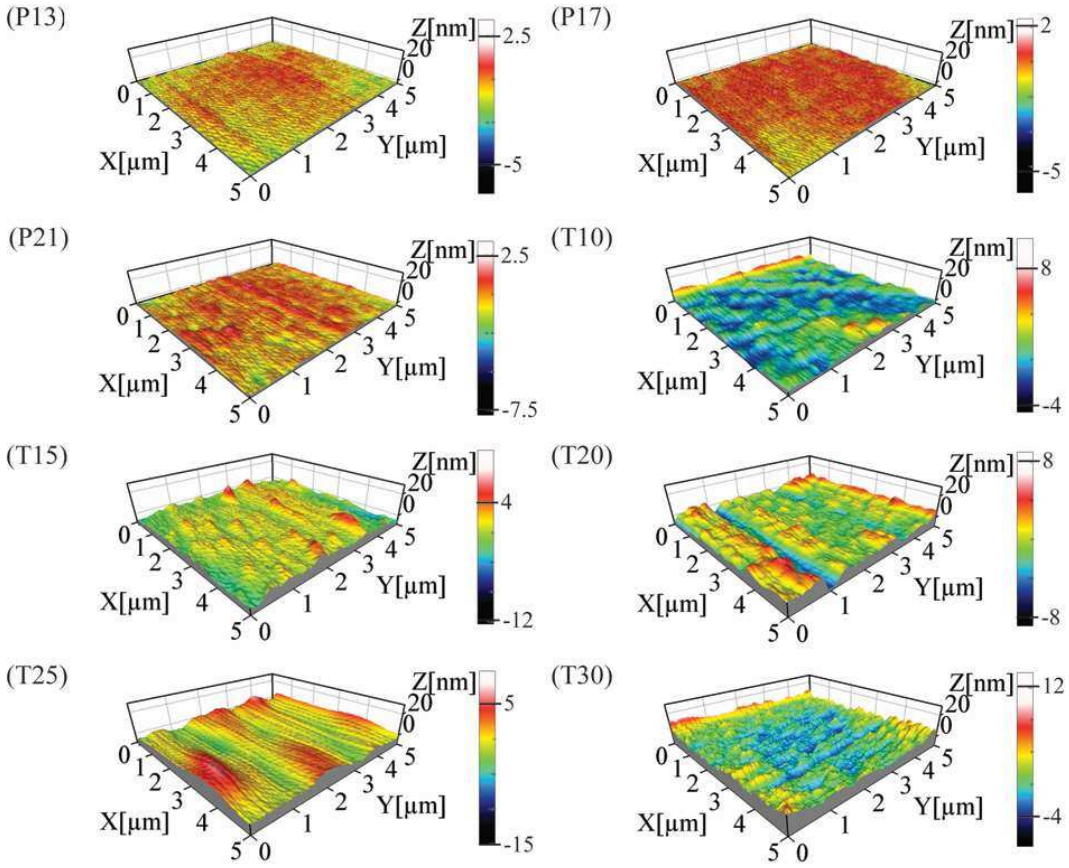

Figure 5-2 Representative AFM images of TiO_2 film as a function of different deposited conditions with their corresponding height scale bar, which is consistent with the sample. (i.e. P13 means T10P13; P17 means T10P17; P21 means T10P21).[12]

5.2.2 Physical properties of as-prepared films

Refractive indexes (n) of the deposited films are shown in Figure 5-4 (a) and (b) and these are extracted from T-R spectra results (representative images have been listed in Figure 5-4 (c)). In Figure 5-4 (a) and (b), the plot shows the refractive index as a function of wavelengths for different samples. With the decrease of O_2 gas flow rate,

the resultant samples show increases of n values in the whole wavelength range (from 350-800 nm).[12]

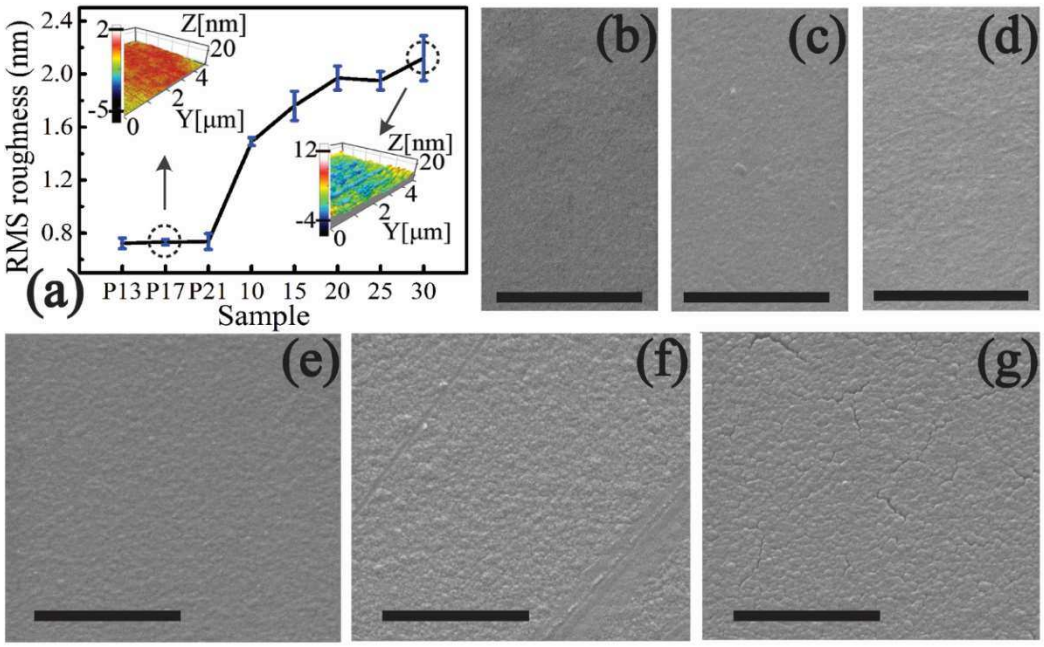

Figure 5-3 RMS roughness values (a) of TiO_2 film as a function of different deposited conditions with their corresponding SEM images (b) T10P13; (c) T10P17; (d) T10P21; (e) T10; (f) T20, and (g) T30. Scale bars in SEM images are 1 ı m.[12]

The n values of the films at a wavelength of 550 nm are increase from 1.8 to 2.1 with the oxygen flow rate is decreased from 30 sccm (T30) to 10 sccm (T10).[12] This decreased trend of n values of the films prepared in different oxygen flow rates is generally attributed to the variation of the packing density, which can be explained using the effective medium formula:[16]

侍嗆 *r* 侍㓗喵媼:嘗 *r* 嫸㖊 (Eq. 5-1)

where n_s and n_v are the refractive indexes of the solid part and voids, respectively.[12]

The packing density of the film *r* is dependent on the evaporant or adatom energy. As the O_2 flow rates and hence partial pressures are increased, the mean free path is shortened and the kinetic energy of the adatoms is dissipated due to molecular collisions

within the evaporant.[12, 17] This effect can be simplified to the images in Figure 5-5 for a better understanding. With the increased O_2 flow during the deposition, the evaporated adatoms do not arrive to substrates from a unique angle any more but chaotically arrive from random directions. Therefore, the condensing adatoms have less kinetic energy to promote surface diffusion, thus a higher O_2 gas flow rate generally results in a lower film packing density.[12]

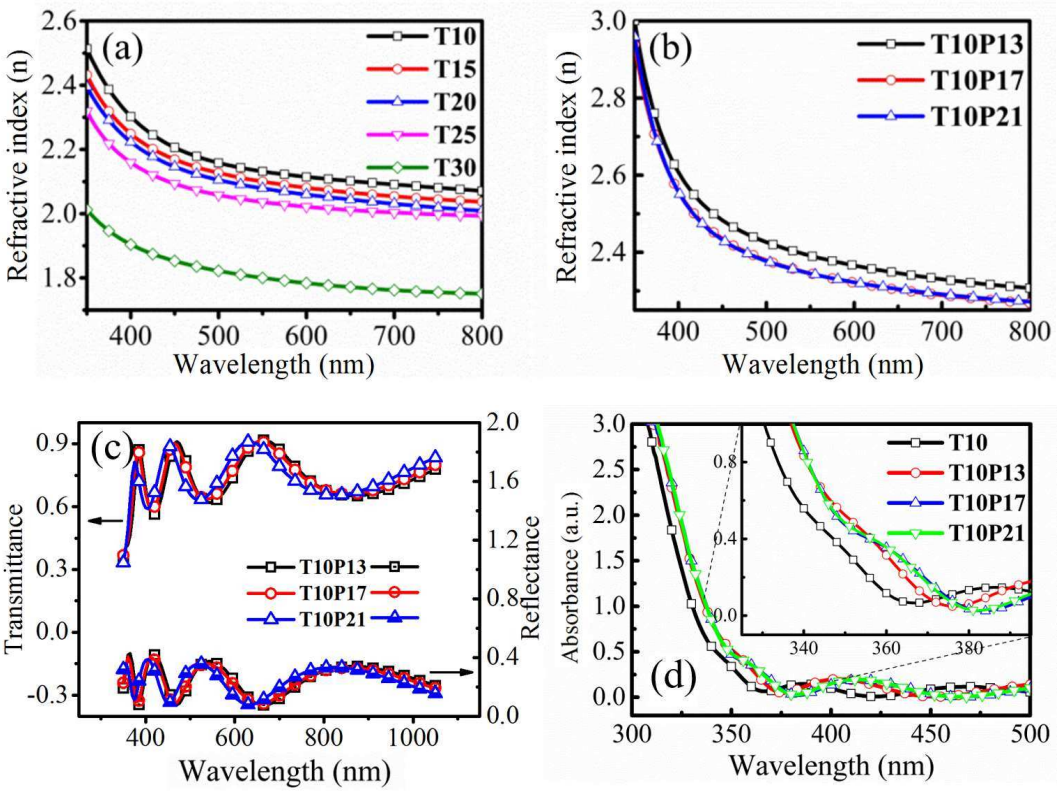

Figure 5-4 Refractive indices of thin films (a) deposited under different O_2 flow rates without plasma; (b) deposited under 10 sccm O_2 gas flow rate but with different plasma current densities; (c) representative T-R spectra results for tested films (d) UV ¯vis absorption spectra of samples prepared with/without plasma. Inset is correlative enlarged spectra.[12]

For the films prepared with plasma, the refractive index is increased from 2.39 to 2.45 (As shown in Figure 5-4 (b)) with the plasma current density increased from 0.63 to 0.78 mA/cm^{-2}, but there is no further increase up to the plasma current density of 0.93 mA/cm^{-2}.[12] In the PIAD process, plasma assistance during deposition provides enough energy to enhance the packing density of the deposited films, thus increasing the

refractive index.[12] However, if the plasma energy is above a critical value, it could cause re-sputtering or bombardment effects, thus affecting the packing density of the film, which can explain the plateau effect at a plasma current density of 0.78mA cm^{-2}.[12] Further increasing in the plasma current density will not change the densities of the films as well as refractive index.[12]

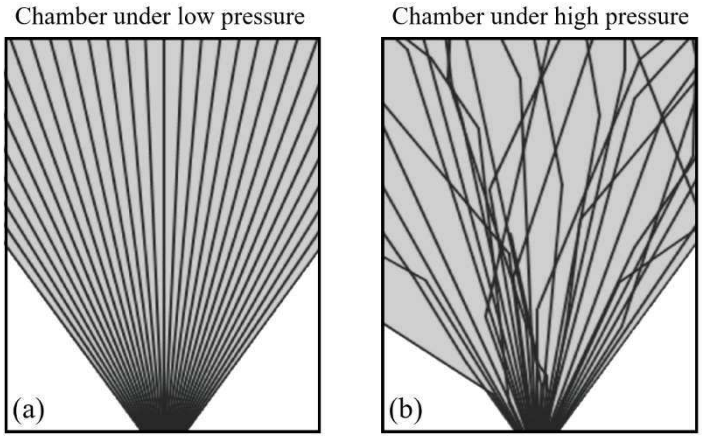

Figure 5-5 Diagrammatic sketch of the evaporated species (material) path under different vacuum conditions: chamber under (a) low pressure and (b) high pressure.[17]

The UV-Vis absorption spectra of TiO_2 films without/with different plasma conditions are shown in Figure 5-4 (d). With plasma assistance during deposition, a slightly higher absorption and a shift of the absorption edge from UV towards the visible range are observed in the inset Figure 5-4 (d). It can be noticed that, for sample T10P17 and T10P21, there is no significant differences of absorption edge which also show a plateau at the plasma current density of 0.78 mA cm^{-2} (T10P17). This is mainly attributed to a combined effect of reduction of O_2 vacancies and densification in the film microstructure, caused by the plasma enhancement during the deposition.[12, 18]

Hardness and Young's modulus of TiO_2 films have been measured and are summarised in Figure 5-6.[12] In Figure 5-6 (a), Young's modulus and hardness of the samples without plasma enhancement are plotted as a function of deposition gas flow rate. A

decreasing trend of both Young's modulus and hardness with the increasing of O_2 gas flow rate can be observed.[12] This observation further confirms the formation of denser microstructures and/or lower levels of porosity in the resultant samples prepared using O_2 gas flow rate at 10 sccm.[12, 19, 20] In the case of plasma assisted samples prepared using the same O_2 gas flow rate at 10 sccm, it can be seen the enhanced Young's modulus and hardness readings compared to those without plasma treatment, indicating formation of denser microstructures.[12, 19, 20] However, samples prepared under different plasma current densities did not show much difference, which agrees the previous results on surface morphology as well as structures.[12]

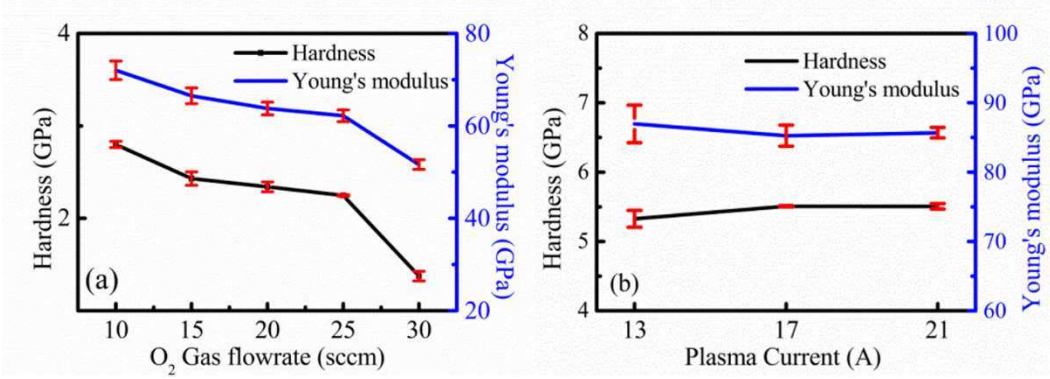

Figure 5-6 Hardness and Young's modulus of TiO_2 films (a) deposited under different O_2 flow rates without plasma treatment; (b) deposited under 10 sccm O_2 flow rate but with different plasma current densities (13A-0.63 mA/cm^2,17A-0.78 mA/cm^2,21A-0.93 mA/cm^2).[12]

5.2.3 Stability and chemical properties of as-prepared films

The stability and chemical activity in the solution environment of as-prepared films were evaluated by photocatalytic study, which strongly depended on the material surface chemical activity properties. Degradation of aqueous solutions of methylene blue (MB) was used to measure the photocatalytic activity of the obtained TiO_2 samples.[12] Samples were immersed in the MB solution for 30 minutes in a dark environment to establish an adsorption equilibrium. A UV-lamp with a power of 4 W

and a peak wavelength of 365 nm was used to activate films for degrading the MB solution.[12] The concentrations of the MB solution were determined using a UV ¯Vis spectrophotometer by comparing the adsorption peak at 665 nm (the adsorption peak of the MB).[12] To keep the testing temperature constant, a water heat sink was used to put the MB container inside.

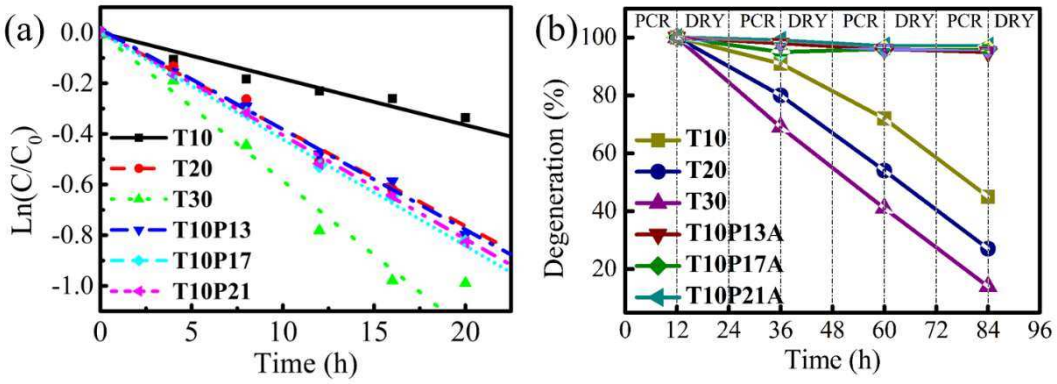

Figure 5-7 (a) Time-course variation of C/C_0 for the methylene blue solution for the TiO_2 films prepared with and without plasma treatment. Stability of the TiO_2 photocatalysts prepared with and without plasma treatment.(PCR step: photocatalytic reaction using as prepared TiO_2 films; DRY step: samples taken out from MB solution and kept in dark at room temperature.)[12]

For the photocatalytic analysis, the Langmuir-Hinshelwood pseudo-first-order kinetics model was used for low MB concentrations:[12, 21]

$$\ln\left(\frac{C_0}{C}\right) = k(t_2 - t_1) = \ln\left(\frac{C_a}{C}\right) \qquad \text{(Eq. 5-2)}$$

where C_0 is the original MB concentration, C is the concentration at time (t), k is the pseudo-first-order rate constant, C_a is the concentration after adsorption. Figure 5-7 (a) shows the evolution of concentration of the MB solution, indicated by changes of values of $\ln(C/C_0)$ plotted as a function of exposure time.[12]

The reaction rates of photocatalytic activity obtained by fitting the data in Figure 5-7 using Eq. 5-2.[12]. The obtained results are summarised in Table 5-2. The obtained k values indicate the reaction rate of photocatalytic activity (it also can be called as

degradation rate of the MB). From sample T10 to sample T30, the reaction rate of photocatalytic activity increased (k values decreased). This improved photocatalytic activity from sample T10 to T30 is mainly due to the increased roughness and porosity of the films. The increased surface roughness can provide more catalytic reaction sites and enhance absorbance of reactive species.[6, 12] Sample of T10 has the lowest surface roughness of all the amorphous samples, and hence the lowest degradation rate of the MB. With the same O_2 flow rate, samples deposited with plasma assistance have a higher slope indicating a better photocatalytic efficiency due to the formation of anatase phase as proven from the XRD result.[12] The increased photocatalytic activity can be explained by formation of anatase films with a higher crystallised state and fewer defects or recombination centres for the excited hole-electron pairs.[10, 12, 22] Unlike the optical and mechanical properties which have peaked values at the plasma current density of 0.78 mA/cm^{-2}, the photocatalytic properties have not been greatly improved with further increase of plasma current density.[12]

Table 5-2 Pseudo-first-order kinetics for photocatalytic degradation of MB for the TiO_2 samples.[12]

Sample	k Value	Standard Error
T10	-0.016	0.00148
T20	-0.042	0.002
T30	-0.055	0.00572
T10P13	-0.039	0.00139
T10P17	-0.041	0.00115
T10P21	-0.041	8.99E-4

The stability of the TiO_2 films in chemical activity was determined by cyclically immersing the TiO_2 samples into the MB solution to degrade them for 12 hours, followed by cleaning and then stabilising of these samples in a dark environment at

room temperature for 12 hours, before re-immersing into a fresh MB solution.[12] Five cycles were performed, and the degeneration (D) as a percentage was calculated using Eq.5-3

$$D\ (\%) = [(C_0 - C_N)/(C_0 - C_1)] \times 100\% \qquad \text{(Eq.5-3)}$$

where C_0 is the concentration of the fresh MB solution, C_1 is residual concentration of the MB solution after the first cycle, and C_N is the residual concentration of the MB solution after the N_{th} cycle.[12]

The stability test results are shown in Figure 5-7 (b), with normalised degeneration readings as a function of number of cycles.[12] After the first photocatalytic cycle, the photocatalytic performance of samples prepared without plasma assistance degraded significantly.[12] The PIAD films still maintain the degeneration rate as high as 97% after 4 cycles. Clearly, the excellent photocatalysts cycling performance and stability make the PIAD film a promising candidate for modification layer applications as well as low temperature substrates such as flexible thin membranes, low cost plastics or textured substrates.[12]

5.3 Summary

The low temperature PIAD process results in the formation of anatase phase, increases both hardness and Young's modulus, and most importantly, increases the photocatalytic stability and efficiency though film surface roughness reduced, compared with those without plasma assistance.[12] The formation of anatase phase after using the plasma assistance is mainly responsible for the improvement in the photocatalytic performance. The improvement in the film microstructure and density is responsible for the increased refractive indexes and hardness.[12] The good optical properties, and improved efficiency and stability of the photocatalytic performance, as well as the nature of the

low temperature processing after applying plasma assistance verifies its advantages in the photocatalytic applications. Therefore, in the next chapter, we will use this PIAD process to make the solar cell devices.[12]

Reference

1. O'Regan, B. and M. Gratzel, A low-cost, high-efficiency solar cell based on dye-sensitized colloidal TiO_2 films. Nature, 1991. 353(6346): p. 737-740.
2. Ghicov, A. and P. Schmuki, Self-ordering electrochemistry: a review on growth and functionality of TiO_2 nanotubes and other self-aligned MO_x structures. Chemical Communications, 2009(20): p. 2791-2808.
3. Li, C. J., J. N. Wang, B. Wang, J.R. Gong, and Z. Lin, A novel magnetically separable $TiO_2/CoFe_2O_4$ nanofiber with high photocatalytic activity under UV¯vis light. Materials Research Bulletin, 2012. 47(2): p. 333-337.
4. Law, M., L.E. Greene, A. Radenovic, T. Kuykendall, J. Liphardt, and P. Yang, ZnOБAl_2O_3 and ZnOБTiO_2 CoreБShell Nanowire Dye-Sensitized Solar Cells. The Journal of Physical Chemistry B, 2006. 110(45): p. 22652-22663.
5. Nakata, K. and A. Fujishima, TiO_2 photocatalysis: Design and applications. Journal of Photochemistry and Photobiology C: Photochemistry Reviews, 2012. 13(3): p. 169-189.
6. Crossland, E.J.W., N. Noel, V. Sivaram, T. Leijtens, J.A. Alexander-Webber, and H.J. Snaith, Mesoporous TiO_2 single crystals delivering enhanced mobility and optoelectronic device performance. Nature, 2013. 495(7440): p. 215-219.
7. Yao, J.K., H.L. Huang, J.Y. Ma, Y.X. Jin, Y.A. Zhao, J.D. Shao, H.B. He, K. Yi, Z.X. Fan, F. Zhang, and Z.Y. Wu, High refractive index TiO_2 film deposited by electron beam evaporation. Surface Engineering, 2009. 25(3): p. 257-260.
8. Yeo, K.S., S. Nakao, Y. Hirose, T. Hasegawa, and Y. Matsuo, Application of sputter-deposited amorphous and anatase TiO_2 as electron-collecting layers in inverted organic photovoltaics. Organic Electronics, 2013. 14(7): p. 1715-1719.
9. Gong, X.Q., A. Selloni, M. Batzill, and U. Diebold, Steps on anatase TiO2(101). Nature Materials, 2006. 5(8): p. 665-670.
10. Yanagisawa, K. and J. Ovenstone, Crystallization of Anatase from Amorphous Titania Using the Hydrothermal Technique: Effects of Starting Material and Temperature. The Journal of Physical Chemistry B, 1999. 103(37): p. 7781-7787.
11. Oliver, J.B., P. Kupinski, A.L. Rigatti, A.W. Schmid, J.C. Lambropoulos, S. Papernov, A. Kozlov, J. Spaulding, D. Sadowski, Z.R. Chrzan, R.D. Hand, D.R. Gibson, I. Brinkley, and F. Placido, Large-aperture plasma-assisted deposition of inertial confinement fusion laser coatings. Applied Optics, 2011. 50(9): p. C19-C26.
12. Zhao, C., D. Child, D. Gibson, E. Placido, and R.Y.Q. Fu, TiO_2 films prepared using plasma ion assisted deposition for photocatalytic application. Materials Research Bulletin, 2014. 60: p. 890-894.
13. Nickel, N.H. and I. Sieber, Influence of oxygen plasma treatments on the structural properties of c-Si. Applied Physics Letters, 1998. 72(21): p. 2683-2685.
14. Yamada, I., J. Matsuo, N. Toyoda, and A. Kirkpatrick, Materials processing by gas cluster ion beams. Materials Science & Engineering R-Reports, 2001. 34(6): p. 231-295.
15. Fujiwara, Y., N. Toyoda, K. Mochiji, T. Mitamura, and I. Yamada, Reduction of surface roughness by Ta_2O_5 film formation with O_2 cluster ion assisted deposition. Nuclear Instruments and Methods in Physics Research Section B: Beam Interactions with Materials and Atoms, 2003. 206(0): p. 870-874.
16. Macleod, H.A., Structure related optical properties of thin films. Journal of Vacuum Science & Technology A: Vacuum, Surfaces, and Films, 1986. 4(3): p. 418-422.
17. Mergel, D. and M. Jerman, Density and refractive index of thin evaporated films. Chin. Opt. Lett., 2010. 8(s1): p. 67-72.
18. Nakamura, I., N. Negishi, S. Kutsuna, T. Ihara, S. Sugihara, and K. Takeuchi, Role of oxygen vacancy in the plasma-treated TiO_2 photocatalyst with visible light activity for NO removal. Journal of Molecular Catalysis A: Chemical, 2000. 161(1¯2): p. 205-212.

19. Borgese, L., E. Bontempi, M. Gelfi, L.E. Depero, P. Goudeau, G. Geandier, and D. Thiaudi·re, Microstructure and elastic properties of atomic layer deposited TiO_2 anatase thin films. Acta Materialia, 2011. 59(7): p. 2891-2900.
20. Lasko, G., Z. Burghard, J. Bill, I. Sch±fer, U. Weber, and S. Schmauder, Simulation of Mechanical Properties of Bio-Inspired TiO_2/PE Nanocomposites. Advanced Engineering Materials, 2013. 15(10): p. 908-920.
21. Li, F. t., X. j. Wang, Y. Zhao, J. x. Liu, Y. j. Hao, R. h. Liu, and D. s. Zhao, Ionic-liquid-assisted synthesis of high-visible-light-activated N¯B¯F-tri-doped mesoporous TiO_2 via a microwave route. Applied Catalysis B: Environmental, 2014. 144(0): p. 442-453.
22. Ohtani, B., Y. Ogawa, and S. i. Nishimoto, Photocatalytic Activity of Amorphous–Anatase Mixture of Titanium(IV) Oxide Particles Suspended in Aqueous Solutions. The Journal of Physical Chemistry B, 1997. 101(19): p. 3746-3752.

Chapter 6 Synthesis of ZnO/TiO_2 hybrid core-shell nanostructures for DSSCs applications

6.1 Introduction

ZnO has been considered as one of the most promising wide bandgap semiconductor for photoanode use in DSSCs, due to its similar band-gap values compared to that of TiO_2 but with a higher bulk electron mobility (three orders of magnitude higher than that of TiO_2).[1-3] It is believed that the enhanced electron mobility of the photoanode can effectively separate the injected electrons from recombination sites (i.e. the adjoining oxidised species of the electrolyte). This could suppress the charge carrier recombination in the DSSCs, thus resulting in increased power conversion.[4] One effective approach for enhancing the charge collection ability of a photoanode is to anchor 1D ZnO nanostructures (such as NRs, NWs or NTs) onto a layer of the TCO rather than using TiO_2 nanoparticles.[3, 5] This can introduce a direct electron pathway to improve electron transport, supply light-scattering centres to trap light, and achieve a good contact with the substrate, thus improving the DSSC˘s performance.[3, 6]

However, current DSSCs assembled using 1D ZnO nanostructure based photoanodes, demonstrated that their performances (i.e. PCE 0.4-2.2%) are still much lower than that of TiO_2 mesoporous photoanode based devices.[2, 7] This is mainly due to: (1) a reduced internal accessible surface area (compared with commonly used nanoparticle based mesoporous films) which limits the dye molecular adsorption and results in a consequent reduction in photo-generated electrons;[8-10] (2) a low electron injection efficiency between the dye and ZnO which results in an increased recombination and energy losses; (3) the formation of Zn^{2+}/dye complexes during the dye loading process,

which will act as recombination centres.[2] Therefore, there are many challenges to improve the PCE of ZnO-NRs based DSSCs. It is essential to increase their internal surface area, suppress recombination, and improve stability and dye injection efficiency.[1, 3] As explained in Chapter 2, ZnO nanostructures can be used as supporting/templates for preparing hybrid nanostructures or composite nanostructured semiconductors. Therefore, a proper combination of crystallised TiO_2 and ZnO nanostructures could not only improve stability and dye matching, but also maintain a high electron mobility in the nanostructures. Additionally, with a crystallised TiO_2 shell on top of ZnO, the formation of Zn^{2+}/dye complexes on the surface of ZnO can be prevented, and also a n-n^+ heterojunction can be formed, which can prevent the injected electrons from accumulating at the top surface of the ZnO nanostructures.[2, 3, 6]

In this Chapter, a cost-effective low temperature process for achieving preparation of ZnO/TiO_2 composites with controllable nanostructure, functional properties as well as applications in DSSCs will be discussed. Particularly, a low-temperature process is developed using two sequential cost-effective processes combining solution processed ZnO NRs (developed in Chapter 4) and plasma ion assisted deposition of anatase TiO_2 (developed in Chapter 5). Therefore, a new photoanode with high electron transporting ability is expected to be obtained.[3]

6.2 ZnO/TiO_2 nanostructure preparation

The low temperature process developed to produce the ZnO/TiO_2 nanostructure contains two sequential steps (see Figure 6-1). In the first step, ZnO NRs were grown on the pre-seeded ITO glass slices using a low temperature (90 ^oC) aqueous solution process as described in Chapter 4 (The detailed experiments process for aqueous solution processed ZnO NRs are listed in section 3.2.1.). Adjusting this process can

help to arrange the ZnO NR core morphology as well as the template function. In the second step, a TiO_2 layer was coated onto the ZnO NRs by plasma assisted e-beam evaporation without external heating (as shown in Chapter 5). By controlling the deposition conditions, anatase TiO_2 layer can be readily applied onto the ZnO NRs core and form core-shell nanorods and foxtail-like nanostructure. The morphologies and microstructures of resultant samples were studied using SEM, TEM and XRD. The photoanode function properties (i.e. dye loading and scattering effect) were tested before completing the solar device structure The performance of the DSSCs was evaluated using various techniques including J-V, EIS and transient measurement.[3]

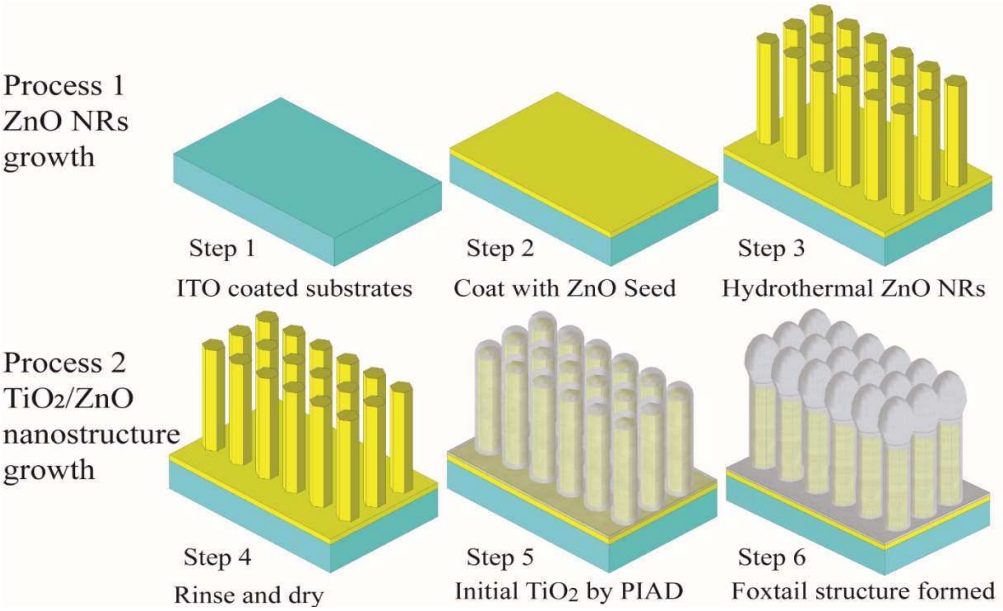

Figure 6-1 Illustration of the formation process of bare ZnO NRs and ZnO/TiO_2 hybrid structures on ITO substrate.[3]

6.3 Morphology and Structure

Figure 6-2 shows typical SEM images (top view and cross-section) of the ZnO NRs (denoted as sample Z0) grown on ITO coated glass slides after 4 hours growth durations at 90 ^oC (as described in Chapter 3.2.1, growth in hexamethylenetetramine aqueous solution, $Zn(NO_3)_2$ and $(CH_2)_6N_4$) concentration is 0.05 M (molar ratio 1:1)). The as-

prepared ZnO NRs arrays have an average length of ~ 3 ı m with a diameter typically ranging from 80 to 150 nm. After obtaining the ZnO NRs using the aqueous solution method, all the ZnO NRs coated samples were rinsed in deionized (DI) water and dried in air. Then the TiO_2 modification layer was deposited onto the samples using plasma enhanced e-beam evaporation without substrate heating. The duration of the depositions was set to 15, 30, 60, 120, and 240 minutes, which was denoted as samples of TZ1, TZ2, TZ3, TZ4 and TZ5, respectively.[3]

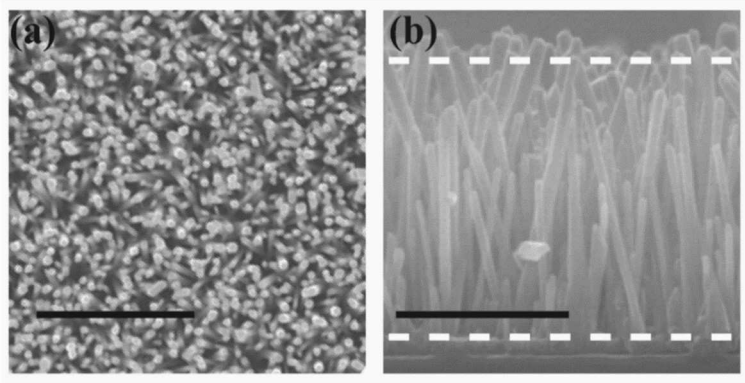

Figure 6-2 Top (a) and side (b) view exemplary SEM images of the bare-ZnO NRs (Z0). The scale bar is 2 ≈m.[3]

Figure 6-3 shows SEM images of the bare ZnO NR arrays and ZnO NR arrays with the TiO_2 modification layer prepared with varying deposition time. The uncoated ZnO NRs show a typical hexagonal morphology with a well-defined hexagonal shape as shown in Figure 6-3 (a-2).[3] After a 30 minute deposition, hexagonal shaped ZnO NRs coated with the TiO_2 changed into a cylindrical morphology, and a central depression on the top of the NRs can be clearly observed in Figure 6-3 (b-1) and (b-2).[3] When the deposition duration was increased to 120 minutes, a foxtail-like TiO_2 layer with rough surface was formed on the top of the NRs as shown in Figure 6-3 (c-1) and (c-2). SEM and TEM images (Figure 6-4) clearly show the core-shell hybrid structures feature of sample TZ2 and TZ4.[3]

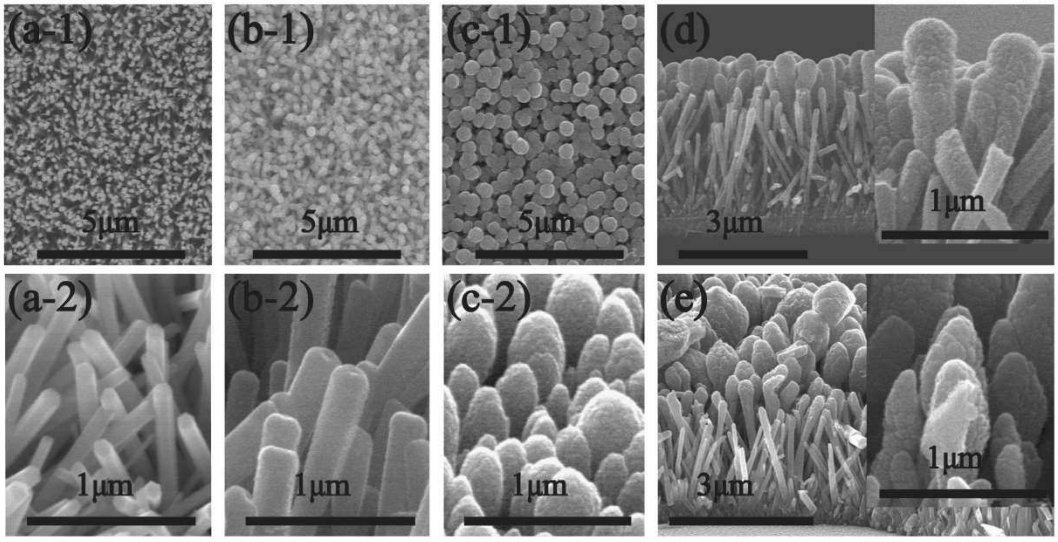

Figure 6-3 SEM images of morphology evolution of bare ZnO NRs to ZnO/TiO_2 hybrid structure. Top view of (a-1) Z0, (b-1) TZ2 and (c-1) TZ4. 45ł titled SEM of (a-2) Z0, (b-2) TZ2 and (c-2) TZ4; cross-sectional SEM image of (d) TZ4 and (e) TZ5. Inserts are enlarged section of the images.[3]

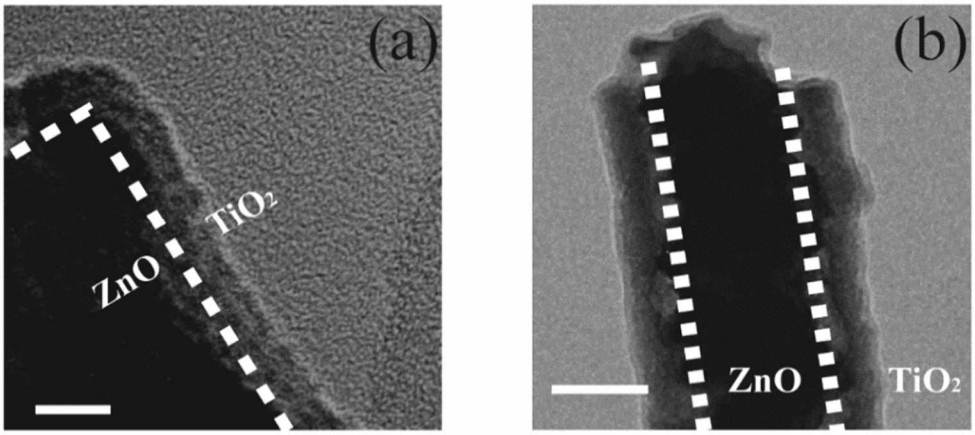

Figure 6-4 TEM image of a single ZnO core-TiO_2 shell hybrid structure with the modification time of (a) 60 minutes (TZ2) and (b) 120 minutes (TZ4). The scale bar is 20 and 100 nm, respectively.

As shown in Figure 6-5 (a) and (b), the chemical element distribution in the nanostructure was studied by EDS along the rod direction (across the region marked with a white bar in Figure 6-5 (a)). Figure 6-5 (b) is the corresponding Ti and Zn element distribution from bottom (0 ı m) to top part of the tested TZ4 sample along the straightened selected testing route. The changes of signals indicated the element distribution changes along the line scan direction.[3] This result confirmed Ti element

was distributed in the whole film and gradually increased with the position up to top of the nanostructure. The formation of the shell was also confirmed by TEM observation. Figure 6-4 shows a thin layer of TiO_2 with ~20 nm (TZ2, Figure 6-4 (a)) and 50 nm (TZ4, Figure 6-4 (b)) thickness covering the wall-side surface of ZnO NRs. The thickness of the modification layer does not increased significantly on the wall side of the ZnO with further increasing the deposition time. However, the TiO_2 modification layer was found to grow much faster on the tip of ZnO NRs.[3] This can be observed more clearly on the longer ZnO NRs facing directly towards the TiO_2 source as they have higher probability to receive more TiO_2. Another reason for this phenomena is the self-shadowing effects of the longer NRs during growth,[11] causing the apparent decrease of the density of the nanostructure as shown in Figure 6-3 (a) to (c). Figure 6-3 (d) and Figure 6-3 (e) show the cross-section SEM images of the samples of TZ4 and TZ5 which were produced with deposition duration of 120 minutes and 240 minutes. The TiO_2 modification layer easily grows on the larger and longer ZnO NRs. Furthermore, the rapid growth of the foxtail-like TiO_2 structures on the preferred ZnO NRs narrows the gaps between them.[3]

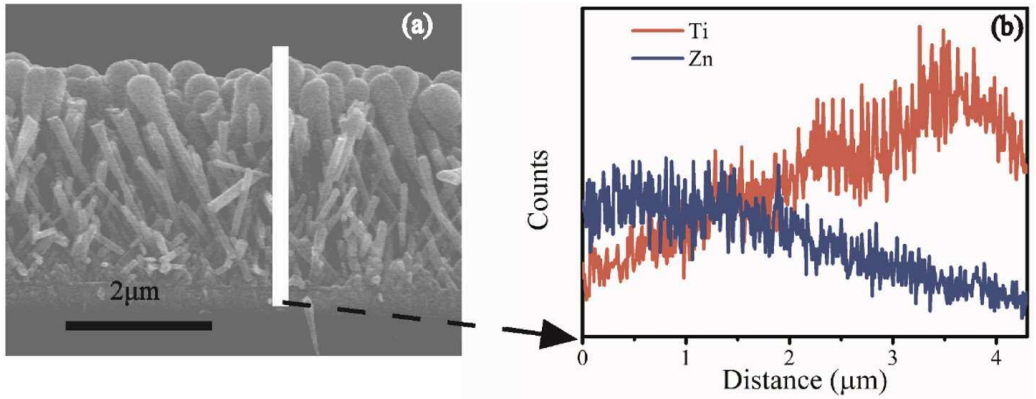

Figure 6-5 (a) Cross section of the TZ4 and (b) the corresponding EDS line scan.[3]

The above phenomena can be explained using electron shadowing effect of plasma as illustrated in Figure 6-6.[3] Atoms and ions are directed perpendicularly to the surface during deposition, and many of them will pass hit the bottom of the NRs, thus the

positive charges are gradually built up both at the bottom and on the surface of the NRs to repel extra ions arriving at the surface of evaporated material due to their low mass.[3] Initially, the ZnO NRs absorb the electrons thus inducing a negative charge on the surface.[3] However, as the TiO_2 nano-layers (with less electron mobility) gradually build up on the ZnO NRs, distorted ion trajectories and reduction of the preferential growth of the TiO_2 will cause the formation of the nano-sculptured foxtail structures.[3]

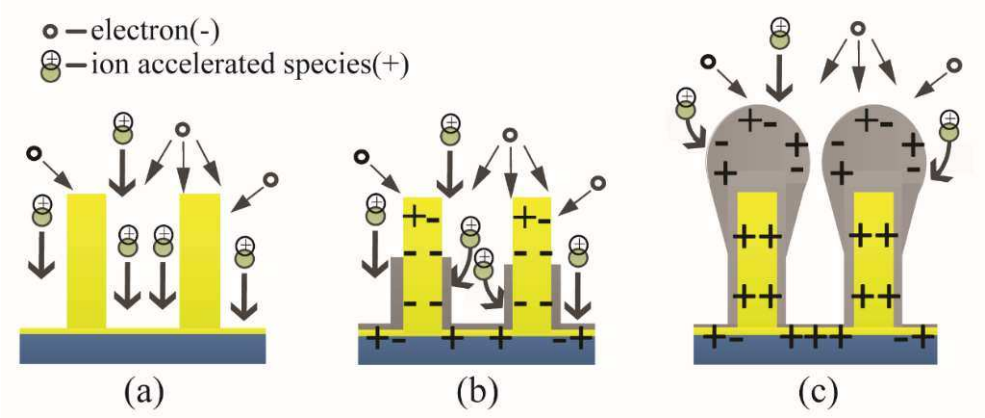

Figure 6-6 Mechanism of electron shading phenomena during plasma enhanced deposition: species comes from evaporated Ti_3O_5.[3]

The crystalline structures of the as-prepared samples were also investigated using XRD. Figure 6-7 shows typical XRD patterns of the pure ZnO NRs (Z0) and hybrid ZnO/TiO_2 samples obtained with varied deposition durations (30 min-TZ2 and 120 min-TZ4).[3] The Z0 sample shows a strong (002) peak, which indicates that the ZnO NRs have a typical wurtzite hexagonal structure with a preferential growth orientation of [0001]. The presence of the wurtzite hexagonal ZnO (PDF-#36-1451) is clearly identified for all the tested samples. For the hybrid samples, the diffraction peaks of the TZ2 and TZ4 are indexed to a combination of wurtzite hexagonal ZnO and anatase TiO_2 (PDF-#21-1272).[3] It also can be noticed that, with increasing in deposition time of the TiO_2 layer, the intensities of the anatase TiO_2 (004) and (101) peaks increase. This is possibly caused by (1) the increased amount of anatase TiO_2 presented in the hybrid

nanostructures; (2) with extend deposition time, some anatase TiO_2 crystals may continue growing larger and crystallinity is improved.[12] Studies of morphology and structure confirmed that the optimised deposition is quite suitable for achieving core-shell structure as well as obtaining crystallised samples without the need to use any high temperature process.[3]

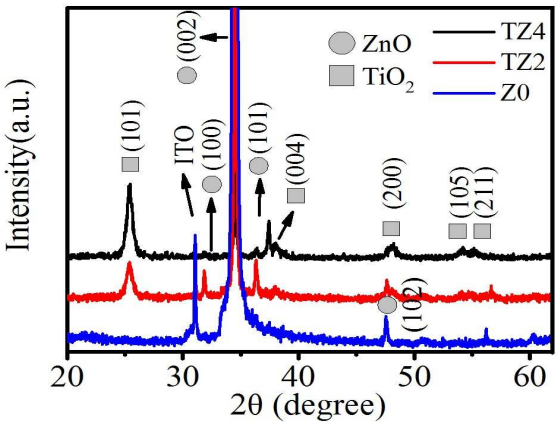

Figure 6-7 XRD patterns of bare ZnO NRs (Z0) and ZnO/TiO_2 (TZ2 and TZ4) hybrid films grown on ITO substrates.[3]

6.4 Scattering and dye loading capability of photoanode

The reflectivity of the photoanode was investigated in order to understand the scattering effects of the hybrid structures.[3] Figure 6-8 (a) shows the diffuse reflectance UV-Vis spectra obtained from the photoanodes before dye absorption.[3] Apparently, the hybrid TiO_2/ZnO films show a higher reflectivity than that of the pure ZnO NRs in the wavelengths ranging from 400 to 700 nm. The intensity of the reflection increases with the deposition durations, suggesting that a thicker TiO_2 layer may lead to a stronger in-plane light scattering effect, which is beneficial for light harvesting and DSSC performance.[3] The changes of image contrast in brightness can be clearly observed in Figure 6-8 (b). Generally, a brighter surface on the device indicates a stronger surface

scattering effect, which may cause an enhanced trapping effect for the interaction of dye with the light.[3]

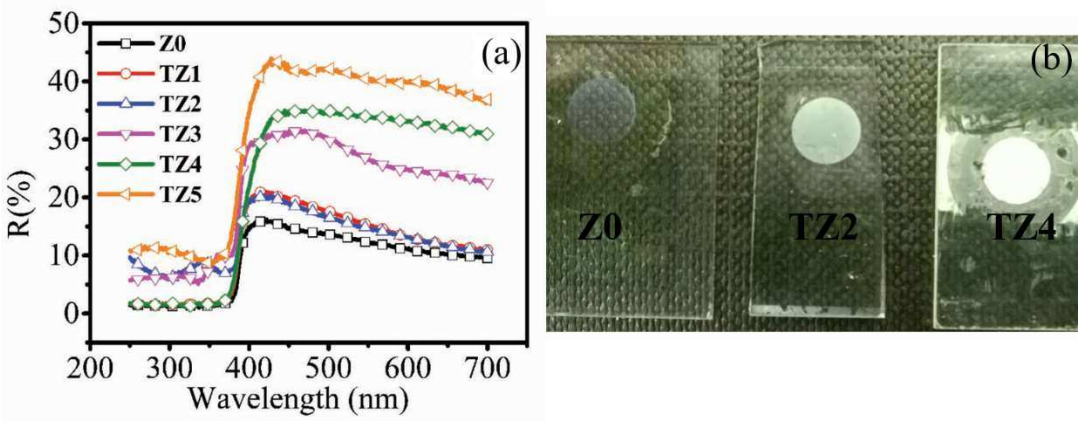

Figure 6-8 (a) Diffuse reflectance spectra of the Z0 and TZ1 to TZ5 films (b) Digital image of identical samples on ITO substrate.[3]

In order to study the hybrid structure effect on the performance of DSSCs, dye loading was also investigated. Figure 6-9 shows the optical absorption spectra of the solutions desorbed from various samples after the dye loading.[3] The concentration of dye loading obtained are listed in the inset Table in Figure 6-9. Compared with those from the pure ZnO NRs (Z0), dye-loading capabilities of the TiO_2/ZnO hybrid structures are increased from TZ1 to TZ4, mainly due to the increased internal surface areas of the hybrid films.[3] However, further increasing the duration above 120 minutes did not continuously improve the dye loading capability.[3] This is probably caused by the formation of: (1) larger sizes of the nanostructure, which normally results in less dye loading;[13] (2) denser foxtail structures, which could cover part of surface atop of the NRs, thus reduce the accessible internal surfaces area.[3, 13]

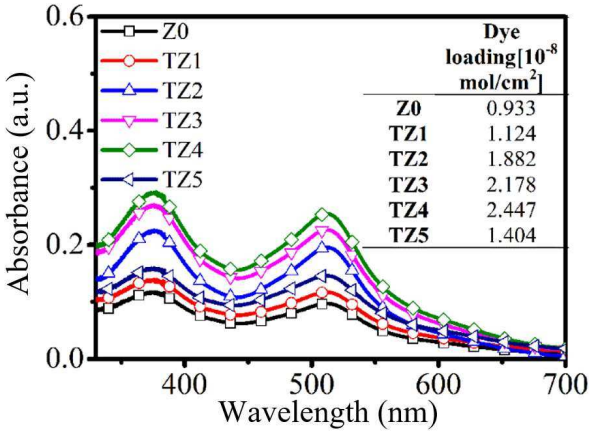

Figure 6-9. Absorption spectra of dye desorbed from Z0 and TZ1 to TZ5 films with an area of 2.2 cm^2.The inserted table is dye loading of corresponding samples: ZnO NRs (Z0) and ZnO/TiO_2 hybrid films (TZ1 to TZ5).[3]

6.5 Dye Sensitized solar cell performance

To evaluate the light harvesting efficiency, the as-prepared hybrid photo-anodes were fabricated into DSSCs and their photovoltaic properties were studied.[3] Figure 6-10 shows the J-V curves of the DSSCs made from the hybrid nanostructures. The photovoltaic data of all the DSSCs are summarised in Table 6-1.[3]

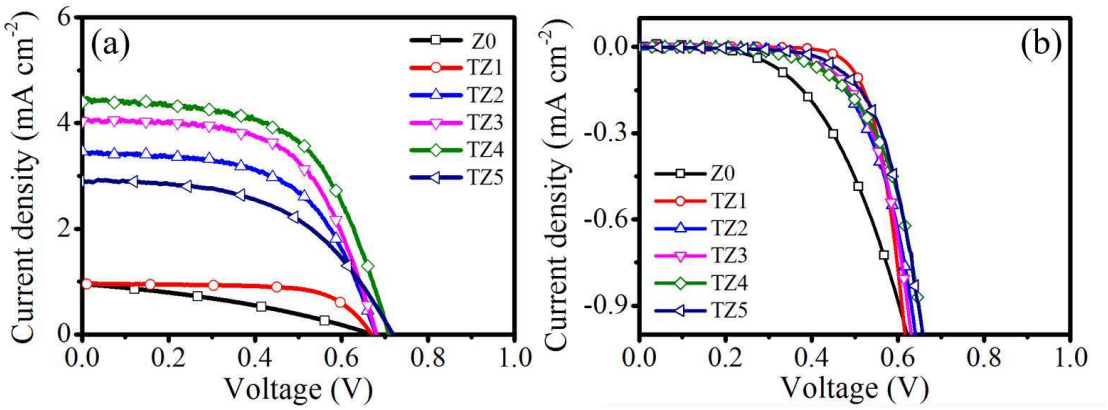

Figure 6-10 Photocurrent-voltage (J-V) curves of DSSCs assembled by synthesised ZnO and ZnO/TiO_2 photoanodes (a) light J-V; (b) dark J-V.[3]

As demonstrated in the J-V curves, the measured Jsc of the pure ZnO NRs (Z0) photoanode is around 0.9 mA/cm^2. A slight increase was observed in the values of Jsc

(up to 1.0 mA/cm^{-2}) with a short time deposition of a TiO_2 layer on ZnO NRs (TZ1).[3] The improved photovoltaic performance is attributed to the presence of the TiO_2 layer which could improve electron injection and formation of heterojunctions at the hybrid structure interface.[3] This layer could prevent back-transfer of electrons and suppress the recombination. In the TiO_2/ZnO hybrid structure, the electrons were injected into the TiO_2 shell structures (which was reported to improve charge injection between the dye and ZnO electrode[14]).[3] They were then transferred to the internal ZnO NRs, rather than diffusing towards the surface of the photoanode where they may recombine with holes.[3] Therefore, the Voc increase when the TiO_2 was applied to the top layer of the ZnO NRs. Simultaneously, the presence of the TiO_2 layer in this design could successfully prevent the formation of Zn^{2+}/dye complexes, thus preventing the passivation of dye molecules, leading to an increased efficiency.[3] This is because the points of zero charge of the TiO_2 (linked with a pH value of 5.5–6.5 [15]) is much lower than that of the ZnO (linked with a pH value of 8–9 [16]), whereas the pH value for the dye solution was ~5. Therefore, in the presence of the TiO_2 shell, the formation of Zn^{2+}/dye complexes might not happen.[3] Additionally, the increased deposition duration led to an increase of dye loading capability, and the hybrid structures showed the increased Jsc values (from 1.01 to 4.40 mA/cm^{-2}) and increased Voc values (from 0.67 to 0.71 V), thus enhancing the PCE values from 0.49% to 1.83%.[3]

However, the DSSCs made of the TZ5 hybrid structure showed a higher Voc value (0.70 V) but a lower Jsc value (2.89 mA/cm^{-2}) and PCE value (1.06%).[3] This is mainly due to the lower dye loading capability for this photoanode, which is mainly caused by the formation of a relatively denser structure thus decreasing the total surface area. [3, 17] Additionally, the dropped FF could be another factor for the lower PCE due to the reduced electron mobility of the TZ5 photoanode in this work (will be further discussed

with EIS and transient results in the following sections).[3, 13, 18] Thus, it can be reasonably argued that an appropriate amount of TiO_2 in these hybrid films is very important to improve the overall performance of the DSSCs.[3] Figure 6-10 (b) shows the dark J-V results for the DSSCs, in which the increase of the values of FF and Voc of the hybrid photo-anodes can be revealed. The potential distribution across the cell in the dark is not the same as that under illumination.[3, 19] It can be used to estimate the extent of the back electron transfer.[3, 20] Compared with the results from the ZnO NRs DSSC, the dark J-V of the hybrid foxtail DSSC showed a shift to a higher potential side and became smaller at the same potential above 0.6 V. These observation indicate a lower recombination rate for the hybrid foxtail DSSCs [3, 21, 22], which will be further investigated in the following section by EIS and transient measurements.

Table 6-1 J-V parameters of DSSCs based on bare ZnO NRs (Z0) and ZnO/TiO_2 hybrid films (TZ1 to TZ5).[3]

Samples	Jsc (mA/cm^{-2})	Voc (V)	PCE (%)	Fill factor (FF)
Z0	0.996	0.673	0.27	0.41
TZ1	1.066	0.670	0.49	0.68
TZ2	2.768	0.680	1.09	0.58
TZ3	3.232	0.682	1.32	0.60
TZ4	4.401	0.709	1.83	0.59
TZ5	2.894	0.706	1.06	0.52

The Nyquist plots of the impedance spectra obtained in the dark environment for the DSSCs are shown in Figure 6-11, the equivalent circuit used in fitting the curves had been demonstrated in Chapter 3.5.2.[3] As previously discussed in Chapter 3, the Nyquist plots of the DSSCs generally have three sections:[3, 23] (1) A low frequency range (<1 Hz), which is assigned to the Warburg diffusion process of I^-/I_3^-; (2) Middle frequency range (from 1 Hz to 10 kHz), which is linked with the charge transfer across

interfaces among the semiconductor/dye/electrolyte; (3) High frequency ranges (in the kHz range and above), which is related to the electrochemical reaction at the Pt CE.[3] However, the EIS results do not show a clear transmission-line feature in this experiment, which is commonly attributed to a good electron transport in the semiconductor oxide (i.e. ZnO).[3, 24-26] For this reason, it is not possible to obtain reliable transport resistance values from the equivalent circuit Etting and the study was limited to analysing the recombination behaviour of the NRs and hybrid nanostructures based DSSCs.[3]

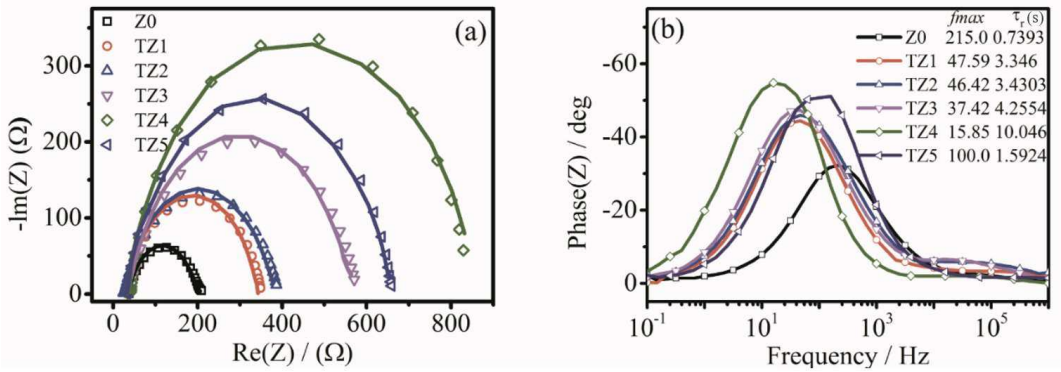

Figure 6-11 (a) Experimental (line) and fit (dots) data of impedance spectra of DSSCs based on Z0, TZ1 to TZ5 photoanode measured at Voc applied bias in dark. Inset is equivalent circuit model used for fitting (b) Bode impedance plot of corresponding samples.[3]

As shown in Figure 6-11, the diameter of the semicircles (related to EIS results in the middle frequency range) is increased with the increase in TiO_2 deposition time, except for sample TZ5.[3] This clearly shows that the recombination resistance increase with TiO_2 deposition time, which results in a lower recombination rate at the interfaces of the semiconductor/dye/electrolyte for the DSSCs using the anchored hybrid photo-anodes. According to previous studies,[3, 27, 28] a core-shell structure would be a good way to suppress recombination by forming a surface energy barrier. In the case of this study, the ZnO core and TiO_2 shell have similar energy levels, thus it is hard to form a strong energy barrier between them in terms of energy level.[3, 29] However, an n-n+

heterojunction could be formed at the ZnO/TiO_2 interface due to the difference of the electron concentration of ZnO/TiO_2 (i.e. 10^{18} cm^{-3} in ZnO and 10^{10} cm^{-3} in TiO_2).[3, 29] Therefore, a built-in potential could be formed in this n-n+ heterojunction to suppress the recombination, which can be described using the following equation [3, 29]:

$$\text{侥}_{\text{Built-in}} \text{唸} \frac{\text{唧}}{\text{呔}} \text{侵} \frac{\text{唄}}{\text{唄}} \qquad \text{(Eq. 6-1)}$$

where k is the Boltzmann˜s constant, q is the electron charge, T is the temperature and 侵 is the ratio of electron concentrations between ZnO-core and TiO_2-shell.[3, 27-29] This $V_{Built-in}$ potential could cause the injected-electrons to flow back against the concentration gradient, and eventually these electrons could be confined in the ZnO NRs. Therefore, the back transfer of the electrons can be suppressed and recombination resistance is increased.[3] The reason why the DSSCs made of the TZ5 hybrid film showed a lower recombination resistance could be due to formation of large and dense island structures of TiO_2 which could lower the electron mobility in the hybrid structures.[3]

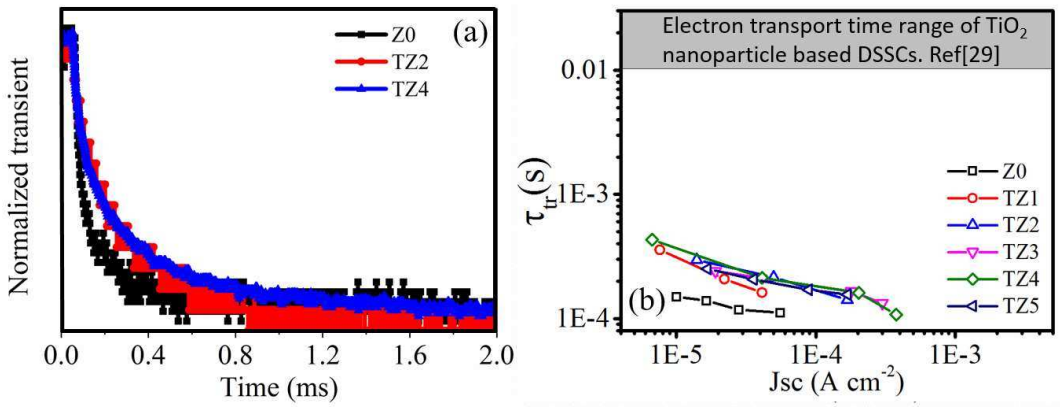

Figure 6-12 (a) Representative transient photo current decay at a short circuit work condition of Z0, TZ2 and TZ4 (b) Fitted electron transport time constants (-$_{tr}$) versus short-circuit current for all the samples.[3, 29]

Figure 6-11 (b) shows that, the peak frequency shifts to a lower value after adding the TiO_2 layer, which indicates that this hybrid photoanode not only increases recombination resistance, but also results in a higher electron lifetime compared to the ZnO NRs sample.[3] The electron lifetime (t_e) can be estimated from EIS measurements by the following equation:[3]

偉 嗯 ⊡ 蟆 鋸 鋸 鋸 鋸 鋸 婕 (Eq. 6-2)

where f_{max} is the maximum angular frequency of the semicircle in Figure 6-11 (a) at the middle range frequencies.[3] The calculated values of the electron lifetimes are summarised in Figure 6-11 (b), in which the peak-shift to the lower frequency side indicates a longer electron recombination lifetime.[3, 30] Figure 6-11 (b) can be used to explain the higher values of the open circuit voltages of this hybrid solar cell by adding a TiO_2 nanostructured layer.[3]

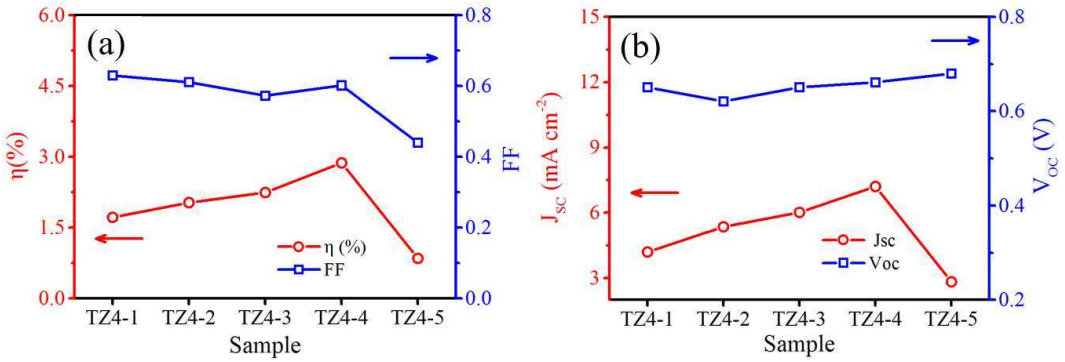

Figure 6-13 Performance parameters of ZnO/TiO_2 photoanode based DSSCs (a) Jsc and Voc (b) PCE and FF with variable ZnO NRs core length.

To further verify the above conclusions, electron transport ability of photoanodes in DSSCs was estimated based on the decay of photocurrent measurements (with results shown in Figure 6-12).[3] Figure 6-12 (a) shows a representative photocurrent decay of the DSSCs assembled by different photoanode.[3] The normalized curve shows that the pure ZnO Z0 decayed faster than those of the TiO_2 coated samples (TZ2 and TZ4). In

details, the values of electron transport (τ_{tr}) for the pure ZnO NRs based photoanode (Z0) DSSCs is much lower than all the TiO_2 coated samples (Figure 6-12 (b)). It also can be noted that samples of TZ1 to TZ5 (all the TiO_2 coated ZnO NRs based photoanodes) do not show significant changes with deposition duration. These results demonstrate that the electron transport in these photoanodes is mainly determined by the ZnO NRs properties.[3, 31] Compared with those from the conventional TiO_2 nanoparticle based mesoporous photoanode, electron transport ability of these ZnO/TiO_2 hybrid photoanodes is at least two orders of magnitude faster, mainly because the ZnO nanorods were used as the basis for the devices.[3, 14]

However, the largest PCE value obtained from this study (i.e. 1.8%) is still lower than those from the conventional TiO_2 nanoparticle-based DSSCs.[2, 3] This is probably caused by the reduced internal surface areas of the 1D-hybrid nanostructures, thus resulting in a lower dye loading rate, when compared to a conventional TiO_2 particulate mesoporous photoanode.[3] This can be improved by increasing reachable surface areas, for example, synthesizing longer hybrid nanostructures with higher aspect ratios or branched complex nanostructures.[2, 3] The capability in growing longer ZnO NRs with high aspect ratio have been discussed in Chapter 4 (section 4.2.2.3). The longer ZnO NRs have higher aspect ratio and may increase surface area for dye loading as well as high electron transport ability improving DSSC performance.[3] Therefore, as a confirmation, different length of ZnO NRs were tested using optimised duration as used in sample TZ4 before assembling to the devices. The ZnO NRs lengths were set to be 3, 5, 7, 9 and 11 μm, then coated with TiO_2, which were denoted as samples of TZ4-1, TZ4-2, TZ4-3, TZ4-4 and TZ4-5, respectively. Performance parameters of these DSSC made by the variable ZnO NRs core length are summarised in Figure 6-13. As expected, increasing the length of the ZnO NRs (TZ4-1 to TZ4-4) leads to an increase in the

DSSC performance (i.e. improved PCE, Jsc as well as Voc). While with further increase ZnO NRs length, the Jsc decreased sharply (TZ4-5). As the thickness of film is still not approaching the electron diffusion length in the ZnO NR DSSCs,[2, 9] it is reasonably to attribute this performance drop to the fusion of the ZnO NRs at the growth root which results in dense structure at the bottom part of the film (as shown in Chapter 4, Figure 4-11 (d)). With widening of each ZnO NR, the reachable surface area for loading dye molecular is decreased.

6.6 Summary

In this chapter, crystallised ZnO-TiO_2 nanostructure was achieved by sequential applying pre-developed low temperature processes comprising aqueous solution method and PIAD. Diffuse reflectance spectra demonstrated that the light-trapping efficiency of the TiO_2/ZnO hybrid nanostructures was improved over that of the pure ZnO NRs due to the effective light-scattering caused by the hybrid nanostructures.[3] Results from dark J-V, EIS and photo current decay indicated a good electron transport capability associated with this hybrid photoanode, and the overall conversion efficiency was increased from 0.27% to 1.8%.[3] Further increasing the ZnO NR length without densification, a higher PCE (3.0%) can be obtained. The 1D ZnO core morphology with TiO_2 shell can not only provide a direct pathway for charge transport, improve charge injection, but also prevent the formation of Zn^{2+}/dye complex (thus reducing the recombination centres in the structure), and increase the surface area (thus resulting in a higher dye loading capability). Most significantly, this method provides an effective strategy to fabricate crystallised TiO_2 modification coatings without high temperature deposition or any post-annealing processes, making it an important technique for reduction of process costs and usage of temperature sensitive substrates/materials.[3]

Reference

1. Luo, Y., D. Li, and Q. Meng, Towards Optimization of Materials for Dye-Sensitized Solar Cells. Advanced Materials, 2009. 21(45): p. 4647-4651.
2. Zhang, Q., C.S. Dandeneau, X. Zhou, and G. Cao, ZnO Nanostructures for Dye-Sensitized Solar Cells. Advanced Materials, 2009. 21(41): p. 4087-4108.
3. Zhao, C., D. Child, Y. Hu, N. Robertson, D. Gibson, S.C. Wang, and Y.Q. Fu, Low temperature growth of hybrid ZnO/TiO_2 nano-sculptured foxtail-structures for dye-sensitized solar cells. RSC Advances, 2014. 4(105): p. 61153-61159.
4. Baxter, J.B. and E.S. Aydil, Nanowire-based dye-sensitized solar cells. Applied Physics Letters, 2005. 86(5): p. -.
5. Yoon, J. H., S. R. Jang, R. Vittal, J. Lee, and K.-J. Kim, TiO_2 nanorods as additive to TiO_2 film for improvement in the performance of dye-sensitized solar cells. Journal of Photochemistry and Photobiology A: Chemistry, 2006. 180(1¯2): p. 184-188.
6. Xu, C., P.H. Shin, L. Cao, J. Wu, and D. Gao, Ordered TiO_2 Nanotube Arrays on Transparent Conductive Oxide for Dye-Sensitized Solar Cells. Chemistry of Materials, 2009. 22(1): p. 143-148.
7. Vomiero, A., I. Concina, M.M. Natile, E. Comini, G. Faglia, M. Ferroni, I. Kholmanov, and G. Sberveglieri, ZnO/TiO_2 nanonetwork as efficient photoanode in excitonic solar cells. Applied Physics Letters, 2009. 95(19): p. -.
8. Law, M., L.E. Greene, J.C. Johnson, R. Saykally, and P. Yang, Nanowire dye-sensitized solar cells. Nature Materials, 2005. 4(6): p. 455-459.
9. Xu, C., P. Shin, L. Cao, and D. Gao, Preferential Growth of Long ZnO Nanowire Array and Its Application in Dye-Sensitized Solar Cells. The Journal of Physical Chemistry C, 2009. 114(1): p. 125-129.
10. Gr±tzel, M., Conversion of sunlight to electric power by nanocrystalline dye-sensitized solar cells. Journal of Photochemistry and Photobiology A: Chemistry, 2004. 164(1¯3): p. 3-14.
11. Tait, R.N., T. Smy, and M.J. Brett, Modelling and characterization of columnar growth in evaporated films. Thin Solid Films, 1993. 226(2): p. 196-201.
12. Law, M., L.E. Greene, A. Radenovic, T. Kuykendall, J. Liphardt, and P. Yang, ZnOБAl_2O_3 and ZnOБTiO_2 CoreБShell Nanowire Dye-Sensitized Solar Cells. The Journal of Physical Chemistry B, 2006. 110(45): p. 22652-22663.
13. Zhang, S., X. Yang, Y. Numata, and L. Han, Highly efficient dye-sensitized solar cells: progress and future challenges. Energy & Environmental Science, 2013. 6(5): p. 1443-1464.
14. Manthina, V., J.P. Correa Baena, G. Liu, and A.G. Agrios, ZnO¯TiO_2 Nanocomposite Films for High Light Harvesting Efficiency and Fast Electron Transport in Dye-Sensitized Solar Cells. The Journal of Physical Chemistry C, 2012. 116(45): p. 23864-23870.
15. Kosmulski, M., The significance of the difference in the point of zero charge between rutile and anatase. Advances in Colloid and Interface Science, 2002. 99(3): p. 255-264.
16. Blok, L. and P.L.D. Bruyn, The ionic double layer at the ZnOsolution interface: I. The experimental point of zero charge. Journal of Colloid and Interface Science, 1970. 32(3): p. 518-526.
17. Yoon, J., A.J. Baca, S.I. Park, P. Elvikis, J.B. Geddes, 3rd, L. Li, R.H. Kim, J. Xiao, S. Wang, T.H. Kim, M.J. Motala, B.Y. Ahn, E.B. Duoss, J.A. Lewis, R.G. Nuzzo, P.M. Ferreira, Y. Huang, A. Rockett, and J.A. Rogers, Ultrathin silicon solar microcells for semitransparent, mechanically flexible and microconcentrator module designs. Nat Mater, 2008. 7(11): p. 907-15.
18. Wang, J.T.-W., J.M. Ball, E.M. Barea, A. Abate, J.A. Alexander-Webber, J. Huang, M. Saliba, I. Mora-Sero, J. Bisquert, H.J. Snaith, and R.J. Nicholas, Low-Temperature

Processed Electron Collection Layers of Graphene/TiO_2 Nanocomposites in Thin Film Perovskite Solar Cells. Nano Letters, 2014. 14(2): p. 724-730.
19. Zaban, A., A. Meier, and B.A. Gregg, Electric Potential Distribution and Short-Range Screening in Nanoporous TiO_2 Electrodes. The Journal of Physical Chemistry B, 1997. 101(40): p. 7985-7990.
20. Bai, Y., H. Yu, Z. Li, R. Amal, G.Q. Lu, and L. Wang, In Situ Growth of a ZnO Nanowire Network within a TiO_2 Nanoparticle Film for Enhanced Dye-Sensitized Solar Cell Performance. Advanced Materials, 2012. 24(43): p. 5850-5856.
21. Huang, S.Y., G. SchlichthØrl, A.J. Nozik, M. Gr±tzel, and A.J. Frank, Charge Recombination in Dye-Sensitized Nanocrystalline TiO_2 Solar Cells. The Journal of Physical Chemistry B, 1997. 101(14): p. 2576-2582.
22. Ferrere, S. and B.A. Gregg, Large Increases in Photocurrents and Solar Conversion Efficiencies by UV Illumination of Dye Sensitized Solar Cells. The Journal of Physical Chemistry B, 2001. 105(32): p. 7602-7605.
23. Adachi, M., M. Sakamoto, J. Jiu, Y. Ogata, and S. Isoda, Determination of Parameters of Electron Transport in Dye-Sensitized Solar Cells Using Electrochemical Impedance Spectroscopy. The Journal of Physical Chemistry B, 2006. 110(28): p. 13872-13880.
24. Bisquert, J., Theory of the Impedance of Electron Diffusion and Recombination in a Thin Layer. The Journal of Physical Chemistry B, 2001. 106(2): p. 325-333.
25. Fabregat-Santiago, F., J. Bisquert, G. Garcia-Belmonte, G. Boschloo, and A. Hagfeldt, Influence of electrolyte in transport and recombination in dye-sensitized solar cells studied by impedance spectroscopy. Solar Energy Materials and Solar Cells, 2005. 87(1¯4): p. 117-131.
26. Guillen, E., E. Azaceta, L.M. Peter, A. Zukal, R. Tena-Zaera, and J.A. Anta, ZnO solar cells with an indoline sensitizer: a comparison between nanoparticulate films and electrodeposited nanowire arrays. Energy & Environmental Science, 2011. 4(9): p. 3400-3407.
27. von Roos, O., A simple theory of back surface field (BSF) solar cells. Journal of Applied Physics, 1978. 49(6): p. 3503-3511.
28. Zhao, R., L. Zhu, F. Cai, Z. Yang, X. Gu, J. Huang, and L. Cao, ZnO/TiO_2 core¯shell nanowire arrays for enhanced dye-sensitized solar cell efficiency. Applied Physics A, 2013. 113(1): p. 67-73.
29. Park, K., Q. Zhang, B.B. Garcia, and G. Cao, Effect of Annealing Temperature on TiO_2Б ZnO CoreБ Shell Aggregate Photoelectrodes of Dye-Sensitized Solar Cells. The Journal of Physical Chemistry C, 2011. 115(11): p. 4927-4934.
30. Desai, U.V., C. Xu, J. Wu, and D. Gao, Hybrid TiO_2¯SnO_2 Nanotube Arrays for Dye-Sensitized Solar Cells. The Journal of Physical Chemistry C, 2013. 117(7): p. 3232-3239.
31. Barnes, P.R.F., K. Miettunen, X. Li, A.Y. Anderson, T. Bessho, M. Gratzel, and B.C. O'Regan, Interpretation of Optoelectronic Transient and Charge Extraction Measurements in Dye-Sensitized Solar Cells. Advanced Materials, 2013. 25(13): p. 1881-1922.

Chapter 7 Low temperature processed nanoflakes for dye-sensitised solar cells

7.1 Introduction

The functional properties of ZnO nanostructured materials are largely dependent on the composition, crystal structure, morphology and their dimension. In particular, solution-processed nanostructures of ZnO with controllable morphologies and suitable band gaps offer great potentials to improve electron transport abilities of the photoanodes used in the DSSCs. Due to their unique advantages including low cost, ease of preparation and structure/component design.[1-5] ZnO based nanostructured (e.g., NWs/NRs, nanotubes, nanoflakes and similar nanostructure) photoanodes can not only provide large accessible surface areas for binding dye molecules (or absorber), but also support the dye molecules (or absorber) and offer electron transport pathways with a reduced recombination. Though the ZnO has advantages including good electron transport with a suitable band gap and flexibility in morphology control, there are still many challenges of successful use of ZnO 1D nanostructured photoanodes for improving device performance. For example, the PCE is still lower than that of nanoparticle based photoanodes,[5-11] because of two major challenges: (1) lower internal surface areas of the 1D and 2D nanostructures (compared with those of the nanoparticles); (2) lower electron injection efficiency and poor chemical stability of the ZnO.[12, 13] As a result, a TiO_2 layer is often used for modification of ZnO nanostructures to stabilize and improve the dye loading capability in the DSSCs (Chapter 6).[5, 14, 15]

The benefit of ZnO nanostructured photoanodes can be further improved by intentionally introducing other elements into ZnO, i.e. introducing doping elements of

group III-(Al, Ga and In) or group IV (Pb, Sn) into the ZnO, which has been proven as an efficient method to enhance its electrical properties.[5, 16-18] Al doped ZnO (AZO) has been extensively investigated/used in solar cell applications because of its high conductivity, low cost and good optical performance.[5, 16, 19] Controllable growth of ZnO nanoflakes (NFs) with vertically grown arrays was also reported to improve the photoanode performance in DSSCs, and the NFs with designed morphology can significantly improve the light trapping and solar cell performance.[5, 20] Recently, Peng et al used simulation analysis based on finite difference in time domain with experimental verification and showed that the NFs with small sizes caused a random light scattering.[20] However, once the NFs reached to a size larger than 2 ı m, the randomly distributed directions of the NFs significantly improved the light trapping effects.[5, 20]

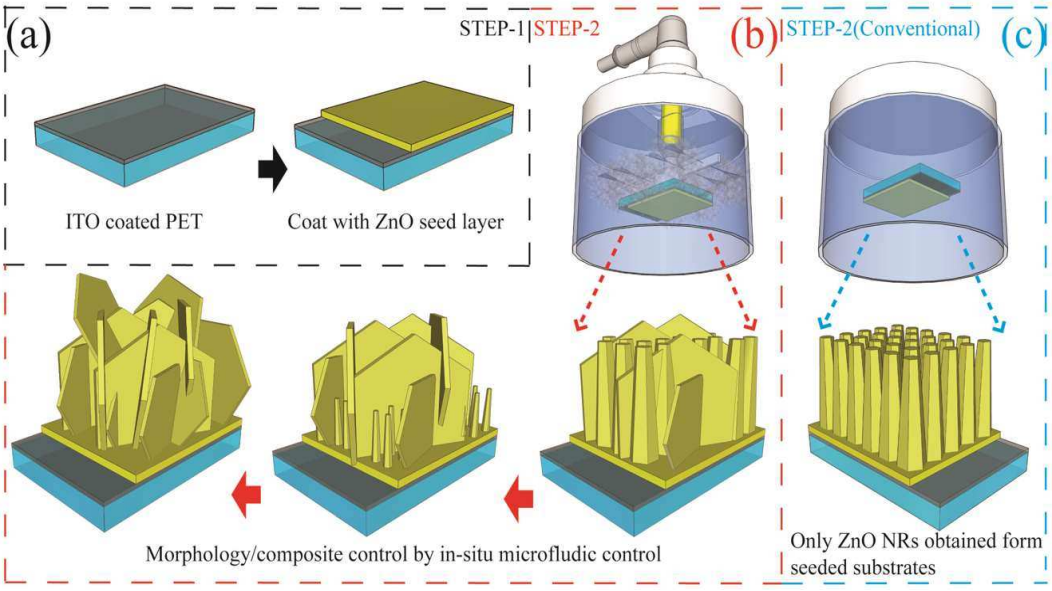

Figure 7-1 Illustration of the strategies for fabrication of controllable AZO nanostructures (a) step 1 for pre-seed substrates; (b) step 2 for in-suit MCU aqueous solution method used for controllable AZO synthesis; (c) a reference experiment used in step 2 by conventional aqueous solution synthesis.[5]

Great effort has been made to achieve the required ZnO nanostructured morphology using various low-cost solution based techniques, such as microwave enhanced hydrothermal methods, electro-chemical and electro spraying technique.[5, 21-24] However, many challenges still exist.[5] It is difficult to control the vertically grown crystallised AZO NFs directly on the target substrate to achieve the desirable light trapping properties with improved adhesion and contact resistance;[5] The synthesis process is to be simplified (i.e. avoiding uses of chemical additives, multi-step process or high temperature processes).[5, 14, 25-28].

Recently, the microfluidic synthesis of nanostructures have received considerable attention in synthesising nanostructure materials due to its several unique advantages on nanostructure control.[29, 30] Typically, microfluidic synthesis has been carried out using a small chamber (several microns to thousands microns) connected with micro-seized channels from which the reaction solution will be introduced into the reaction chamber. The growth solution can be rapidly transported into the small reaction chamber by micro-channels from outside source (i.e., pressure pump). The reaction solution mixture and temperature can be precisely controlled by using multiple separated micro-channels and micro-heater during growth. Joo et al.[29] using micro channel as a reaction vessel which was attached on the target surface of ITO coated substrates for the fabrication of metal¯insulator¯semiconductor light emitting diode.[29] The micro channel not only works as the reaction chamber to control the reaction condition and position, but also acts as a bottom-up assemble vessel for multilayer assembly (ZnO NRs-insulating layer-solder).[29] Yang et al.[30] reported that ZnO nanorods can by locally synthesized on the micro-sized interdigitated electrode directly. The reaction solution was placed in a polydimethylsiloxane (PMDS) chamber which

was attached on the interdigitated electrode platform. After heating up the interdigitated electrode, the nanostructure was obtained on the electrode.[30]

In this chapter, a unique low-temperature, template-free approach to produce vertically aligned AZO NFs and ZnO NRs/AZO NFs hybrid structures will be demonstrated and its usage as the photoanode in DSSC will be investigated.[5] In particular, ZnO nanostructures with composite and structure control have been achieved using a simple and cost-effective solution process. As shown in Figure 7-1, an in-situ microfluidic control unit (MCU) was designed and applied into an aqueous solution reaction vessel. The applied MCU works as a supplier of separate reactant. The additive reactant solution can be supplied directly to the seeded substrates area in the reaction vessel.[5] This process is performed with the microchannel in the MCU driven by a syringe pump. It results in a localized reaction zone where the desired surface/sample was exposed, thus producing a localised nanostructure growth.[5] The fresh precursor chemicals in the bulk solutions are continuously supplied to the reaction area using the convective mass transfer,[26] and the additive reagent solution is continuously supplied during the growth of the nanostructures.[5] The advantages of this method include:[5] (1) The nanostructures are directly anchored on the desired surface areas without any extra assembly process (no need for doctor-blade or spin coating processes);[5] (2) The reagents (such as the Al source in this work) could be directly delivered to the pre-seeded reaction area which reduces any homogenous nucleation or consumption of the reagents in the bulk solution.[5] Therefore, the morphology and components of the vertically grown nanostructure on indium tin oxide (ITO) coated PET substrate can be readily controlled.[5] (3) ZnO NRs, AZO/ZnO hybrid nanostructures and AZO NFs are obtained vertically, which can meet the critical requirement (i.e., large accessible surfaces and long-range electronic connectivity) of a DSSCs photoanode.[5, 31, 32]

7.2 Results and Disscussion

7.2.1 Nanoflakes of photoanode

To verify the function and effect of the in-situ MCU in the aqueous solution synthesis process, one control experment group (AZ1-C, 1 mM) was designed using the conventional aqueous solution process (without in-situ MCU) with the same reactants and reaction conditions (i.e. temperature, solvent and duration) as the other samples. As shown in the SEM images (Figure 7-2 (a)), without applying the MCU, only needle-like ZnO NRs can be observed on the pre-seeded substrate.[5] On the other hand, sample (AZ1) prepared by applying the MCU in the aqueous solution synthesis with Al^{3+} reactant supply shows a hybrid nanostructures of needle-liked NRs and hexagonal NFs on ITO coated substrates. To clarify the substrate effects on the nanostructures, sample AZ1 had also been synthesised on one piece of ITO coated glass substrate (AZ1-G, 1 mM). The hybrid nanostructures obtained on ITO coated glass substrate (Figure 7-2 (b)) is similar to the hybrid nanostructures on ITO coated PET substrate (Figure 7-2 (c) & (d), AZ1, 1 mM). This observation indicated this morphology was not caused by the flexible PET substrates. The elemental composition of the nanostructures was investigated using EDS (as demonstrated in Figure 7-2 (e) & (f)). In the control group experiment (AZ1-C), the needle-liked NRs only contain Zn and O elements (Figure 7-2 (e)). The additive Al^{3+} does not involve the formation of the nanostructure, but only acts as the electrostatic control agent. The face-selective electrostatic control caused by Al^{3+} can suppress the side wall growth of ZnO NRs which resulted in ZnO needle-liked NRs.[33] In the sample AZ1, the elemental compositions of the NRs and NFs were confirmed using EDS analysis as shown in Figure 7-2 (f). In the obtained hybrid nanostructures, the needle-liked NRs only contain Zn and O elements but hexagonal

NF contains Zn, Al and O elements. The morphology and nanostructures can be tuned by varying the supply speeds or concentrations of the additives (i.e. Al reactants in this work) with the MCU in the synthesis process.[5] The top views of the resultant ZnO/AZO nanostructures prepared at various injected concentrations of the additive Al^{3+} sources are shown in Figure 7-2 (c) to (d) and Figure 7-3.[5]

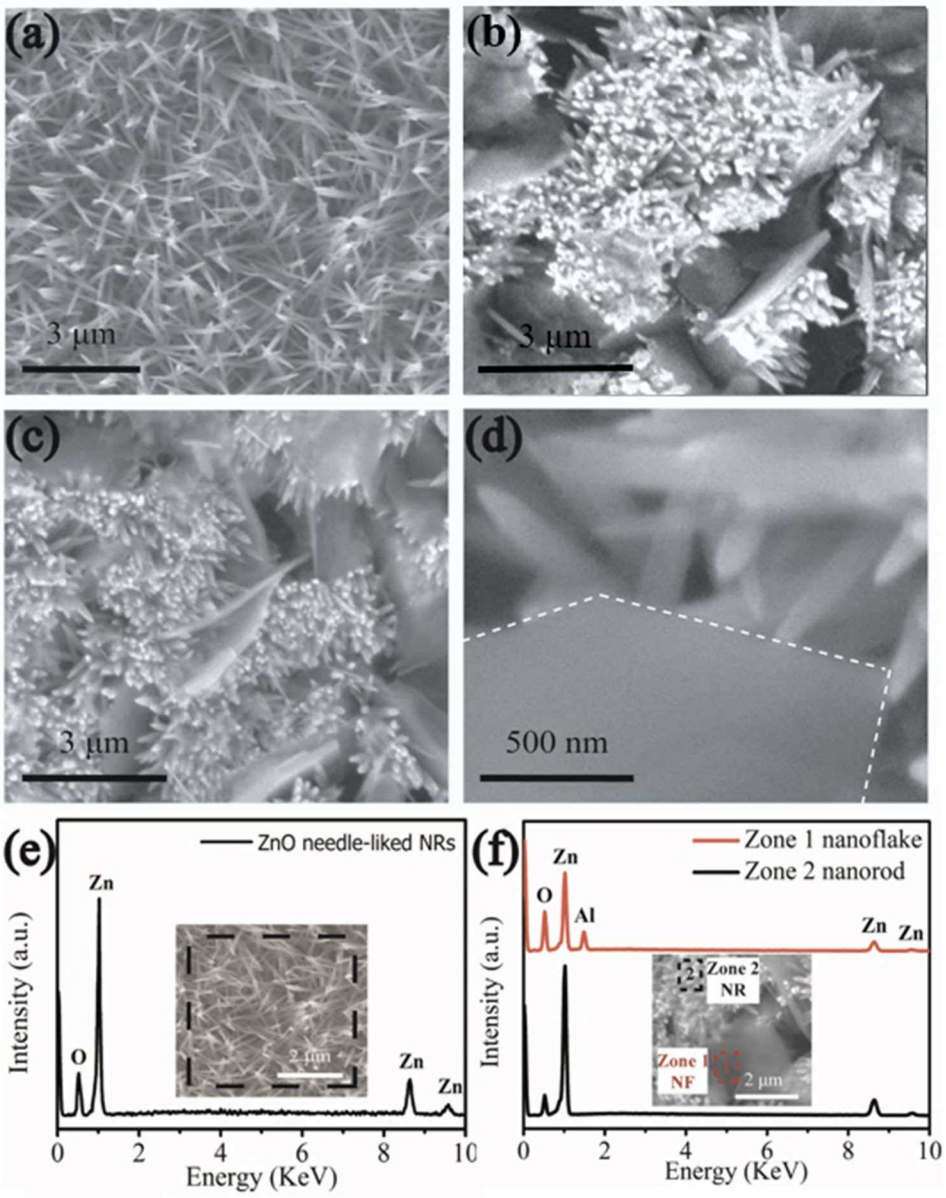

Figure 7-2 Top view SEM images of nanostructures prepared without/with MCU. (a) AZ1-C (1 mM, without MCU); (b) AZ1-G (1mM with MCU, on ITO coated glass substrate); (c) & (d) AZ1 (1mM with MCU); (e) and (f) corresponding EDS obtained from selected area in sample AZ1-C and AZ1, respectively. Inset SEM image in (e) & (f) with dash line rectangle indicate the EDS testing area respectively.[5]

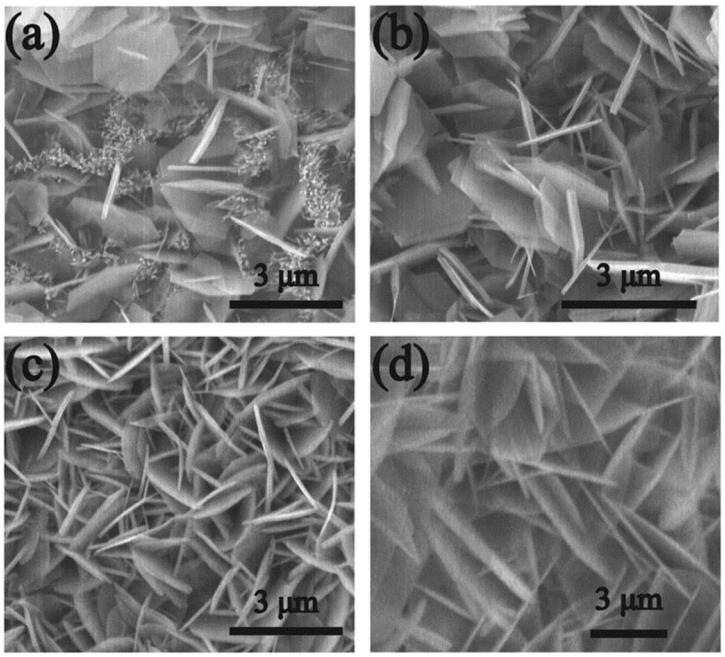

Figure 7-3 Top view SEM images of the ZnO/AZO nanostructures obtained with MCU by varying Al reactant supply concentration (a) to (d): (a) AZ2 (2 mM), (b) AZ3 (3 mM), (c) AZ4 (4 mM) and (d) AZ5 (5 mM).[5]

As demonstrated in the control experiment group, when the in-situ MCU was applied in the aqueous solution synthesis with Al^{3+} reactant supply, hybrid nanostructures of ZnO NRs and AZO NFs (Figure 7-2 (c) and (d), AZ1, 1 mM) were obtained.[5] With further increase of the supplied additives (Al reactant) concentration (2 to 5 mM), the morphology changed gradually (evolution of the nanostructures is shown in Figure 7-3 (a) to (d)).[5] The hexagonal-shaped AZO NFs gradually became dominant and were mostly interlaced with each other and perpendicular to the substrate surface. Under the synthesis conditions with lower injected concentrations of Al reactants (Figure 7-2 (c), AZ1, 1 mM), the needle-liked ZnO NRs were observed to be dominant in the resultant hybrid nanostructure.[5] As demonstrated in Figure 7-3 (a) to (b), increasing the Al reactant injection concentration (2 mM to 3 mM, i.e. AZ2 to AZ3) by using the MCU results in increased hexagonal AZO NFs instead of the needle-liked NRs. After increasing the Al reactant injected concentration up to 4 mM (AZ4), the hexagonal AZO NFs showed porous network structures with average pore sizes in a range of ~0.3-1

ı m.[5] Inter-connected AZO NFs are composed of interwoven plates with a thickness of 70-140 nm as shown in Figure 7-3 (c).[5] Upon further increasing the injected Al reactant concentrations up to 5 mM (AZ5), a porous network structure with larger sizes was observed (Figure 7-3 (d)). A similar phenomenon of film microstructure evolution was observed after varying the injection speeds of Al reagents (Figure 7-4 (a) to (c)).[5]

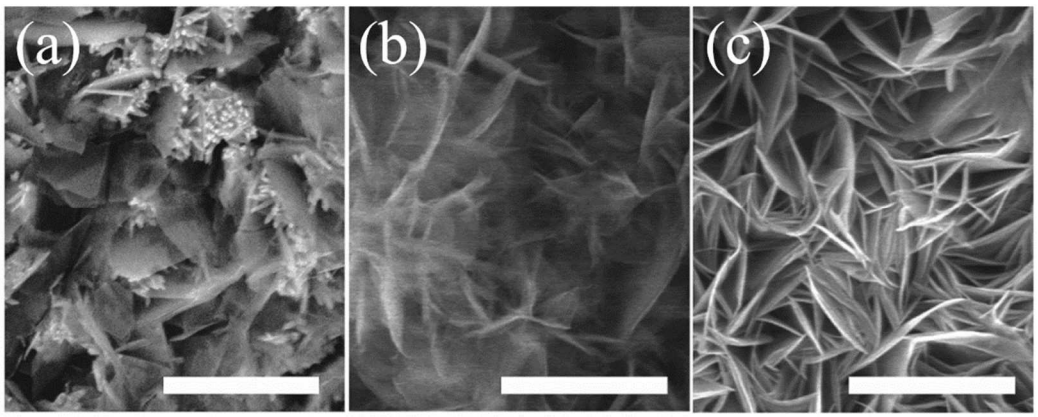

Figure 7-4 SEM images of AZO NFs films grown on ITO coated PET substrates with different injection speeds (a) 2 ml/hr-AZ1S (b) 3 ml/hr-AZ2S (c) 4 ml/hr-AZ3S. Scale bar in each image is 3 ≈m.[5]

Cross-sectional SEM images of the represented samples revealed that the ZnO NRs and the porous network AZO NFs all started to grow from the seed layer and were mostly perpendicular to the seed layer.[5] Figure 7-5 (a) clearly reveals that the AZ1 hybrid nanostructures are a mixture of needle-like ZnO NRs and AZO NFs. As shown in Figure 7-5 (b), the AZ2 sample has vertically aligned flake nanostructures on the substrate with an average lateral size of ~ 3.9 to 4.7 ≈m.[5] When the Al reactant injection concentration was increased to 4 mM (AZ4), a networking morphology of the NFs can be observed as shown in Figure 7-5 (c). Further increasing the Al reactant injection concentration up to 5 mM, the network morphology became dense and the NFs were found to connect at the roots (Figure 7-5 (d)).[5] This may be due to the increased growth rate caused by a higher reaction solution concentrations and increase of the NF size as they grew larger, which was commonly reported for growth of ZnO

nanostructures using the solution based process.[5, 34, 35] The formation of the NFs can be further confirmed from the TEM image shown in Figure 7-6 (a), which reveals a single AZO NF was obtained from the AZ4 with a hexagonal morphology.[5] The corresponding electron diffraction pattern is shown in the inset of Figure 7-6 (a) for the AZ4 NF along the [0001] zone axis, which is parallel to the vertical direction of its top-side. Clearly it indicates the single crystalline wurtzite structure of the AZO NFs.[5] This could also be verified from the XRD results shown in Figure 7-6 (e). Elemental analysis and its distribution of the AZ4 NF sample was carried out using the TEM together with the equipped EDS. Element mapping results shown in the Figure 7-6 (b) to (d) clearly reveal that Zn, Al and O elements are homogeneously distributed inside the AZO NFs.[5]

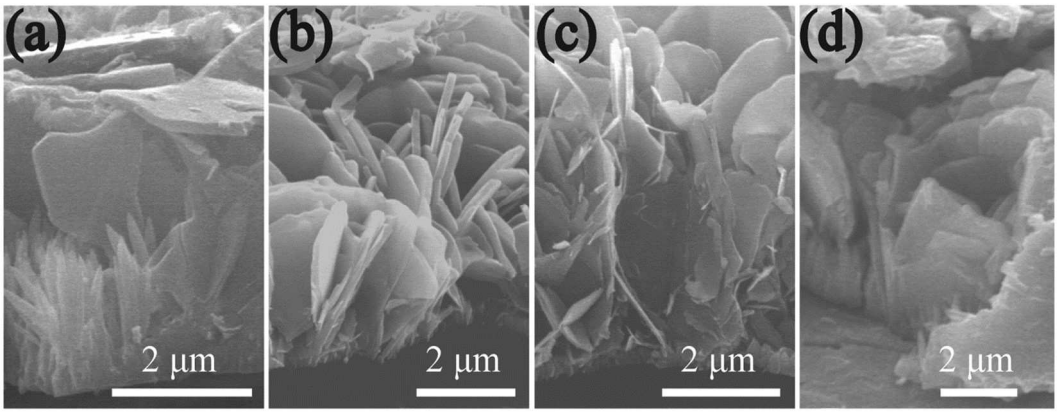

Figure 7-5 Side-view SEM images of represented AZO nanostructures (a) AZ1, (b) AZ2 (c) AZ4 and (d) AZ5.[5]

Evolution of the resultant nanostructures with changing additive reactant concentration can be explained using both `competing reaction_ and `heterogeneous nucleation growth_ mechanisms.[5, 22, 34] During nanostructure growth, the ZnO precursor (i.e. solution-phase $Zn(OH)_n^{2-n}$, $Zn(NH_3)_n^{2+}$, n=1,2,3,4) can either react with $Al(OH)_4^-$ to form AZO or react with OH^- to form ZnO.[5] For the reaction conditions used in this experiment (pH range of the solution used) with continuous Al^{3+} supplied by MCU , the ZnO precursor reacts preferentially with the Al complex (i.e. $Al(OH)_4^-$, etc.) because

it is thermodynamically favored.[5, 22, 36] During the growth process using the MCU, the Al^{3+} can be continuously delivered directly to the reaction zone, thus avoiding the possibility that most of Al reactants would be consumed by a homogeneous nucleation in the bulk solution.[5] Therefore, with the increase of the amount of Al^{3+} supplied to the reaction area (i.e. the solution surrounding the seeded substrate), the larger amount of Al complex will form during this period.[5] A large amount of Al complex will consume most of the ZnO precursor and thus suppress OH^- reaction with these precursors to from ZnO. Therefore, with the increased injection concentrations of Al reactant added by the MCU, the ZnO NRs grown from the seed-layer gradually change into the AZO NFs as observed from the SEM analysis.[5]

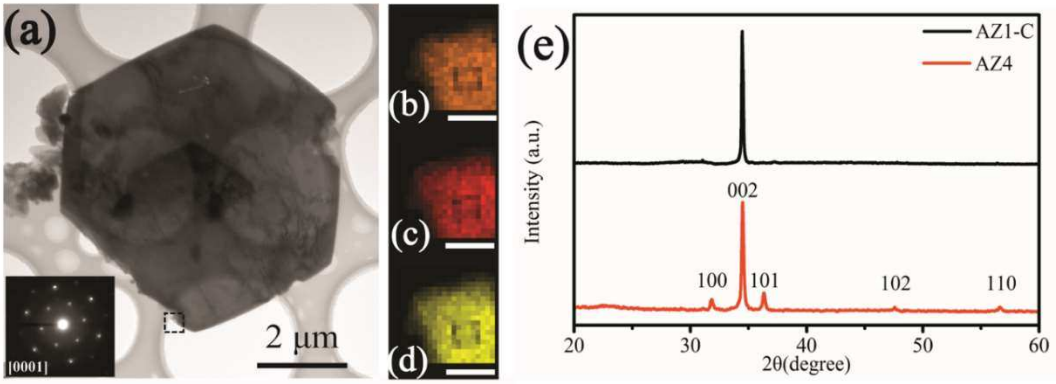

Figure 7-6 (a) TEM image of a single NF from AZ4; Insert is the corresponding selected area electron diffraction (SAED) pattern of AZ4; (b) to (d) Element mapping of Zn, Al and O in a selected area (high light by dot line cube in (a)) of the NF, scale bar is 100 nm. (e) XRD patterns of AZ1-C and AZ4 on PET substrates.[5]

The reZectivity of the nanostructured photoanode was firstly investigated to understand their scattering effect before being assembled into DSSCs. The diffuse reflectance UV-Vis spectra is shown in Figure 7-7, which was obtained from the nanostructured photoanodes (AZ1 to AZ5) before their sensitization process. Obviously, insignificant reflectivity (between 0 to 5 %) was observed in the UV range for all the tested photoanodes (AZ1 to AZ5).[5] This was caused by the strong UV absorption of wide-

band gap semiconductor (i.e. ZnO).[37] Additionally, all the tested photoanodes (AZ1 to AZ5) containing the AZO NFs showed higher reflectivity values in the wavelength ranges from 400 to 700 nm than those of the photoanode based on the pure ZnO NRs (AZ1-C).[5]

Figure 7-7 shows that there is an increase of the intensity of the reflection as the percentage of the AZO NFs is increased in the nanostructured photoanode. This indicated that the light scattering effects were increased from samples from AZ1-C, AZ1, and then to AZ2. The increase of the scattering effect in the range from 400 to 700 nm can be attributed to combined effects of hybrid nanostructures from both NRs and NFs.[38, 39] It can also be noticed that the intensities of the reflection started to decrease from samples of AZ2 to AZ5. This is probably because the AZO NFs started to be predominant in the hybrid nanostructure and their sizes (compare to NRs) could improve light trapping.[20]

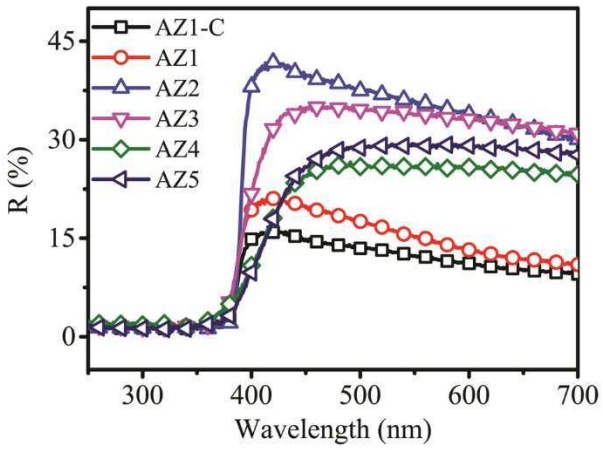

Figure 7-7 Diffuse reflectance spectra of the AZ1-C and AZ1 to AZ5 photoanode.[5]

7.2.2 Characterisation of the DSSCs

7.2.2.1 J-V testing

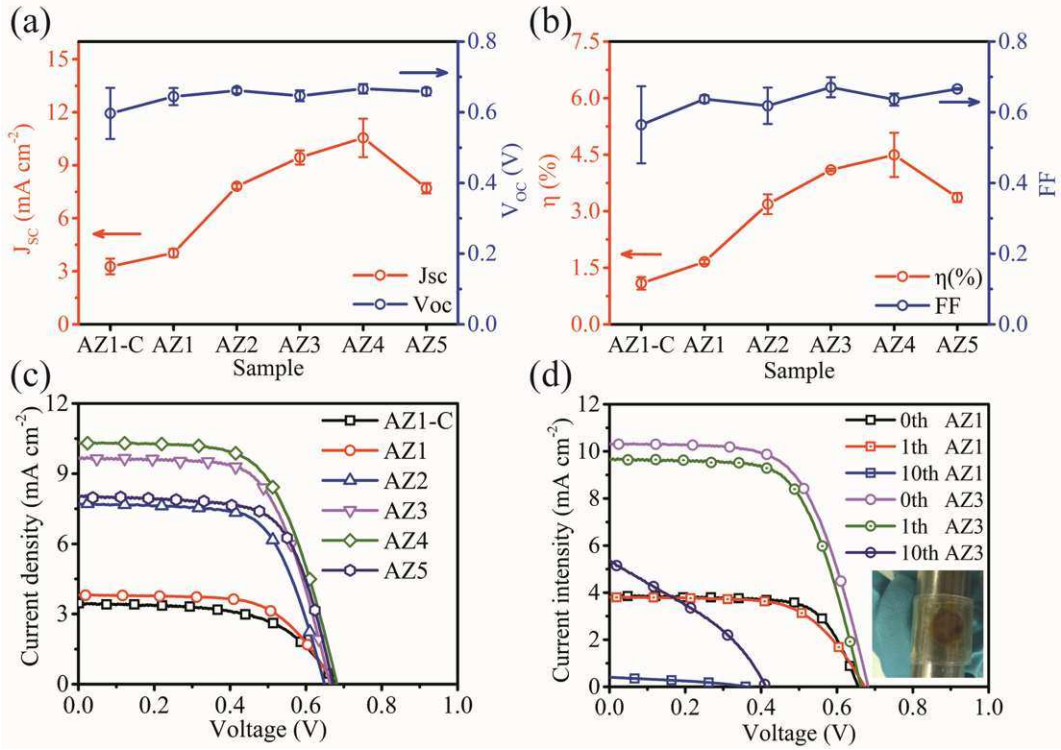

Figure 7-8 J-V characteristics of DSSCs assembled by nanostructured photoanode prepared under different Al reactant injection concentration. (a) and (b) the parameters of DSSCs extracted form J-V measurement. (c) the represented J-V curves of different structured photoanode under simulated AM1.5, 100 mW/cm^2 solar irradiation (d) J-V curves of DSSCs made by AZ1 and AZ3 after 1th and 10th cycle bending at bending radius of 10 mm. Inset: photography by wrapping the DSSCs around a 10 mm diameter steel rod.[5]

The resultant photoanodes were sensitised with N719 dye and then assembled into the DSSCs. The J-V testing was firstly carried out, and the key parameters of the solar cell performance extracted from the J-V curves are summarised in Figure 7-8 (a) and (b). Obviously, there is an enhancement of the DSSC performance after introducing the AZO NFs into the photoanode. The DSSCs based on ZnO NRs (AZ1-C) photoanode and ZnO NRs dominated (AZ1) hybrid nanostructured (NRs and NFs) photoanode showed that the average PCE value was 1.09% (Jsc = 3.27 mA cm^{-2}, V_{OC} = 0.59 V, FF = 0.56) and 1.66% (Jsc = 4.04 mA cm^{-2}, Voc = 0.64 V, FF = 0.64), respectively.[5] The performance of the DSSC was significantly improved by using the AZ2 as the photoanode, which obtained a higher Al reactant injection concentration (2 mM) than

those used in the AZ1. V alues of the J sc and Voc were both increased with typical values of 7.82 mA cm^{-2} and 0.66 V, respectively, achieving a PCE of 3.19%. With further increase of the injection concentration (3 mM to 4 mM, AZ3 to AZ4) supplied by the MCU during growth, the AZO NFs began to dominate in the hybrid nanostructures.[5] The performance parameters of the DSSCs based on the AZO NF dominant photoanodes (AZ3 and AZ4) showed average PCE values of 4.10% and 4.50%, respectively.[5] However, the DSSC based on AZ5 photoanode, which was obtained with the highest Al reactant injection concentration up to 5 mM in this study, has a decreased average PCE of 3.37% (J sc = 7.71 mA cm^{-2}, Voc = 0.66 V, FF = 0.67).[5]

7.2.2.2 Bending test

The DSSC samples were bent under different bending cycles under +180° to -180° cyclic bending at a radius of 10 mm. Figure 7-8 (d) shows the J-V characteristics of DSSCs made from the AZ1 and AZ3 photoanodes under different bending cycles.[5] It can be noticed that no significant degradation in the J-V performance of the DSSCs was observed after the cyclic bending. Recently, flexible DSSCs were extensively investigated in order to improve their performance (e.g. using new materials of transparent conducting film or planar-structure design of electrodes).[5, 40, 41] According to those studies, the mesoporous TiO_2 material layer was vulnerable to cracking and spallation.[5] After even one bending cycle, the performance of the devices was dramatically deteriorated. However, in this study, the performance of the DSSCs did not show apparent deterioration under cyclic bending (as shown in Figure 7-9). This suggests that the nanostructures indeed have good adhesion to the ITO coated flexible substrates and high resistance to cracking due to direct growth process.[5] However, as shown in Figure 7-8 (d), after bending from -180° to +180° with a bending speed at 0.1

Hz for 10 cycles, both the AZ1 and AZ3 devices showed degradation of their performance. The value of Jsc of the AZ1 was decreased from 3.81 to 0.40 mAXcm^{-2}, and the value of Voc was decreased from 0.67 to 0.36 V.[5]

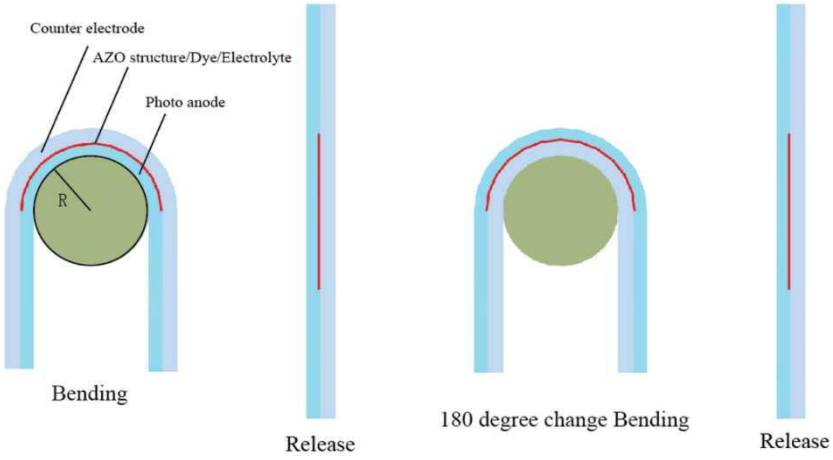

Figure 7-9 One complete bending test cycle : stretch-release-compression-release.[5]

For the AZO NF-dominated sample (AZ3), the Jsc value of DSSCs was decreased from 9.68 to 5.33 mA cm^{-2}, and the value of Voc was decreased from 0.66 to 0.41 V. During cyclic bending of the DSSCs, the nanostructured MO layer experienced significant repeated tensile/compressive strains.[5] This process apparently caused the fracture (and/or cracking) of the nanostructured MO photoanode, which may also cause the metal layer peeling off from the ITO conducting layer, thus significantly degrading the performance of the DSSCs.[5, 40, 41] Furthermore, the conducting property of the ITO electrode was degraded with increased bending cycles as shown in Figure 7-10. After 4 cycles of bending from -180º to +180º, the resistance of the ITO electrode was increased sharply. This degradation of the conducting layer should affect the performance of the DSSCs. This could be improved by using specially designed conducting electrodes (for examples, planar-structured electrodes, or double mesh electrode) and/or transparent conducting materials with good flexible properties (e.g. graphene) to replace the conventional sandwiched solar cell structures.[5, 40-42]

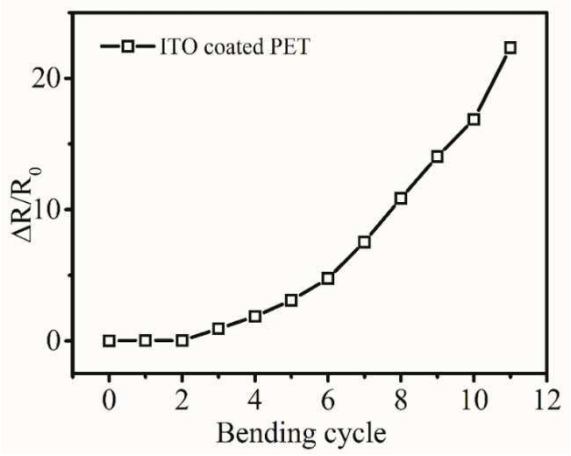

Figure 7-10 Electrical conductivities of ITO-PET substrates under different -180° to +180° bending cycles. R_0 and ΔR correspond to the sheet resistance of the ITO-PET substrates before and after bending.[5]

7.2.2.3 Dye loading evaluation

To gain a better insight into the improvement of the device performance, dye loading capability of the nanostructured photoanode was evaluated. The dye was desorbed from each sensitised photoanode into a typical desorption solution and measured using the UV–Vis spectrophotometer.

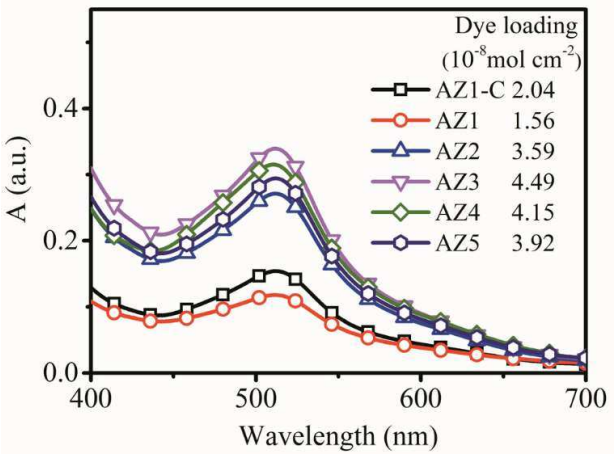

Figure 7-11 Absorption spectra of dye desorbed from AZ1-C and AZ1 to AZ5 films with an area of 1.6 cm^2. The insert table is dye loading of corresponding samples.[5]

Figure 7-11 shows the optical absorption spectra obtained from the solutions desorbed from each nanostructured photoanode. An increasing trend in dye-loading capabilities

with the increased Al reactant injection concentrations (0 mM to 4 mM, AZ1-C, AZ1 to AZ4) can be observed.[5] Compared with the pure ZnO NRs based photoanode (AZ1-C), nanostructured AZO NFs show a better dye loading capability. The improved dye loading capability is mainly because the increased internal surface areas (due to the formation of network porous structures of the AZO NFs) result in an increased dye loading, thus an improved light harvesting ability.[5]

However, compared with the pure ZnO NR based photoanode (AZ1-C), the AZ1 hybrid nanostructured photoanode did not show an apparent increase in the amount of dye loading like the other AZO based photoanodes. This is probably attributed to a reduction in the dye-accessible surface areas of the AZ1 photoanode nanostructure.[5] This could be caused by the following reasons: (1) Larger size AZO NFs (compared to the ZnO NRs in AZ1) grown in the rod-to-rod spaces of the ZnO NRs which could block the original surface area between a group of NRs (the spaces between rod to rod); (2) The amount of the NFs in the AZ1 is low and has not yet achieved a NFs network porous structure in this sample.[5, 43, 44] Although dye loading in the AZ1 hybrid structures was lower than that of the AZ1-C, all the key parameters of the DSSCs based on the AZ1 sample have been improved. Additionally, a similar trend was observed for the devices of AZ3 and AZ4.[5] Though the dye loading of the AZ4 sample was slightly lower than that of the AZ3, all the other key parameters of the DSSCs based on sample AZ4 were improved (Jsc = 10.55 mA cm^{-2}, Voc = 0.67 V, FF = 0.64), resulting in an increased PCE value of 4.50%.[5] It is noticeable that the AZ5 device showed decreased Jsc and PCE values but a relatively large Voc value. This could be attributed to the significant decrease in dye loading in the sample of AZ5 (as shown in Figure 7-11) which could be caused by the reduction of surface areas because of the connections of the roots of the nanostructures.[5, 35] Bai et al reported the enhancement of all the key

parameters of the DSSCs while dye loadings were decreased for a photoanode made from hybrid nanostructures of ZnO nanowires network within TiO_2 nanoparticle films.[5, 44] They found that proper amount of ZnO NRs embedded inside TiO_2 nanoparticle films could improve the overall performance of DSSCs although dye loading was reduced, due to the retardation of electron-recombination losses by improved electron mobility of the hybrid film.[5, 45, 46] It is worth noting that for the samples AZ3 and AZ4, solar cell performance, particularly the values of Voc and Jsc, were improved despite the slightly lower amount of adsorbed dye.[5] Specifically, the Voc value of the AZ4 is larger than that of the AZ3, which should be attributed to the suppressed electron-recombination in these devices. Therefore, it can be predicted that the performance of the DSSCs can be further enhanced by improving dye loading ability of AZO NFs based photoanodes.[5]

Normally, for the 1D &2D nanostructured photoanodes, a thicker nanostructured photoanode (i.e. the longer nanorods) could achieve a larger accessible surface area and thus improve dye loading ability of the photoanode, and the overall performance of the DSSC. Accordingly, the synthesis parameters used in the AZ4 photoanode (gives best DSSC performance in this study) were chosen to investigate the thickness effect of nanostructured photoanode (Figure 7-12). Figure 7-12 (a) reveals the thickness of the AZO nanostructure layer as a function of reaction time. It can be noticed that the growth during the reaction period of 0 hours to 4 hours is relatively fast. After 4 hours, the growth rate of the thickness of AZO nanostructured layer became slow. Similar to most solution based processes, long term reaction will results in the rapid growth of the nanostructures not only in length but also in diameter. As a result, the original separated nanostructures grow together, and the pores/spaces have been filled after a longer growth duration as shown in Figure 7-12 (b) to (d).

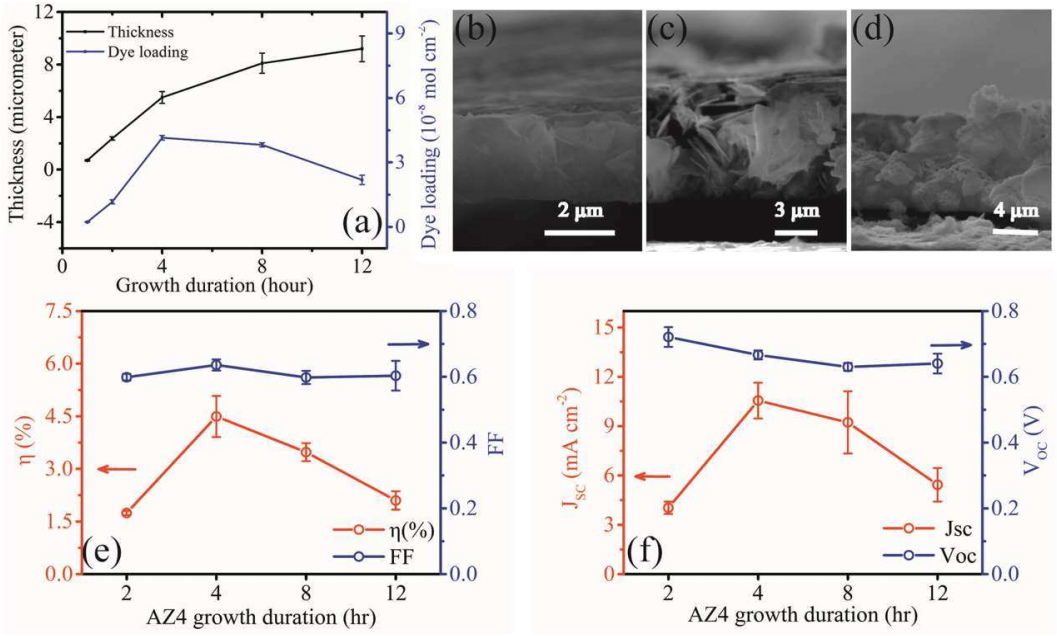

Figure 7-12 Dependence of the DSSCs on the growth duration under the injection concentration set to 4 mM. (a) film thickness plot as a function of growth time; (b) to (d) represented cross-section image of sample (b) AZ4¯2hr; (c) AZ4¯8hr; (d) AZ4-12hr, (e) PCE and FF (f) Jsc and Voc of DSSCs based on AZO nanostructure photoanodes prepared under different growth duration.[5]

This also explains the degradation of the dye loading capability with increase of film thickness as shown in Figure 7-12 (a). Performance parameters of the DSSCs made at different durations are summarised in Figure 7-12 (e) and (f). As expected, the reaction duration influenced the performance as it did in dye loading of the photoanodes. The effects can be separated into two stages: (1) The nanostructured layer keeps growing thicker with a large porosity; (2) The nanostructured layer keeps growing thicker and becomes dense. In the first stage (from 0 hours to 4 hours), increasing the reaction duration leads to a significant increase in the value of Jsc as well as the PCE of the DSSCs. Photoanode prepared after one-hour growth showed nearly no output due to its little dye loading. When the duration was increased from 2 hours to 4 hours, the values of Jsc and PCE were increased from about 4.2 to 11.1 mA cm^{-2}, 1.6 to 4.5 % respectively. When the reaction duration was further increased up to 12 hours, the

values of Jsc and PCE of the DSSCs started to decrease to 8.7 mA cm^{-2} and 2.3 %, respectively. As shown in the Figure 7-12 (b) to (d), during this second phase, long term reaction duration cause the structure widening and fusion together which results in reduction of accessible surface area for dye loading (as confirmed in Figure 7-12, dye loading degradation). Therefore, we can attribute the decreasing of the DSSC performance to the densification of the nanostructure after a long term reaction duration. The best performance of the device was achieved with the DSSC sample of AZ4 (after 4 hours growth), which had the highest dye loading in this study.[5]

7.2.2.4 Transient measurement

To evaluate the electron transport property and the suppression of charge-carrier recombination in these nanostructure photoanode based DSSCs, optoelectronic transient measurements were carried out. Figure 7-13 shows the electron transport and recombination kinetics for the DSSCs made from different photoanodes (AZ1-C, AZ1 to AZ5).[5] The charge carrier lifetime ($-_{e,}$) can be evaluated by extracting the information from optical perturbation voltage (voltage decay) measurements as shown in Figure 7-14 (a). The inset in Figure 7-14 (a) shows a representative result of optical perturbation voltage (voltage decay) in the Voc values as a function of time (black dots).[5] The red line shows in the inset is the curve-fitted results using a single exponential decay. [47] The resultant $-_e$ values of different samples obtained over a range of light intensities are plotted against the corresponding Voc value as shown in Figure 7-13 (a). It is noticed that the $-_e$ values were shifted to larger values with increasing injection concentrations of Al reactant (AZ1-C, AZ1 to AZ5), which demonstrated a similar trend to that of the Voc results as shown in Figure 7-8 (a).[5] This shows that the electron-recombination process was retarded. It can also be noticed that the $-_e$ values

are shifted significantly to larger values once the AZO NFs become dominated (AZ2 to AZ5).[5] The n-n$^+$ heterojunction could be formed between the ZnO based nanostructures and TiO_2 modification layers which would bring a built-in potential between them, thus suppressing the recombination. This build-in potential is proportional to the ratio of electron concentration between ZnO/AZO based nanostructures and TiO_2 modification layers. [5, 15, 48, 49] In this case, the AZO has a higher electron concentration than ZnO, thus the increased ratio of electron concentration between ZnO/AZO based nanostructure and TiO_2 modification layer results in a higher build-in potential, which further enhances the suppress of recombination.[5]

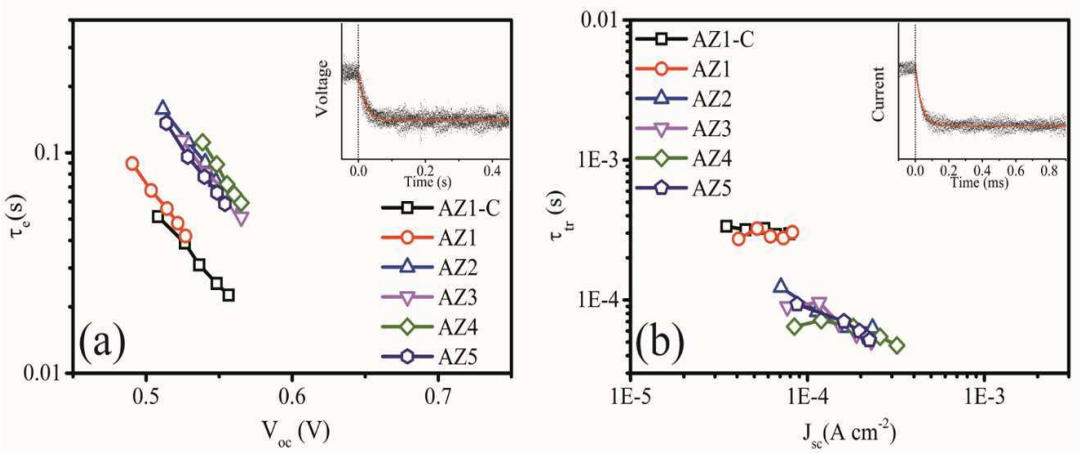

Figure 7-13 Electron transport and recombination kinetics for DSSCs made by different photoanode (AZ1-C, AZ1 to AZ5): (a) Electron lifetime constant extracted from devices with varying pulse light intensity. (b) Electron transport constant estimated from current transient decay obtained under different pulse intensity. Insert of each image is an example of voltage-transient/ current transient with an exponential decay fit, respectively.[5]

The benefits of reduced charge carrier recombination in the AZO dominated samples can also be viewed in the dark current measurements as shown in Figure 7-14. It is generally agreed that, in the dark condition, the potential distribution across the cell is different from that under illumination.[5] The dark current proceeds from the reduction

of I^{3-} by the electrons on the ITO electrode.[5, 44] It causes a decrease in photocurrent due to recombination, and can be used to estimate the extent of the back electron transfer.[5, 44] In Figure 7-14, the dark current as a function of sweep voltage was demonstrated. The measurements of the nanostructure based DSSC (AZ1-C, AZ1 to AZ5) showed a shift to a higher potential value and the dark current became smaller at the same potential (i.e. 0.6 V). [5]

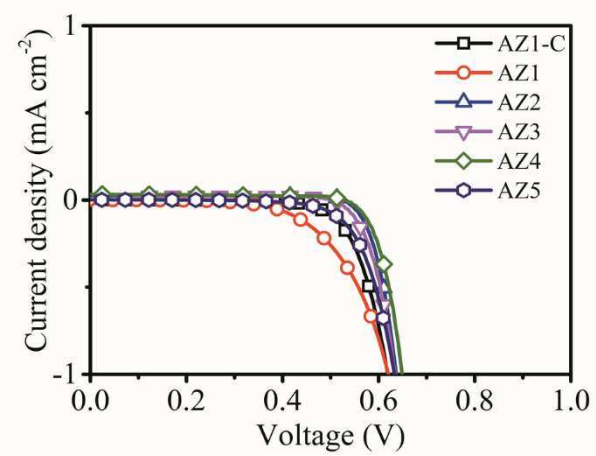

Figure 7-14 J-V characteristics of DSSCs based on nanostructures photoanode prepared under different injection concentration in dark condition.[5]

These observations agreed with our electron lifetime constant results as shown in Figure 7-13 (a) indicating a lower recombination rate between the transferred electrons and I^{3-} ions for the AZO dominated photoanodes. To verify the assumption that the AZO NFs could improve the electron mobility of the DSSC photoanode, the current transient measurements were performed at short circuit conditions for the DSSCs made by AZ1-C to AZ5 photoanode.[5] Each transient result was fitted by a single exponential decay as shown in the inset of Figure 7-13 (b) for one representative example. The electron transport time constant (τ_{tr}) of different samples obtained over a range of light intensities are plotted against the corresponding Jsc values as shown in Figure 7-13 (b). The samples of AZ2 to AZ5 did not show significant differences in the value of τ_{tr}, however,

their time constants are significantly lower than those of the AZ1-C and AZ1.[5] Again, the AZO NF dominated sample group shows a significant shift of electron transport time when compared with those of the ZnO-dominated samples. Consequently, the enhanced PCE of the AZO NF dominated samples (AZ2 to AZ5) can be attributed to the network structures with less grain boundaries and defects, thus realising the suppressed recombination for a fast electron transport, longer electron lifetime.[5, 50] Similar trends have also been observed in AZO NRs based DSSCs by Sining et al [5, 51], and they reported that the Al doped ZnO NRs showed a remarkable enhancement of performance because of their increased electrical conductivity compare to those of the pure ZnO NRs.[5]

7.3 Summary

An in-situ MCU in an aqueous solution synthesis process was developed to achieve a controllable approach to obtain AZO NFs and ZnO/AZO hybrid structures directly on flexible polymer substrates. Results from TEM, EDS and XRD analysis confirm that the morphology and composition of the nanostructure can be readily changed from crystalline ZnO NRs, to a hybrid structures of ZnO NRs/AZO NFs, and finally to AZO NFs. We then demonstrated that flexible DSSCs can be fabricated based on these nanostructures, and diffuse reflectance spectra suggested that the light-trapping efficiency of the AZO nanostructures was improved over those of the pure ZnO NRs due to an effective light-scattering caused by the NFs and hybrid nanostructures. The AZO NFs vertically aligned on the flexible substrates improved the accessible surfaces (i.e. benefit from improving dye loading) with a demand for a long range electronic connectivity (i.e. benefit for reducing recombination). As a result, the power conversion efficiency of the AZO-based DSSCs has been improved. The current transient study

indicated that electron transport property of AZO samples has been improved and recombination in the AZO dominated samples has been suppressed. This in-situ MCU aqueous solution method is promising for low cost, low temperature and efficient fabrication of hybrid nanostructures due to its simple setup and reliability.[5]

Reference

1. Tian, J., Z. Zhao, A. Kumar, R.I. Boughton, and H. Liu, Recent progress in design, synthesis, and applications of one-dimensional TiO_2 nanostructured surface heterostructures: a review. Chemical Society Reviews, 2014. 43(20): p. 6920-6937.
2. Surojit, C., C. Li-Chyong, and C. Kuei-Hsien, Energy production and conversion applications of one-dimensional semiconductor nanostructures. NPG Asia Mater, 2011. 3: p. 74-81.
3. Concina, I. and A. Vomiero, Metal Oxide Semiconductors for Dye- and Quantum-Dot-Sensitized Solar Cells. Small, 2015. 11(15): p. 1744-1774.
4. Xu, S. and Z. Wang, One-dimensional ZnO nanostructures: Solution growth and functional properties. Nano Research, 2011. 4(11): p. 1013-1098.
5. Zhao, C., J. Zhang, Y. Hu, N. Robertson, P.A. Hu, D. Child, D. Gibson, and Y.Q. Fu, In-situ microfluidic controlled, low temperature hydrothermal growth of nanoflakes for dye-sensitized solar cells. scientific reports, 2015. 5: p. 17750.
6. Wu, W.Q., H.S. Rao, Y.F. Xu, Y.F. Wang, C.Y. Su, and D.B. Kuang, Hierarchical Oriented Anatase TiO_2 Nanostructure arrays on Flexible Substrate for Efficient Dye-sensitized Solar Cells. scientific reports, 2013. 3: p. 1892.
7. Qiu, J., M. Guo, and X. Wang, Electrodeposition of hierarchical ZnO nanorod-nanosheet structures and their applications in dye-sensitized solar cells. ACS Applied Materials & Interfaces, 2011. 3(7): p. 2358-67.
8. Liao, J.Y., B.X. Lei, H.Y. Chen, D.B. Kuang, and C.Y. Su, Oriented hierarchical single crystalline anatase TiO_2 nanowire arrays on Ti-foil substrate for efficient flexible dye-sensitized solar cells. Energy & Environmental Science, 2012. 5(2): p. 5750-5757.
9. Vomiero, A., I. Concina, M.M. Natile, E. Comini, G. Faglia, M. Ferroni, I. Kholmanov, and G. Sberveglieri, ZnO/TiO_2 nanonetwork as efficient photoanode in excitonic solar cells. Applied Physics Letters, 2009. 95(19): p. 193104.
10. Guerin, V. M. and T. Pauporte, From nanowires to hierarchical structures of template-free electrodeposited ZnO for efficient dye-sensitized solar cells. Energy & Environmental Science, 2011. 4(8): p. 2971-2979.
11. Zhong, D., B. Cai, X. Wang, Z. Yang, Y. Xing, S. Miao, W.-H. Zhang, and C. Li, Synthesis of oriented TiO_2 nanocones with fast charge transfer for perovskite solar cells. Nano Energy, 2015. 11(0): p. 409-418.
12. Lu, H., W. Tian, J. Guo, and L. Li, Interface Engineering through Atomic Layer Deposition towards Highly Improved Performance of Dye-Sensitized Solar Cells. Sci. Rep., 2015. 5.
13. Anta, J.A., E. Guill¶n, and R. Tena-Zaera, ZnO-Based Dye-Sensitized Solar Cells. The Journal of Physical Chemistry C, 2012. 116(21): p. 11413-11425.
14. Qian, J., P. Liu, Y. Xiao, Y. Jiang, Y. Cao, X. Ai, and H. Yang, TiO_2-Coated Multilayered SnO_2 Hollow Microspheres for Dye-Sensitized Solar Cells. Advanced Materials, 2009. 21(36): p. 3663-3667.
15. Zhang, Q., C.S. Dandeneau, X. Zhou, and G. Cao, ZnO Nanostructures for Dye-Sensitized Solar Cells. Advanced Materials, 2009. 21(41): p. 4087-4108.
16. Jagadamma, L.K., M. Al-Senani, A. El-Labban, I. Gereige, G.O. Ngongang Ndjawa, J.C.D. Faria, T. Kim, K. Zhao, F. Cruciani, D.H. Anjum, M.A. McLachlan, P.M. Beaujuge, and A. Amassian, Polymer Solar Cells with Efficiency > 10% Enabled via a Facile Solution-Processed Al-Doped ZnO Electron Transporting Layer. Advanced Energy Materials, 2015: p. n/a-n/a.
17. Yun, S., J. Lee, J. Yang, and S. Lim, Hydrothermal synthesis of Al-doped ZnO nanorod arrays on Si substrate. Physica B: Condensed Matter, 2010. 405(1): p. 413-419.
18. Baxter, J.B. and E.S. Aydil, Nanowire-based dye-sensitized solar cells. Applied Physics Letters, 2005. 86(5): p. 053114.

19. Lee, D. J., H. M. Kim, J. Y. Kwon, H. Choi, S. H. Kim, and K. B. Kim, Structural and Electrical Properties of Atomic Layer Deposited Al-Doped ZnO Films. Advanced Functional Materials, 2011. 21(3): p. 448-455.
20. Yin, P.-F., T. Ling, Y. R. Lu, Z. W. Xu, S. Z. Qiao, and X.-W. Du, CdS Nanoflake Arrays for Highly Efficient Light Trapping. Advanced Materials, 2015. 27(4): p. 740-745.
21. Mahmood, K., R. Munir, B.S. Swain, G.-S. Han, B.-J. Kim, and H.S. Jung, Study on the enhanced and stable field emission behavior of a novel electrosprayed Al-doped ZnO bilayer film. RSC Advances, 2014. 4(18): p. 9072-9077.
22. Cho, S., S.-H. Jung, J.-W. Jang, E. Oh, and K.-H. Lee, Simultaneous Synthesis of Al-Doped ZnO Nanoneedles and Zinc Aluminum Hydroxides through Use of a Seed Layer. Crystal Growth & Design, 2008. 8(12): p. 4553-4558.
23. Rahman, M.M., M.K.R. Khan, M.R. Islam, M.A. Halim, M. Shahjahan, M.A. Hakim, D.K. Saha, and J.U. Khan, Effect of Al Doping on Structural, Electrical, Optical and Photoluminescence Properties of Nano-Structural ZnO Thin Films. Journal of Materials Science & Technology, 2012. 28(4): p. 329-335.
24. Liu, J., L. Xu, B. Wei, W. Lv, H. Gao, and X. Zhang, One-step hydrothermal synthesis and optical properties of aluminium doped ZnO hexagonal nanoplates on a zinc substrate. CrystEngComm, 2011. 13(5): p. 1283-1286.
25. Li, Z., Y. Zhou, G. Xue, T. Yu, J. Liu, and Z. Zou, Fabrication of hierarchically assembled microspheres consisting of nanoporous ZnO nanosheets for high-efficiency dye-sensitized solar cells. Journal of Materials Chemistry, 2012. 22(29): p. 14341-14345.
26. Qiu, Y., W. Chen, and S. Yang, Facile hydrothermal preparation of hierarchically assembled, porous single-crystalline ZnO nanoplates and their application in dye-sensitized solar cells. Journal of Materials Chemistry, 2010. 20(5): p. 1001-1006.
27. Shi, Y., C. Zhu, L. Wang, W. Li, C. Cheng, K.M. Ho, K.K. Fung, and N. Wang, Optimizing nanosheet-based ZnO hierarchical structure through ultrasonic-assisted precipitation for remarkable photovoltaic enhancement in quasi-solid dye-sensitized solar cells. Journal of Materials Chemistry, 2012. 22(26): p. 13097-13103.
28. Wu, D., Z. Gao, F. Xu, Z. Shi, W. Tao, and K. Jiang, Nanosheet-based hierarchical ZnO structure decorated with TiO_2 particles for enhanced performance in dye-sensitized solar cell. CrystEngComm, 2012. 14(23): p. 7934-7941.
29. Joo, J., B.Y. Chow, M. Prakash, E.S. Boyden, and J.M. Jacobson, Face-selective electrostatic control of hydrothermal zinc oxide nanowire synthesis. Nat Mater, 2011. 10(8): p. 596-601.
30. Yang, D., D. Kim, S.H. Ko, A.P. Pisano, Z. Li, and I. Park, Focused Energy Field Method for the Localized Synthesis and Direct Integration of 1D Nanomaterials on Microelectronic Devices. Advanced Materials, 2015. 27(7): p. 1207-1215.
31. Docampo, P., S. Guldin, U. Steiner, and H.J. Snaith, Charge Transport Limitations in Self-Assembled TiO_2 Photoanodes for Dye-Sensitized Solar Cells. The Journal of Physical Chemistry Letters, 2013. 4(5): p. 698-703.
32. Crossland, E.J.W., N. Noel, V. Sivaram, T. Leijtens, J.A. Alexander-Webber, and H.J. Snaith, Mesoporous TiO_2 single crystals delivering enhanced mobility and optoelectronic device performance. Nature, 2013. 495(7440): p. 215-219.
33. Nazeeruddin, M.K., A. Kay, I. Rodicio, R. Humphry-Baker, E. Mueller, P. Liska, N. Vlachopoulos, and M. Graetzel, Conversion of light to electricity by cis-X2bis(2,2'-bipyridyl-4,4'-dicarboxylate)ruthenium(II) charge-transfer sensitizers (X = Cl-, Br-, I-, CN-, and SCN-) on nanocrystalline titanium dioxide electrodes. Journal of the American Chemical Society, 1993. 115(14): p. 6382-6390.
34. Chen, H., F. Zhang, S. Fu, and X. Duan, In Situ Microstructure Control of Oriented Layered Double Hydroxide Monolayer Films with Curved Hexagonal Crystals as Superhydrophobic Materials. Advanced Materials, 2006. 18(23): p. 3089-3093.

35. Xu, C., J. Wu, U.V. Desai, and D. Gao, Multilayer Assembly of Nanowire Arrays for Dye-Sensitized Solar Cells. Journal of the American Chemical Society, 2011. 133(21): p. 8122-8125.
36. Liu, J., X. Huang, Y. Li, K.M. Sulieman, X. He, and F. Sun, Facile and Large-Scale Production of ZnO/Zn–Al Layered Double Hydroxide Hierarchical Heterostructures. The Journal of Physical Chemistry B, 2006. 110(43): p. 21865-21872.
37. Wang, M., F. Ren, J. Zhou, G. Cai, L. Cai, Y. Hu, D. Wang, Y. Liu, L. Guo, and S. Shen, N Doping to ZnO Nanorods for Photoelectrochemical Water Splitting under Visible Light: Engineered Impurity Distribution and Terraced Band Structure. scientific reports, 2015. 5: p. 12925.
38. Joshi, P., L. Zhang, D. Davoux, Z. Zhu, D. Galipeau, H. Fong, and Q. Qiao, Composite of TiO_2 nanofibers and nanoparticles for dye-sensitized solar cells with significantly improved efficiency. Energy & Environmental Science, 2010. 3(10): p. 1507-1510.
39. Terakawa, M., Y. Tanaka, G. Obara, T. Sakano, and M. Obara, Randomly-grown high-dielectric-constant ZnO nanorods for near-field enhanced Raman scattering. Applied Physics A, 2011. 102(3): p. 661-665.
40. Li, H., Q. Zhao, W. Wang, H. Dong, D. Xu, G. Zou, H. Duan, and D. Yu, Novel Planar-Structure Electrochemical Devices for Highly Flexible Semitransparent Power Generation/Storage Sources. Nano Letters, 2013. 13(3): p. 1271-1277.
41. Li, H., Q. Zhao, H. Dong, Q. Ma, W. Wang, D. Xu, and D. Yu, Highly-flexible, low-cost, all stainless steel mesh-based dye-sensitized solar cells. Nanoscale, 2014. 6(21): p. 13203-13212.
42. Zhang, J., P. Hu, X. Wang, Z. Wang, D. Liu, B. Yang, and W. Cao, CVD growth of large area and uniform graphene on tilted copper foil for high performance flexible transparent conductive film. Journal of Materials Chemistry, 2012. 22(35): p. 18283-18290.
43. Zhang, S., X. Yang, Y. Numata, and L. Han, Highly efficient dye-sensitized solar cells: progress and future challenges. Energy & Environmental Science, 2013. 6(5): p. 1443-1464.
44. Bai, Y., H. Yu, Z. Li, R. Amal, G.Q. Lu, and L. Wang, In Situ Growth of a ZnO Nanowire Network within a TiO_2 Nanoparticle Film for Enhanced Dye-Sensitized Solar Cell Performance. Advanced Materials, 2012. 24(43): p. 5850-5856.
45. Guillen, E., E. Azaceta, L.M. Peter, A. Zukal, R. Tena-Zaera, and J.A. Anta, ZnO solar cells with an indoline sensitizer: a comparison between nanoparticulate films and electrodeposited nanowire arrays. Energy & Environmental Science, 2011. 4(9): p. 3400-3407.
46. Kieven, D., T. Dittrich, A. Belaidi, J. Tornow, K. Schwarzburg, N. Allsop, and M. Lux-Steiner, Effect of internal surface area on the performance of ZnO/In_2S_3/CuSCN solar cells with extremely thin absorber. Applied Physics Letters, 2008. 92(15): p. 153107.
47. Correa Baena, J.P. and A.G. Agrios, Antimony-Doped Tin Oxide Aerogels as Porous Electron Collectors for Dye-Sensitized Solar Cells. The Journal of Physical Chemistry C, 2014. 118(30): p. 17028-17035.
48. Park, K., Q. Zhang, B.B. Garcia, X. Zhou, Y.H. Jeong, and G. Cao, Effect of an ultrathin TiO_2 layer coated on submicrometer-sized ZnO nanocrystallite aggregates by atomic layer deposition on the performance of dye-sensitized solar cells. Adv Mater, 2010. 22(21): p. 2329-32.
49. Park, K., Q. Zhang, B.B. Garcia, and G. Cao, Effect of Annealing Temperature on TiO_2–ZnO Core–Shell Aggregate Photoelectrodes of Dye-Sensitized Solar Cells. The Journal of Physical Chemistry C, 2011. 115(11): p. 4927-4934.
50. Wu, W. Q., B. X. Lei, H. S. Rao, Y. F. Xu, Y. F. Wang, C. Y. Su, and D.-B. Kuang, Hydrothermal Fabrication of Hierarchically Anatase TiO_2 Nanowire arrays on FTO Glass for Dye-sensitized Solar Cells. scientific reports, 2013. 3: p. 1352.

51. Yun, S., J. Lee, J. Chung, and S. Lim, Improvement of ZnO nanorod-based dye-sensitized solar cell efficiency by Al-doping. Journal of Physics and Chemistry of Solids, 2010. 71(12): p. 1724-1731.

Chapter 8 Conclusions and future work

8.1 Conclusions

Various ZnO based nanostructures and anatase TiO_2 modification layers have been successfully prepared using low-temperature synthesis processes in this thesis. The morphology control factors were firstly studied, including solution reaction conditions (i.e. concentration, temperature and duration) and deposition parameters (i.e. gas flow rate, plasma energy and duration). The material properties (i.e. morphology, optical properties and crystal structure) of the obtained nanostructures as well as the influences of these resultant nanostructures properties on the DSSCs performance have been investigated. Crystallised metal oxides (ZnO, TiO_2, ZnO-TiO_2, AZO-TiO_2) have been successfully achieved using the low-temperature synthesis methods. They demonstrated easy morphology control as well as good photoanode properties. Followings are some detailed conclusions form this thesis:

- Temperature, concentration and duration played important roles in the growth and morphology control in the reaction solution only containing $Zn(NO_3)_2$ and $(CH_2)_6N_4$, which demonstrated a good controllable growth of short ZnO NRs (0-4 ı m).
- Ammonia involved in the alkali aqueous solution with the PEI used as additives could be used for achieving longer ZnO NRs (0-15 ı m). The calculated solubility can be used as an indicator for supersaturation which has a strong relationship with ZnO NRs growth. Crystalline and optical properties of the as-prepared ZnO NRs samples by variable reaction factors indicated all the ZnO NRs samples are single crystalline with highly oriented wurtzite structure.
- With plasma assistant deposition, the resultant film showed anatase phase,

increased hardness and Young˘s modulus, and most importantly, increased photocatalytic stability and efficiency. The formation of anatase phase after using the plasma assistance is mainly responsible for the improvement in the photocatalytic efficiency.

¿ The good electron transport properties of result nanostructure based photoanodes in DSSCs are confirmed by dark J-V, EIS and photo-current decay experiment. Using 3 ı m ZnO NRs alone as photoanode, the resultant DSSC only achieved 0.27%. With the different durations of TiO_2 modification on top of ZnO NRs, the overall PCE can be extended to 1.8%. Using the optimised TiO_2 modification duration modified on top of longer ZnO NRs, a higher PCE (3.0%) can be obtained.

¿ We demonstrated a novel in-situ MCU assistant aqueous solution synthesis which achieved Al-doped ZnO nanostructures (ZnO/AZO hybrid and AZO NFs) directly on flexible ITO-PET substrates. The XRD, SEM, TEM and EDS studies showed morphology and composition of the nanostructures can be readily changed from crystalline ZnO NRs, to a hybrid structures of ZnO NRs/AZO NFs, and finally to AZO NFs.

¿ After applied TiO_2 modification layer on these nanostructures, the flexible DSSCs have been fabricated and studied. The properly controlled morphology of AZO nanostructured photoanode demonstrated increased dye loading capability. Transient current/voltage study shown the improved electron transport property of resultant DSSC as well as suppressed recombination. Result in an improved PCE (4.5%)

8.2 Suggested future work

Various kinds of new absorber materials (i.e. new dyes, perovskite-methylammonium lead trihalide) and electrolytes have been emerging from the continuous development of the DSSCs. In this regard, the development of photoanode plays an important role in improving the overall efficiency. Additionally, the material cost of the photoanode and the complexity of the preparation processes directly affect the production and application potential. Therefore, good metal oxide photoanodes will be an important development direction for achieving cost effective DSSCs.

The following work is suggested in the specific areas list below:

- Improvement in aqueous solution process. NRs with controllable density and desirable crystal growth direction is one of the key aspects for the DSSC and its applications. We demonstrated using the PEI for aspect ratio control as well as improving utilization of the reactants by suppressing nucleation in the bulk solution. The preliminary results with reasonable improved growth rate and long NRs with high aspect ratio were achieved in this thesis. However, there are difficulties in preventing growth of roots of the NRs (i.e. NRs growth together) for much longer NRs and/or varying the NRs density in a thin to dense range would give more opportunities for the performance in DSSCs and related solar cell applications. Local catalyst synthesis would be an alternative option for achieving a better morphology control (i.e. density and aspect ratio).
- Improvement of the in-situ MCU assistant aqueous solution process. In this thesis, a novel in-situ MCU was developed and demonstrated its advantages on performing localised reactions for achieving Al doped ZnO nanostructure. Further improvement of this process would give a better understanding of the solution

growth mechanisms with fluid dynamics. Further using this method with localised heating and microfluidic channel may achieve a programmable nanostructure growth at the target positions. This would be beneficial to complex nanostructure synthesis and optical trapping (i.e. gradient control of nanostructure in liner scale) for the DSSC applications. It is also believed that similar approach of this method can be used for the synthesis other metal oxide (i.e. TiO_2, MoO_3, NiO and MgO) materials.

¿ DSSC development of using newly designed electrolyte and absorber. Liquid electrolyte based DSSCs generally suffer leakage and long-term durability problems. However, solid electrolyte generally causes poor-filling on the conventional particulate based mesoporous photoanodes which result in a reduced effective electron diffusion length to few micrometers thus degradation of overall DSSCs performance. The nanostructured photoanodes produced in this thesis can be used as an alternative approach for solving poor pore-filling problem. Thus it would be interesting to test these photoanodes for their performance in solid DSSCs and study electron transport dynamic. This further study may lead to development of optimised photoanodes for the solid state DSSCs. Further exploration of the potentials of these nanostructure photoanodes with new absorbers could also be an option for achieving high performance DSSCs. Chemical stability of resultant nanostructure under different absorber loading environments also needs to be evaluated.

Appendix

Matlab codes used for ZnO solubility calculation

```
clear;
close all;

global OH Kzoh1 Kzoh2 Kzoh3 Kzoh4 Kznh1 Kznh2 Kznh3 Kznh4 Kzhn Kzox
Cn

%values definition

Kzoh1 = 5.0;
Kzoh2 = 11.1;
Kzoh3 = 13.6;
Kzoh4 = 14.8;
Kznh1 = 2.21;
Kznh2 = 4.5;
Kznh3 = 6.86;
Kznh4 = 8.89;
Kzox=-15.52;
Kzhn = 4.39;

number = 100;
Cn = 0;
Rmax = 1; % Nitrogen concent change numbers
step = 14/(number-1);
k = 0:step:14;

% allocate storage space
NH3 = zeros(number,Rmax);

Z = zeros(number,Rmax);
ZOH1 = zeros(number,Rmax);
ZOH2 = zeros(number,Rmax);
ZOH3 = zeros(number,Rmax);
ZOH4 = zeros(number,Rmax);
ZN1 = zeros(number,Rmax);
ZN2 = zeros(number,Rmax);
ZN3 = zeros(number,Rmax);
ZN4 = zeros(number,Rmax);
Ztot = zeros(number,Rmax);

NZ = zeros(number,Rmax);
NZOH1 = zeros(number,Rmax);
NZOH2 = zeros(number,Rmax);
NZOH3 = zeros(number,Rmax);
NZOH4 = zeros(number,Rmax);
NZN1 = zeros(number,Rmax);
NZN2 = zeros(number,Rmax);
```

```
NZN3 = zeros(number,Rmax);
NZN4 = zeros(number,Rmax);
NZChP = zeros(number,Rmax);
NZChN = zeros(number,Rmax);
NZNonCh = zeros(number,Rmax);

figure;

for j=1:Rmax
    Cn = Cn + 0.2;
    for i=1:number
        pH = step*(i-1);
        OH = 10^(pH-14);
        %solver
        x0 = 0.1;
        options = optimset('Display',
'off','NonlEqnAlgorithm','dogleg','LargeScale','off','MaxFunEvals',5
000,'MaxIter', 500, 'TolFun',1e-9, 'TolX', 1e-4 );
        [S, fval, exitflag,output] = fsolve(@revisit,x0,options);
            % S(1)-> NH3

        if exitflag == 0
            disp('number of iternation, evaluation exceeded.');
        else if exitflag == -1
                disp('Algorithm terminated by output function.');
            else if exitflag == -2
                    disp('Algorithm appears to be converging a
noon-root point.');
                else if exitflag == -3
                        disp('Trust radium became too small.');
                    else if exitflag == -4
                            disp('Line search error.');
                        end
                    end
                end
            end
        end


        % Calculate all variables
        Z(i,j) = (OH^-2)*(10^Kzox); %[Zn2+]
        NH3(i,j) = S; %[NH3]
        ZOH1(i,j) = Z(i,j)* OH * (10^Kzoh1); %[Zn(OH)+]
        ZOH2(i,j) = Z(i,j)* OH^2 * (10^Kzoh2); %[Zn(OH)2]
        ZOH3(i,j) = Z(i,j)* OH^3 * (10^Kzoh3); %[Zn(OH)3 -]
        ZOH4(i,j) = Z(i,j)*(OH^4) * (10^Kzoh4); %[Zn(OH)4 2-]
        ZN1(i,j) = Z(i,j)* NH3(i,j)* (10^Kznh1); %[Zn(NH3) 2+]
        ZN2(i,j) = Z(i,j)* (NH3(i,j)^2) * (10^Kznh2); %[Zn(NH3)2 2+]
        ZN3(i,j) = Z(i,j)* (NH3(i,j)^3) * (10^Kznh3); %[Zn(NH3)3 2+]
        ZN4(i,j) = Z(i,j)* (NH3(i,j)^4) * (10^Kznh4); %[Zn(NH3)4 2+]


       Ztot(i,j)=log10(Z(i,j)+ZOH1(i,j)+ZOH2(i,j)+ZOH3(i,j)+ZOH4
(i,j)+ZN1(i,j)+ZN2(i,j)+ZN3(i,j) +ZN4(i,j));
```

```
        NZ(i,j) = Z(i,j)/(10^Ztot(i,j));
        NZOH1(i,j) = ZOH1(i,j)/(10^Ztot(i,j));
        NZOH2(i,j) = ZOH2(i,j)/(10^Ztot(i,j));
        NZOH3(i,j) = ZOH3(i,j)/(10^Ztot(i,j));
        NZOH4(i,j) = ZOH4(i,j)/(10^Ztot(i,j));
        NZN1(i,j) = ZN1(i,j)/(10^Ztot(i,j));
        NZN2(i,j) = ZN2(i,j)/(10^Ztot(i,j));
        NZN3(i,j) = ZN3(i,j)/(10^Ztot(i,j));
        NZN4(i,j) = ZN4(i,j)/(10^Ztot(i,j));
        NZChP(i,j) = NZ(i,j) + NZOH1(i,j) + NZN1(i,j) + NZN2(i,j) +
NZN3(i,j) + NZN4(i,j);
        NZChN(i,j) = NZOH3(i,j) + NZOH4(i,j);
        NZNonCh(i,j) = NZOH2(i,j);

    end

    plot(k, ztot(:,j));
    plot(k, Altot(:,j),'r');

end

figure(1);
xlabel ('pH');
ylabel ('Total [Zn]');
title  ('Zn solubility plot');

% Generating the solve function
function F =revisit
% x represent the value in NH3
global OH Kzhn Kznh1 Kznh2 Kznh3 Kznh4 Kzox Cn

Z=(OH^-2)*(10^Kzox);

% Calculate F

F = x*(1/OH)*(10^-Kzhn) +  Z*x*(10^Kzn1) + 2* Z* x^2 *(10^Kzn2) +
3*Z* x^3 *(10^Kzn3) + 4*Z* x^4 *(10^Kzn4) - Cn;

end
```